Laboratoire Temps-Fréquence

ALL-OPTICAL MICROWAVE GENERATION USING FREQUENCY COMBS

Thèse présentée à la Faculté

Faculté des Sciences
Université de Neuchâtel

pour l'obtention du grade de

Docteur ès Sciences

par

Vladimir Dolgovskiy

Dipl.-Phys. (Université d'Etat de Moscou Lomonosov)

acceptée le 11.07.2012 sur proposition du jury :

Prof. Dr Thomas Südmeyer, Directeur

Prof. Dr Yann Kersalé, Rapporteur

Prof. Dr Pierre Thomann, Rapporteur

Dr Stéphane Schilt, Rapporteur

Neuchâtel, 2012

UNIVERSITÉ DE
NEUCHÂTEL

FACULTE DES SCIENCES
Secrétariat-Décanat de la faculté
Rue Emile-Argand 11
CH-2000 Neuchâtel

IMPRIMATUR POUR LA THESE

All-optical microwave generation using frequency combs

Vladimir DOLGOVSKIY

UNIVERSITE DE NEUCHATEL

FACULTE DES SCIENCES

La Faculté des sciences de l'Université de Neuchâtel autorise l'impression de la présente thèse

sur le rapport des membres du jury :

Prof. Thomas Südmeyer, directeur de thèse, Université de Neuchâtel
Prof. hon. Pierre Thomann, Université de Neuchâtel
Prof. Yann Kersalé, Institut FEMTO-ST, Besançon, France
Dr Stéphane Schilt, Université de Neuchâtel

Le doyen

Prof. Peter Kropf

Neuchâtel, le 15 novembre 2012

Téléphone : +41 32 718 21 00 E-mail : secretariat.sciences@unine.ch www.unine.ch/sciences

Acknowledgments

I would like to thank my supervisor Prof. Thomas Südmeyer for his confidence and a given full freedom of action in the end of my PhD. Without his wise and resolute direction this dissertation would not have been possible.

I am truly indebted and thankful to my advisor Dr. Stéphane Schilt for his remarkable support and assistance which helped me a lot in solving the problems and overcoming the obstacles and always pulled me out of despair. His enthusiasm and dedication to work have inspired me to take my fascination with physics seriously.

I owe sincere and earnest thankfulness to Prof. Pierre Thomann and Dr. Gianni Di Domenico who have invited me to join Laboratoire Temps-Fréquence and who have supported me with their encouragement, excellent guidance and thorough knowledge all along this PhD dissertation, being always helpful and open for discussions.

I would like to thank Laurent Giriens for the efficient and pleasant collaboration in our long-lasting yet more productive discussions on the design of the vacuum chamber and the multilayer enclosures destined to mount the high-finesse cavity.

I would like to show my gratitude to Daniel Varidel for his interest and involvement, which made the work with electronics so enjoyable and fun. I would also like to thank Marc Dürrenberger, Dominique Schenker and Patrick Scherler for their contribution and experience which they were kind to share.

Many thanks to Christian Hêche and to all the mechanical workshop, André Cornu and Isidro Fernandez, for your welcomeness, your amazing apéros and thank you for working late during the deadlines. It was a great pleasure to have you so close all that time.

I would like to thank the whole Time and Frequency department in Femto-ST in Besançon, for their hospitality and superior knowledge in the physics of microwave oscillators. It was an amazing time working together with Serge Grop and Benoît Dubois during the move of ULISS to Neuchâtel. I am indebted to Prof. Vincent Giordano, thanks to whom the collaboration and as a fact the evaluation of

our microwaves was possible, and many thanks to Prof. Yann Kersalé and Prof. Enrico Rubiola for having peerless discussions with all of you.

I would also like to address particular thanks to Prof. Ursula Keller's Ultrafast Laser Physics group from ETH Zurich for the collaboration and the development of the ERGO frequency comb, and for putting this nice laser at our disposal, without which an important part of the work presented here would not have been possible. Special thanks to Dr. Max Stumpf and Dr. Selina Pekarek for their suggestions and the conveyed experience.

Special thanks to Muriel Vallery for providing aid with the organization of conference travels and taking care of my inscription to the University. I would not have been able to spend as much time working on the dissertation unless Muriel helped out so much.

I would also like to show my gratitude to all my colleagues for the friendly and relaxed ambience which you were ensuring for most of the time. It was delightful to meat you all here and to make friends with you.

I sincerely appreciate the emotional support from my parents and girlfriend. I thank them for understanding and resisting my writing period. Besides, I would like to thank myself for not giving up.

Keywords – Mots clés

Keywords

optical frequency combs, ultra-stable lasers, time and frequency metrology, microwave generation, optical oscillator, mode-locked lasers, diode-pumped solid-state lasers, noise measurements, frequency discriminators, high finesse optical cavity

Mots clés

peignes de fréquences optiques, lasers ultra-stables, métrologie temps-fréquence, génération de micro-onde, oscillateur optique, lasers à verrouillage de modes, lasers à corps solide pompés par diode, mesures de bruit, discriminateurs de fréquence, cavité optique à haute finesse

Abstract

This thesis describes the development and realization of an ultra-stable microwave oscillator based on optical-to-microwave frequency transfer using two different optical frequency comb technologies.

Optical frequency combs establish a phase-coherent flywheel bridging between radio frequencies (RF) and optical frequencies. The main comb technologies are realized today through femtosecond Ti:sapphire (Ti:Sa) and fiber modelocked lasers as well as through recent systems based on diode-pumped solid state lasers (DPSSL). The best results on microwave generation have been obtained using Ti:Sa frequency combs thanks to their low noise levels. However, the use of those systems suffers from some practical disadvantages, such as their bulkiness, high-cost and non-efficient green pumping, limiting the area of applicability. The fiber-based ultrafast lasers represent a good alternative to Ti:Sa laser, which allow overcoming those drawbacks. However, they are less favorable in terms of noise and modulation bandwidth that is essential for the comb control. DPSSL combs proved themselves as a very promising technology yielding high peak powers without the need of any further amplification, resulting in a low quantum noise limit. These combs are beneficent in terms of low-cost diode pumping and they feature a few more important properties and achievements, such as high repetition rates, attractive for low-noise microwave generation.

In this thesis the noise properties of an Er:Yb:glass laser oscillator frequency comb, referred to as ERGO and developed in ETH Zurich, have been investigated in comparison to a commercial Er:fiber optical frequency comb. The stabilization of the CEO frequency to an RF reference results in a residual fractional frequency stability improved by a factor 20 compared to the Er:fiber comb. The measured CEO integrated phase noise is only 0.72 rad rms, which is one of the lowest values reported for a self-referenced comb the 1.5-µm spectral region.

This thesis provides new insights to the understanding of the noise in a fiber frequency comb not only from the experimental point of view but also by providing a theoretical model that studies the cross-influence between the CEO and repetition

rate stabilization loops. A significant impact of the CEO stabilization loop to both the repetition rate and an optical comb line was reported. A theoretical model was developed and showed a very good agreement with experimental data. This model enables not only the frequency noise of any comb line to be predicted, but also gives useful information on the optimization of the two feedback loop parameters required to achieve a desired noise performance at a given optical frequency.

Within this thesis, a multilayer vacuum enclosure system was designed, built, assembled and characterized, with the aim of achieving a high filtering of any external thermal perturbation that might affect the high-finesse Fabry-Perot cavity used as an optical reference in the realization of an all-optical frequency oscillator. A novel planar-waveguide external cavity diode laser technology was tested and implemented to build an ultra-stable optical reference. This laser showed several advantages in comparison to a conventional external-cavity diode laser, such as its compactness, reliability and smaller drift.

Furthermore, microwave signals were generated via optical-to-microwave frequency division using both the ERGO and an Er:fiber frequency combs. The evaluation of the generated microwave signals was conducted in collaboration with Femto-ST Besançon, who provided us a transportable ultra-stable microwave frequency reference based on a cryogenically-cooled sapphire oscillator. The microwave signals generated with the two combs showed a similar fractional frequency stability of 5×10^{-15} at 1 s and several possible present limitations have been investigated. However, the use of the ERGO comb proved to be beneficial compared to the Er:fiber comb in terms of close-to-carrier phase noise of the microwave signal, resulting in a 20 dB improvement in a large Fourier frequency range (100 Hz – 100 kHz) offset from a 10-GHz carrier. The benefit of the ERGO comb is not only favorable in the conditions of the experiments reported in this thesis, but the achieved results are also comparable or even overcoming the lowest phase noise reported to date for commercial Er:fiber combs in the same 1.5-µm spectral range using a similar stabilization scheme without the implementation of special tools. This achievement highlights a new track for the developers of photonic oscillators, such as the use of the high-repetition DPSSLs and the flexibility on the choice of wavelength achievable with various DPSSL combs.

Table of Contents

List of Acronyms

AM	amplitude modulation
AN	amplitude noise
AOM	acousto-optic modulator
BW	bandwidth
CEO	carrier-envelope offset
CSO	cryogenically-cooled sapphire oscillator
CTE	coefficient of thermal expansion
DDS	direct digital synthesizer
DFB	distributed feedback laser
DPSSL	diode-pumped solid state laser
DRO	dielectric resonator oscillator
DWDM	dense wavelength division-multiplexing
ECDL	external cavity diode laser
EDFA	erbium-doped fiber amplifiers
ELISA	cryo-cooled sapphire oscillator built by Femto-ST for ESA

EOM	electro-optic modulator
ERGO	Er:Yb:glass laser oscillator
ESA	European Space Agency
FFT	fast Fourier transform
FM	frequency modulation
FN	frequency noise
FPGA	field-programmable gate array
FSR	free-spectral range
FWHM	full width at half maximum
GPO	group-phase offset
GTI	Gires-Tournois interferometer
HF2PLL	dual input digital lock-in amplifier extended with dual PLL capabilities used as a numerical phase detector
HWHM	half-width at half maximum
ITU	international telecommunication union
LHe	liquid helium
LTF	Laboratoire Temps-Fréquence
NCO	numerical controlled oscillator

MIMO	multiple-input multiple-output
PBG	planar Bragg grating
PDH	Pound-Drever-Hall
PI	proportional-integral
PID	proportional-integral-derivative
PLC	planar lightwave circuit
PLL	phase lock loop
PM	polarization-maintaining
PM-HNLF	polarization-maintaining, highly nonlinear fiber
PSD	power spectral density
PW-ECL	planar-waveguide external cavity laser
PZT	piezoelectric transducer
RF	radio-frequency
RIN	relative intensity noise
SESAM	semiconductor saturable absorber mirror
SFP	scanning Fabry-Perot interferometer
SSB	single-sideband
TEC	thermoelectric cooler

Ti:Sa	Ti:sapphire
ULE	ultra-low thermal expansion
ULISS	ultra-low instability signal source
VCO	voltage-controlled oscillator
VCPS	voltage controlled phase shifter
VLBI	very long baseline interferometry
WGM	whispering gallery mode

Publications

Parts of this thesis are published in the following journal papers and conference proceedings.

Journal papers

1. S. Schilt, N. Bucalovic, V. Dolgovskiy, C. Schori, M.C. Stumpf, G. Di Domenico, S. Pekarek, A.E.H. Oehler, T. Südmeyer, U. Keller, P. Thomann
   Fully stabilized optical frequency comb with sub-radian CEO phase noise from a SESAM modelocked 1.5-μm solid-state laser
   Opt. Express **19**(24), 24171-24181 (2011)

2. S. Schilt, N. Bucalovic, L. Tombez, V. Dolgovskiy, C. Schori, G. Di Domenico, M. Zaffalon, P. Thomann
   Frequency discriminators for the characterization of narrow-spectrum heterodyne beat signals: application to the measurement of a sub-hertz carrier-envelope-offset beat in an optical frequency comb
   Rev. Scient. Instr. **82**(12), 123116 (2011)

3. S. Schilt, V. Dolgovskiy, N. Bucalovic, C. Schori, M.C. Stumpf, G. Di Domenico, S. Pekarek, A.E.H. Oehler, T. Südmeyer, U. Keller, P. Thomann
   Noise properties of an optical frequency comb from a SESAM-modelocked 1.5-μm solid-state laser stabilized to the 10^{-13} level
   Appl. Phys. B **109**(3), 391-402 (2012),
   DOI 10.1007/s00340-012-5072-z

4. V. Dolgovskiy, N. Bucalovic, P. Thomann, C. Schori, G. Di Domenico, S. Schilt
   Cross-influence between the two servo-loops of a fully-stabilized Er:fiber optical frequency comb
   J. Opt. Soc. Am. B, **29**(10), 2944-2957 (2012)

5. N. Bucalovic, V. Dolgovskiy, C. Schori, P. Thomann, G. Di Domenico, S. Schilt
   Experimental Validation of a Simple Approximation to Determine the Linewidth of a Laser from its Frequency Noise Spectrum
   Appl. Optics, **51**(20), 4582-4588 (2012)

6. V. Giordano, S. Grop, B. Dubois, P.-Y. Bourgeois, Y. Kersalé, G. Haye, V. Dolgovskiy, N. Bucalovic, G. Di Domenico, S. Schilt, J. Chauvin, D. Valat, E. Rubiola
   New-generation cryogenic sapphire microwave oscillators for space, metrology and scientific applications
   Rev. Sci. Instrum. 83(8), 085113 (2012)
7. N. Bucalovic, V. Dolgovskiy, M. Stumpf, C. Schori, G. Di Domenico, U. Keller, S. Schilt, and T. Südmeyer
   Effect of the Carrier-Envelope-Offset Dynamics on the Stabilization of a Diode-Pumped Solid-State Frequency Comb
   Opt. Lett. 37(21), 4428-4430 (2012)
8. V. Dolgovskiy, N. Bucalovic, G. Di Domenico, S. Schilt, S. Grop, B. Dubois, V. Giordano, M.C. Stumpf, S. Pekarek, U. Keller, T. Südmeyer
   Ultra-stable microwave generation with a diode-pumped solid-state laser in the 1.5-µm range
   In preparation

Conference papers

1. V. Dolgovskiy, S. Schilt, G. Di Domenico, D. Hofstetter, P. Thomann
   Thermal design of a high-finesse cavity enclosure for an ultra-stable laser
   EFTF 2010, 24$^{\text{th}}$ European Frequency and Time Forum, Noordwijk, The Netherland, poster
2. V. Dolgovskiy, S. Schilt, G. Di Domenico, D. Hofstetter, P. Thomann
   Towards an all-optical ultra-stable microwave oscillator based on an optical frequency comb
   Annual Meeting of the Swiss Physical Society, Basel, Switzerland, June 21-22, 2010, poster #222
3. S. Schilt, M.C. Stumpf, L. Tombez, N. Bucalovic, V. Dolgovskiy, G. Di Domenico, D. Hofstetter, S. Pekarek, A.E.H. Oehler, T. Südmeyer, U. Keller, P. Thomann
   Phase noise characterization of a near-infrared solid-state laser optical frequency comb for ultra-stable microwave generation
   Optical Clock Workshop, Torino, Italy, December 1-3, 2010, oral presentation
4. S. Schilt, V. Dolgovskiy, N. Bucalovic, L. Tombez, M.C. Stumpf, G. Di Domenico, C. Schori, S. Pekarek, A.E.H. Oehler, T. Südmeyer, U. Keller, P. Thomann
   Optical frequency comb with sub-radian CEO phase noise from a SESAM-modelocked 1.5-µm solid-state laser
   CLEO-2011, Baltimore, USA; May 1-6, 2011, oral CFK3
5. V. Dolgovskiy, S. Schilt, G. Di Domenico, N. Bucalovic, C. Schori, P. Thomann
   1.5-µm Cavity-Stabilized Laser for Ultra-Stable Microwave Generation
   Joint IFCS/EFTF Conference, San Francisco, USA, May 1-5, 2011, poster #228

6. S. Schilt, N. Bucalovic, V. Dolgovskiy, C. Schori, L. Tombez, G. Di Domenico, M.C. Stumpf, S. Pekarek, A.E.H. Oehler, T. Südmeyer, U. Keller, P. Thomann
Low-Noise Near-Infrared Optical Frequency Comb from a Solid-State Femtosecond Laser
Joint IFCS/EFTF Conference, San Francisco, USA, May 1-5, 2011, oral #132

7. S. Schilt, G. Di Domenico, N. Bucalovic, V. Dolgovskiy, L. Tombez, C. Schori, P. Thomann
Characterization of Narrow-Linewidth Beat Signals using Different Frequency Discriminators
IFCS/EFTF Conference, San Francisco, USA, May 1-5, 2011, poster #229

8. S. Schilt, V. Dolgovskiy, N. Bucalovic, L. Tombez, M.C. Stumpf, G. Di Domenico, C. Schori, S. Pekarek, A.E.H. Oehler, T. Südmeyer, U. Keller, P. Thomann
Low-Noise Near-Infrared Optical Frequency Comb from a Femtosecond Diode-Pumped Solid State Laser
CLEO-Europe 2011, Munich, Germany; May 22-26, 2011, poster EG.P.5 TUE

9. S. Schilt, N. Bucalovic, V. Dolgovskiy, C. Schori, L. Tombez, G. Di Domenico, M.C. Stumpf, S. Pekarek, A.E.H. Oehler, T. Südmeyer, U. Keller, P. Thomann
Noise properties of an optical frequency comb stabilized to the 10^{-13} level
8th International Conference on Tunable Diode Laser Spectroscopy (TDLS), Zermatt, Switzerland, July 11-15, 2011, oral presentation L2

10. N. Bucalovic, S. Schilt, V. Dolgovskiy, C. Schori, L. Tombez, G. Di Domenico, M.C. Stumpf, S. Pekarek, A.E.H. Oehler, T. Südmeyer, U. Keller, P. Thomann
Er:Yb:Glass Oscillator (ERGO): a Low-Noise Optical Frequency Comb for Frequency Metrology
Joint Annual Meeting of the Austrian & Swiss Physical Societies, EPF Lausanne, Switzerland, June 15-17, 2011, poster #236

11. V. Dolgovskiy, S. Schilt, G. Di Domenico, C. Schori, P. Thomann
All-optical low-noise microwave generation from a 1.5-μm ultra-stable laser
Joint Annual Meeting of the Austrian & Swiss Physical Societies, EPF Lausanne, Switzerland, June 15-17, 2011, poster #237

12. N. Bucalovic, S. Schilt, V. Dolgovskiy, C. Schori, L. Tombez, G. Di Domenico, M.C. Stumpf, S. Pekarek, A.E.H. Oehler, T. Südmeyer, U. Keller, P. Thomann
Er:Yb:Glass Oscillator (ERGO): a Low-Noise Optical Frequency Comb for Frequency Metrology
43rd Congress of the European Group on atomic Systems (EGAS), Fribourg, Switzerland, June 28-July 2, 2011, poster #AAP-002

13. V. Dolgovskiy, S. Schilt, G. Di Domenico, C. Schori, P. Thomann
All-optical low-noise microwave generation from a 1.5-μm ultra-stable laser
43rd Congress of the European Group on atomic Systems (EGAS), Fribourg, Switzerland, June 28-July 2, 2011, poster #AAP-005

14. T. Südmeyer, S. Pekarek, M.C. Stumpf, A.E.H. Oehler, S. Schilt, V. Dolgovskiy, N. Bucalovic, C. Schori, L. Tombez, G. Di Domenico, C. Fiebig, K. Paschke, G. Erbert, P. Thomann, U. Keller
Compact frequency combs
20th International Laser Physics Workshop, Sarajevo, Bosnia and Herzegovina, July 11-15, 2011, invited talk

15. V. Dolgovskiy, N. Bucalovic, C. Schori, P. Thomann, G. Di Domenico, S. Schilt
Correlated Impact of the Feedback Loops on the Noise Properties of an Optical Frequency Comb
DPG conference, Stuttgart, Germany; March 12-16, 2012, oral Q 28.4

16. N. Bucalovic, V. Dolgovskiy, M.C. Stumpf, C. Schori, P. Thomann, G. Di Domenico, S. Pekarek, A.E.H. Oehler, T. Südmeyer, U. Keller, S. Schilt
Importance of the Carrier-Envelope-Offset Dynamics in the Stabilization of an Optical Frequency Comb
EFTF 2012, 26th European Frequency and Time Forum, Gothenburg, Sweden; April 23-27, 2012, oral #3148

17. N. Bucalovic, V. Dolgovskiy, C. Schori, P. Thomann, G. Di Domenico, S. Schilt
Experimental Validation of a Simple Approach to Determine the Laser Linewidth from the Frequency Noise Spectrum
EFTF 2012, 26th European Frequency and Time Forum, Gothenburg, Sweden; April 23-27, 2012, poster 3147

18. V. Dolgovskiy, N. Bucalovic, C. Schori, P. Thomann, G. Di Domenico, S. Schilt
Impact of the Coupling between the Two Servo-Loops in a Self-Referenced Er:Fiber Optical Frequency Comb
EFTF 2012, 26th European Frequency and Time Forum, Gothenburg, Sweden; April 23-27, 2012, poster 3167

19. N. Bucalovic, V. Dolgovskiy, C. Schori, P. Thomann, G. Di Domenico, S. Schilt
Experimental Validation of a Simple Approximate Relation Between Laser Frequency Noise and Linewidth
CLEO-2012, San Jose, USA; May 6-11, 2012, oral CF1C.7

20. N. Bucalovic, V. Dolgovskiy, C. Schori, P. Thomann, G. Di Domenico, S. Schilt
Experimental Validation of a Simple Approximate Relation Between Laser Frequency Noise and Linewidth
Annual Meeting of the Swiss Physical Society, Zurich, Switzerland, June 21-22, 2012, poster #282

21. V. Dolgovskiy, N. Bucalovic, S. Schilt, G. Di Domenico, P. Thoman, S. Grop, B. Dubois, V. Giordano, M. Stumpf, S. Pekarek, U. Keller, T. Südmeyer
Comparison of low-noise microwave generation from ultrafast fiber and DPSSL frequency combs
Europhoton, Stockholm, Sweden, August 26-31, 2012, oral # ThD.4

22. N. Bucalovic, V. Dolgovskiy, C. Schori, P. Thomann, G. Di Domenico, S. Schilt
Experimental Validation of a Simple Relation Between Laser Frequency Noise and Linewidth
Europhoton, Stockholm, Sweden, August 26-31, 2012, poster # ThP.1

Chapter 1

Introduction

Since 1967, the unit of time of the International System of units (the SI second) has been defined to be the duration of 9'192'631'770 periods of the radiation corresponding to the transition between the two hyperfine levels of the ground state of the isotope 133 of the cesium atom. The most accurate atomic clocks to date are cold cesium atom fountain clocks with a demonstrated relative uncertainty below 10^{-15} [1]. In the last decade, novel optical clocks taking advantage of the much higher number of oscillations per unit time occurring at optical frequencies have already surpassed the best cesium fountain clocks in term of relative stability, so that a re-definition of the SI second is being discussed in the time and frequency community.

The seminal step to the realization of optical clocks was the demonstration of a self-referenced optical frequency comb by Th. Hänsch and J. Hall, honored by the Nobel Prize in Physics in 2005. This discovery has revolutionized the field of frequency metrology by enabling a direct and phase-coherent link to be established between optical and microwave frequencies, allowing microwave-to-optical and optical-to-microwave frequency transfers and comparisons to be performed in a single step. A second essential component of an optical clock is the reference optical oscillator, an ultra-stable laser with extremely narrow linewidth at the Hz level or even below that acts as a short-term flywheel oscillator before being locked to an atomic transition at longer term. A notable work in this field was published in 1999 by B. Young *et al.* [2], where a cavity stabilized laser with a fractional frequency stability at the level of 3×10^{-16} at 1 s was first reported.

Apart from their application in optical atomic clocks, optical frequency combs

and ultra-stable lasers have another important application in the generation of ultra-low noise microwave signals. Ultra-low noise microwave references are of essential importance in various applications such as high-precision radar systems and synchronization, and advanced very long baseline interferometry (VLBI). Until recently, the lowest phase noise microwave was achieved with cryogenically-cooled sapphire oscillator (CSOs) based on a high-Q whispering gallery mode in a sapphire cavity cooled down to cryogenic temperature. However, CSOs have some drawbacks related to their high cost of maintenance imposed by the liquid helium (LHe) cooling. A notable exception is the cryocooled sapphire oscillators developed at Femto-ST in Besançon, which do not require LHe-cooling and has even been made transportable [3].

The lowest phase noise microwave generation was demonstrated in 2011 using Ti:sapphire (Ti:Sa) optical frequency combs referenced to an ultra-stable laser [4]. In such a system, a frequency comb is phase-stabilized to an ultra-stable optical reference in order to transfer the high relative frequency stability of the laser to a microwave signal. In this scheme, the comb acts as a frequency divider that scales down the phase noise of the laser by a huge number corresponding to the ratio of the optical and microwave frequencies, leading to the very low phase noise of the generated microwave signal.

In this thesis, *ultra-stable microwave generation has been developed and characterized based on a 1.5-μm optical reference*. This has required three main tasks to be performed [4,5]:

i) Development and characterization of a reference optical oscillator;
ii) Full characterization of the noise properties of optical frequency combs used as a phase-coherent bridge between optical and microwave frequencies;
iii) Microwave generation using a frequency comb acting as an optical-to-microwave frequency divider and evaluation of the generated microwave signal.

Two different laser technologies have been used and compared for the realization of the ultra-stable laser, i.e. an external cavity diode laser (ECDL) and a planar-waveguide external cavity laser (PW-ECL). An ultra-low thermal expansion (ULE) high-finesse Fabry-Perot cavity was used as an ultra-stable optical frequency

reference for the laser stabilization. A two-layer thermal enclosure has been designed, machined and implemented to thermally-isolate the cavity from external temperature fluctuations. A special emphasis was put on obtaining a high homogeneity of the cavity temperature and a good insulation from external temperature variations, which was achieved by a measured thermal time constant of more than 6 days.

Two different frequency comb technologies have been characterized and studied with respect to their potential for low-noise microwave generation. A commercial Er:fiber comb, which has already been widely and successfully used in optical-to-microwave frequency division, was compared with a novel fully-stabilized optical frequency comb generated from a diode-pumped solid state laser (DPSSL) in the 1.5-µm spectral region. Despite their reliability and moderate cost in comparison to Ti:Sa combs, Er:fiber combs suffer from a few drawbacks such as a low-Q factor cavity and a limited gain bandwidth. In contrast to Er:fiber combs, DPSSL combs usually have a high-Q cavity and can emit a much higher optical power than Er:fiber combs, making possible coherent octave spanning supercontinuum generation without the need for further amplification or pulse compression. Furthermore, they still exhibit the advantages of higher reliability and lower cost diode-pumping as compared to Ti:Sa combs. A passively modelocked Er:Yb:glass oscillator, referred to as ERGO and developed at ETH Zurich has been characterized in details with respect to its noise properties and has been compared to the Er:fiber comb. The advantages of this novel comb technology in the 1.5-µm spectral range are demonstrated.

The full-stabilization of a frequency comb (to either a microwave or an optical reference) requires the two degrees of freedom of the comb to be stabilized. This is generally done using two actuators to apply a feedback signal to stabilize the comb repetition rate and the carrier-envelope offset (CEO). However, these two stabilization loops are not independent and some coupling may occur. The impact of these coupled servo loops has been studied in an Er:fiber comb, showing for the first time how a positive impact of the CEO frequency stabilization improves the noise of the repetition rate and of an optical comb mode. A theoretical model predicting the impact of this coupling has been also developed.

Combining these different developments, ultra-stable microwave signals were

generated by optical frequency division from the same developed ultra-stable optical reference using each comb technology. The evaluation and detection of the microwave signal was performed in collaboration with Femto-ST (Besançon), using the transportable ultra-low instability signal source (ULISS) developed by this group based on a cryogenically-cooled sapphire oscillator. Results of the microwave generation have shown some beneficial use of the ERGO comb compared to the Er:fiber comb that will be discussed.

The thesis is organized as follows: Chapter 2 provides an overview of the characterization of oscillators in terms of frequency noise and stability, and presents experimental tools used for the characterization of the noise properties of lasers and frequency combs. In Chapter 3 the ultra-stable laser is introduced, starting with the basics of laser stabilization to high-finesse cavities and given a further detailed characterization of the different elements composing the ultra-stable optical oscillator. The reference cavity is characterized from the point of view of its spectral and thermal properties. A discussion of the fundamental limits is provided and the design of a thermal enclosure for the cavity is reported. In Chapter 4, stabilization of an Er:fiber comb is studied, starting with the basics of frequency combs and providing a detailed characterization of the stabilization of a commercial Er:fiber comb. A complementary theoretical model accounting for the correlated noise sources is presented and verified experimentally for the description of the stabilized comb noise properties. The effect of the coupling between the stabilization loops in this fiber comb is shown experimentally and a prediction on the noise of an arbitrary comb line is given. A novel self-referenced DPSSL comb is described in Chapter 5, followed by its complete noise characterization. The microwave generation using the two types of frequency comb discussed in the previous chapters is described in Chapter 6, starting from referencing the comb to an optical oscillator and further microwave detection and evaluation. A brief description of the reference CSO used in the experiment is presented and the microwave signals generated from the Er:fiber and DPSSL combs are evaluated and compared in terms of fractional frequency stability and phase noise. A summary of the main results is given in Chapter 7.

Chapter 2

Noise in oscillators and characterization methods

2.1 Introduction

All along this thesis, one had to deal with the characterization of low-noise signals, such as ultra-stable lasers, optical frequency combs and ultra-stable microwave. This chapter introduces some basic analytical tools and experimental methods for the characterization of such signals, in terms of phase/frequency noise and fractional stability (Allan deviation).

Section 2.2 first reviews some basics of time and frequency.

A simple concept to determine the linewidth of a laser from its frequency noise spectrum was recently proposed by Laboratoire Temps-Fréquence (LTF) [6]. This concept provides a simple metric to determine which noise spectral components contribute to the laser linewidth and has thus been regularly used throughout this thesis. This simple approach is presented in Section 2.3.

Experimental methods to characterize the noise properties of such signals are also presented in this chapter. For this purpose, various frequency discriminators that have been extensively used in the experimental work of this thesis for the characterization of the frequency noise properties of lasers, frequency combs or ultra-stable microwave, are presented and characterized in Sections 2.4 and 2.5, respectively.

2.2 Basics

2.2.1 Phase and frequency noise

The linewidth, defined as the full width at half maximum of the lineshape function, is a commonly used parameter to describe the spectral properties of a laser. However, this parameter depends on the observation time and contains poor information about the spectral distribution of the laser noise. A more useful tool to measure the spectral purity of an oscillator is based on the direct recording of the phase time series $\phi(t)$ and further Fourier transformation of this signal. In the case of a deterministic signal, the power spectral density (PSD) is defined as the square modulus of the Fourier transform. However in the case of a random process $x(t)$, the formal definition of the PSD slightly differs and is written in the case of the one-sided PSD defined in the positive-frequency plane as:

$$S_x(\omega) = 2\int_{-\infty}^{+\infty} R(\tau)e^{-i\omega\tau}d\tau\,, \tag{2.1}$$

where

$$R(\tau) = \mathbb{E}\big\{x(t)x(t+\tau)\big\} \tag{2.2}$$

is the autocorrelation function of the process $x(t)$. $\mathbb{E}\{\ \}$ denotes a mathematical expectation. The angular frequency ω is used all along this thesis to represent the variable in the Fourier domain to be compatible with the notations used and explained in Chapter 4 (see Section 4.4).

In practice it is sometimes easier to estimate $S_x(\omega)$ from the Wiener-Khinchin theorem for an ergodic stationary process with a power spectrum measured by averaging a multiple number of realizations:

$$S_x(\omega) = \lim_{T\to\infty}\left\langle \frac{2}{T}\left|\int_{-\infty}^{+\infty} x(t)e^{-i\omega t}dt\right|^2\right\rangle. \tag{2.3}$$

For instance, in a fast Fourier transform (FFT) spectrum analyzer the spectrum is inferred from a digitized time series and the measured PSD represents directly the amplitude noise PSD of the input signal in V^2/Hz.

Measurement of the phase noise PSD requires the implementation of a phase discriminator, converting phase fluctuations into measurable amplitude fluctuations.

The one-sided phase noise PSD of the phase fluctuations $\phi(t)$ is referred to as $S_\phi(\omega)$, measured in rad^2/Hz. Another quantity widely used by the engineers is the single-sideband (SSB) phase noise, defined as:

$$\mathcal{L}(\omega) = 10\log\left(\frac{1}{2}S_\phi(\omega)\right), \tag{2.4}$$

and measured in dBc/Hz.

Frequency fluctuations of an oscillator are interrelated with its phase fluctuations as

$$\Delta\nu(t) = \frac{\Delta\dot{\phi}(t)}{2\pi}. \tag{2.5}$$

From this equation one can easily derive the frequency noise PSD, related to the phase noise PSD as

$$S_{\delta\nu}(\omega) = \left(\frac{\omega}{2\pi}\right)^2 S_\phi(\omega). \tag{2.6}$$

2.2.2 Allan deviation

For the description of clocks and frequency standards in terms of stability, the fractional frequency fluctuations $y(t) = \big(\nu(t) - \nu_0\big)\big/\nu_0$ are usually considered, where $\nu(t)$ is the fluctuating clock frequency and ν_0 is the nominal frequency of the oscillator. The stability of an oscillator is commonly measured with a frequency counter, where the reading of the counted oscillator frequency is averaged over a measurement time interval of duration τ. Denoting the time averaging by an overbar, the average of the fractional frequency fluctuation at the k-th measurement interval can be written as

$$\overline{y}_k(\tau) = \frac{1}{\tau}\int_{k\tau}^{(k+1)\tau} y(t)dt. \tag{2.7}$$

The Allan deviation is a conventional tool for the characterization of clocks and frequency standards. It is defined as a mathematical expectation of a two sample variance, which is replaced by a simple mean in practice, i.e.

$$\sigma_y(\tau) = \sqrt{\frac{1}{N-1}\sum_{k=1}^{N-1}\frac{\left(\overline{y}_{k+1}(\tau) - \overline{y}_k(\tau)\right)^2}{2}}\,. \tag{2.8}$$

The Allan deviation can be obtained from the frequency (or phase) noise PSD as:

$$\sigma_y(\tau) = \sqrt{\int_0^{+\infty} \frac{S_\nu(\omega)}{{\nu_0}^2} 2\frac{\sin^4(\omega\tau/2)}{(\omega\tau/2)^2}\frac{d\omega}{2\pi}}\,, \tag{2.9}$$

which shows that the Allan deviation filters the frequency noise PSD.

The inverse operation, however, is impossible as the information about the frequency noise is lost in the measured stability data.

2.3 A simple approximation for the linewidth of a laser

It is possible to calculate the line profile from the frequency noise PSD containing the complete information about the laser noise at different frequency components, while the reverse process is not possible. However, the analytical solution exists only in the ideal case of a pure white frequency noise [7], which leads to the well-known Lorentzian lineshape described by the Schawlow-Townes-Henry linewidth [8,9]. The universal linewidth determination procedure derived by D. Elliott *et al.* [10] involves a two-step numerical integration procedure, where the autocorrelation function of the electric field is determined in the first integration step

$$\Gamma_E(\tau) = {E_0}^2 e^{i2\pi\nu_0\tau} \exp\left\{-2\int_0^{+\infty} S_{\delta\nu}(\omega)\frac{\sin^2(\omega\tau/2)}{(\omega/2\pi)^2}d(\omega/2\pi)\right\}, \tag{2.10}$$

and the PSD of the laser optical field is obtained in a second-step integration,

$$S_E(\nu) = 2\int_{-\infty}^{+\infty} e^{-i2\pi\nu\tau}\Gamma_E(\tau)d\tau\,. \tag{2.11}$$

This is a rather complicated procedure that requires to evaluate $\Gamma_E(\tau)$ in Eq. (2.10) over an ensemble of correlation times τ, determining the resolution (overall τ range) and the Nyquist frequency of the calculated optical spectrum (τ sampling rate).

A simple approximation for the determination of the linewidth of a laser from the frequency noise PSD has been recently proposed by our group [6]. The concept of the β-separation line introduced in the frequency noise PSD in [6] allows identifying the spectral components that contribute to the linewidth (Figure 2.1):

i) The frequency noise PSD is separated into two regions by the β-separation line, defined as:

$$S_{\delta\nu}(\omega) = \frac{8\ln 2}{\pi^2} \cdot (\omega/2\pi)\,, \tag{2.12}$$

with a significantly different influence on the profile of the optical line.

ii) Only the slow frequency modulation area, where $S_{\delta\nu}(\omega) > (8\ln 2/\pi^2) \cdot (\omega/2\pi)$ contributes to the linewidth of the signal.

iii) In the fast frequency modulation area, where $S_{\delta\nu}(\omega) < (8\ln 2/\pi^2) \cdot (\omega/2\pi)$ the frequency fluctuations only contribute to the wings of the lineshape, but not to the linewidth itself.

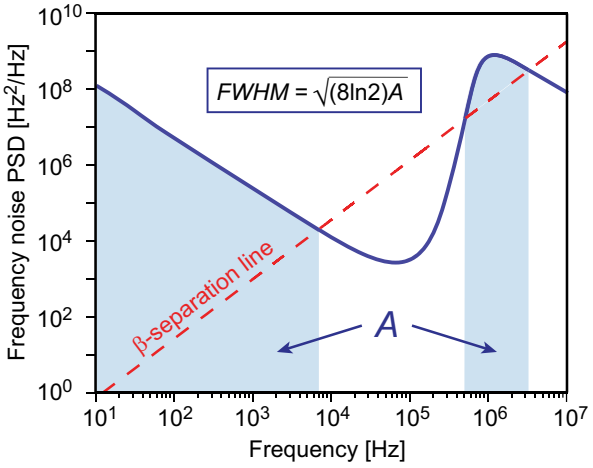

Figure 2.1: Graphical representation of the simple approximation proposed to determine the linewidth of a laser from its frequency noise PSD $S_{\delta\nu}(\omega)$, calculated from the surface A of the slow modulation area. The shadowed areas on this schematized frequency noise spectrum represent the surface A that encloses all spectral components for which $S_{\delta\nu}(\omega)$ exceeds the β-separation line $S_{\delta\nu}(\omega) = (8\ln 2/\pi^2) \cdot (\omega/2\pi)$.

Following this approach, the linewidth (full width at half maximum, FWHM) can be estimated from the area under the frequency noise PSD at low modulation frequencies, i.e. at those frequencies at which the frequency noise PSD exceeds the

β-separation line:

$$FWHM = \sqrt{8 \ln 2 \; A} \, . \tag{2.13}$$

The flicker noise ($1/f$ noise) makes the linewidth strongly depend on the observation time t_0. Mathematically, the area is obtained by integrating the product between the frequency noise PSD and the Heaviside step function $\mathcal{H}(x)$ ($\mathcal{H}(x) = 0$ if $x < 0$ and $\mathcal{H}(x) = 1$ if $x \geq 1$) from a low-frequency cutoff proportional to the inverse of the observation time t_0, introduced here to prevent the divergence of the integral

$$A = \int_{2\pi/t_0}^{+\infty} \mathcal{H}\left(S_{\delta\nu}(\omega) - \frac{8 \ln 2}{\pi^2} (\omega/2\pi) \right) S_{\delta\nu}(\omega) d(\omega/2\pi) \, . \tag{2.14}$$

In absence of diverging low-frequency noise the integration down to zero frequency (infinite observation time) is possible.

2.4 RF discriminators

As it was mentioned in Section 2.1 the FWHM linewidth gives only an incomplete characterization of an optical oscillator and does not allow assessing the phase noise frequency distribution. It is however possible to determine the white-frequency noise and the flicker noise from the respective Lorentzian and Gaussian contributions to the Voigt line profile [11]. In order to assess the frequency noise of a laser it is required to convert frequency fluctuations into amplitude fluctuations, which is the role of a frequency discriminator.

Basically, frequency discriminators can be split into two categories: optical discriminators and radio-frequency (RF) discriminators. Optical frequency discriminators directly convert optical frequency fluctuations of a laser into intensity fluctuations that are detected by a photodetector. Optical discriminators are typically devices displaying a frequency-dependent transmission in a restricted frequency range, such as gas-filled cells near an atomic/molecular resonance (Doppler-broadened [12-14] or sub-Doppler [15]), Fabry-Perot resonators [16] or unbalanced two-beam interferometers [17].

As it is not always possible to have a proper optical discriminator at the considered laser wavelength, another approach consists in heterodyning the laser under test with a second laser, either similar to the first one or with a negligible frequency

noise, and subsequently analyzing the generated RF beat signal. The frequency noise of the heterodyne beat can be analyzed in the frequency domain using a suitable RF discriminator. In this section, different types of RF frequency discriminators are presented and discussed in view of their extensive use for the characterization of lasers, frequency combs and ultra-stable microwave in the next chapters of this thesis.

A frequency discriminator is characterized by its sensitivity (or discrimination slope D_ν in [V/Hz]), i.e. its ability to convert frequency fluctuations $\delta\nu(t)$ of the input signal into variations of an output voltage $V(t)$. The discriminator slope is an important parameter: the higher D_ν , the better the frequency noise conversion. The frequency noise PSD of the input signal ($S_{\delta\nu}(\omega)$ in [Hz^2/Hz], where $\omega/2\pi$ is the Fourier frequency) is retrieved from the PSD of the output voltage ($S_V(\omega)$ in [V^2/Hz]) taking into account the discriminator slope:

$$S_{\delta\nu}(\omega) = \frac{S_V(\omega)}{{D_\nu}^2}. \tag{2.15}$$

2.4.1 Analog phase-locked loop discriminator

Following the work of L. Turner *et al.* [18], an analog phase lock loop (PLL) frequency discriminator was built and characterized in detail. The basic principle of this discriminator is to phase-lock a voltage-controlled oscillator (VCO) to the RF beat signal to be analyzed, using a high-bandwidth PLL. If the loop bandwidth is sufficient, the VCO follows any frequency fluctuations $\delta\nu(t)$ of the input RF beat and the control voltage of the VCO $V(t)$ reflects the frequency fluctuations of the input signal. Once the response of the VCO is known (in [Hz/V]), the analysis of the fluctuations of the control voltage can be directly converted into frequency fluctuations of the input RF beat (within the loop bandwidth). While L. Turner *et al.* used a single integrated circuit PLL for their frequency discriminator, the PLL discriminator presented here uses discrete off-the-shelf analog components (VCO, phase detector and servo controller). This approach offers a larger flexibility in the adjustment of the PLL parameters (gain, bandwidth), which enables the PLL characteristics to be optimized with respect to the properties of the signal under test (e.g. to achieve the largest bandwidth or the lowest noise floor). A scheme of the PLL discriminator is shown in Figure 2.2. The VCO (Mini-Circuits ZX95-209-S+)

operates in the 199-210 MHz range, with a nominal tuning coefficient of 1.5 MHz/V. A double-balanced mixer (Mini-Circuits ZP-1LH) is used as a phase detector, followed by a 10-MHz low-pass filter to suppress high frequency components. Finally, the loop is closed with a high-speed servo controller (New-Focus LB1005-S) with a proportional-integral (PI) corner frequency adjustable from 10 Hz up to 1 MHz and a proportional gain between −40 dB and +40 dB.

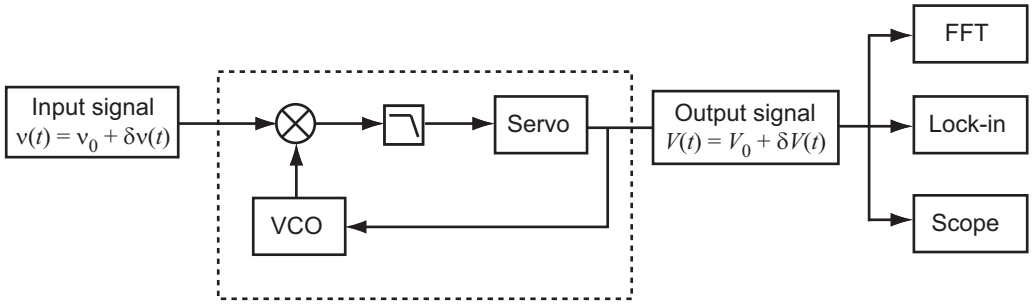

Figure 2.2: Schematic representation of the analog PLL discriminator. The control voltage $V(t)$ of the VCO constitutes the output signal that replicates the input frequency variations $\delta\nu(t)$. This signal is analyzed using an oscilloscope, a lock-in amplifier or an FFT spectrum analyzer.

2.4.2 Miteq RF discriminator

Simple plug-and-play RF discriminators are commercially available in different frequency ranges from various suppliers of RF components. The model FMDM 21.4/2-4 from Miteq as been used, which operates in the 18-26 MHz range, with a typical peak-to-peak bandwidth of 8 MHz and a linear bandwidth of 4 MHz as specified by the manufacturer. The operation of this discriminator is based on the use of an input limiting amplifier to drive two staggered tuned L-C circuits. Opposing rectification of the circuits creates the discriminator "S" curve and a video amplifier is finally utilized to provide adequate output slope. The ability to precisely align the skirts of the tuned circuits, which represents the discriminator linear bandwidth, is an advantage of this type of design. The nominal response of this discriminator is 1 V/MHz.

2.4.3 Numerical phase-locked loop HF2PLL discriminator

The HF2LI from Zurich Instruments, Switzerland, is an all-numerical instrument consisting of a dual input digital lock-in amplifier extended with dual PLL capabilities. The lock-in amplifiers have a frequency bandwidth ranging from 1 µHz to 50 MHz (with a sampling rate of 210 Msamples/sec), a dynamic reserve of 120 dB and an input voltage noise of 5 $\mathrm{nV}/\sqrt{\mathrm{Hz}}$. The instrument is based on a Field-Programmable Gate Array (FPGA) which permits computations with large numerical precision and short processing time. Moreover, the lock-in shortest integration time constant of 800 ns, lower by one order of magnitude than in other commercially-available lock-in amplifiers, makes it suitable for wide bandwidth demodulation and as a phase detector for a PLL (referred to as HF2PLL) that replaces all the analog components in the dotted box in Figure 2.2 by their numerical counterparts.

The HF2PLL runs directly on the lock-in FPGA, ensuring a precise control of the PLL dynamics and resulting in a maximum −3 dB bandwidth of 60 kHz. The HF2PLL has similar functional blocks as the analogue PLL described in Section 2.4.1, with two notable differences:

i) The phase detector makes use of the lock-in demodulation chain (including its low-pass filters) since its purpose is to determine the phase difference between input and reference signals. This phase difference is the lock-in output channel *Theta*, as calculated directly from the quadrature (Y) and in-phase (X) components of the demodulated signal. The advantage of this approach compared to the analog PLL is its high rejection of amplitude modulations of the input signal, thereby minimizing the amplitude noise sensitivity of the HF2PLLdiscriminator. *Theta* is the error signal and constitutes the input of the following numerical proportional-integral-derivative (PID) controller, as in the analog case.

ii) The VCO is replaced by a functionally equivalent numerical controlled oscillator (NCO), whose role is to keep track of the reference signal phase (from which the in-phase and quadrature reference signals are derived). The rate at which the NCO phase changes, which is the reference signal instantaneous frequency, is $f(t) = f_c + dF$, where f_c is a selectable PLL center frequency and the frequency deviation dF (in Hz) is the PID con-

troller output. When the HF2PLL discriminator is used to characterize a heterodyne beat signal, *dF* is output as an analog signal with a software-selected gain (from 0.75 nV/Hz to 1.6 V/Hz).

In comparison with the analog PLL where all electronic components suffer from $1/f$ and white noise, the noise sources in the digital PLL are confined to the analog-to-digital converter at the lock-in input stage and to the analog *dF* output, since the numerical noise can be made arbitrarily small by increasing the internal numerical precision. On the other hand, the measurement bandwidth of analog PLLs is usually larger than their digital counterparts.

2.4.4 Digital phase detector DXD200

A digital phase detector (DXD200 module from MenloSystems, Germany) with a wide linear range of operation of $\pm 32 \times 2\pi$ has been characterized for comparison with the other frequency discriminators. The basic element of this digital phase detector is a differential period counter, where the reference signal counts up and the RF beat signal counts down [19]. The counter has a range from 0 to 64 and is initialized at 32. The phase error can track a $\pm 32 \times 2\pi$ phase difference between the two signals. The counter signal is then fed into a digital to analog converter to generate a signal proportional to the relative phase, with a nominal phase discrimination factor $D_\phi = 3.3\ \text{V}/(32 \times 2\pi) = 0.016$ [V/rad]. While this detector should provide an ideal linear response in a phase range of $\pm 32 \times 2\pi$, this is not the case in reality due to the presence of several nonlinearities in its range of operation. This effect was investigated over the entire range of operation of the phase detector by comparing two signals with a slightly different frequency ($f_1 = f_{\text{ref}} = 20$ MHz, $f_2 = f_1 + \Delta$ with Δ in the range of 10-100 mHz), in order to slowly scan the output voltage (phase difference resulting from the accumulated phase shift between the two signals). Some of the nonlinearities are directly observable in the DC output voltage of the phase detector (see Figure 2.3a). Next, a small frequency modulation (at a rate $\omega_{\text{mod}}/2\pi = 10$ kHz with a span of $\Delta f = 50$ Hz) was applied to one of the 20-MHz carrier in order to measure the frequency response (in amplitude and phase) of the phase detector using a lock-in amplifier and to subsequently determine the detector sensitivity (in V/rad), as also described in Section 2.5.1. In order to be able to resolve the narrow peaks that occur at some specific points in the detector response as a result of the nonlinearities, a small modulation index

$\beta = (\Delta f/2)/(\omega_{\mathrm{mod}}/2\pi)$ was used. In that case, the measured lock-in signal corresponds to the derivative of the phase detector response and the sensitivity was obtained by normalizing this signal by the modulation depth β. The outputs of the lock-in amplifier (X and Y components) were recorded with an acquisition card (National Instruments NI USB-6008), together with the phase detector operating DC voltage, during a phase sweep.

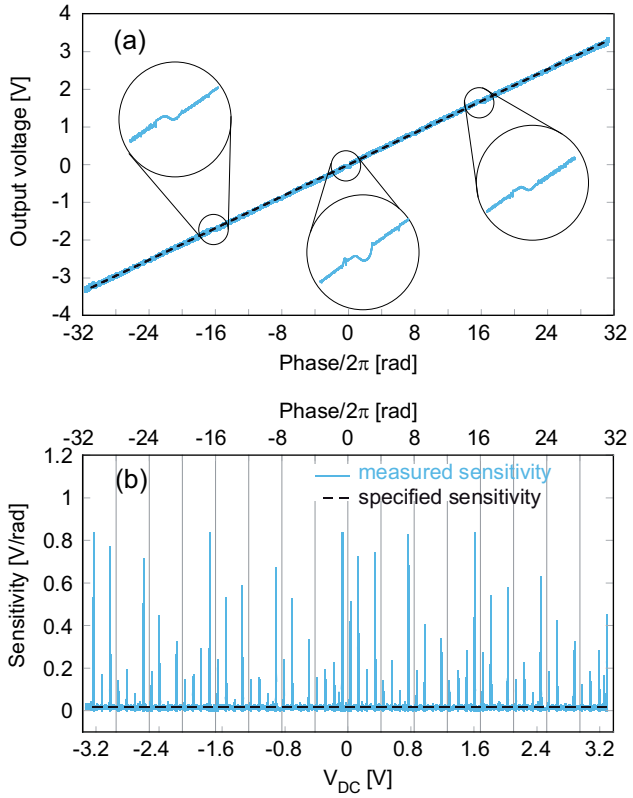

Figure 2.3: Difference between the ideal (dashed line) and actual (light thick curve) response of the digital phase detector. (a) DC analog output voltage as a function of the phase difference between the two inputs; some nonlinearities are visible at the encircled points. (b) Highlight of the nonlinearities of the detector occurring roughly every 2π phase difference. This curve has been obtained by applying a frequency-modulated carrier at one input of the device and performing lock-in detection at the output to determine the discriminator sensitivity. The dashed line corresponds to the average slope of the DC curve (a).

The actual response displayed in Figure 2.3b is not as smooth as expected and shows the presence of many nonlinearities, regularly separated by a 2π phase difference. At these points, the sensitivity of the detector for small signals can be locally

enhanced by a factor up to 50 (0.8 V/rad). In order to have a proper discriminator of known sensitivity, the digital phase detector should be operated at a point where its response is constant, i.e., away from the nonlinear points. All the results shown in the following sections are obtained in such conditions. Finally, we should notice that the DXD200 acts as a phase discriminator, so that the corresponding frequency sensitivity is given by $D_\nu(\omega) = D_\phi/(\omega/2\pi)$.

2.5 Characterization of RF discriminators

2.5.1 Sensitivity and bandwidth

The sensitivity of each discriminator has been determined by applying a frequency-modulated input signal with a modulation amplitude (peak-to-peak) $\Delta f = 1$ kHz ($\Delta f = 100$ Hz in the case of the digital phase detector DXD200) at a varying modulation frequency $\omega_{\mathrm{mod}}/2\pi$ using a calibrated, high-bandwidth reference VCO. A 207-MHz carrier frequency was used with the analog PLL discriminator and a 20-MHz carrier frequency with the other discriminators, obtained by mixing the 207-MHz VCO signal with a 227-MHz reference signal and subsequent low-pass filtering. The modulation frequency $\omega_{\mathrm{mod}}/2\pi$ was scanned in the range from 0.1 Hz to 10 MHz and the demodulated output signal of the discriminators was measured in amplitude and phase using a lock-in amplifier referenced to $\omega_{\mathrm{mod}}/2\pi$ (standard lock-in, model Stanford Research Systems SR830, up to 100 kHz and RF lock-in, model SR844, at higher frequency). Finally, the transfer function of each device was obtained by normalizing the lock-in output signal to the input frequency modulation amplitude Δf. One defines here the bandwidth of a discriminator as the frequency range in which the discriminator sensitivity remains within $\pm 10\%$ (± 0.9 dB) of its value at $\omega_{\mathrm{mod}}/2\pi = 1$ kHz. The sensitivities (or discriminator slopes, in V/Hz) reported here are generally given for the discriminator output connected to a high impedance load. The only exception concerns Miteq discriminator, used with a 93-Ω load as specified in the manufacturer's datasheets.

The amplitude and phase of the transfer function of each discriminator are displayed in Figure 2.4. The result for the analog PLL is shown for a maximum PI corner frequency of 1 MHz and a PI gain adjusted to optimize the PLL operation. The response of the analog PLL slightly depends on the PLL settings (gain and PI-corner): the low frequency sensitivity is unaffected by the PLL parameters, but at

high frequency, the position and amplitude of the oscillation (servo bump) varies with these parameters.

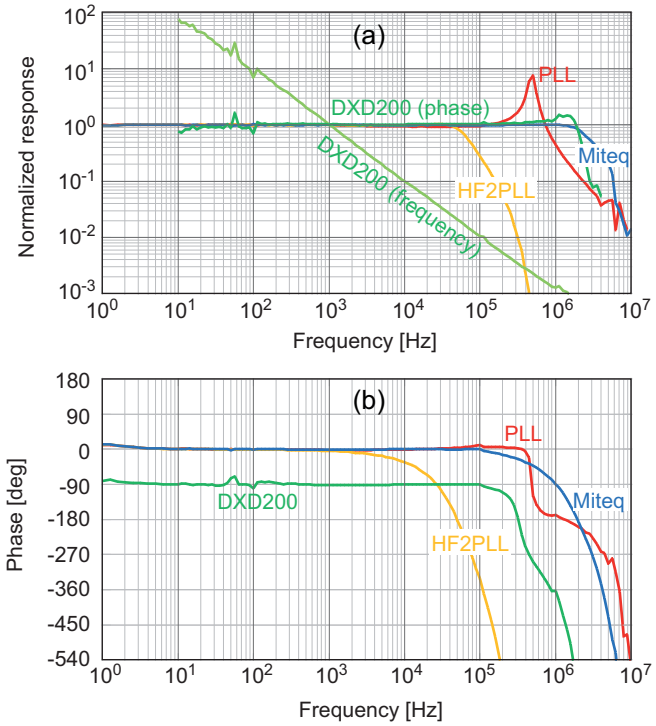

Figure 2.4: Amplitude (a) and phase (b) of the normalized transfer function of the different discriminators, measured by applying a frequency-modulated input carrier and performing lock-in detection of the discriminator demodulated signal. Each transfer function has been normalized by the discriminator sensitivity measured at 1 kHz modulation frequency ($D_\nu = 7 \cdot 10^{-7}$ [V/Hz] for PLL, $D_\nu = 1.25 \cdot 10^{-6}$ [V/Hz] for Miteq, $D_\nu = 10^{-3}$ [V/Hz] for HF2PLL, $D_\nu = 1.8 \cdot 10^{-5}$ [V/Hz] or $D_\phi = 1.8 \cdot 10^{-2}$ [V/rad] for DXD200). The amplitude response of the digital phase detector DXD200 is represented both in terms of response to frequency and phase modulation.

The analog PLL has a typical bandwidth of 200 kHz (defined at ±0.9 dB as mentioned before) with a discriminator slope of 0.7 V/MHz. The Miteq discriminator has the largest bandwidth of 2 MHz with a discriminator slope of 1.25 V/MHz, obtained for 0 dBm input signal, but this sensitivity significantly depends on the signal amplitude (e.g., it is reduced to 0.86 V/MHz at −6 dBm input signal). The HF2PLL has a lower bandwidth of 50 kHz, but its sensitivity is much higher and can be adjusted by software in the range from 0.75 nV/Hz to 1.6 V/Hz. For the Miteq- and analog PLL discriminators, an instantaneous response to frequency fluc-

tuations is obtained up to $\omega_{\text{mod}}/2\pi > 100$ kHz, while a significant phase shift is introduced at higher frequencies. In the HF2PLL, the phase shift occurs at much lower frequency, which is compatible with the amplitude attenuation. The sensitivity of the digital phase detector DXD200 decreases as $(\omega_{\text{mod}}/2\pi)^{-1}$ as the module acts as a phase comparator. The measured phase discriminator is around 0.018 V/rad (0.016 V/rad expected from specifications, corresponding to $D_\phi = 3.3\ \text{V}/(32 \cdot 2\pi)$). The phase detector introduces a $-90°$ phase shift at low Fourier frequency as it acts as a phase detector and we are assessing its response in terms of frequency. At Fourier frequencies higher than 100 kHz, a significantly larger phase shift appears. The ±0.9 dB bandwidth of DXD200 is ~1 MHz.

2.5.2 Frequency range

The *total frequency range* of each discriminator is defined here as the frequency interval in which the discriminator operates, and the *linear frequency range* as the frequency interval in which the response is within ±10% (±0.9 dB) of the discriminator sensitivity determined in Section 2.5.1. The frequency range of each discriminator, measured at 1 kHz modulation frequency, is shown in Figure 2.5. Both the analog PLL and the Miteq discriminators have a wide linear frequency range of several megahertz (7 MHz for the analog PLL and 9 MHz for Miteq). For the numerical PLL, the situation is different. The input carrier frequency can be anywhere in the range of ~1-49 MHz, but the amplitude of the maximum detectable frequency fluctuations around this carrier depends on the selected sensitivity of the demodulator output. As the analog output of the HF2LI instrument is limited to ±10 V, the maximum frequency fluctuation Δf_{max} which can be measured for a sensitivity D_ν (in V/Hz) is $\Delta f_{\text{max}} = \pm 10\ \text{V}/D_\nu$. While a high sensitivity can be selected with the HF2PLL instrument, the drawback is a reduced frequency range.

Finally, the digital phase detector DXD200 can operate at any carrier frequency between 0.5 MHz and more than 200 MHz (provided that a reference signal at the same frequency is available), but the range of detectable fluctuations is limited to $\pm 64\pi$ in terms of phase and is thus extremely narrow.

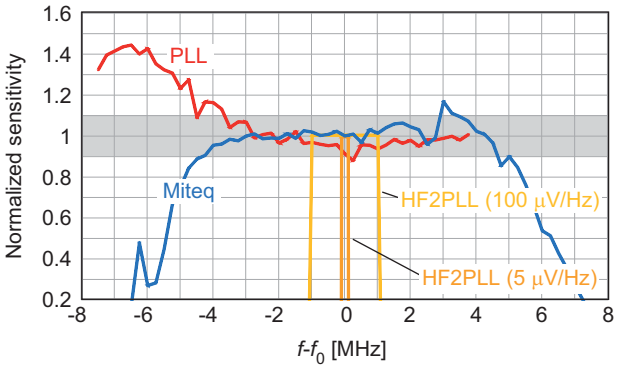

Figure 2.5: Normalized sensitivity of the frequency discriminators (measured for 1 kHz modulation frequency) as a function of the carrier frequency detuning. The grey area indicates the linear frequency range Δf_{lin} of each discriminator, defined as the frequency interval for which the discriminator response differs by less than ±10% (±0.9 dB) from its nominal sensitivity. The frequency range of the HF2PLL is inversely proportional to the software-selected sensitivity D_ν ($\Delta f_{\text{lin}} = \pm 10\ \text{V}/D_\nu$) and is shown here for two particular cases ($D_\nu = 100$ µV/Hz and $D_\nu = 5$ µV/Hz) for illustration.

2.5.3 Noise floor

A relevant characteristic of a frequency discriminator is its noise floor, which represents the smallest detectable frequency fluctuations with a signal-to-noise ratio of one. The noise floor of the different discriminators was measured with an FFT spectrum analyzer for Fourier frequencies up to 100 kHz and with an electrical spectrum analyzer at higher frequencies, when a stable, low-noise carrier was applied to the input. As previously, a 207-MHz carrier was used with the analog PLL discriminator and a 20-MHz carrier frequency with the other discriminators. The PSD of the discriminators output voltage has been converted into frequency noise PSD using the corresponding sensitivities previously determined. Results are shown in Figure 2.6.

The noise floor of the analog PLL-discriminator significantly depends on the amplitude of the input signal and on the gain settings of the PI controller. It is presented here for a PI gain adjusted to optimize the noise floor. Operation at too-high gain may increase the noise floor by one or two orders of magnitude at Fourier frequencies above 10 Hz. In the range 100 Hz – 10 kHz, a white frequency noise floor is observed (~10^{-3} Hz^2/Hz). Out of this range, the noise floor scales as $(\omega/2\pi)^{-2}$ at low frequency, resulting from the VCO white frequency noise that is multiplied by

$(\omega/2\pi)^{-2}$ due to the Leeson effect [20] and linearly with $\omega/2\pi$ at high frequency, resulting from the PLL servo bump.

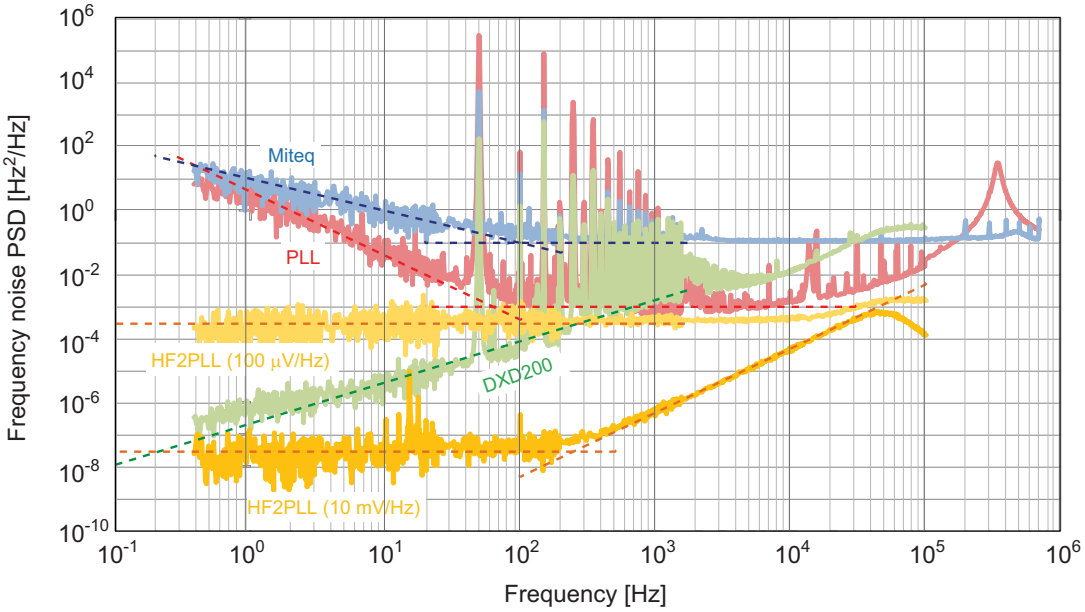

Figure 2.6: Noise floor of the different discriminators. The noise floor of the analog PLL depends on the PI gain and is presented here in an optimized configuration. The white frequency noise of the HF2PLL (at low frequency) results from white noise at the analog output and thus scales as $1/D_\nu^2$ for sensitivities up to $D_\nu = 10$ mV/Hz. It is displayed here for two cases, $D_\nu = 100$ µV/Hz and $D_\nu = 10$ mV/Hz. The dashed lines represent an approximation of the noise floor of each discriminator in terms of a power series of $\omega/2\pi$, i.e. $(\omega/2\pi)^{-2}$, $(\omega/2\pi)^{-1}$, $(\omega/2\pi)^{0}$, $(\omega/2\pi)^{1}$, $(\omega/2\pi)^{2}$.

The noise floor of the Miteq discriminator is white frequency noise (~0.1 Hz²/Hz) at frequencies $\omega/2\pi > 100$ Hz and increases as $(\omega/2\pi)^{-1}$ at lower frequency. The digital phase detector DXD200 has a typical $(\omega/2\pi)^{-1}$ phase noise floor, which translates into a small frequency noise floor at low Fourier frequency ($<10^{-5}$ Hz²/Hz at 10 Hz). The frequency noise floor increases with $\omega/2\pi$ with a slope slightly larger than unity in a log-log plot (the experimentally observed dependence is $(\omega/2\pi)^{-\alpha}$ with $\alpha \sim 1.3$), and surpasses the noise floor of the two prior frequency discriminators at Fourier frequencies over 1 kHz (compared to the analog PLL discriminator) or 30 kHz (compared to Miteq). The noise floor of the HF2PLL has two contributions, white frequency noise at low Fourier frequency and white phase noise at high frequency. The white frequency noise floor results from white noise in the analog port that outputs the frequency deviation dF. When converted

into an equivalent frequency noise using the discriminator sensitivity, this leads to a frequency noise floor that depends on the selected sensitivity D_ν and which scales as $1/D_\nu^2$ for D_ν below 10 mV/Hz. For higher sensitivities, the frequency noise floor starts to increase again, due to other noise contributions. The lowest noise floor is about $3 \cdot 10^{-8}$ Hz^2/Hz, obtained for $D_\nu = 10$ mV/Hz. On the other hand, the white phase noise ($\sim 5 \cdot 10^{-13}$ rad^2/Hz) at high frequency is due to white noise at the input port of the HF2LI lock-in and is thus insensitive to the PLL output gain. The HF2PLL has the lowest noise floor in the frequency range from 1 Hz to 50 kHz. Owing to its digital operation it is not affected by 50-Hz noise present in the spectra of all other discriminators.

2.5.4 AM/AN cross-sensitivity

An ideal frequency discriminator should be sensitive to frequency modulation (FM) or frequency noise (FN) only and insensitive to amplitude modulation (AM) or amplitude noise (AN). However, the situation is different in a real device and the cross-sensitivity of each discriminator has been investigated, both in terms of AM and AN. In the first case, a pure AM signal was applied to the input of the discriminator (with an AM depth ranging from 10% to 100% depending on the discriminator) and the output signal was measured using a lock-in amplifier. In the second case, white AN was added at the input of the discriminators and the output voltage PSD was recorded using an FFT spectrum analyzer. The sensitivity of each discriminator (in V/Hz) was used to convert the measured AM (AN) response into an equivalent FM (FN) signal. Then, an AM-FM (AN-FN) conversion factor (in Hz/%) was determined for each discriminator by normalizing the measured equivalent frequency response by the applied AM or AN (this latter was separately measured using a power detector, model Mini-Circuits ZX47-55LN-S+).

Figure 2.7 shows that all discriminators have some cross-sensitivity to AM and AN, the magnitude of which being very similar in both cases. The analog PLL and the DXD200 show a similar AM (AN) sensitivity, which increases approximately linearly with the modulation frequency, meaning that these discriminators are more sensitive to fast AM (AN). The general trend is similar for HF2PLL, but the AM (AN) sensitivity is two orders of magnitude weaker. Miteq discriminator has by far the highest AM sensitivity, with a constant conversion factor of 5 kHz/%.

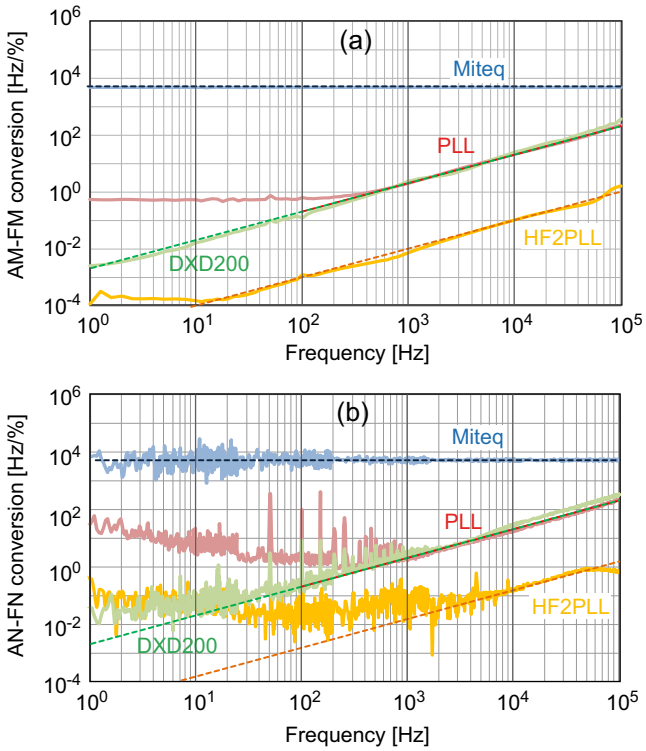

Figure 2.7: Cross-sensitivity of the discriminators to (a) amplitude modulation and (b) to amplitude noise, expressed in terms of AM-FM (AN-FN) conversion factor (in Hz/%). The dashed lines represent an approximation of the AM-FM (AN-FN) conversion factor as a constant level (for Miteq) or proportional to $\omega/2\pi$ (for the other discriminators), obtained in the high frequency range where the measurements are out of the noise floor of each discriminator. These trend lines are used to extract numerical values for the AN-FN cross-sensitivity of each discriminator as listed in Table 2.1.

It was also observed that the AM-FM conversion factor in the analog PLL depends somewhat on some loop parameters, such as the amplitude of the input carrier and the servo gain. In this discriminator, the origin of this AM sensitivity lies in some imperfections in the PLL, which slightly shift the operating point out of its nominal position. In a perfect analog PLL, the two input signals (LO and RF) are locked in quadrature (90° out-of-phase), as the error signal (mixer output) is zero in this phase condition. In such an ideal situation, it can be demonstrated that a PLL is fully insensitive to AM. However, a small electronic offset (e.g. induced at the servo input) may slightly shift the PLL operating point from the quadrature condition, making it sensitive to AM. The response to AM thus directly scales with the small phase shift from the quadrature point. Fine adjustment of the input offset of

the PI servo controller allows to retrieve the correct PLL quadrature operation point and to minimize the AM sensitivity compared to the result shown in Figure 2.7, obtained without input offset correction. Such adjustment is quite straightforward in presence of pure AM, which is easy to detect, but is more critical in presence of simultaneous AM and FM, or, even worse, in presence of AN and FN.

2.6 Comparison of RF discriminators

Table 2.1 summarizes the main properties of each discriminator extracted from the characterization measurements of Section 2.5. A convenient means to compare the characteristics of the different discriminators is to graphically depict their respective domain of application in the plane $(\omega/2\pi,\ S_{\delta\nu})$. The idea is to represent a frequency or phase discriminator as a surface delimited by the following boundaries (Figure 2.8a): the discriminator noise floor $S_{\min}$, its bandwidth $\omega_{\mathrm{BW}}/2\pi$, and the maximum measurable frequency noise PSD $S_{\max}$. While the noise floor and the bandwidth of each discriminator are straightforwardly extracted from the measurements shown in Section 2.5, the upper frequency noise limit has been indirectly determined from the discriminator linear frequency range Δf_{lin}, taking into account the relationship that links the frequency noise spectrum and the linewidth (see Section 2.3).

A correct measurement of the frequency noise of a beat signal requires that the linewidth of the analysed signal be narrower than the discriminator linear range: $FWHM \ll \Delta f_{\mathrm{lin}}$. To have a sufficient margin, one requests that $FWHM \leq \Delta f_{\mathrm{lin}}/n$ and one considers $n = 3$. In this condition, the fraction of the spectral power which is out of the discriminator operating range can be shown to be 0.04% for a Gaussian lineshape (valid for $(8\ln 2/\pi^2)\cdot(\omega_{\mathrm{BW}}/2\pi) < S_{\max}$ and 21% for a Lorentzian lineshape (valid for $(8\ln 2/\pi^2)\cdot(\omega_{\mathrm{BW}}/2\pi) > S_{\max}$). Assuming a white frequency noise in a bandwidth $\omega_{\mathrm{BW}}/2\pi$, $S_{\delta\nu}(\omega < \omega_{\mathrm{BW}}) = S_{\max}$, the surface of the slow modulation area is simply $A = S_{\max}\cdot(\omega_{\mathrm{BW}}/2\pi) = FWHM^2/8\ln 2$, so that $S_{\max} \leq (\Delta f_{\mathrm{lin}}/n)^2/(8\ln 2\cdot(\omega_{\mathrm{BW}}/2\pi))$. For a given discriminator range Δf_{lin}, the maximum measureable frequency noise thus decreases as the inverse of the discriminator bandwidth $\omega_{\mathrm{BW}}/2\pi$. This relation is valid as long as $S_{\max} > (8\ln 2/\pi^2)\cdot(\omega_{\mathrm{BW}}/2\pi)$. When $S_{\max} < (8\ln 2/\pi^2)\cdot(\omega_{\mathrm{BW}}/2\pi)$, $S_{\max}$ becomes independent of the bandwidth, $S_{\max} = \Delta f_{\mathrm{lin}}/(n\pi)$. This results from the fact that the

additional frequency noise occurring in a bandwidth increment does not contribute to the signal linewidth, as it is entirely below the β-separation line. The upper limit $S_{\max}$ of the frequency discriminators has been determined for a white frequency noise; however, one has to keep in mind that a higher frequency noise level acting in a narrower bandwidth would still be measurable if its surface A was smaller than $S_{\max} \cdot (\omega_{\mathrm{BW}}/2\pi)$.

			Discriminator			
			Analog PLL	**HF2PLL**	**Miteq**	**DXD200**
Frequency domain	**Total**	[MHz]	199-210	1-49	16-30	0.5-200
	Linear	[MHz]	203-210	--	18-27	--
	Center Freq	[MHz]	206.5	--	22.5	--
	Total range	$\Delta f_{\max}$	11 [MHz]	$20/D_\nu$ [Hz]	14 [MHz]	128π [rad]
	Linear range	Δf_{lin}	7 [MHz]	$20/D_\nu$ [Hz]	9 [MHz]	128π [rad]
Sensitivity	$\boldsymbol{D_\nu}$		$7 \cdot 10^{-7}$ [V/Hz]	$0.8 \cdot 10^{-9}$ – 1.6 [V/Hz]	$1.25 \cdot 10^{-6}$ [V/Hz]	0.018 [V/rad]
±0.9 dB BW	$\boldsymbol{\omega_{\mathrm{BW}}/2\pi}$	[kHz]	200	50	2000	1000
Noise floor [Hz²/Hz], $S(\omega) \sim \omega^\alpha$	Range 1	$-2 < \alpha < -1$	$4 \cdot (\omega/2\pi)^{-2}$	--	$10 \cdot (\omega/2\pi)^{-1}$	--
	Range 2	$\alpha = 0$	10^{-3}	$3 \cdot 10^{-12} \cdot D_\nu^{-2}$	10^{-1}	--
	Range 3	$1 < \alpha$	$1 \cdot 10^{-7} \cdot (\omega/2\pi)$	$5 \cdot 10^{-13} \cdot (\omega/2\pi)^2$	--	$1.5 \cdot 10^{-7} \cdot (\omega/2\pi)^{1.3}$
AN-FN conversion	[Hz/%]		$2 \cdot 10^{-3} \cdot (\omega/2\pi)$	$1.5 \cdot 10^{-5} \cdot (\omega/2\pi)$	$5 \cdot 10^3$	$2 \cdot 10^{-3} \cdot (\omega/2\pi)$

Table 2.1: Summary of the main properties of the frequency (phase) discriminators. The noise floor is approximated by a power series in $(\omega/2\pi)^\alpha$ with up to three different exponents corresponding to flicker frequency noise (range 1, $-2 < \alpha < -1$), white frequency noise (range 2, $\alpha = 0$) and flicker phase noise or white phase noise (range 3, $1 < \alpha < 2$).

The geometrical illustration of the phase discriminator is slightly different, as it first has to be represented in the phase noise plane ($\omega/2\pi$, S_ϕ). In that plane, the

discriminator is also depicted by a rectangular surface, limited by the following boundaries (Figure 2.8b): the discriminator noise floor $S_{\phi,\min}$, its bandwidth $\omega_{BW}/2\pi$, and the maximum measurable phase noise $S_{\phi,\max}$. As for the frequency discriminators previously considered, the maximum measurable phase noise $\Delta\phi_{rms}$ must be smaller than the discriminator linear range $\Delta\phi_{lin}$: $\Delta\phi_{rms} \leq \Delta\phi_{lin}/(2n)$ and one again chooses $n = 3$. Assuming a low-pass filtered white phase noise $S_\phi(\omega < \omega_{BW}) = S_{\phi,\max}$, the rms phase fluctuations are given by the integrated phase noise ${\Delta\phi_{rms}}^2 = \int_0^{\omega_{BW}/2\pi} S_\phi(\omega) d(\omega/2\pi) = S_{\phi,\max} \cdot (\omega_{BW}/2\pi)$, so that $S_{\phi,\max} \leq (\Delta\phi_{lin}/2n)^2/(\omega_{BW}/2\pi)$. To have a constant phase excursion $\Delta\phi_{rms}$, the maximum phase noise PSD must be inversely proportional to the discriminator bandwidth.

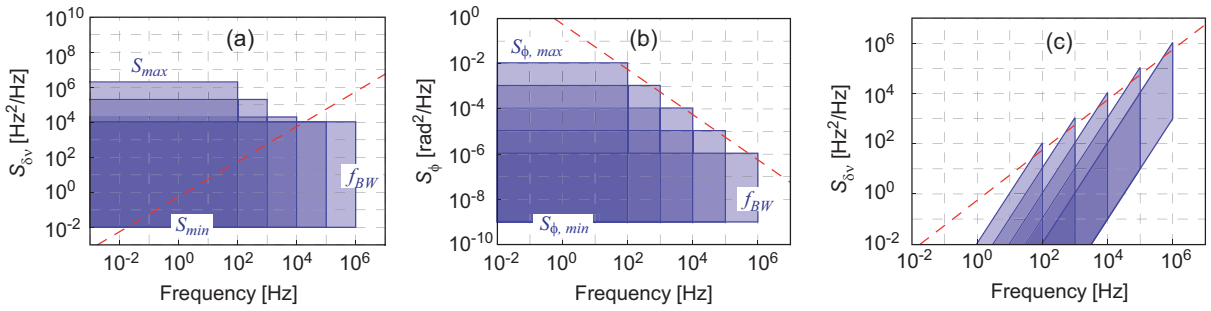

Figure 2.8: Examples of a graphical representation of a frequency/phase discriminator with different bandwidths ($\omega_{BW}/2\pi$ = 100 Hz, 1 kHz, 10 kHz, 100 kHz, 1 MHz): (a) frequency discriminator in the plane ($\omega/2\pi$, $S_{\delta\nu}$); (b) phase discriminator in the plane ($\omega/2\pi$, S_ϕ) and (c) phase discriminator in the plane ($\omega/2\pi$, $S_{\delta\nu}$). The frequency discriminator has a range of Δf = 100 kHz and a noise floor $S_{\min}$ = 0.01 Hz²/Hz; the phase discriminator has a range $\Delta\phi = 2\pi$ and a noise floor $S_{\phi,\min} = 10^{-9}$ rad²/Hz. The dashed line represent the β-separation line ($S_{\delta\nu} = (8 \ln 2/\pi^2) \cdot (\omega/2\pi)$) in the frequency noise spectrum and its correspondent ($S_\phi = (8 \ln 2/\pi^2)/(\omega/2\pi)$) in the phase noise spectrum.

In order to compare the frequency and phase discriminators in the same plot, the rectangular surface representing the phase detector in the plane ($\omega/2\pi$, S_ϕ) is converted into the ($\omega/2\pi$, $S_{\delta\nu}$) plane by applying the transformation $\big((\omega/2\pi), S_\phi(\omega)\big) \rightarrow \big((\omega/2\pi), (\omega/2\pi)^2 \cdot S_\phi(\omega)\big)$, as $S_{\delta\nu}(\omega) = (\omega/2\pi)^2 \cdot S_\phi(\omega)$. The constant lower and upper phase noise limits of the phase discriminator thus convert into lines of slope +2 in terms of frequency noise (Figure 2.8c). One also notices that the maximum frequency noise value moves parallel to the β-separation line as a function of the discriminator bandwidth, as it corresponds to

$S_{\max} = S_{\phi,\max} \cdot (\omega_{\mathrm{BW}}/2\pi)^2 = \Delta\phi_{\mathrm{rms}} \cdot (\omega_{\mathrm{BW}}/2\pi)$ and is thus proportional to the Fourier frequency like the β-separation line. From this observation, one can deduce the phase fluctuations that correspond to the β-separation line: $\Delta\phi_{\mathrm{rms}} = \sqrt{8\ln 2}/\pi \cong 0.75$ [rad].

The graphical comparison of the different discriminators is shown in Figure 2.9. One notices that the analog PLL-discriminator and the Miteq passive RF discriminator have very similar properties in terms of minimum and maximum measurable frequency noise (slightly better for the analog PLL), but the Miteq discriminator has a wider bandwidth. Their noise floor below the 1 $\mathrm{Hz}^2/\mathrm{Hz}$ level over a wide frequency range and their intersection with the β-separation line at a Fourier frequency of a few Hertz should enable these discriminators to characterize beat signals with a few Hertz linewidth (assuming a white frequency noise), provided that no other undesirable effect will degrade the noise floor, as might be the case in presence of amplitude noise. The digital phase detector DXD200 enables to detect much smaller frequency fluctuations, especially at low Fourier frequencies, as a result of its sensitivity to the phase fluctuations of the input signal. Owing to its applicability to a large fraction of the slow modulation area which is below the β-separation line, this discriminator is suitable for the characterization of coherent beat signals with sub-radian integrated phase noise. But the maximum frequency noise measurable with this device is limited to $4.5 \cdot 10^{-3} \cdot (\omega/2\pi)^2$ [$\mathrm{Hz}^2/\mathrm{Hz}$] due to its 128π phase coverage.

The HF2PLL combines several advantages of the other discriminators. Its very low-noise performances resulting from the numerical operation convert into a low noise floor, which can be as small as $3 \cdot 10^{-8}$ $\mathrm{Hz}^2/\mathrm{Hz}$ (for $D_\nu = 10$ mV/Hz). This makes this discriminator slightly more sensitive than the DXD200 for the characterization of low-noise beat signals with down to sub-radian integrated phase noise, at Fourier frequencies higher than 100 Hz. However, its bandwidth is slightly lower than for the other discriminators. At lower Fourier frequencies, the HF2PLL discriminator does not compete with the superior capabilities of the digital phase detector DXD200, which results from its white phase noise floor. The flexibility offered by the computer-selectable discriminator value D_ν in the HF2PLL also makes possible the characterization of much wider beat signals with a linewidth ranging from kilohertz to megahertz, which is by far not possible with the digital phase de-

tector. The analog PLL and the Miteq discriminators are also suitable for such broad linewidths.

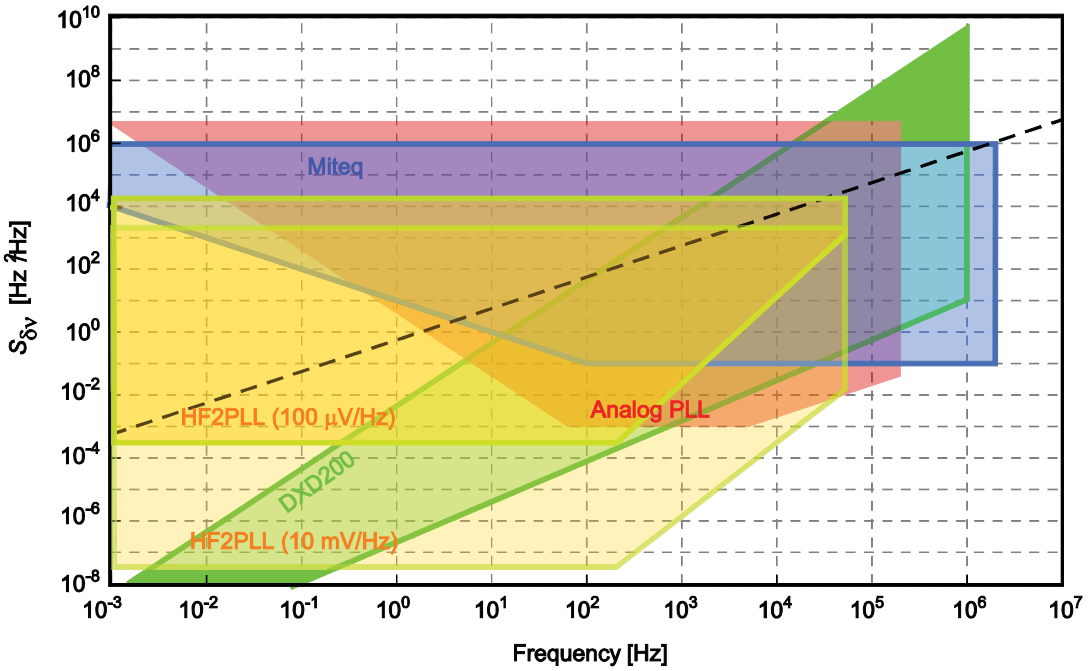

Figure 2.9: Graphical comparison of the characteristics of the different discriminators. Each discriminator is represented by a surface delimited by its noise floor S_{min}, its bandwidth $\omega_{\mathrm{BW}}/2\pi$ and the maximum measureable frequency noise PSD S_{max}. The situation for HF2PLL depends on the selected discriminator value D_ν and is shown here for two cases, $D_\nu = 100$ µV/Hz and $D_\nu = 10$ mV/Hz. The dashed line represents the β-separation line $S_{\delta\nu} = (8 \ln 2/\pi^2) \cdot (\omega/2\pi)$.

2.7 Conclusion

A PLL frequency discriminator developed to analyze the frequency noise properties of an RF signal, e.g. an optical beat signal between two lasers or between a laser and a frequency comb, has been described and fully characterized. Owing to its large linear frequency range of 7 MHz, its bandwidth of 200 kHz and its noise floor below 0.01 Hz²/Hz in the range ~10 Hz – 100 kHz, this frequency discriminator is able to fully characterize the frequency noise of a beat signal with a linewidth ranging from a couple of megahertz down to a few hertz. It thus has a wide range of applications, for instance for the characterization of the frequency noise spectrum of free-running lasers, the measurement of transfer functions in free-running optical frequency combs (for the CEO, the repetition rate or an individual optical comb

line), or for the characterization of the frequency noise properties of stabilized frequency combs and ultra-narrow linewidth cavity-stabilized lasers. This frequency discriminator has been widely used for such characterizations all along this thesis.

For comparison, three other commercially available discriminators of different types have also been characterized, (i) a Miteq RF discriminator, (ii) a numerical PLL (HF2PLL) encompassed in a high-frequency lock-in amplifier and (iii) a digital phase detector (DXD200). From their measured characteristics, these discriminators were compared with respect to their respective domain of application in the frequency noise plane ($\omega/2\pi$, $S_{\delta\nu}$). These discriminators have complementary properties that make them applicable to different types of input signals.

The Miteq discriminator is the simplest to use. With its wide linear range of operation, it is perfectly suitable to the characterization of free-running lasers or frequency combs. Its white frequency noise floor of $0.1\,\mathrm{Hz^2/Hz}$ reached at $\omega/2\pi > 100$ Hz with a $(\omega/2\pi)^{-1}$ increase at lower frequency should make it applicable also for the analysis of narrow-linewidth signals. However, this discriminator has shown a strong sensitivity to amplitude modulation and amplitude noise with a conversion factor of ~5 kHz/%, which strongly limits its use for low frequency noise signals in presence of amplitude noise.

The HF2PLL has a computer-selectable output gain allowing to achieve a broad range of discrimination factors, and thus to straightforwardly adjust its domain of operation. This flexibility, combined with its low intrinsic noise floor, makes this discriminator applicable to the characterization of lasers with a wide range of linewidths. However, the lower bandwidth of this discriminator prevents a complete characterization of the frequency noise spectrum of lasers with MHz-range linewidth, such as distributed feedback (DFB) lasers. Furthermore, the potential capability of this discriminator to reach a very low noise floor at low Fourier frequencies, and thus to characterize low-noise beat signals with sub-radian integrated phase noise, is somewhat limited by the impracticality to use a high discriminator factor with a real signal. At low Fourier frequencies, a noise floor of $\sim 10^{-3}$ $\mathrm{Hz^2/Hz}$, prevents the detection of smaller frequency fluctuations, despite the much lower intrinsic noise floor of the HF2PLL in the $3 \cdot 10^{-8}$ $\mathrm{Hz^2/Hz}$ range obtained at a higher discriminator factor of 10 mV/Hz.

Finally, the digital phase detector DXD200 is very sensitive to small frequency

fluctuations at low Fourier frequency owing to its sensitivity to phase fluctuations, which makes it the most sensitive device for the characterization of a real beat signal containing simultaneous frequency noise and amplitude noise.

Chapter 3

Ultra-stable laser

3.1 Introduction

Ultra-stable lasers are essential to the operation of optical atomic clocks [21], for space-borne gravitational wave detector [22] and for distant clock comparison via optical fiber links [23]. Recent progresses in the design and manufacturing of high-finesse Fabry-Perot cavities made possible ultra-narrow linewidth lasers to be achieved with residual fractional frequency fluctuations in the low 10^{-15} range for integration times of 0.1 to 100 s [21,24,25]. This makes such optical oscillators very attractive for the generation of ultra-stable microwave signals using an optical frequency comb as an optical-to-microwave frequency divider to transfer the fractional frequency stability of the laser to a microwave signal [4].

Ultra-stable optical frequency oscillators are commonly realized by stabilizing a distributed Bragg reflector fiber laser or an ECDL to a Fabry-Perot cavity using the Pound-Drever-Hall (PDH) technique [26]. Despite the fact that the core element of an ultra-stable laser is the optical reference cavity, the characteristics and noise properties of the free-running laser are of great importance. The physical dimensions, intensity noise, robustness, reliability and frequency drift of the laser are relevant parameters for the realization of a compact ultra-stable laser. But more important, the linewidth of the free-running laser must be substantially narrower than the achievable feedback loop bandwidth to allow significant linewidth narrowing to be achieved.

Two laser technologies are considered here for the realization of an ultra-stable laser in the 1.55 µm spectral range: an ECDL and a PW-ECL.

PW-ECLs constitute a relatively new technology of low phase noise semicon-

ductor laser [27] that represents an attractive alternative to fiber lasers for the realization of robust ultra-stable optical frequency standards. In the first demonstration of a stabilized PW-ECL reported by K. Numata *et al.* [28], a fractional frequency stability at the 10^{-13} level was obtained by frequency stabilization to the P(16) acetylene ($^{13}C_2H_2$) ro-vibrational transition at 1542.383 nm. This result was later on surpassed by C. Clivati *et al.* [29], who stabilized a PW-ECL to a high-finesse Fabry-Perot cavity with a resulting fractional frequency stability of 2×10^{-14}, comparable to a distributed Bragg reflector fiber laser stabilized to the same cavity.

In this chapter we compare an ECDL with a PW-ECL in terms of noise and frequency control and demonstrate the stabilization of both lasers to a high finesse cavity. The stabilization principle is discussed along with the basics of PDH stabilization in Section 3.2. The lasers (ECDL and PW-ECL) are presented in Section 3.3 together with the measured transfer functions and noise characteristics. The high-finesse cavity is described in Section 3.4 and the thermal assembly designed to support the cavity and shield it from external perturbations is presented in Section 3.5. Section 3.6 describes the implemented laser stabilization scheme and demonstrates the locking efficiency of the lasers, based on the characterization of the in-loop error signals. The cavity resonance is characterized with a phase-locked probe PW-ECL as discussed in Section 3.7. The thermal properties of the cavity assembly and the cavity itself are presented in 3.8.

3.2 Laser stabilization

3.2.1 Basics of servo loops

The frequency stabilization of a laser can be schematically described by a feedback loop composed of the three following elements as illustrated in Figure 3.1 [30,31]:

i) A frequency discriminator, characterized by its transfer function $D(\omega)$ in V/Hz, is used to detect the frequency fluctuations of the laser relative to a reference frequency and to generate an error signal $\tilde{e}(\omega)$, which is proportional to the difference $\delta\tilde{\nu}(\omega)$ between the stabilized input signal frequency $\tilde{\nu}^{\mathrm{stab}}(\omega)$ and the reference frequency $\tilde{\nu}^{0}$: $\tilde{e}(\omega) = D(\omega)\cdot\delta\tilde{\nu}(\omega) = D(\omega)\cdot\left(\tilde{\nu}^{\mathrm{stab}}(\omega) - \tilde{\nu}^{0}\right)$. Variables in the frequency (Fourier) domain are labeled with a tilde (e.g. $\tilde{e}(\omega)$) or by a capital letter

(e.g. $D(\omega)$) in the case of transfer functions all along this thesis to be compatible with the notations used and explained in Chapter 4 (see Section 4.4).

ii) A servo-controller with a transfer function $G(\omega)$, which amplifies the error signal to produce a correction signal $\tilde{u}^{\mathrm{cor}}(\omega) = G(\omega) \cdot D(\omega) \cdot \delta\tilde{\nu}(\omega)$.

iii) A frequency transducer or actuator with a transfer function $C(\omega) = \tilde{\nu}(\omega)/\tilde{u}(\omega)$ (in Hz/V), is used to correct the frequency fluctuations of the laser by an amount $\tilde{\nu}^{\mathrm{cor}}(\omega) = C(\omega) \cdot \tilde{u}^{\mathrm{cor}}(\omega)$ from the correction voltage $\tilde{u}^{\mathrm{cor}}(\omega)$.

Following the standard description of servo systems [30,31], the frequency $\tilde{\nu}^{\mathrm{stab}}(\omega)$ in the fully-stabilized laser (closed loop) is related to the free-running frequency $\tilde{\nu}^{\mathrm{free}}(\omega)$ (open loop) by:

$$\tilde{\nu}^{\mathrm{stab}}(\omega) = \tilde{\nu}^{\mathrm{free}}(\omega) + \tilde{\nu}^{\mathrm{cor}}(\omega). \tag{3.1}$$

A positive sign is considered in Eq. (3.1) and Figure 3.1 in order to use the same notations as in Chapter 4.

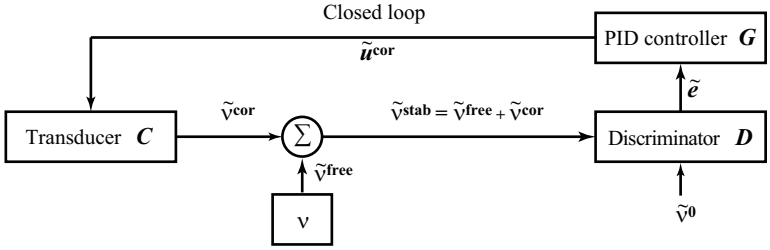

Figure 3.1: Schematic representation of a closed feedback loop.

The square modulus of the deviations of the laser frequency from its reference value $\tilde{\nu}^0$ in the free-running ($\Delta\tilde{\nu}(\omega) = \tilde{\nu}^{\mathrm{free}}(\omega) - \tilde{\nu}^0$) and in the stabilized laser ($\delta\tilde{\nu}(\omega) = \tilde{\nu}^{\mathrm{stab}}(\omega) - \tilde{\nu}^0$) are proportional to the frequency noise PSDs $S_{\Delta\nu}$ and $S_{\delta\nu}$.

The total loop transfer function is given by $H(\omega) = C(\omega) \cdot G(\omega) \cdot D(\omega)$. From Eq. (3.1), the correction signal produced by the actuator is given by:

$$\tilde{\nu}^{\mathrm{cor}}(\omega) = H(\omega)\Big(\Delta\tilde{\nu}(\omega) + \tilde{\nu}^{\mathrm{cor}}(\omega)\Big), \tag{3.2}$$

The following expression is obtained for the frequency deviation of the stabilized laser:

$$\delta\tilde{\nu}(\omega) = \frac{\Delta\tilde{\nu}(\omega)}{1 - H(\omega)}, \tag{3.3}$$

With this expression, the residual frequency deviations of the stabilized laser ($\delta\tilde{\nu}(\omega)$) can be calculated from the frequency deviations of the free-running laser ($\Delta\tilde{\nu}(\omega)$), provided that the gain $H(\omega)$ of the loop is known. The measurement of the open-loop transfer functions of the frequency discriminator $D(\omega)$, of the servo controller $G(\omega)$ and frequency transducer $C(\omega)$ allow determining the entire loop gain $H(\omega)$.

The contribution of the noise of the frequency reference $\tilde{\nu}^0$ used in the loop has not been taken into account here and ideal noiseless reference has been considered. In case the reference noise $\Delta\tilde{\nu}^{\mathrm{ref}}(\omega)$ is not negligible the noise of the laser stabilized to such a reference follows the noise of the reference for $\left|H\right| \to \infty$:

$$\delta\tilde{\nu}(\omega) = \frac{\Delta\tilde{\nu}(\omega) - H(\omega)\Delta\tilde{\nu}^{\mathrm{ref}}(\omega)}{1 - H(\omega)}, \tag{3.4}$$

Ideally the highest possible gain is desired as it makes the laser to follow the reference frequency as closely as possible. Usually the frequency transducer has a limited bandwidth meaning that a significant phase shift arises at some frequency. A low-pass filter behaviour is typical for the frequency discriminator as well. For example, when an optical frequency cavity is used as a frequency discriminator, its bandwidth is limited by the cavity resonance width. This leads to a significant phase shift induced to the entire loop transfer function $H(\omega)$ at high frequencies. As a consequence, the transfer function of the PID controller needs to be tailored in such a way to compensate for the phase shift induced by the other transfer functions. Otherwise, for $H \to 1$ an oscillation will occur, meaning that the correction signal causes the laser to move more than the original perturbation. To avoid this, one must ensure that the loop gain is less than unity in a frequency range where the loop phase shift approaches 0°. The goal of the servo-loop controller is to ensure a high enough gain at low frequencies while keeping a unity gain frequency low enough to keep the system stable. A high gain at low frequencies is achieved with an integrator in the servo controller. To improve the low frequency gain, an additional integration can be introduced in a limited range leading to a double integrating behaviour with a slope of −40 dB/decade.

3.2.2 Basics of Pound-Drever-Hall stabilization

The PDH stabilization is a commonly used technique for laser frequency stabilization to a high-finesse cavity, allowing for strong laser linewidth narrowing. It uses RF modulation to probe the narrow resonance of an optical cavity. Two FM sidebands are added to the laser carrier, using an external electro-optic phase modulator (EOM) as schematized in Figure 3.2.

The modulation frequency f_{m} is chosen much larger than the resonance width $\Delta\nu_{\mathrm{c}}$, so that only one sideband interacts at a given time with the cavity resonance. The use of a modulation frequency in the MHz range (typ. 20 MHz), provides a good immunity to low-frequency laser noise as well as to low-frequency photodetector technical noise, while offering at the same time a high bandwidth feedback capability.

When the optical carrier is in resonance with the cavity, a strong reflection signal arises from the weak leakage of the field stored in the cavity. This field interferes (destructively) with the carrier field promptly reflected on the high-reflectivity entrance mirror of the cavity, leading to a resulting field whose phase varies linearly with the detuning of the laser frequency from the resonance center. This phase detuning produces an AM signal as a result of the interference (beating) between the carrier field and the two sidebands, which are only promptly reflected by the entrance mirror and are thus not affected by the cavity resonance. They are just used as reference sidebands to measure the phase shift undergone by the optical carrier around the resonance frequency. This AM signal occurs at the modulation frequency, which avoids most low-frequency noise sources. It is detected using a high-speed photodiode and is then demodulated to base-band. The resulting signal is directly proportional to the difference between the laser frequency and the cavity resonance frequency, so that it can be used as an error signal in a feedback loop to lock the laser to the cavity resonance.

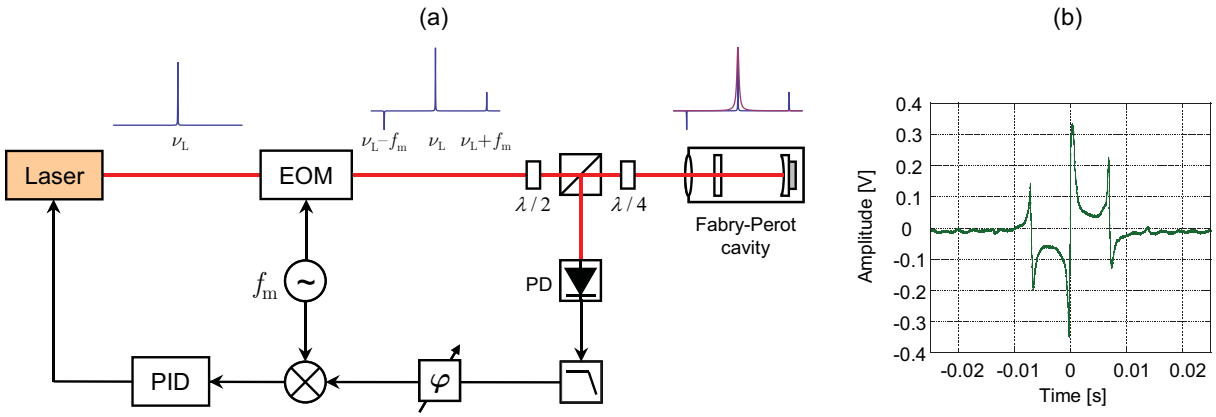

Figure 3.2: (a) Scheme of the PDH stabilization. (b) Typical PDH error signal obtained when scanning the laser through the cavity resonance. PD: photodetector; PID: proportional-integral derivative controller; EOM: electro-optic modulator.

The PDH error signal (Figure 3.2b) represents the dispersive response of the cavity resonance obtained in FM spectroscopy, displaying the characteristic steep slope at the resonance frequency that is used as a frequency (phase) discriminator to measure the frequency (phase) fluctuations of the laser from the resonance center. The phase of the reference signal in the demodulation needs to be adjusted to obtain the dispersive PDH signal, i.e. in-phase with the EOM phase modulation (or in quadrature with the laser FM). The amplitude of the PDH signal is maximized for a frequency modulation index $\beta = 1.08$, which provides the highest discriminator slope.

The PDH error signal constitutes a dispersive curve of width $\Delta\nu_c$, corresponding to the cavity resonance FWHM:

$$e(\nu_L) = 2E_0{}^2 J_0(\beta) J_1(\beta) \frac{\dfrac{2(\nu_L - \nu_0)}{\Delta\nu_c}}{1 + \left(\dfrac{2(\nu_L - \nu_0)}{\Delta\nu_c}\right)^2}. \tag{3.5}$$

Here ν_L is the laser angular frequency, ν_0 is the cavity resonance frequency, E_0 is the amplitude of the electric field and $J_0(\beta)$ and $J_1(\beta)$ are Bessel functions of the first kind.

Another nice feature of the PDH stabilization scheme is its broad capture range, given by the modulation frequency only and not limited by the width of the resonance. It thus simultaneously offers a high frequency noise discrimination (using

a narrow cavity resonance in the kHz range) and a broad locking range (±20 MHz, given by the modulation frequency).

3.3 Lasers

3.3.1 Description

The development of an ultra-stable optical oscillator puts several requirements on the laser source used in the setup. The laser should be tunable (in order to enable tuning over at least one free-spectral range (FSR) of the reference cavity) and possess a narrow linewidth. The bandwidth of the actuator used to drive the laser frequency is also of great importance.

We used two all solid-state semiconductor laser diodes in an external cavity configuration to make an ultra-stable optical oscillator.

A single-mode ECDL (model TLB-6328 from NewFocus) was compared with a PW-ECL (ORION module from Redfern Integrated Optics Inc.) in terms of noise, frequency control and stabilization.

3.3.1-1 ECDL

A diagram of the ECDL is shown in Figure 3.3. It is based on a Littman-Metcalf design [32]. The light emitted by the diode and collimated by a lens is diffracted by a grating towards a high-reflectivity tuning mirror. The light is reflected back on the same path by the tuning mirror to the back facet of the laser diode forming the second end of the laser cavity. The zero-order diffraction at a grazing angle forms the output beam. Single-mode (longitudinal) laser operation is guaranteed by the spectral selectivity of the grating and by the extended cavity length. The double passage of the light beam on the grating in each round trip results in a narrowband filtering of the output beam. The cavity configuration enables continous mode hop-free tuning over a broad wavelength range from 1520 nm to 1570 nm.

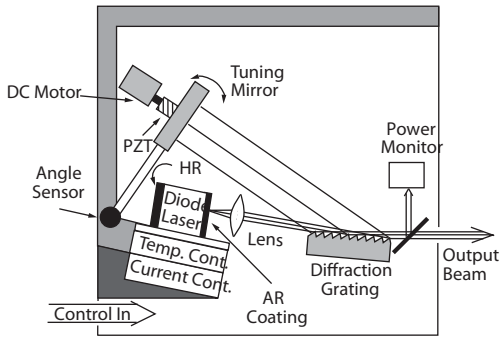

Figure 3.3: Schematic representation of the ECDL cavity. HR: highly reflective; AR: anti-reflective [33].

A thermoelectric cooling element (TEC) is used to control the diode temperature to within 1 mK. The coarse adjustment of the laser wavelength is performed by rotating the tuning mirror, mounted on a stiff arm, around the pivot point with a DC motor driven screw. The fine adjustment of the laser frequency is performed by a piezoelectric transducer (PZT). The PZT can change the laser frequency in a range of ~56 GHz with a tuning coefficient of 9.6 GHz/V within a 2-kHz bandwidth.

A higher feedback bandwidth can be granted by the control of the laser diode injection current (through the laser driver). A static tuning coefficient of the laser frequency of −20 MHz/V is achieved with a conversion coefficient of the controller of 0.2 mA/V.

3.3.1-2 PW-ECL

We investigated the use of a commercial fiber-coupled laser module (ORION from Redfern Integrated Optics Inc.), which includes a butterfly-packaged PW-ECL with thermo-electrical control, a laser driver and a control interface. The butterfly-packaged PW-ECL uses a planar Bragg grating (PBG) on silica-on-silicon planar lightwave circuit (PLC).

The schematic of the PW-ECL is shown in Figure 3.4. The light from an InP gain chip is coupled into a waveguide Bragg grating on a PLC, forming an external cavity. The sub-assembly of the PW-ECL (Figure 3.4b) is placed on a TEC. The collimated optical output beam passes through an optical isolator and is then focused into a polarization-maintaining (PM) single mode fiber. The laser has a preset center frequency of 192.50 THz, corresponding to the ITU-25 channel of the

dense wavelength division-multiplexing (DWDM) grid of the international telecommunication union (ITU). It can be frequency-tuned over a couple of GHz either via its injection current or by changing the diode temperature.

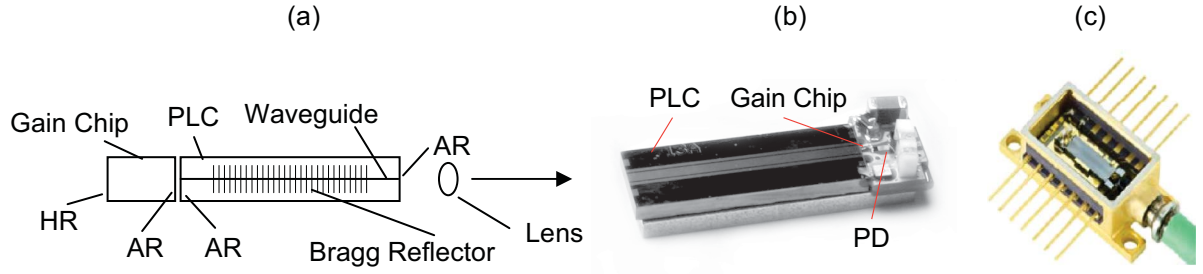

Figure 3.4: (a) Scheme of the PW-ECL cavity. HR: highly-reflective coating, AR: anti-reflective coating, PLC: planar lightwave circuit. (b) Photograph of the silica-on-silicon PLC [34]. (c) Picture of a PW-ECL cavity placed in a standard 14-pin butterfly package.

The static response of the PW-ECL frequency to a change of the injection current has been determined from the heterodyne beat between the laser and an optical mode of a frequency comb stabilized to an H-maser. The result is shown in Figure 3.5 together with the dependence of the optical power versus injection current. A static tuning coefficient of 56 MHz/mA is obtained,

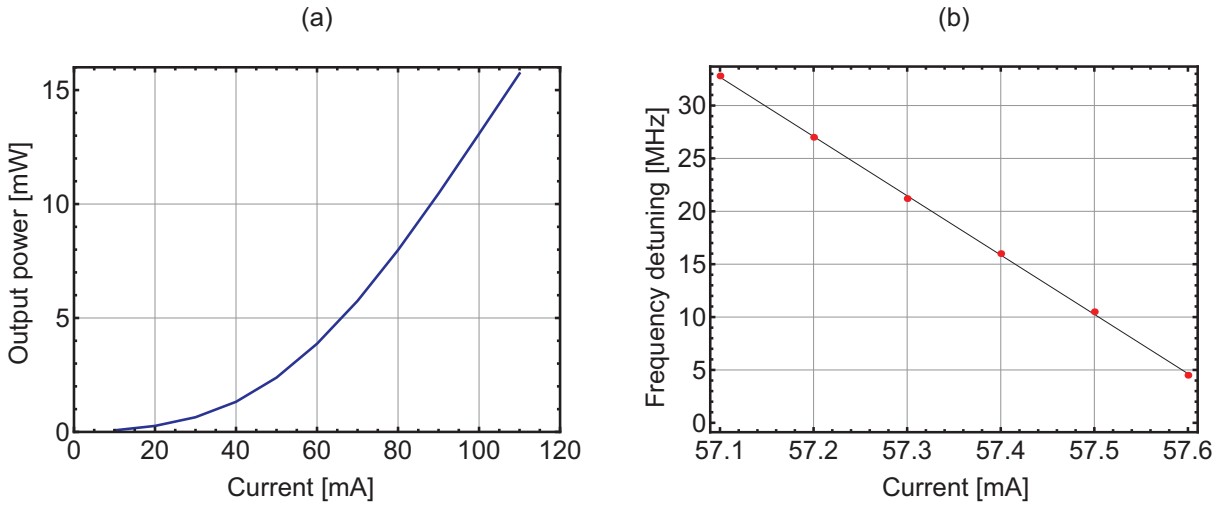

Figure 3.5: Laser power (a) and static frequency tuning (b) of the PW-ECL as a function of the injection current.

3.3.2 Lasers transfer functions

The dynamic response of the lasers to a modulation of the injection current was measured in amplitude and phase. A diagram of the measurement scheme of the ECDL transfer function is depicted in Figure 3.6. A low finesse Fabry-Perot etalon with a resonance FWHM of 20 MHz was used as an optical frequency discriminator to convert the frequency modulation of the laser into a measurable voltage modulation. The voltage signal was recorded with a lock-in amplifier. The laser was frequency-stabilized to this Fabry-Perot etalon with a low-bandwidth (below a few Hz) side-of-fringe locking technique. The laser frequency was maintained in the linear range of the Fabry-Perot etalon resonance by control of the PZT actuator.

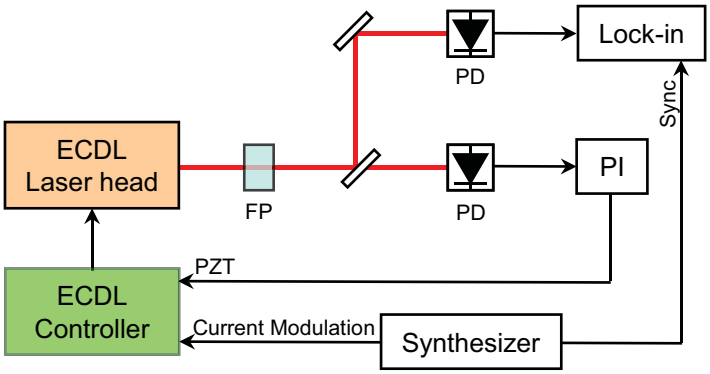

Figure 3.6: Experimental scheme used for the measurement of the transfer function of the ECDL controller Current Modulation input. PD: photodetector; PI: proportional-integral controller; FP: Fabry-Perot etalon.

The measurement of the frequency modulation response (in amplitude and phase) of the PW-ECL as a function of the injection current modulation frequency was performed by demodulating the heterodyne beat note signal between the PW-ECL and a frequency comb referenced to an H-maser, using an RF frequency discriminator (Miteq FMDM 21.4/2-4, see Section 2.4.2) and a lock-in detection.

The frequency modulation response (in amplitude and phase) of the ECDL and PW-ECL measured as a function of the injection current modulation frequency is depicted in Figure 3.7. The measured transfer function of the ECDL stays nearly constant at 1-2 MHz/V up to a modulation frequency of 40 kHz. Then a slight decrease is observed above 40 kHz and a peak around 2 MHz is noticed. A cutoff with a 20 dB/dec slope is observed above 2 MHz.

In the PW-ECL the transfer function is nearly constant up to 100 Hz followed

by a slight decrease and a 10 dB/dec slope above 10 kHz. The 3-dB roll-off point is observed at ~3 kHz.

For both lasers, the close to −180° phase of the transfer function observed at low modulation frequency reflects the fact that the laser frequency decreases with increasing current.

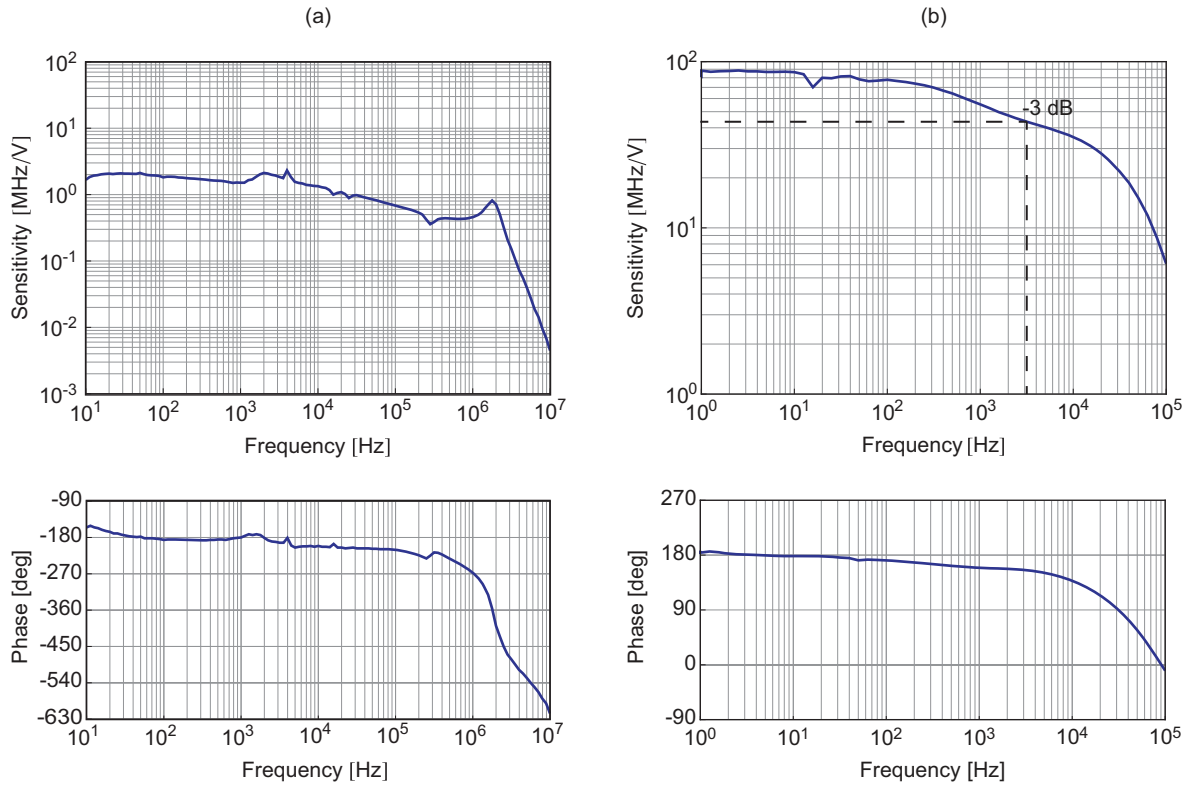

Figure 3.7: Transfer function in amplitude and phase of the ECDL (a) and of the PW-ECL (b).

3.3.3 Free-running lasers noise

3.3.3-1 Intensity noise

The measured relative intensity noise (RIN) of the ECDL and the PW-ECL is compared in Figure 3.8. The RIN of the ECDL is almost two orders of magnitude higher than the RIN of the PW-ECL in a wide range of Fourier frequencies (0.1 Hz – 100 kHz).

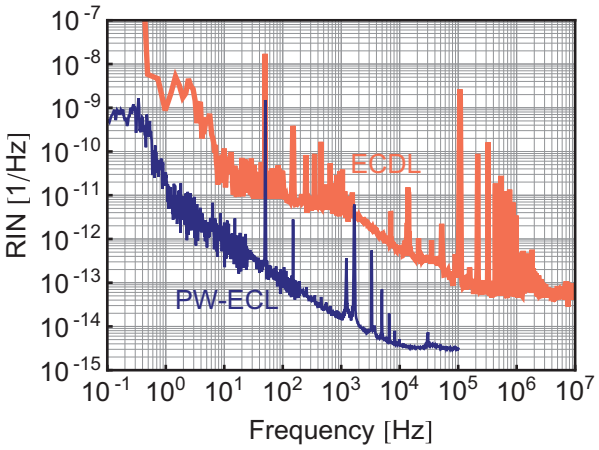

Figure 3.8: RIN spectrum of the free-running lasers: ECDL (light (red) thick curve) and PW-ECL (dark (blue) thin curve).

3.3.3-2 Frequency noise PSD

The frequency noise of the free-running ECDL was measured using the resonance of a scanning Fabry-Perot interferometer (FPI 100 from Toptica) as a frequency discriminator. One mirror of this cavity is attached to a PZT actuator controlling the cavity length and the cavity has a resonance FWHM of 2 MHz. This cavity was weakly locked (bandwidth <2 Hz) to the laser via feedback applied to the cavity PZT using the error signal generated in a PDH scheme. This enables this cavity to be used as an optical frequency discriminator nearly insensitive to laser intensity noise. The noise PSD error signal was recorded with an FFT spectrum analyzer and then converted into frequency noise PSD using the measured frequency discriminator of the cavity. A diagram of the ECDL frequency noise measurement setup is depicted in Figure 3.9.

The measured frequency noise PSD of the free-running ECDL shows a general $(\omega/2\pi)^{-\alpha}$ trend between 1 Hz and 100 kHz (Figure 3.10a), with $\alpha \sim 1.8$. Additional noise observed in some spectral regions (e.g. the bump in the range 10^2 – 10^4 Hz) is of technical origin, mainly due to mechanical noise in the laser external cavity. The contribution of the current source noise to the laser frequency noise is also shown in Figure 3.10a.

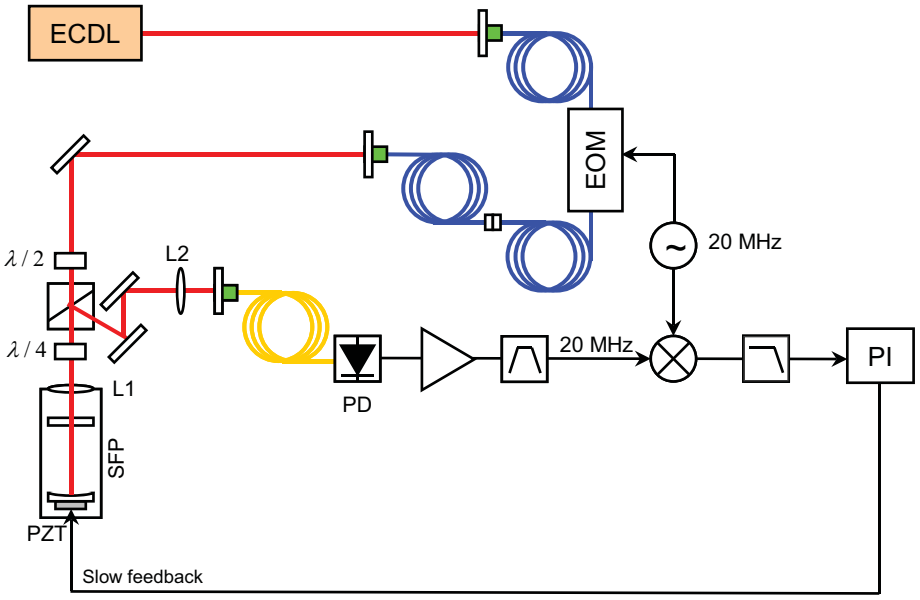

Figure 3.9: Schematic representation of the free-running ECDL frequency noise measurement setup. PD: photodetector, EOM: electro-optic modulator, PI: proportional-integral controller, SFP: scanning Fabry-Perot interferometer, light (yellow) lines correspond to standard single mode fibers, dark (blue) lines correspond to polarization maintaining fibers. The SFP is weakly locked to the free-running ECDL via the slow feedback applied to the PZT controlling the SFP length.

The current noise of the ECDL controller was measured using a dummy simulating a laser head with all the controls (TEC, PZT, etc.). Basically the laser head remained connected to the controller via this dummy cable with the laser diode replaced with a 6.8-Ω resistance. The voltage noise across this resistance was measured with a high impedance FFT spectrum analyzer. An equivalent frequency noise PSD (in Hz^2/Hz) due to the contribution of the laser source was calculated from the measured current noise spectrum of the driver and using the measured ECDL transfer function. Apart from a few peaks (at 10, 50, 100 Hz and 30 kHz) the contribution of the laser source noise to the frequency noise PSD of the free-running ECDL was found negligible.

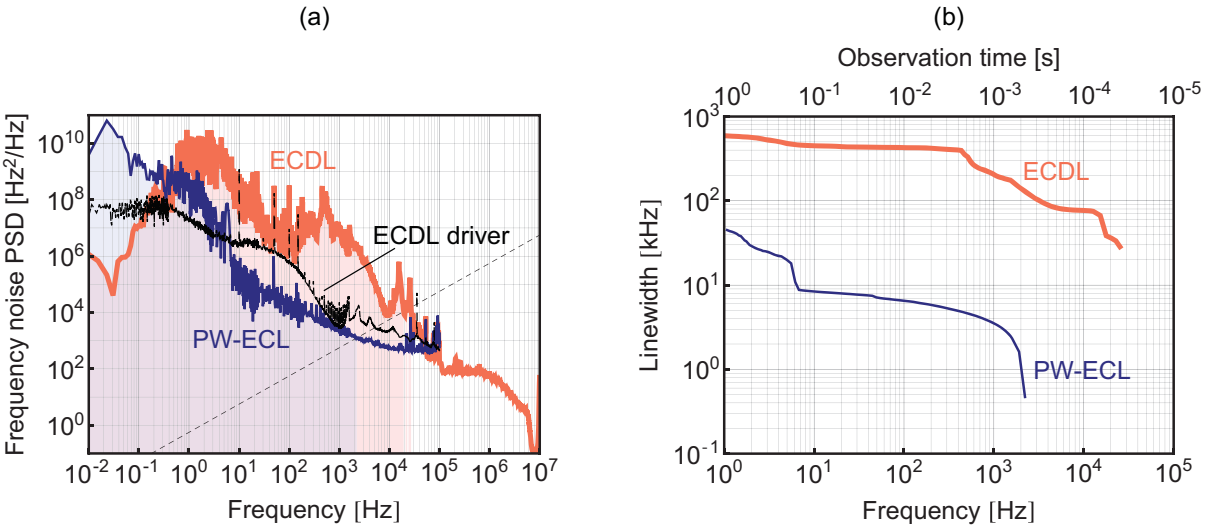

Figure 3.10: (a) Frequency noise spectrum of the free-running ECDL (light (red) thick line) and PW-ECL (dark (blue) thin line). The free-running ECDL was measured using the resonance of a scanning Fabry-Perot interferometer as a frequency discriminator. Below 2 Hz, the measured frequency noise is reduced by the weak lock of the cavity to the laser. The free-running PW-ECL was measured using the beat-note with a cavity-stabilized ECDL. The black dotted line corresponds to the contribution of the ECDL driver to the laser frequency noise. The β-separation line (see Section 2.3) is also shown on the same graph (dashed line). (b) Linewidth of the ECDL (light (red) thick curve) and of the PW-ECL (dark (blue) thin curve) calculated from the spectra of the free-running lasers using the simple approximation Eq. (2.13) in Section 2.3.

The laser linewidth $\Delta\nu$ (FWHM) can be determined from the frequency noise spectrum using the approximation presented in Section 2.3. The parts of the frequency noise PSD contributing to the linewidth are shown in Figure 3.10a with a filled area. Due to the $(\omega/2\pi)^{-\alpha}$ type of noise, the linewidth of the free-running ECDL depends on the observation time (inverse of the low cut-off frequency considered in the frequency noise spectrum integration). The evolution of the laser linewidth as a function of the cut-off frequency is shown in Figure 3.10b.

The frequency noise PSD of the PW-ECL laser is more difficult to measure due to its narrower linewidth. For this reason the ECDL was first PDH-stabilized to a high-finesse cavity. Then the heterodyne beat between the free-running PW-ECL and the PDH-stabilized ECDL was used in order to obtain the frequency noise PSD of the PW-ECL. The frequency noise of the beat signal, which represents the frequency noise of the PW-ECL as a result of the negligible contribution of the cavity-stabilized ECDL, was measured using an RF frequency discriminator (Miteq

FMDM 21.4/2-4, see Section 2.4.2) and an FFT spectrum analyzer.

The measured frequency noise PSD of the free-running PW-ECL is displayed in Figure 3.10a. The frequency noise of the free-running PW-ECL shows that the noise contributing to the laser linewidth extents up to Fourier frequencies of 2-3 kHz only, according to the β-separation line concept introduced in Section 2.3. The measured frequency noise PSD of the free-running PW-ECL shows a general $(\omega/2\pi)^{-2}$ trend between 0.02 Hz and 15 Hz and $(\omega/2\pi)^{-1}$ between 15 Hz and 4 kHz. The corresponding linewidth calculated from the frequency noise PSD using the simple approximation of Section 2.3 amounts to <10 kHz (for an observation time of 0.1 s).

3.4 High-finesse Fabry-Perot cavity

3.4.1 ULE cavity

An ultra-low thermal expansion (ULE) reference cavity is used for laser stabilization. Our target relative frequency stability in the low 10^{-15} at 1 s requires the same challenging stability in the cavity length, which must be made as little sensitive as possible to any external perturbation, such as temperature, pressure or vibration. We use a commercially available ULE glass cavity (ATFilms) with both spacer and mirror substrates made out of ULE material. The ULE material has a zero coefficient of thermal expansion (CTE) around room temperature. It is required to stabilize the cavity temperature in order to keep the thermal sensitivity low. In this process the thermal power transmitted to the cavity by the heater (or taken away by the cooler) creates a temperature gradient along the cavity. Having a zero CTE close to ambient temperature minimizes the induced temperature gradients and thus allows reducing the sensitivity of the cavity to thermal fluctuations.

The cavity is of the same horizontal design as described in [35]. The spacer is a cylinder with two horizontal grooves for mounting the cavity and an axial channel for the laser beam. The air is evacuated from this channel through a small conduit ending on the top of the spacer. Mirrors with a very high reflectivity coating at 1.55 µm are optically contacted to the spacer. A plano-concave resonator is formed from a flat- and a concave- mirror with a curvature radius of 50 cm. A photograph of the ULE Fabry-Perot cavity is shown in Figure 3.11.

Figure 3.11: Photograph of the horizontal Fabry-Perot cavity (ATFilms) with both cavity spacer and mirror substrates made out of ULE material.

The horizontally-mounted 10-cm long cavity has a measured finesse of ~185'000 and an FSR of ~1496.4 MHz (see Section 3.7.2). The cavity is placed in a vacuum chamber at 4×10^{-8} mbar residual pressure within a 2-layer thermal enclosure described in Section 3.5.3 with an active temperature control.

3.4.2 Thermal noise limit

The fundamental limit for the frequency noise of a high-finesse rigid cavity is set by the Brownian motion. A theoretical estimation for the thermal fluctuation spectrum was obtained by K. Numata *et al.* in [36] based on the mechanical loss of the cavity material and using the fluctuation dissipation theorem. The one-sided power spectrum of the displacement of one end of a cavity spacer at Fourier frequency $\omega/2\pi$ is given by

$$S_L^{\text{spacer}}(\omega) = \frac{4k_{\text{B}}T}{\omega}\frac{L}{3\pi R^2 E}\gamma_{\text{spacer}}\,, \tag{3.6}$$

where k_{B} is the Boltzmann constant, $T = 295.61$ K is the cavity temperature (see Section 3.8), $L = 10$ cm is the spacer length, $R = 5$ cm is the spacer radius, and $E = 67.6$ GPa and $\gamma_{\text{spacer}} = 1/(6\times10^4)$ are the Young's modulus and the mechanical loss of the ULE material, respectively [24]. The resulting displacement noise of one end of the cavity spacer is $\sqrt{S_L^{\text{spacer}}} = 1.6\times10^{-18}$ m/$\sqrt{\text{Hz}}$ at 1 Hz.

The contribution to the overall thermal noise from the cavity mirror substrate, which is also made out of ULE material is determined from:

$$S_L^{\mathrm{sub}}(\omega) = \frac{4k_{\mathrm{B}}T}{\omega}\frac{1-\sigma^2}{\sqrt{\pi}Ew_{\mathrm{FP}}}\gamma_{\mathrm{sub}}\,, \tag{3.7}$$

where $w_{\mathrm{FP}} = 314$ µm is the beam waist (see Section 3.4.3), $\gamma_{\mathrm{sub}} = 1/(6{\times}10^4)$ and $\sigma = 0.17$ are the mechanical loss and Poisson's ratio of the ULE material. The contribution of the calculated displacement noise of one mirror substrate is $\sqrt{S_L^{\mathrm{sub}}} = 3.3\times10^{-17}$ m/$\sqrt{\mathrm{Hz}}$ at 1 Hz.

The last contribution to the thermal noise of the cavity which should be accounted for comes from the additional loss $\gamma_{\mathrm{coat}} = 4{\times}10^{-4}$ [24] introduced by the coating of the mirrors

$$S_L^{\mathrm{coat}}(\omega) = \frac{4k_{\mathrm{B}}T}{\omega}\frac{1-\sigma^2}{\sqrt{\pi}Ew_{\mathrm{FP}}}\gamma_{\mathrm{sub}}\left(\frac{2}{\sqrt{\pi}}\frac{1-2\sigma}{1-\sigma}\frac{\gamma_{\mathrm{coat}}}{\gamma_{\mathrm{sub}}}\frac{d}{w_{\mathrm{FP}}}\right), \tag{3.8}$$

where $d = 5.3$ µm is a typical coating thickness [24]. The coating also has non negligible contribution of $\sqrt{S_L^{\mathrm{coat}}} = 2.0\times10^{-17}$ m/$\sqrt{\mathrm{Hz}}$ at 1 Hz to the displacement noise.

The displacement noise of the cavity can be estimated by considering the contributions from the spacer, from the substrates and the coating of the mirrors uncorrelated. Summing the noise for two ends of the spacer and the two mirrors (including coating and substrate) in quadrature gives the overall displacement noise equal to $\sqrt{S_L^{\mathrm{cavity}}} = 5.5\times10^{-17}$ m/$\sqrt{\mathrm{Hz}}$ at 1 Hz.

The fractional frequency stability is related to the displacement noise as

$$\sigma_y(\tau) = \sqrt{2\ln 2\,\frac{\omega}{2\pi}S_L^{\mathrm{cavity}}(\omega)}\,, \tag{3.9}$$

which leads to a constant thermal noise limit in terms of fractional frequency stability.

The calculated thermal noise floor of the described ULE cavity is $\sigma_y = 6.5\times10^{-16}$. This is a fundamental limit imposed on the expected frequency stability of the cavity-stabilized laser. This calculation is based on a typical coating thickness of 5.3 µm as considered in former publications [24], but at different wavelengths and the real coating thickness for our cavity is unknown. Moreover, numerical calculations are required in order to find the thermal noise level with a better accuracy [36]. Thus, this estimation might be subjected to some imprecision.

3.4.3 Mode-matching

The modes in a plano-concave resonator can be described by Hermite-Gaussian beams. The electric field in the transverse fundamental mode of the propagating Gaussian beam is described by [37]:

$$E(\mathbf{r},t) = \frac{1}{2} E_0 \frac{w_0}{w(z)} \exp\left\{ i(2\pi\nu t - kz) - \frac{\rho^2}{w^2(z)} - ik\frac{\rho^2}{2R(z)} - i\zeta(z) \right\} + \text{c.c.}, \qquad (3.10)$$

where $w(z) = w_0\sqrt{1 + z^2/{z_0}^2}$ is the transverse beam size, $R(z) = z + {z_0}^2 / z$ is the wavefront curvature, w_0 is the waist size, $\mathrm{z}_0 = k{w_0}^2/2$ is the Rayleigh range, $\zeta(z)$ is the phase and z and ρ are the cylindrical coordinates.

The propagation of the Gaussian beams in terms of the beam size and the curvature of the wavefronts is usually described by a complex-valued q-parameter:

$$\frac{1}{q(z)} = \frac{1}{R(z)} - i\frac{2}{kw^2(z)}. \qquad (3.11)$$

In order to fulfill the mode-matching condition it is required that the wavefront curvature matches the curvature of each mirror. To achieve this, it is only necessary to have the beam waist of a given size w_{FP} at the flat entrance mirror of the cavity. This beam waist can be determined from the curvatures of the mirrors (∞ for the flat mirror and $r = 50$ cm for the second mirror) of the ULE cavity and from the distance between these mirrors, $L = 10$ cm. From the definition of the wavefronts curvature and the Rayleigh range (see Eq. (3.11)) one finds

$$w_{\mathrm{FP}} = \sqrt[4]{\frac{4L(r-L)}{k^2}}, \qquad (3.12)$$

which leads to the value of 314 µm.

In practice, the laser beam (coming out from a collimator in our experiment, see Figure 3.12) needs to have its waist on the flat entrance mirror of the Fabry-Perot cavity mounted in a vacuum chamber with a fixed position and the size of this waist must be adjusted in order to fulfill the mode-matching condition. This can be achieved with a set of two lenses. Indeed, let us consider the scheme shown in Figure 3.12 and denote the q-parameter of the collimator output beam at the position of its waist as $q(0) = q_0$. Then the q-parameter of the beam $q(z) = q_2$ can be described with ABCD matrices.

$$q_2 = \frac{a_1 q_0 + b_1}{c_1 q_0 + d_1}, \text{ where } \begin{pmatrix} a_1 & b_1 \\ c_1 & d_1 \end{pmatrix} = \mathbf{FECBA}\,, \tag{3.13}$$

$$\mathbf{A} = \begin{pmatrix} 1 & z_1 \\ 0 & 1 \end{pmatrix}, \ \mathbf{B} = \begin{pmatrix} 1 & 0 \\ -1/f_1 & 1 \end{pmatrix}, \ \mathbf{C} = \begin{pmatrix} 1 & z_{12} \\ 0 & 1 \end{pmatrix}, \ \mathbf{E} = \begin{pmatrix} 1 & 0 \\ -1/f_2 & 1 \end{pmatrix} \tag{3.14}$$

$$\text{and } \mathbf{F} = \begin{pmatrix} 1 & z - (z_1 + z_{12}) \\ 0 & 1 \end{pmatrix}, \tag{3.15}$$

where z_1 is the position of the first lens, $z_{12} = z_2 - z_1$ is the distance between the lenses, f_1 and f_2 are the focal lengths of the lenses.

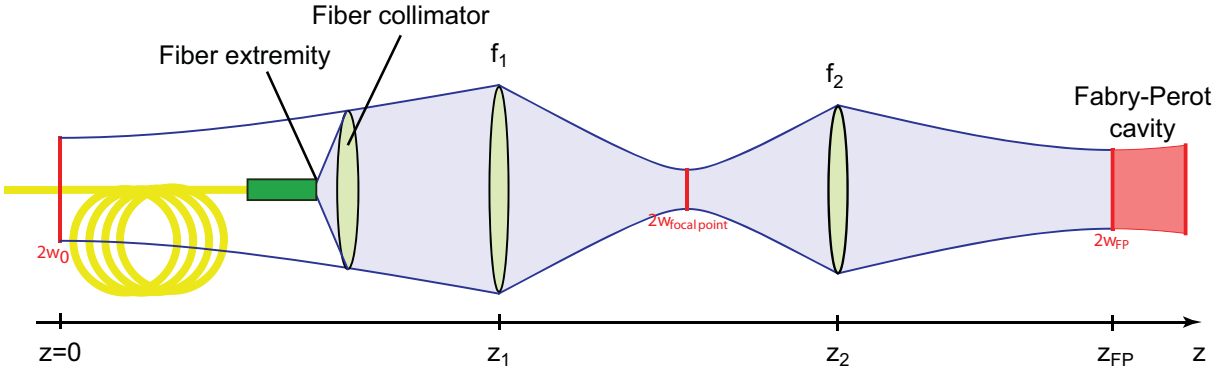

Figure 3.12: Schematic representation (not to scale) of the mode-matching to the Fabry-Perot cavity with two lenses. w_0 is the waist of the beam leaving the fiber collimator, z_1, z_2 and f_1, f_2 are the positions and the focal lengths of the lenses, $w_{\mathrm{FP}} = 314$ µm is the required beam waist on the flat mirror of the Fabry-Perot cavity.

The implied condition of the mode-matching is satisfied when

$$\frac{1}{q_2(z_{\mathrm{FP}})} = -i\frac{2}{k{w_{\mathrm{FP}}}^2}, \tag{3.16}$$

which determines the positions z_1 and z_2 of the lenses for a set of lenses with given focal lengths f_1 and f_2 and a known beam waist w_0 at $z = 0$ as a function of the Fabry-Perot cavity position z_{FP} and waist w_{FP}.

In practice, depending on the set of chosen lenses it is possible to decouple the effect of the lenses on the beam waist position and size. For instance, with our cavity configuration and with a set of lenses of $f_1 = 200$ mm and $f_2 = 150$ mm the posi-

tion of the waist is determined by the position of the first lens, when the two lenses are translated together and the waist size is nearly unchanged, while the size of the waist mainly depends on the distance between the two lenses. In order to select the most appropriate set of lenses for our cavity and experimental setup (a scheme of which will be shown later in Figure 3.15), several sets of standard lenses (both concave and convex) have been considered, with a special emphasis on the required precision of the lenses position. This was performed by quantifying the sensitivity of the beam parameters (waist size and position) for small variations of the position of each lens. The calculated tolerances displayed in Table 3.1 are expressed in terms of fractional sensitivity of the waist size ($\Delta w/w_{\mathrm{FP}}$) and shift of the waist position (Δz) with respect to the position z_1 of the set of lenses (translated together) and to the distance z_{12} between the two lenses.

In this calculation the following parameters are used: $w_{\mathrm{FP}} = 314$ µm and $z_1 = 600$ mm. The beam waist of $w_0 = 410$ µm was measured at the output of the fiber collimator at ~40 cm behind the collimator (as schematized in Figure 3.12). This implies a condition on the positioning of the first lens ($z_1 > 40$ cm).

From the results of Table 3.1, two sets of lenses show a minimal sensitivity to small deviations of the lens from their nominal position: $f_1 = 200$ mm, $f_2 = 150$ mm and $f_1 = -300$ mm and $f_2 = 300$ mm. The second set of lenses was chosen as it was easier to be implemented in practice. In order to verify the calculation and perform a pre-alignment of the beam to the cavity, the beam waist was measured at the position of the cavity entrance mirror. The measured value of 310 µm fits well with the calculated value. A fine tuning of the lens positions is performed later when the laser is stabilized to the ULE cavity by maximizing the transmission signal.

f_1	f_2	z_{FP}	z_{12}	$\frac{\Delta w/w_{FP}}{\Delta z_{12}}$	$\frac{\Delta z}{\Delta z_{12}}$	$\frac{\Delta w/w_{FP}}{\Delta z_1}$	$\frac{\Delta z}{\Delta z_1}$
[mm]	[mm]	[mm]	[mm]	[1/mm]	[1/mm]	[1/mm]	[1/mm]
50	50	1205	108	-0.177	-64.0	-0.0014	1.20
50	75	1493	136	-0.115	-76.0	-0.0014	1.03
75	100	1517	197	-0.064	-33.1	-0.0015	1.14
100	75	1161	202	-0.050	-6.3	-0.0010	1.43
100	100	1353	233	-0.042	-12.5	-0.0013	1.30
150	150	1511	378	-0.017	-3.8	-0.0011	1.37
200	150	1440	464	-0.010	0.5	-0.0004	1.56
-100	150	1710	86	-0.039	-31.2	-0.0014	0.88
-150	200	1725	122	-0.020	-14.2	-0.0014	0.86
-200	250	1825	165	-0.013	-8.9	-0.0014	0.84
-250	250	1670	149	-0.011	-5.6	-0.0014	0.87
-250	300	1936	217	-0.009	-6.0	-0.0014	0.81
-300	300	1814	205	-0.008	-4.1	-0.0014	0.83

Table 3.1: Comparison of different sets of lenses for modematching. $w_0 = 0.41$ mm, $w_{FP} = 0.314$ mm, $z_1 = 600$ mm (see figure Figure 3.12). f_1 and f_2: focal lengths of the lenses. z_{FP}: position of the Fabry-Perot cavity. z_{12}: distance between the lenses. $(\Delta w/w_{FP})/\Delta z_{12}$: relative waist size sensitivity to the distance between the lenses. $\Delta z/\Delta z_{12}$: waist position sensitivity to the distance between the lenses. $(\Delta w/w_{FP})/\Delta z_1$: relative waist size sensitivity to the position of the first lens z_1, when two lenses are translated together. $\Delta z/\Delta z_1$: waist position sensitivity to the position of the first lens z_1, when two lenses are translated together. The set of chosen lenses is shown with light-gray fill.

3.5 Cavity thermal enclosure

3.5.1 Motivation

To set the scale for the required high-finesse cavity length stability one notes that the relative frequency variations of a laser stabilized to the cavity are identical to the relative variations of the distance between the mirrors. One can notice, that in order to reach a target stability of 10^{-15} with a mirror separation $L = 10$ cm in the ULE cavity, the maximum tolerable length variations are on the order of one-tenth of the proton radius.

This is the reason why any deforming forces caused by seismic and/or technical vibrations must be attenuated to minimize the excess cavity noise [38]. Several cavity assemblies with different designs exist to date. A horizontally-oriented cavity

designed in SYRTE [35] was used in this thesis. The optimal mounting position of the supporting points in order to minimize the sensitivity to vibrations were calculated by J. Millo *et al.* in [35] and were used to define the mounting position of the ULE cavity.

The radiation pressure fluctuations are usually considered negligible, however the environmental fluctuations could affect the cavity resonance frequency by changing the optical length between the mirrors via the refractive index variations and thermal expansivity of the material. This is why it is required to keep the cavity well isolated from temperature fluctuations in high vacuum conditions.

3.5.2 Sensitivity of Fabry-Perot cavity to external perturbations

3.5.2-1 Pressure

It is well known that the refractive index of air changes with pressure [39]. Thus, pressure fluctuations lead to fluctuations of the index of refraction and as a consequence of the cavity optical length. It is not obvious to evaluate pressure fluctuations at pressures below 10^{-4} mbar. We assume here that relative pressure fluctuations are at the level of 10%. In order to establish a relationship between the optical length of the cavity and the pressure, let us define the difference in the refraction index of air at atmospheric pressure and in vacuum:

$$\delta n_{\mathrm{s}} = (n_{\mathrm{s}} - 1)\,, \tag{3.17}$$

where n_{s} is the refractive index of dry air at 15 °C and 101325 Pa, containing 0.045% by volume of CO_2, which can be determined from [39]:

$$\begin{aligned} \delta n_{\mathrm{s}} = & \left(8342.54 + 2406147 \cdot \left(130 - \left(\frac{1}{\lambda} \right)^2 \right)^{-1} \right. \\ & \left. +15998. \left(38.9 - \left(\frac{1}{\lambda} \right)^2 \right)^{-1} \right) \times 10^{-8}, \end{aligned} \tag{3.18}$$

where λ is the wavelength in µm.

At the wavelength of 1.55 µm one obtains $\delta n_{\mathrm{s}} = 0.000273265$. The refraction index of air as a function of temperature and pressure [39] is

$$\delta n(T,p) = \delta n_s \times \frac{\frac{p}{100}\left(1 + \frac{p}{100}(60.1 - 0.972\,T)\times 10^{-10}\right)}{96095.43(1 + 0.003661\,T)}, \tag{3.19}$$

where $\delta n(T,p) = n(T,p) - 1$, $n(T,p)$ is the refraction index at pressure p in mbar and temperature T in °C.

Figure 3.13 shows the plot of $n(T,p)$ as a function of p for the fixed temperature of $T = 23$ °C. In order to reach a target fractional frequency stability of 10^{-15} of the laser locked to the high finesse cavity, it is necessary to keep the fluctuations of the refractive index below this limit as it directly leads to a fluctuation of the cavity optical length. Thus, considering a 10% relative pressure variation, it requires the cavity pressure to be maintained at below 4×10^{-8} mbar.

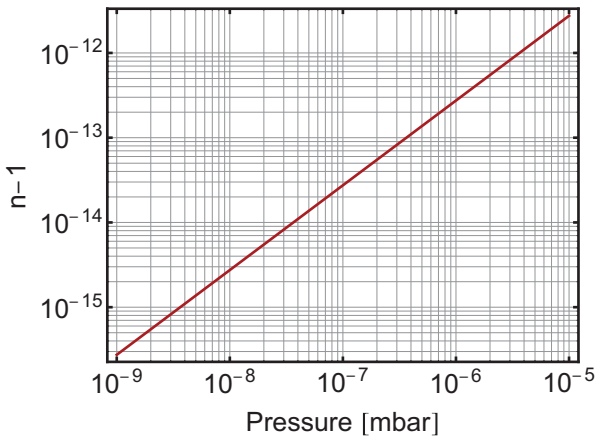

Figure 3.13: Index of refraction of air as a function of pressure.

3.5.2-2 Temperature

Another issue that affects the frequency stability of a reference cavity for averaging times longer than several seconds is the dimensional stability due to temperature variations [38].

For these reasons a cavity with a spacer made out of ULE material was chosen. ULE is a titania-doped silicate glass which has a zero thermal expansion coefficient at a temperature T_0 close to room temperature (see Section 3.8). When the cavity temperature is kept close to T_0 the relative length has a quadratic residual temperature dependence:

$$\Delta L/L = \Delta\nu/\nu \sim 10^{-9}\ [\mathrm{K}^{-2}] \cdot (T - T_0)^2\,, \tag{3.20}$$

where T is the temperature of the cavity and the rate of variation of the CTE around the turning point is $\sim 10^{-9}$ $[\mathrm{K}^{-2}]$ (see Section 3.8).

Thus one can estimate the maximum tolerable temperature variations being at the mK level in order to reach a stability of 10^{-15}.

The temperature variations could be divided into spatial and temporal variations. However these two types of temperature variations are interrelated. A step in the ambient temperature will lead to a change of the average temperature of the cavity placed in a vacuum chamber. This consequently changes the length of the cavity due to the thermal expansion of the material at a long term.

Spatial temperature fluctuations are attributed to the temperature inhomogeneity of the cavity, while the temporal fluctuations occur due to environmental temperature variations. It is important to notice that various temperature fluctuations become important on different time scales. Thus the temperature inhomogeneity could be attributed to the short term and Fabry-Perot cavity temporal temperature change to the long term frequency fluctuations respectively. As the temperature variations on different time scales significantly differ from each other, one can neglect the temporal temperature fluctuations at a short term of typically not exceeding 1 s. At a longer term the cavity temperature is maintained with a phase-locked loop controlling a TEC element.

A TEC element keeping the cavity at its zero-CTE temperature takes away some power creating a temperature gradient inside the cavity. It is obvious that in order to have a smaller gradient induced, the thermal conductivity of the enclosure walls should be maximized (ideally copper). In general there are three main mechanisms of heat transfer: conduction, convection and radiation; however at pressure of 10^{-8} mbar at which the cavity is maintained the convection can be neglected. Only radiative and conductive heat exchanges take place.

First of all let us consider a reasonably simple model. While dealing with nearly uniform cavity placed inside the vacuum chamber, it makes sense to imagine the cavity as a ball placed inside a spherical envelope. Or in other words, we work within a model where two concentric spheres are enclosed into one another.

The heat radiated from the surfaces of both spheres could be represented as a

sum of emitted body radiation and reflected heat;

$$\begin{cases} P_{ie} = S_i \varepsilon_i \sigma_{\mathrm{B}} T_i^4 + (1-\varepsilon_i) P_i, \\ P_{ei} = S_e \varepsilon_e \sigma_{\mathrm{B}} T_e^4 + (1-\varepsilon_e) P_e, \end{cases} \tag{3.21}$$

where σ_{B} – Stefan-Boltzmann constant, $S_{i,e}$ – surface, $\varepsilon_{i,e}$ – emissivity, $T_{i,e}$ – temperature, $P_{i,e}$ – received power, and $P_{ie,ei}$ – radiated power, for the internal and external spheres respectively. Here indices e and i denote external and internal spheres respectively.

Due to geometry, only a fraction η of the radiation emitted by the external sphere could be absorbed by the internal one. The remaining power will be reabsorbed within the external sphere. Thus the balance equations will look as follows:

$$\begin{cases} P_e = P_{ie} + (1-\eta) P_{ei}, \\ P_i = \eta P_{ei}, \end{cases} \tag{3.22}$$

where

$$\eta = \frac{S_i}{S_e}. \tag{3.23}$$

From the Eqs. (3.21) – (3.23) one can find the net power $P_i^{\mathrm{TOT}} = P_{ie} - P_i$ transferred from the external sphere to the internal;

$$P_i^{\mathrm{TOT}} = \frac{\varepsilon_i \varepsilon_e S_i \sigma_{\mathrm{B}} \left(T_i^4 - T_e^4 \right)}{\varepsilon_e + \eta \varepsilon_i (1-\varepsilon_e)}. \tag{3.24}$$

From this final equation it becomes obvious that in order to minimize the power exchange it is required to reduce the emissivities on both external and internal surfaces of the internal and external spheres respectively. At 10^{-8} mbar the molecular heat exchange has ~100-fold smaller impact and can be neglected.

To conclude, a simplified model of two concentric spheres considered to estimate the heat exchange here shows that:

i) Gaseous conduction is negligible at pressure level of 10^{-8} mbar.

ii) Radiative heat transfer is the dominant mechanism.

iii) It is required to minimize the solid-state conduction in the contact points between the layers, described by their thermal resistances.

3.5.3 Design

We have designed and manufactured a 2-layer enclosure to hold the ULE cavity and minimize its temperature sensitivity.

The configuration is optimized to achieve a high temperature stability by efficiently attenuating external temperature fluctuations. A special emphasis was put on the cavity temperature homogeneity. A 2-layer enclosure made of an internal copper "cradle" and an external aluminum thermal screen placed in a high-vacuum chamber ($<4\times10^{-8}$ mbar) has been designed, aiming at partially decoupling the two following functionalities:

i) A thermal exchange as homogeneous as possible between the cavity and the cradle is intended and radiative heat transfer between cavity and cradle was made as high as possible in a cylindrical symmetry configuration. For this purpose, the inner surface of the cradle should act as a blackbody in radiative thermal equilibrium with the cavity. The cradle is made of a massive (2 cm thick) copper cylinder for its high thermal conductivity. Its external surface is gold-coated to minimize thermal exchanges with the external screen.

ii) The external screen, temperature-stabilized with four TECs, produces a temporal filtering of external temperature fluctuations. It is made out of 2-cm thick aluminum block gold-coated on both sides to minimize heat exchange with the cradle and the vacuum chamber.

In order to eliminate the heat transfer from the outer enclosure, the heat conduction between the screen and the cradle has been minimized. Therefore, the cradle was supported by punctual points of contact using small balls as an intermediate suspending material. In order to fix all the degrees of freedom of the cavity the balls were positioned in Kelvin Clamp kinematic coupling. Some photographs of the cavity assembly are shown in Figure 3.14.

The cavity is placed onto four viton cylindrical pads according to the positions calculated in SYRTE for exactly the same spacer [35]. In that work it was shown that the acceleration sensitivity coefficient can be zeroed by placing the cavity on these points of contact. The vacuum chamber is placed onto an active vibration compensation system (AVI 300-LT/LP from TableStable) positioned on a marble block.

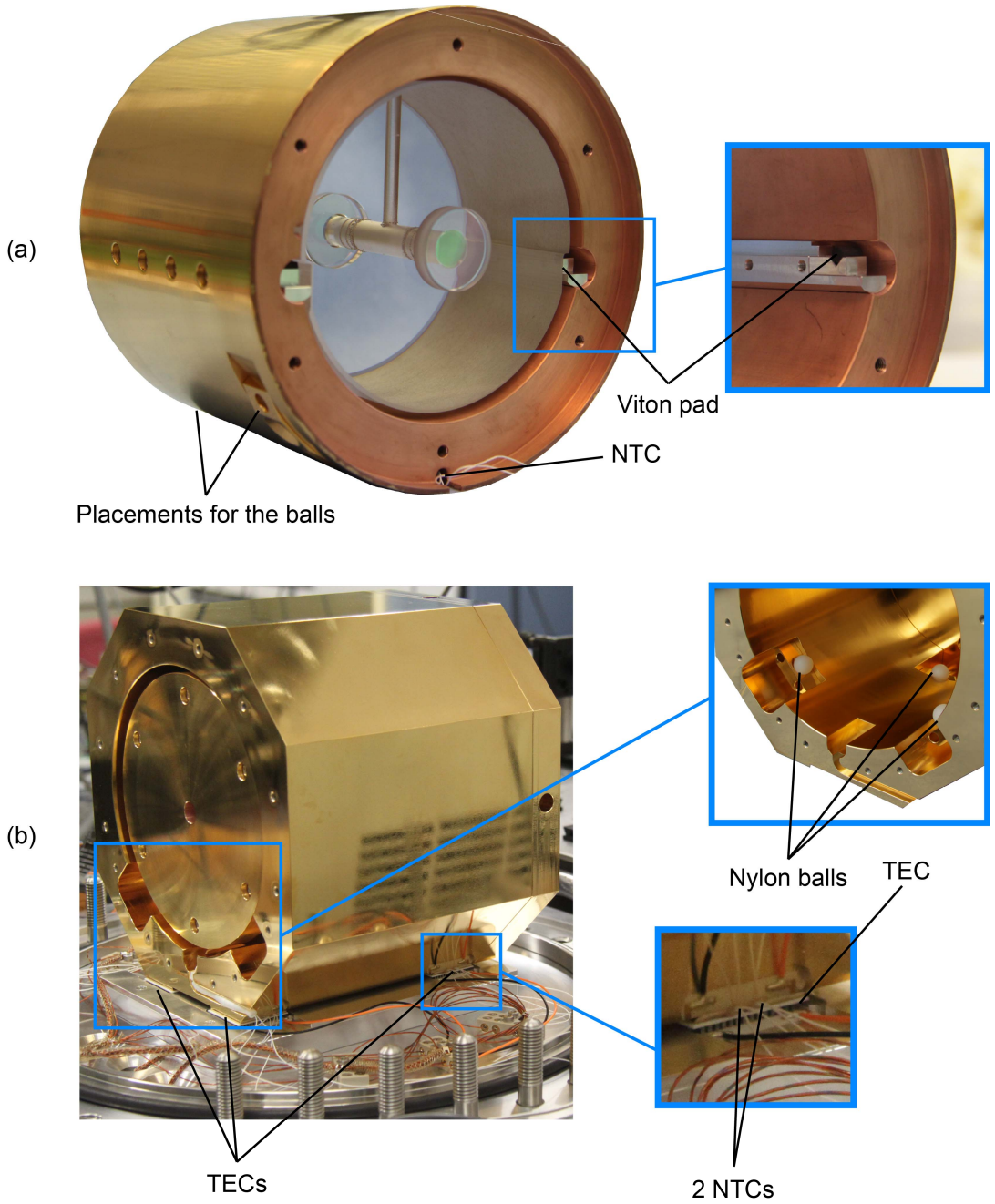

Figure 3.14: (a) The cavity is supported in the copper cradle with gold-coated external surface by four Viton cylindrical pads at Airy points. (b) The cradle containing the cavity is supported with three nylon balls into the thermal screen to minimize conductive thermal exchange.

3.6 Pound-Drever-Hall Stabilization

3.6.1 Scheme

Both lasers were stabilized to the ULE cavity and it was possible to maintain both lasers in a stable operation state simultaneously. However, no direct comparison between the two lasers stabilized to the common ULE cavity was performed and most of the times the lasers were stabilized to the cavity separately.

The implemented schematic diagram of the laser stabilization to the ULE cavity with the PDH technique is depicted in Figure 3.15. Both lasers (ECDL and PW-ECL) were stabilized in exactly the same setup, when not used simultaneously. An EOM (model PM-150-005 from JDSU) was used to generate 20-MHz FM sidebands in the laser spectrum for the PDH stabilization. The cavity reflection signal was demodulated using a commercial PDH demodulator (PDD 110 from Toptica). When the two lasers were used simultaneously, the servo-loops were disentangled by selecting different modulation frequencies with the two respective EOMs (20 MHz and 30 MHz), and the neighbouring cavity resonances were used to eliminate optical interference. The laser power at the input of the ULE cavity was kept low (~50 µW) to minimize power-to-frequency conversion in the cavity that can significantly degrade the stability of an optical oscillator. This optical power is typically 10 times higher than used by other groups [35]. However, the corresponding power fluctuations appear to be lower than the stability achieved with the optical-to-microwave frequency division (as will be shown in Section 6.6.2) and are thus not a limiting factor in the present configuration.

The stabilization of the ECDL is achieved by directly providing a feedback to the PZT (for slow corrections) and to the laser diode current (fast corrections) using the fast double-integration PID controller (FALC110 from Toptica).

With a tuning coefficient of 56 MHz/mA, the PW-ECL frequency cannot be tuned with the injection current by more than 3 FSRs of the ULE cavity (~27 mA/FSR), limited by the laser threshold (~10 mA) on one side and by the maximum operating current (110 mA) on the other side. Thus, the temperature of the laser was set to 23.5 °C in order that the laser frequency was in coincidence with a cavity resonance at an injection current of ~60 mA located in the center of the laser current range, which offers the largest current-tuning capability. The corresponding laser optical power was 4.55 mW.

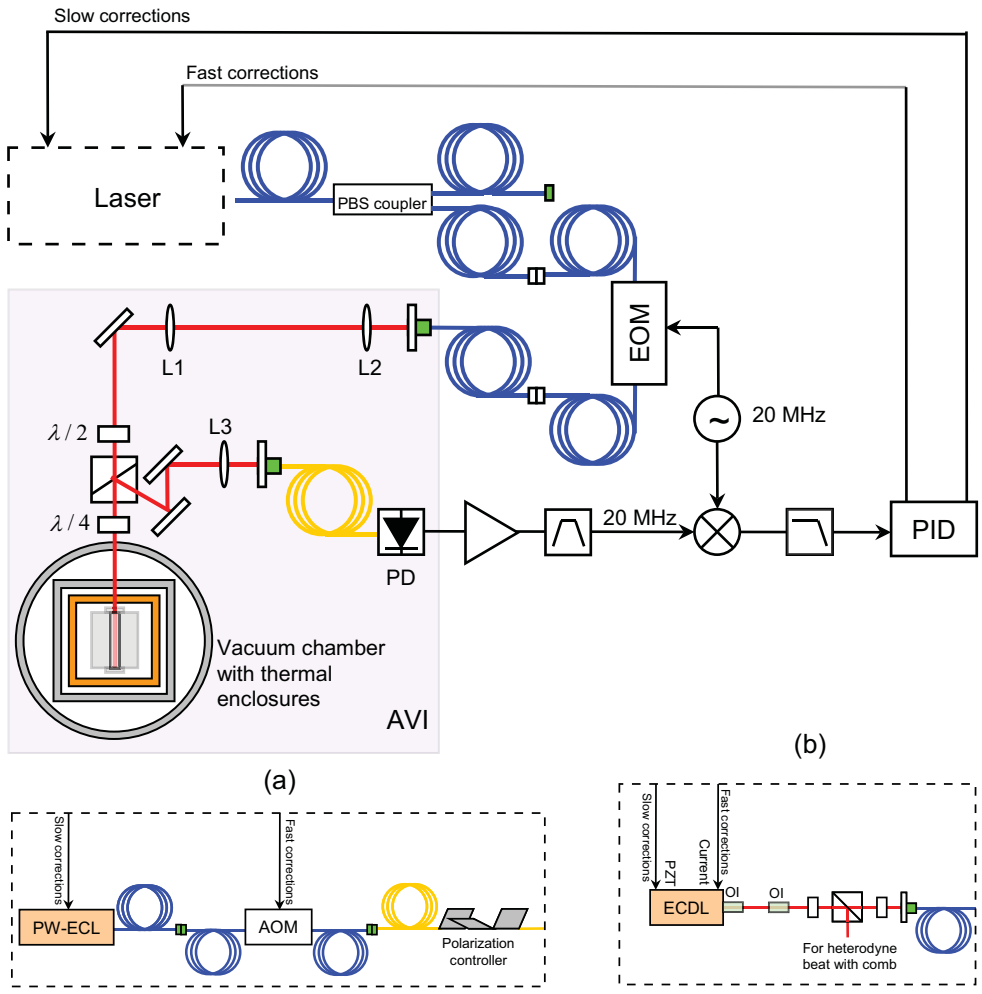

Figure 3.15: Scheme of the PDH stabilization of the PW-ECL (a) and the ECDL (b) to the ULE cavity. EOM: electro-optic modulator; AOM: acousto-optic modulator; PBS: polarization beamsplitter; L1-L2: mode matching lenses; L3: focusing lens; PD: photodiode; DBM: double-balanced mixer; AVI: active vibration isolation platform; OI: optical isolator. Darker (blue) fibers are PM fibers; lighter (yellow) fibers are standard singlemode fibers.

While the PW-ECL has a low frequency noise, a direct tight lock to the ULE cavity by feedback to the laser injection current only is prevented by the low frequency modulation bandwidth of this laser (see Figure 3.7). Therefore, a 40-MHz acousto-optic modulator (AOM, model FCM-40.8E5C from IntraAction Corp.) was used to achieve a higher feedback bandwidth (up to 100 kHz). Fast corrections were applied to the FM input of the AOM driver (DE-401M) after amplification in the same fast PID controller (FALC110 from Toptica) as for ECDL. To prevent a drift of the AOM driving frequency that would result from the relative frequency drift

between the free-running PW-ECL and the cavity resonance, slow corrections were applied to the laser current. This maintains the AOM driving frequency at its nominal value of 40 MHz, where the AOM diffraction efficiency is maximized. This minimizes power-to-frequency noise conversion that may result from a change of the optical power impinging on the cavity.

3.6.2 Noise of the stabilized lasers

3.6.2-1 In-loop frequency noise and locking efficiency

Due to our lack of a suitable optical reference (e.g. another similar cavity or a second independent ultra-narrow linewidth laser) to quantify the frequency noise of the lasers stabilized to the ULE cavity, only the in-loop error signal was considered to assess the performances of the stabilization loop.

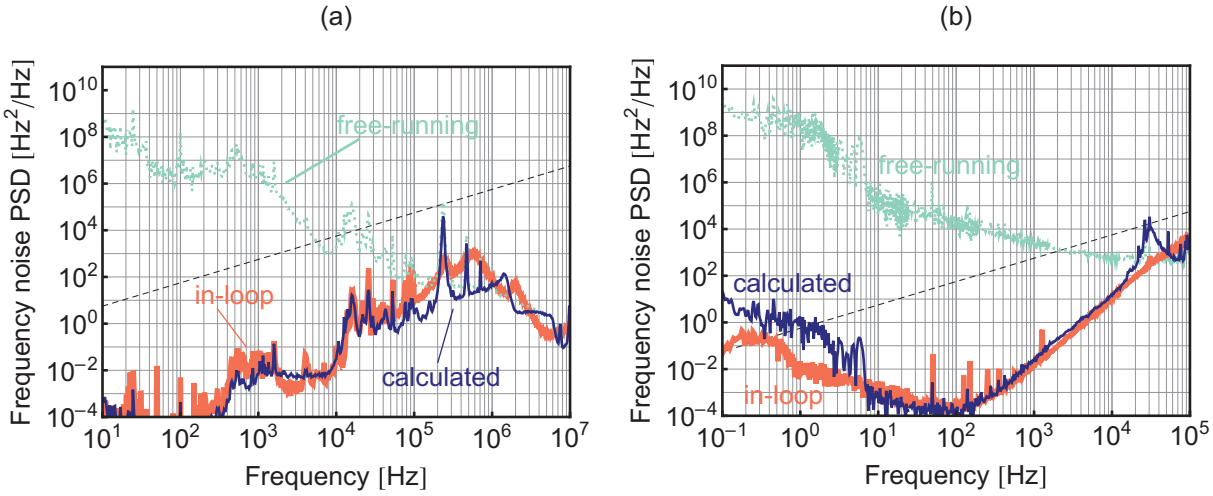

Figure 3.16: (a) Frequency noise spectrum of the free-running ECDL (dotted light (green) curve) and locked to the ULE cavity (light (red) thick curve). The frequency noise calculated from the measured transfer functions of the laser and PID controller and calculated transfer function of the ULE cavity is also shown (dark (blue) thin curve). (b) Frequency noise PSD of the free-running PW-ECL (dotted light (green) curve) and locked to the ULE cavity (light (red) thick curve). The noise of the locked laser is determined from the in-loop error signal. The frequency noise calculated from the measured transfer functions of the laser and calculated transfer functions of the ULE cavity and PID controller is also shown (dark (blue) thin curve). The β-separation line that is relevant for the determination of the laser linewidth (see Section 2.3) is also shown by the dashed line. The noise of the free-running lasers was measured as described in Section 3.3.3.

Absolute frequency noise of the laser (and true laser linewidth) can thus not be inferred from the analysis of this signal. However, Figure 3.16 shows that the residual noise of the in-loop error signal lies well below the β-separation line in the entire analyzed frequency range. Therefore, no additional contribution to the laser linewidth is induced by the PDH stabilization. With the servo loop bandwidths of ~0.6 MHz and >100 kHz, respectively, assessed from the servo bumps, the ECDL and PW-ECL thus faithfully follow the cavity resonance and the frequency noise (and linewidth) of the lasers will be ultimately limited by the cavity noise only.

The frequency noise measured from the in-loop error signal is in a very good agreement with the frequency noise PSD calculated from the noise of free-running laser and from the total loop gain assessed from the transfer functions individually measured in amplitude and phase for the laser controllers, cavity discriminator and PID controller (blue thin curves in Figure 3.16).

The fractional frequency stability calculated from the in-loop error signal using the relation between the Allan deviation and frequency noise PSD (see Eq. (2.9) in Section 2.2.2) is depicted in Figure 3.17. This figure shows that the residual servo loop noise contributes only $<4\times10^{-16}$ (at 1 s) to the laser frequency instability.

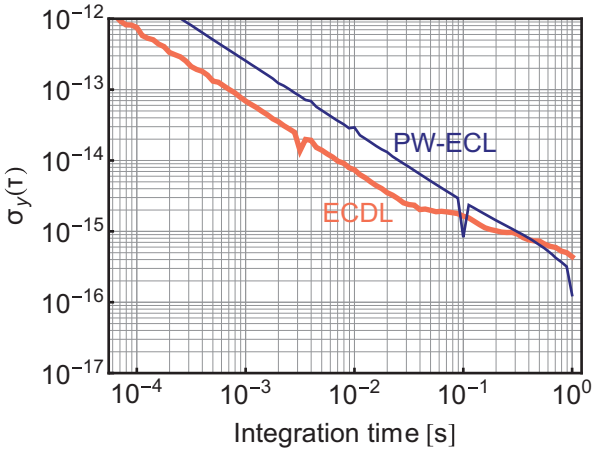

Figure 3.17: Fractional frequency stability calculated from the measured in-loop error signals of the ECDL and PW-ECL.

3.7 High-finesse Fabry-Perot cavity characterization

3.7.1 Cavity ring down time

One of the important parameters characterizing the cavity is the finesse. The width of the cavity resonance has been determined experimentally from a ring-down time measurement. For this purpose, the laser was locked to the cavity resonance and the light transmitted through the cavity was monitored on a photodiode. Following a sudden laser switch off, the time decay of the photodiode signal was recorded on an oscilloscope.

The cavity ring-down time measurement is depicted in Figure 3.18. Fitting the experimental data by an exponential decay function gives a cavity decay time of $\tau = 19.6$ µs, corresponding to a resonance width (FWHM) $\Delta\nu = 1/(2\pi\tau)$ of 8.1 kHz. For the 1.5-GHz FSR of the cavity, this translates into a finesse of about 185'000.

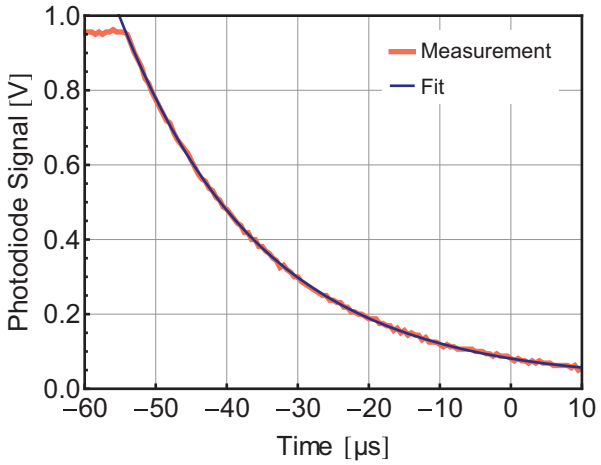

Figure 3.18: Cavity lifetime determined by a ring-down time measurement. A decay time of 19.6 µs is obtained from the exponential fit.

3.7.2 Characterization of a resonance with a phase-locked PW-ECL

The low-noise properties of the PW-ECL make this laser very attractive for various applications where a very narrow linewidth is required. Here the use of the PW-ECL for the characterization of our ULE cavity is demonstrated. In this ap-

proach not only the linewidth, but the entire lineshape of the cavity resonance was experimentally measured. An accurate measurement of the narrow cavity resonance requires a very coherent and stable laser to be tuned through the resonance. For this purpose, the ECDL was locked to one resonance of the ULE cavity using the PDH technique. FM sidebands for the PDH locking were generated with EOM1 (PM-150-005 from JDSU) with 25 MHz modulation frequency and the cavity reflection signal was demodulated using a commercial PDH demodulator (PDD 110/F from Toptica).

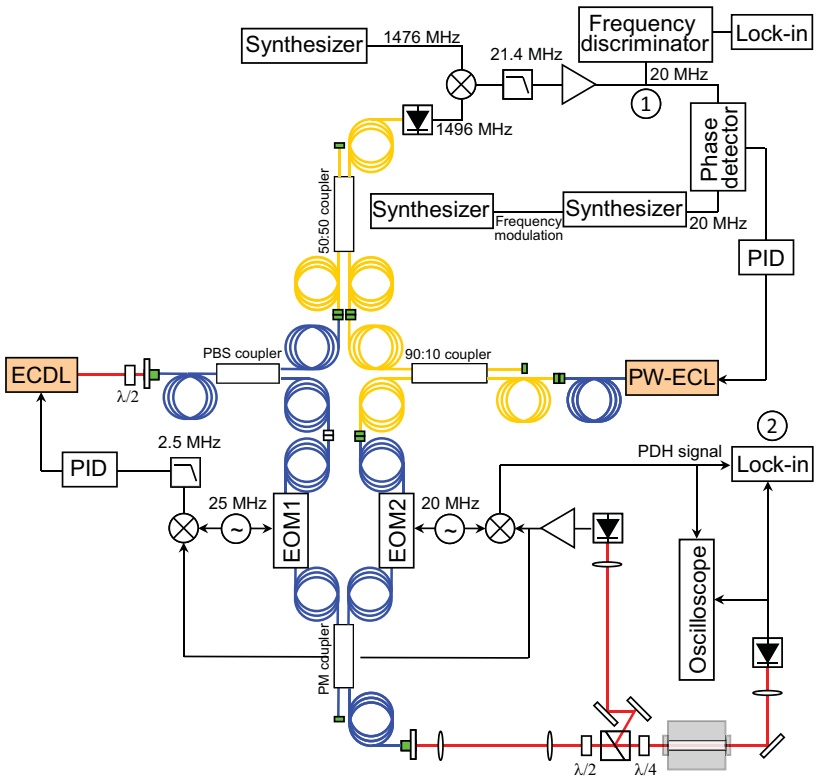

Figure 3.19: Schematic representation of the cavity resonance characterization with a PW-ECL. EOM: electro-optic modulator; PBS: polarization beamsplitter; PM: polarization maintaining. Dark (blue) fibers are PM fibers; light (yellow) fibers are standard singlemode fibers. For the measurement of the cavity transfer functions, a frequency modulation was applied to the PW-ECL and the output signal at point (2) was measured using a lock-in amplifier to extract the component (in amplitude and phase) at the modulation frequency of the PW-ECL around the resonance center. The modulation response of the PW-ECL carrier frequency was determined at measurement point (1) by demodulating the heterodyne beat between the two lasers using an RF frequency discriminator.

The PW-ECL was phase-locked to the ECDL with an offset frequency corresponding to one FSR of the ULE cavity, so as to probe the adjacent cavity resonance. For this purpose, the heterodyne beat at 1496 MHz between the two lasers was detected with a fast photodiode (model 1434 from New Focus) and was subsequently frequency down-converted by mixing with a 1476 MHz signal from a frequency synthesizer (SMF 100A from Rhode&Schwartz). The resulting 20-MHz signal was compared to a 20-MHz reference signal from a frequency synthesizer (Agilent 33250A) in a digital phase detector (DXD200) to generate an error signal. The error signal was amplified in a PID controller and the corrections were applied to the modulation input of the PW-ECL current driver only. No fast feedback to an AOM was used here. The schematic representation of the phase lock of the PW-ECL to the cavity-stabilized ECDL used for the characterization of the cavity resonance is shown in Figure 3.19. With this scheme, not only the cavity resonance lineshape was accurately measured, but also the cavity transfer functions in transmission and reflection, enabling the cavity resonance to be fully characterized.

3.7.2-1 Cavity resonance lineshape

With the achieved phase-lock, both lasers have a linewidth much narrower than the width of the ULE cavity resonance, even though the limited modulation bandwidth of the PW-ECL current leads to some excess phase noise due to the servo bump. By slowly sweeping the offset frequency between the two lasers (by changing the synthesizer reference frequency at a sweep rate of 10 kHz/s), the PW-ECL carrier frequency was scanned through the cavity resonance. A slow sweep was needed as a consequence of the high cavity finesse and of the resulting long photon lifetime. Two different photodiodes were used to measure the cavity resonance in transmission and reflection during the frequency sweep of the PW-ECL. The same photodetector as used for PDH stabilization of the ECDL (PDA-10CF-EC from Thorlabs) was used to measure the cavity resonance in reflection, while a second photodiode (PDA-10CS-EC from Thorlabs) was used in transmission.

The resonance lineshape measured in transmission is shown in Figure 3.20. A FWHM linewidth of 8.3 kHz is obtained from a Lorentzian fit, which is in a very good agreement with the value obtained from the cavity ring-down time measurement.

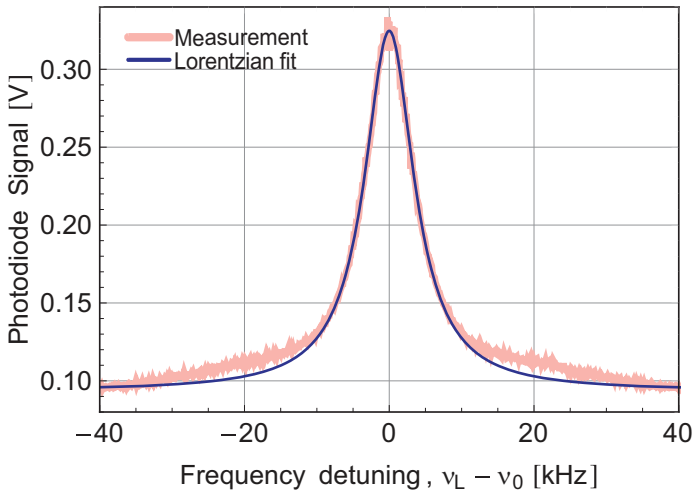

Figure 3.20: ULE cavity resonance measured in transmission (light (pink) thick curve) and fit by a Lorentzian function (dark (blue) thin curve). The pedestal observed in the measured lineshape (at 5-30 kHz offset frequency from line center) and which makes the lineshape deviates from the Lorentzian fit arises from the phase noise of the PW-ECL resulting from its limited feedback bandwidth.

3.7.2-2 Cavity transfer function

The transfer function of the cavity was measured both in transmission and in reflection by modulating the offset frequency between the ECDL (stabilized to one cavity resonance) and the PW-ECL (probing the adjacent cavity resonance) with a sine waveform of varying frequency:

i) For the cavity transfer function in transmission, the PW-ECL was tuned to the side of the resonance (at half-height) by shifting the offset-frequency from the ECDL by one half width of the cavity resonance (i.e. the average offset frequency between the two lasers was set to 1496.396 MHz) and the flank of the resonance was used as a frequency discriminator to convert the laser frequency modulation into an intensity modulation that was detected by the transmission photodiode. The photodiode output signal was then demodulated in a lock-in amplifier to extract the component (in amplitude and phase) at the modulation frequency.

ii) For the cavity transfer function in reflection, the PW-ECL was tuned to the center of the resonance by setting the offset frequency between the two lasers to exactly one FSR of the cavity (1496.400 MHz) and the PDH

signal was used as a frequency discriminator to convert the frequency modulation of the PW-ECL into a measurable voltage modulation. The PDH signal for the PW-ECL was generated by using a second EOM (EOM2, MPZ-LN-10 from Photline) with a modulation frequency of 20 MHz which was sufficiently far away from the modulation frequency used in EOM1 for the ECDL to avoid any cross-talk between the two demodulations, as the PDH signals for the two lasers were obtained from the cavity reflection using the same photodiode. The PDH demodulation for the PW-ECL (at 20 MHz) was realized using a second PDD 110/F demodulator and the output signal was measured in a lock-in amplifier to extract the component (in amplitude and phase) at the modulation frequency of the PW-ECL around the resonance center.

For an accurate measurement of the cavity transfer functions, the frequency modulation depth applied to the PW-ECL needs to be known, to be used in the normalization of the measured lock-in signal. This modulation depth varies as a function of the modulation frequency, mainly for the following reasons: (i) the limited modulation bandwidth of the synthesizer used in the phase lock loop between the two lasers; (ii) the phase lock loop filters out the modulation frequencies that are out of its bandwidth. Therefore, the modulation response of the PW-ECL carrier frequency was experimentally measured by demodulating the heterodyne beat between the two lasers using an RF frequency discriminator and this result was used to normalize the cavity transfer function.

The cavity transfer functions measured in reflection and in transmission are shown in Figure 3.21. Their fit by a low-pass filter function of the 1^{st} order (in reflection) and 2^{nd} order (in transmission) shows the much faster response of the cavity reflection, which is a relevant feature of the PDH stabilization technique [40]. The filter cut-off frequencies of 4.09 kHz and 4.14 kHz obtained from the fits, corresponding to the resonance half-width at half maximum (HWHM), are in a good agreement with the 8.1-kHz and 8.3-kHz resonance FWHM previously obtained from the direct resonance lineshape measurement as well as from the former ring down time.

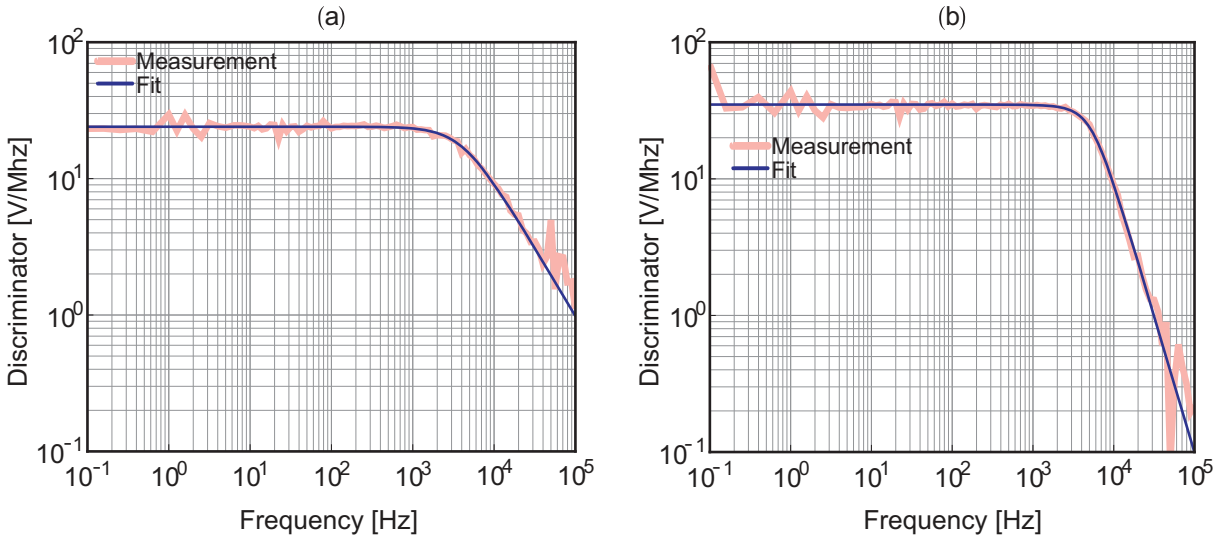

Figure 3.21: Measured ULE cavity transfer functions (light (pink) thick lines) in reflection (a) and in transmission (b). The dark (blue) thin lines represent a fit by a low-pass filter of first order for the reflection curve and of second order for the transmission curve.

3.8 Thermal properties

Two experiments have been implemented to characterize the thermal properties of the cavity, in particular to determine the turning point at which the cavity CTE is zeroed. In the first experiment, a simple 1-layer cavity enclosure made of an uncoated aluminum cradle was used to obtain a rough determination of the ULE cavity turning point. The second experiment was performed with the final 2-layer gold-coated enclosure to determine the turning point more accurately.

In each case, the cavity temperature was ramped and the shift of the resonance frequency was recorded from the beat note signal between the ECDL locked to the cavity and a fully stabilized frequency comb. The turning point can be determined from the curve of the laser-comb beat frequency as a function of the cavity temperature. However, the cavity temperature is not directly known and must be determined.

As the cavity temperature cannot be directly measured, it must be determined from the temperature measured on the surrounding cradle. The cavity temperature (T_{ULE}) is related to the cradle temperature (T_{cradle}) through the time constant τ of the heat flow between cavity and cradle:

$$T_{\mathrm{ULE}}(t) = T_{\mathrm{cradle}}(0)e^{-\frac{1}{\tau}t} + \frac{1}{\tau}\int_0^t e^{-\frac{1}{\tau}(t-\xi)}T_{\mathrm{cradle}}(\xi)d\xi\,. \tag{3.25}$$

The time constant is unknown, but it can be determined if simultaneous measurements of the beat frequency and cradle temperature are performed once when the system is cooled down and then heated. Calculating the cavity temperature from (3.25) for both measurements, the time constant can be determined from the closest overlap between the heating and cooling curves [24], provided that the initial cavity temperature is known for each measurement. This requires a long time (several time constants) to be waited at a constant temperature before starting each temperature ramp, in order to ensure that the cavity is in thermal equilibrium with the surrounding cradle. The initial cavity temperature is thus considered to be equal to the measured cradle temperature.

3.8.1 Coarse measurement with a simple cavity enclosure

The simple 1-layer cavity enclosure used in a first phase is shown in Figure 3.22. It is made of an uncoated aluminum cradle without any internal active temperature stabilization, mounted in a vacuum chamber evacuated at typically 10^{-7} mbar.

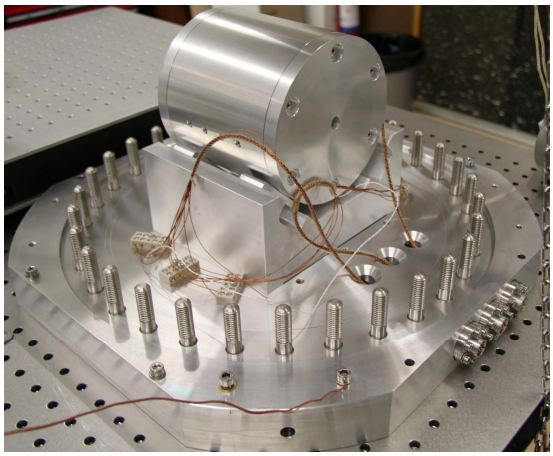

Figure 3.22: ULE cavity in a simple 1-layer aluminum enclosure.

The cavity temperature has been changed in the range 10-26 °C by heating or cooling the baseplate of the vacuum chamber using heaters or a set of 8 TECs (for

cooling). A photograph of the baseplate temperature control is shown in Figure 3.23.

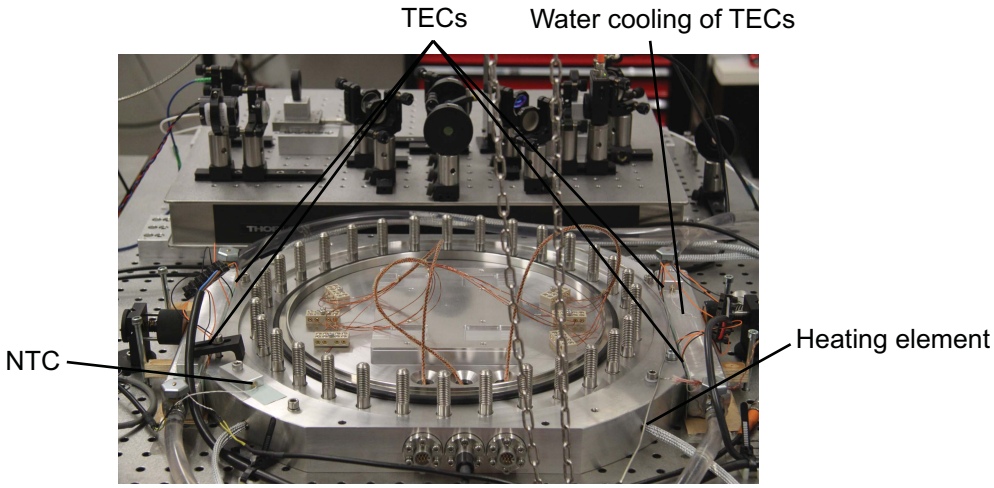

Figure 3.23: Baseplate temperature control. The baseplate is cooled with 8 TECs from the sides, and the power is evacuated from the TECs with circulating cold water at ~10 °C. The heating of the baseplate is achieved with the heating elements positioned inside the baseplate.

The results of the simultaneous measurements of the beat frequency and cradle temperature versus time once when the system is cooled and then when it is heated are shown in Figure 3.24.

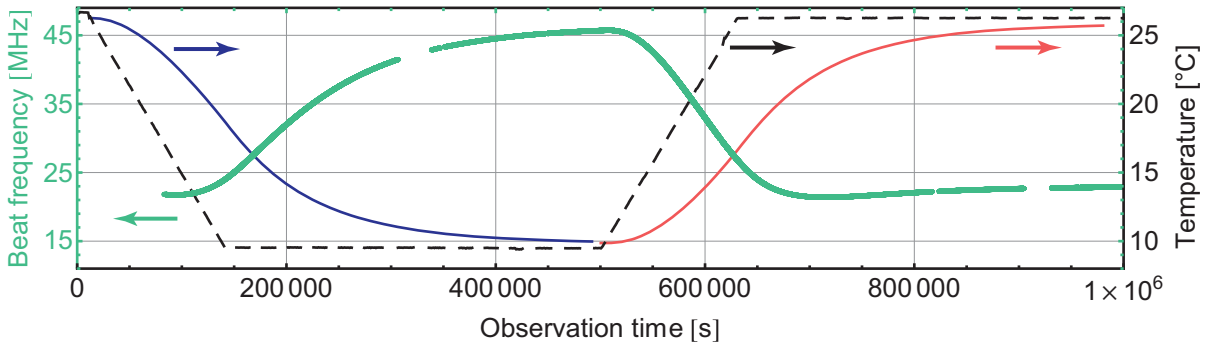

Figure 3.24: Simultaneous measurement of the evolution of the beat frequency between the ECDL stabilized to the ULE cavity and an optical frequency comb (light (green) thick curve) and of the baseplate temperature (dashed black line). The cavity temperature (dark (blue) and light (red) thin lines) is calculated using the time constant $\tau = 77'000$ s, obtained from the closest overlap between the heating and cooling curves (see Figure 3.25). The baseplate is first cooled from 26 to 10 °C with the TECs and then heated to the same temperature.

The beat frequency obtained as a function of the cavity temperature is shown in Figure 3.25a. The evolution of the cavity temperature corresponding to this closest overlap is shown in Figure 3.24.

The turning point of the cavity corresponding to its zero CTE (Figure 3.25b) was thus determined to be 22.6 °C and the time constant 77'000 s. This value is achieved with a simple prototype cavity enclosure and a much higher value is expected for the final 2-layer enclosure.

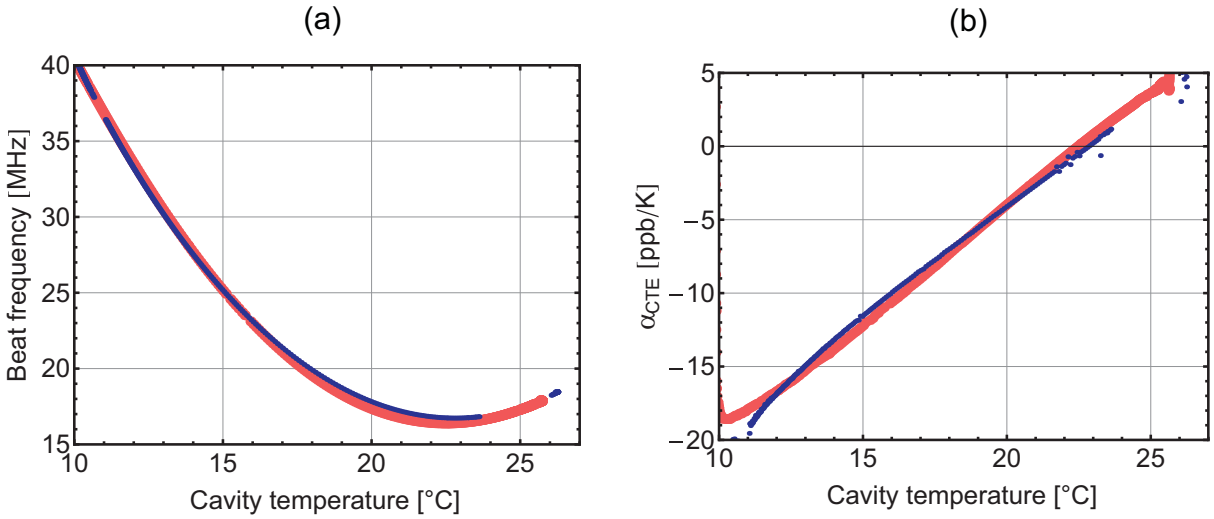

Figure 3.25: (a) Beat frequency as a function of the cavity temperature obtained from the heating (light (red) thick line) and cooling data (dark (blue) thin line). (b) The coefficient of thermal expansion (CTE) of the cavity calculated from heating (light (red) thick line) and cooling (dark (blue) thin line) data.

3.8.2 Precise measurement in the final enclosure

In order to achieve the best performances of the ultra-stable laser it is required to stabilize the temperature of the ULE cavity exactly at its zero CTE temperature. This requires a precise determination of the turning point which can be done in the final 2 layer enclosure described in Section 3.5.

Laser stabilization to a cavity resonance has been implemented using this final enclosure. The tuning curve of the resonance frequency as a function of temperature was measured from the evolution of the beat note between the ECDL locked to the ULE cavity and a fully stabilized frequency comb. The cavity temperature has been changed by heating or cooling the aluminum thermal screen placed on 4 TEC ele-

ments. The difference from the measurement performed with a prototype enclosure is a much longer time constant. Thus a measurement over one month duration is required. The measurement was performed in a narrower range of ~5 °C around the turning point obtained from the measurement with a prototype enclosure. The results of the simultaneous measurements of the beat frequency and cradle temperature versus time are shown in Figure 3.26. The dashed line is the temperature of the TEC elements controlling the screen temperature monitored with the NTCs placed in the aluminum thermal screen in close proximity to the TECs. The solid line is the temperature of the cradle measured with another thermistor.

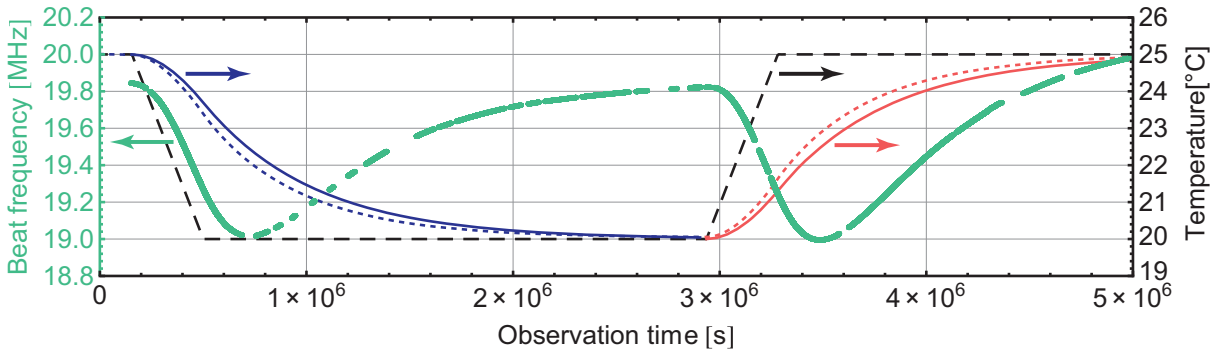

Figure 3.26: Simultaneous measurement of the evolution of the beat frequency between the ECDL stabilized to the ULE cavity and an optical frequency comb (light (green) thick curve) and of the screen temperature (dashed black line). Cavity temperature (dark (blue) and light (red) thin lines) is calculated using the time constant $\tau = 550'000$ s, obtained from the closest overlap between the heating and cooling curves (see Figure 3.27) of the cavity is calculated using. The screen is first cooled from 25 to 20 °C with TECs and then heated to the same temperature. The measured temperature of the cradle is also shown in the same graph (dark (blue) and light (red) dotted lines).

The cavity temperature calculated from the temperature of the screen for both measurements using Eq. (3.25) is shown in Figure 3.26. The time constant is determined from the closest overlap between the heating and cooling curves. The beat frequency obtained as a function of the cavity temperature is shown in Figure 3.27a.

The turning point of the cavity corresponding to its zero CTE (Figure 3.27b) was thus determined to be 22.46 °C and the time constant 550'000 s (6.4 days).

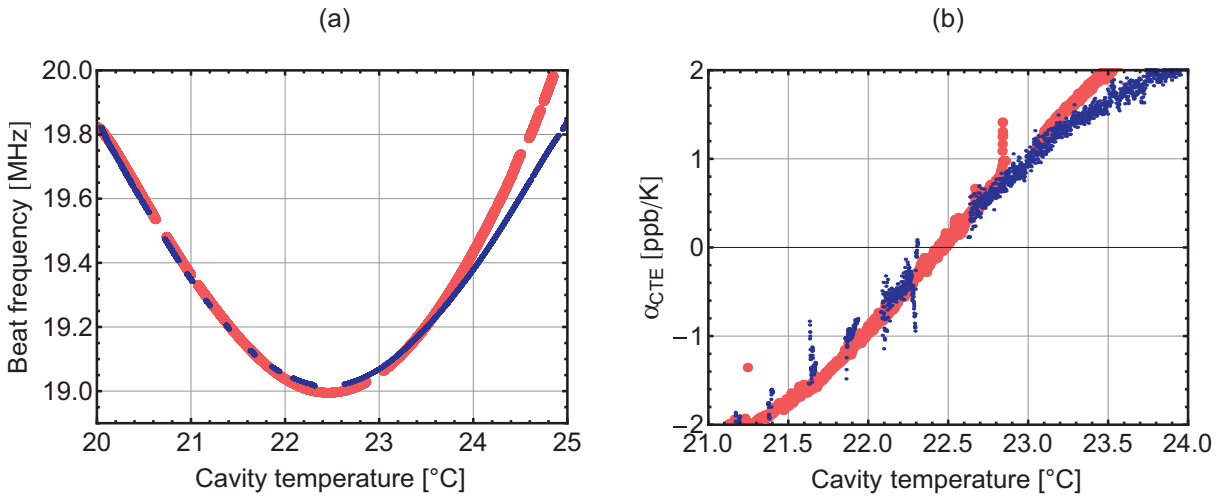

Figure 3.27: (a) Beat frequency as a function of the cavity temperature obtained from the heating (light (red) thick line) and cooling data (dark (blue) thin line). (b) Cavity CTE calculated from heating (light (red) thick line) and cooling (dark (blue) thin line) data.

3.9 Conclusion

Two laser technologies, a commercial ECDL (TLB-6328 from NewFocus) and a PW-ECL (ORION module from Redfern Integrated Optics Inc.) have been used to realize an ultra-stable laser based on PDH stabilization to an ultra-high finesse ULE cavity. A thermal enclosure has been designed to support the cavity and filter out external thermal fluctuations with the measured time constant of more than 6 days. The cavity thermal expansivity was obtained experimentally, resulting in a variation rate of $\sim 2 \cdot 10^{-9}$ K^{-2} around the turning point of 22.46 °C.

The ECDL stabilization was achieved by feedback to the laser injection current, while an AOM was used to correct for fast frequency fluctuations of the PW-ECL as a result of the limited control bandwidth of the laser injection current.

The size and robustness of the PW-ECL make it a very attractive candidate for ultra-stable lasers intended for microwave generation and optical frequency standards. In addition, the low-noise characteristics of the PW-ECL enabled us to perform an accurate characterization of an ultra high-finesse Fabry-Perot cavity. By phase-locking this laser to an ECDL stabilized to the cavity using feedback to the injection current only, a very low-noise probe laser was generated to characterize the narrow cavity resonance of 8.2 kHz, not only in terms of its lineshape, but also by measuring its complete dynamic response to a frequency modulation, both in re-

flection and in transmission. The cavity resonance width, extracted from these measurements, is in agreement with the resonance width obtained from the measured resonance lineshape, as well as with ring-down time measurements.

Chapter 4

Coupled servo-loops in a fully-stabilized Er:fiber optical frequency comb

4.1 Introduction

Optical frequency combs from modelocked femtosecond lasers have revolutionized the field of frequency metrology by providing a direct, phase-coherent link between optical and microwave frequencies and by allowing an optical frequency to be measured with extreme precision in terms of the unit of time of the international system of units, the SI second [40,41]. This has led to the development of new generations of optical atomic clocks with a stability, unreachable with microwave clocks [42-45].

In the last decade, the interest in frequency combs has increased considerably, leading to further developments of the underlying femtosecond laser technology [46-48]. The first frequency combs [49-51] were based on solid-state Ti:Sa lasers due to their high peak power. Ti:Sa lasers are to date the only lasers capable of directly generating the octave-spanning spectrum required for comb self-referencing [52], they can operate at a high repetition rate of several gigahertz [53] and also benefit from low-noise properties owing to the high intracavity power that results from the high Q-factor of their optical resonator. Therefore, Ti:Sa combs are still widely employed today, despite several disadvantages associated with their complexity, high

cost and inefficient pumping. A first breakthrough in the search for simpler and more cost-efficient systems was the demonstration of a self-referenced Er:fiber comb [54]. Owing to several important advantages such as their compactness, robustness, efficient diode pumping and low cost, Er:fiber combs have emerged as a valuable alternative to Ti:Sa laser combs in the past years and now constitute a commonly-used comb technology. They have the further advantage of covering the 1.5-µm transmission window of optical fibers, so that the broad laser spectrum can be distributed over large distances through proper noise-cancellation fiber links for simultaneous comparison of distant optical and microwave frequency standards [55].

A frequency comb provides a phase-coherent link between the microwave and optical domains, in either direction, i.e. RF-to-optical or optical-to-RF. In an RF-to-optical transfer, the comb is stabilized to an RF reference. Accurate optical frequencies are generated, which can be used to measure an absolute optical frequency, i.e. referred to the SI second. In that case, the comb acts as a frequency multiplier that multiplies the frequency of the RF reference by a large integer number N to an optical frequency. In an optical-to-RF transfer, the comb is stabilized to an optical reference and acts as a frequency divider, which divides the optical frequency by a large integer number N into a microwave frequency.

In this chapter, the behavior of a comb used as an RF-to-optical multiplier is studied. In this process, two feedback loops are involved to fully stabilize the comb to a microwave reference (see Section 4.2), but these loops are not independent. The coupled dynamics of these two feedback loops is presented in this chapter for an Er:fiber comb. The use of the comb as a frequency divider will be addressed in Chapter 6 for the generation of ultra-stable microwave from an optical reference.

The content of this chapter is organized as follows. Fundamentals of frequency combs are recalled in Section 4.2. In Section 4.3, one briefly describes the frequency comb used in this study and the experimental methods applied to characterize its noise properties. In Section 4.4, one presents the dynamic response of the comb measured for pump power and PZT modulation and the concept of the frequency-dependent quasi-fixed point is introduced as an outcome of these measurements. Section 4.5 is devoted to the presentation of a model implemented to describe the coupled servo-loops and its validation by experimental results showing the impact of the CEO servo-loop onto the noise of the repetition rate. In Section 4.6, this

model is applied to quantify the impact of the servo-loop coupling on the frequency noise and resulting linewidth of a comb line in different spectral regions of the comb. A conclusion is presented in Section 4.7.

4.2 Fundamentals of frequency combs

4.2.1 Frequency combs and degrees of freedom

Laser sources can be classified as either continuous wave (cw) or pulsed lasers. The so-called modelocking mechanism enables a fixed phase relation between all longitudinal modes of a laser resonator to be established, which results in the formation of a short optical pulse propagating back and forth in the laser cavity. A small fraction of the pulse escapes from the cavity after each round trip, leading to the emission of a train of pulses. The Fourier transform of such a continuous train of equally spaced pulses represents a comb structure in the frequency domain. Therefore, such modelocked lasers are referred to as optical frequency combs.

The modelocked lasers can emit a train of ultrashort pulses at a high repetition rate (0.05 – 10 GHz). The repetition rate f_{rep} corresponds to the inverse of the laser cavity round-trip time. Pulse duration of only a few hundreds of femtoseconds leads to a small number of cycles of the optical field oscillating at the optical carrier frequency in the pulse envelope. A pulse-to-pulse phase-slip occurs between the optical carrier and the pulse envelope due to the different phase- and group-velocities at which the carrier and the envelope propagate (Figure 4.1a). The difference in the propagation velocities ($v_{\mathrm{gr}} - v_{\mathrm{ph}}$) is induced by dispersion. In case of a constant dispersion the difference in velocities remains unchanged and, thus, the phase difference $\Delta\phi_{\mathrm{CEO}}$ between the carrier and the envelope in two consecutive pulses is given by:

$$\Delta\phi_{\mathrm{CEO}} = \frac{v_{\mathrm{gr}} - v_{\mathrm{ph}}}{2\pi\nu_{\mathrm{c}}}. \tag{4.1}$$

The frequency domain representation of a train of pulses with a phase slip between the carrier and the envelope corresponds to equally-spaced frequency components given by:

$$\nu_{N'} = N' \cdot f_{\text{rep}} + \frac{\Delta\phi_{\text{CEO}}}{2\pi} f_{\text{rep}}. \tag{4.2}$$

This equation indicates that the equidistant optical comb lines are shifted from exact harmonics of the repetition rate by a frequency offset

$$f_{\text{GPO}} = \frac{\Delta\phi_{\text{CEO}}}{2\pi} f_{\text{rep}}, \tag{4.3}$$

referred to as the group-phase offset (GPO) frequency. In practice it is more convenient to use a frequency $f_{\text{CEO}} = f_{\text{GPO}} \pm k \cdot f_{\text{rep}}$, down-converted to $|f_{\text{CEO}}| < f_{\text{rep}}/2$, referred to as the carrier-envelope offset (CEO) frequency. Using this definition, the position of any optical component of the comb is given by the comb equation as a multiple integer of the repetition rate plus a constant offset f_{CEO}:

$$\nu_N = f_{\text{CEO}} + N f_{\text{rep}}, \tag{4.4}$$

where $N = N' \pm k$. Time and frequency domains representation of an optical frequency comb from a modelocked laser are shown in Figure 4.1.

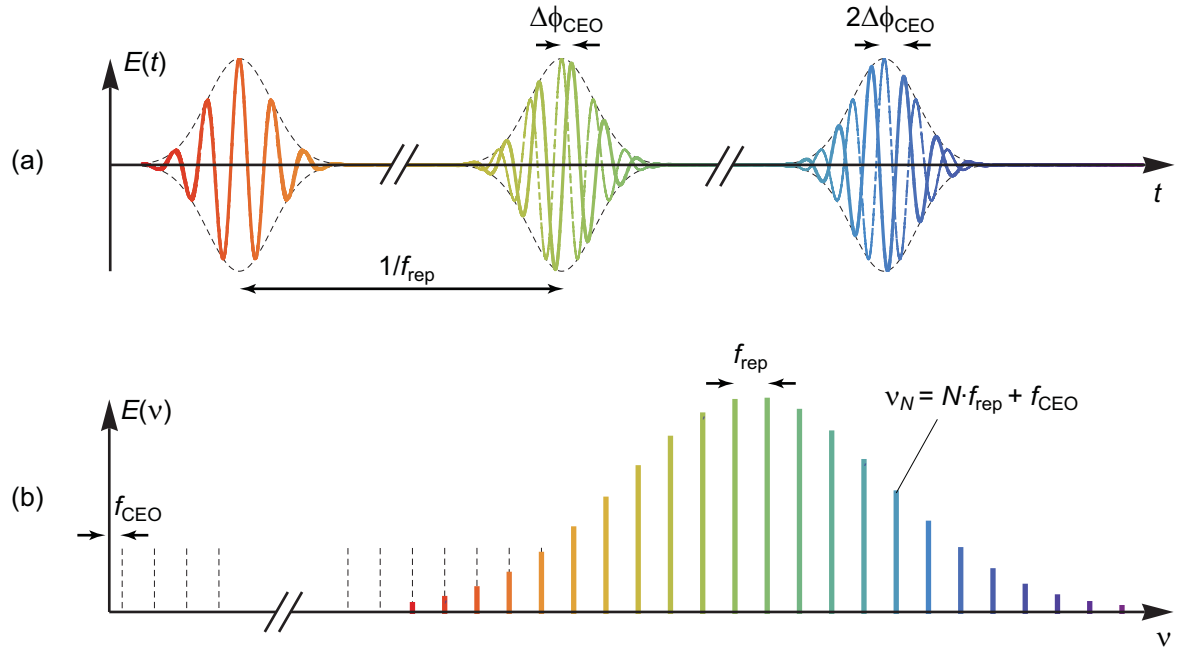

Figure 4.1: Frequency comb representation in time (a) and frequency (b) domains.

As it follows from Eq. (4.4), the position of every comb line is determined by

only two parameters (f_{rep} and f_{CEO}), thus it is only required to stabilize the repetition rate and the CEO frequency in order to fully stabilize the optical frequency comb.

4.2.2 Self-referencing

The stabilization of the repetition rate to an RF reference is straightforward. One can detect the repetition rate frequency using a photodiode, and then the stabilization is achieved by controlling the laser cavity length using a PZT actuator. Stabilization of the CEO frequency is less evident. First of all, one must be able to detect the CEO frequency. It has become only possible after a breakthrough in supercontinuum generation and the development of the *f*-to-2*f* interferometric method [49]. In this scheme the low-frequency part of the comb optical spectrum is frequency-doubled in a nonlinear crystal. The heterodyne beat between this doubled frequency $2\nu_N = 2f_{\mathrm{CEO}} + 2Nf_{\mathrm{rep}}$ and the adjacent comb line of the fundamental comb spectrum at $\nu_{2N} = f_{\mathrm{CEO}} + 2Nf_{\mathrm{rep}}$ occurs at f_{CEO}. The principle of the *f*-to-2*f* interferometer is shown in Figure 4.2. ,

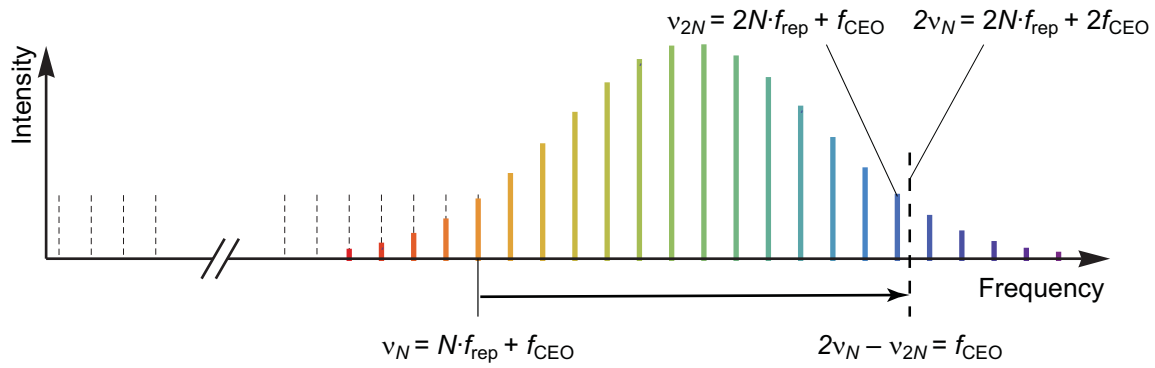

Figure 4.2: A diagram of the CEO detection in an *f*-to-2*f* interferometer.

The control and stabilization of the CEO can be performed by controlling the dispersion in the laser cavity. The pump power has a direct influence on the pulse parameters, such as the pulse duration and energy, which directly translates into a change of f_{CEO}. Therefore, the current of the pump laser can be used for fine tuning and stabilization of f_{CEO}, which is the standard stabilization method for diode-pumped femtosecond lasers [56]. A coarse adjustment of f_{CEO} is usually performed with an intra-cavity element, such as a dispersion wedge.

In order to detect the CEO in an *f*-to-2*f* interferometer, an octave-spanning frequency comb is required. It is possible to achieve an optical spectrum broader than one octave from Ti:Sa modelocked lasers directly. For all other modelocked lasers, spectral broadening out of the laser cavity is required, e.g. in a highly nonlinear fiber. The comb is said to be self-referenced when the CEO is stabilized.

4.2.3 Noise sources in frequency combs

The two parameters defining the frequency comb, i.e. the repetition rate f_{rep} and the carrier-envelope offset frequency f_{CEO}, are both affected by a specific type of intra-cavity perturbation, so that their noise is usually correlated [57,58]. Hence, for each intra-cavity noise (such as environmental perturbations, pump-induced noise or amplified spontaneous emission), there is one specific comb mode for which the resulting noise is minimized in the free-running comb. This has been previously described by a breathing motion of the comb around a so-called fixed point according to the elastic tape model introduced by H. Telle *et al.* [59]. In Telle's original model, as well as in subsequent experimental studies [60,61], the fluctuations induced in f_{rep} and f_{CEO} by a given perturbation were implicitly assumed to be fully correlated (in phase) or anti-correlated (180° out-of-phase) so that the resulting noise cancels out at the fixed point. In this chapter, it will be shown from experimental data obtained in an Er:fiber comb that a different phase shift may occur between the response of f_{rep} and f_{CEO} to a given modulation. In that case, a true fixed point (at which the fluctuations induced by f_{rep} and f_{CEO} compensate exactly) does not exist and the concept of a quasi-fixed point is introduced instead, at which the fluctuations induced to the optical comb line by f_{rep} are minimized by the fluctuations induced by f_{CEO}. It will also be shown that this quasi-fixed point is not unique for a given source of perturbation, but instead varies with the Fourier frequency of the perturbation, leading to a frequency-dependent quasi-fixed point.

Furthermore, the fixed point concept applies to a free-running comb only and there has been little investigation of the impact of the correlation between f_{rep} and f_{CEO} in a fully-stabilized comb so far. Full stabilization of a frequency comb is generally achieved using two phase lock loops to coherently stabilize f_{rep} and f_{CEO} to an RF reference [62]. Control of the laser cavity length using a PZT is the traditional method to stabilize the repetition rate, whereas the pump power is generally used to stabilize f_{CEO} [56,63]. However, these two actuators are not independent and each of

them has a simultaneous influence on the two comb parameters. Such kind of behavior was predicted by the theory of N. Newbury and B. Washburn [64], but a precise experimental evidence of this effect is reported in this chapter. Similar transfer functions, including for the femtosecond laser output power, have recently been reported for an Er:fiber frequency comb that makes use of an intra-cavity EOM for high-bandwidth stabilization of f_{rep} to an optical reference [65]. In that case, a strong focus was put on the comb dynamic response to the EOM modulation. Here, the target of the study is completely different and the measured transfer functions for PZT and pump power modulation provide new insights into the noise of a free-running frequency comb. Furthermore, the first quantitative characterization of the impact of the coupling between the CEO and repetition rate servo loops is demonstrated in Section 4.5.3 in an Er:fiber comb stabilized to an RF reference. In Section 4.5.1 a theoretical model is introduced to describe the impact of the CEO servo loop on both the repetition rate and an optical comb mode.

4.3 Er:fiber frequency comb

4.3.1 Er:fiber comb architecture

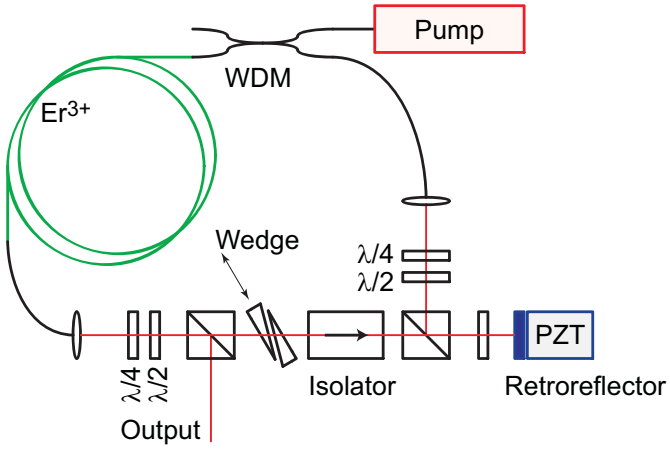

Figure 4.3: A diagram of the passively modelocked Er:fiber ring cavity laser.

A commercial Er:fiber frequency comb (FC1500 from MenloSystems) was used in the experimental investigations. The ultrafast M-Comb laser is a passively modelocked Er:fiber ring laser with a center wavelength of 1560 nm, an output power of >10 mW and a pulse width of less than 150 fs. The repetition rate is tuned to

f_{rep} = 250 MHz with a wedge inside the ring-resonator. A fast photodetector in the laser head is used for repetition rate detection and stabilization. The fine tuning of f_{rep} is performed with a PZT actuator displacing a free-space retroreflector in the laser resonator. A monitor port with 0.6 mW radiation is used for independent detection of the laser repetition rate. The main output radiation is split into two fiber-coupled output ports feeding two external erbium-doped fiber amplifiers (EDFAs). Each of these ports has an output power of >600 mW centered at 1.5 µm.

The first EDFA seeds a nonlinear fiber for the generation of an octave-spanning spectrum that features a free space output with up to 600 mW of laser radiation ranging from 1050 to 2100 nm. Part of the supercontinuum power is used into an *f*-to-2*f* interferometer for CEO frequency detection and stabilization.

The second EDFA features both a free space output and a fibered output with up to 600 mW total optical power between 1500 and 1600 nm. The free-space output is used for heterodyne beating with the high finesse cavity-stabilized laser (see photograph in Figure 4.4).

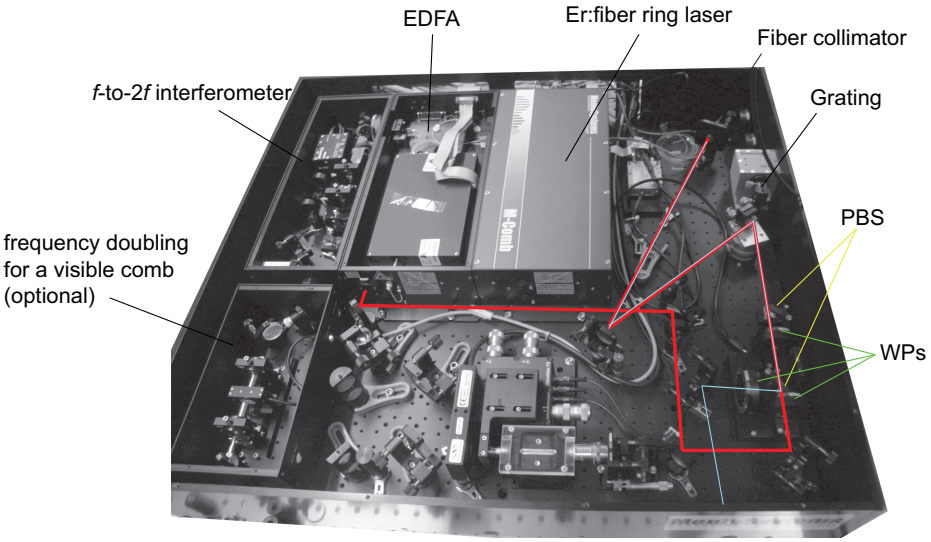

Figure 4.4: Photograph of the commercial Er:fiber comb. In the free-space part the comb is spectrally filtered to a 0.3-nm (40 GHz) width using a diffraction grating and the aperture of the fiber collimator for heterodyne beating with the high finesse cavity-stabilized laser (see Section 4.6.1). The polarization and power of the light for the beat is adjusted with a set of half- and quarter- waveplates (WPs) and polarization beamsplitter (PBS) cubes. The free-space optical path of the comb is shown in thick line (red). The optical path of the ECDL used for heterodyne beating is shown in thin line (light blue).

4.3.2 Er:fiber comb stabilization

The repetition rate is stabilized by feedback to a PZT that makes fine control of the laser cavity length. The error signal is generated by mixing down the 4th harmonic of f_{rep} (1 GHz) with a 980-MHz reference signal from a dielectric resonator oscillator (DRO-980, from WORK Microwave GmbH) referenced to an H-maser. The resulting 20-MHz signal is compared to a stable reference signal from a direct digital synthesizer (DDS) in a double-balanced mixer acting as an analog phase detector, whose output constitutes the error signal. This error signal is amplified in a PID controller (PIC210) and is fed back to a high-voltage amplifier with 23 dB gain that drives the PZT. We call here u_{PZT} the input signal of the high-voltage amplifier.

The CEO-beat is detected in a standard *f*-to-2*f* interferometer [49] after spectral broadening of the laser output spectrum to one octave in a highly-nonlinear fiber. Coarse tuning of the CEO frequency is performed by an intra-cavity wedge, whereas fine tuning and stabilization are achieved by controlling the injection current of one of the pump diodes of the fs-laser. This is performed via a standard laser driver without any customization for fast pump power modulation as implemented in some cases [66]. The CEO-beat frequency is phase-locked to a 20-MHz oscillator referenced to an H-maser. For this purpose, phase fluctuations between the CEO-beat and the reference signal are detected in a digital phase detector (DXD200, whose characteristics have been described in Section 0) with a large, linear detection range of $\pm 32 \times 2\pi$ phase difference. The resulting error signal is forwarded to a PID controller (PIC201) that drives the pump laser current source. We label u_{pump} the input signal that controls the pump laser driver.

In order to study the impact of the coupling between these two stabilization loops, an extensive characterization of the comb has been performed in terms of frequency noise, dynamic response and complete loop transfer functions, both for the repetition rate and the CEO-beat. Furthermore, the frequency noise and dynamic response of an optical comb line at 1.56 µm were also characterized, by beating the comb with the ultra-narrow linewidth cavity-stabilized laser described in Chapter 3, to validate the model. Various frequency (phase) discriminators described in Section 2.4 were used to demodulate the repetition rate, the CEO-beat and the heterodyne beat with the cavity-stabilized laser, in order to measure the frequency noise or the

modulation response of these signals. In the present study, the digital phase-lock loop discriminator HF2PLL (see Section 2.4.3) was mainly used for the characterization of low-noise signals, e.g. for the repetition rate, and an RF discriminator with a broader frequency range (Miteq FMDM 21.4/2-4, see Section 2.4.2) for signals with a higher noise, such as the CEO-beat or the comb-laser heterodyne beat. Frequency noise spectra were obtained by measuring the PSD of the discriminator output voltage using an FFT spectrum analyzer. The dynamic response of the comb to a modulation of the cavity length or of the pump power was obtained by synchronously detecting the output signal of the discriminator using a lock-in amplifier referenced to the modulation frequency.

4.4 Frequency comb dynamic response

In this Section, the dynamic response of the comb is discussed, i.e. the response of f_{CEO} and f_{rep} experimentally measured for a modulation of the cavity length or pump power (Section 4.4.1). From these results, new insights about the comb fixed point concept are extracted in Section 4.4.2.

4.4.1 Repetition rate and CEO dynamic control

The two actuators used to control the CEO and the repetition rate in a frequency comb are not fully independent. A voltage applied to the PZT controlling the repetition rate also induces a shift of the CEO frequency, whereas the pump current influences both the CEO and the repetition rate frequencies. In order to quantify these coupled contributions, we measured four transfer function matrix elements determining the response of the comb to the various actuators as

$$\begin{pmatrix} \tilde{f}_{\mathrm{CEO}}(\omega) \\ \tilde{f}_{\mathrm{rep}}(\omega) \end{pmatrix} = \begin{pmatrix} C_{f_{\mathrm{CEO}}\, u_{\mathrm{pump}}}(\omega) & C_{f_{\mathrm{CEO}}\, u_{\mathrm{PZT}}}(\omega) \\ C_{f_{\mathrm{rep}}\, u_{\mathrm{pump}}}(\omega) & C_{f_{\mathrm{rep}}\, u_{\mathrm{PZT}}}(\omega) \end{pmatrix} \begin{pmatrix} \tilde{u}_{\mathrm{pump}}(\omega) \\ \tilde{u}_{\mathrm{PZT}}(\omega) \end{pmatrix}. \tag{4.5}$$

Here we define the Fourier transform of a function $u(t)$ by $\tilde{u}(\omega) = \lim_{T\to\infty} \int_{-T/2}^{+T/2} u(t) e^{i\omega t} dt$. Throughout this work, variables in the frequency (Fourier) domain are labeled with a tilde (e.g. $\tilde{u}(\omega)$) or by a capital letter (e.g. $C_{f_{\mathrm{CEO}}\, u_{\mathrm{pump}}}(\omega)$) in the case of transfer functions. The frequency dependence in the Fourier domain is denoted by the angular frequency ω to make the distinction from frequencies in the carrier domain that are labeled by f (e.g. f_{CEO} or f_{rep}).

First of all, the static tuning rates were determined by measuring the change in

f_{rep} and f_{CEO} with respect to the DC voltage u_{pump} or u_{PZT} applied to the pump laser driver or to the PZT high voltage amplifier, respectively. The CEO and repetition rate frequencies were measured with either an electrical spectrum analyzer or a frequency counter. The positive sign of the CEO-beat frequency was unambiguously determined by observing the displacement of the beat frequency between one comb line and the 1.56-µm cavity-stabilized laser when f_{rep} and f_{CEO} were successively scanned. A linear regression of the frequency versus applied voltage was performed to extract the static tuning coefficients, which correspond to the local slope of the variation of f_{rep} (f_{CEO}) as a function of the control voltage u_{PZT} or u_{pump} (see Figure 4.5).

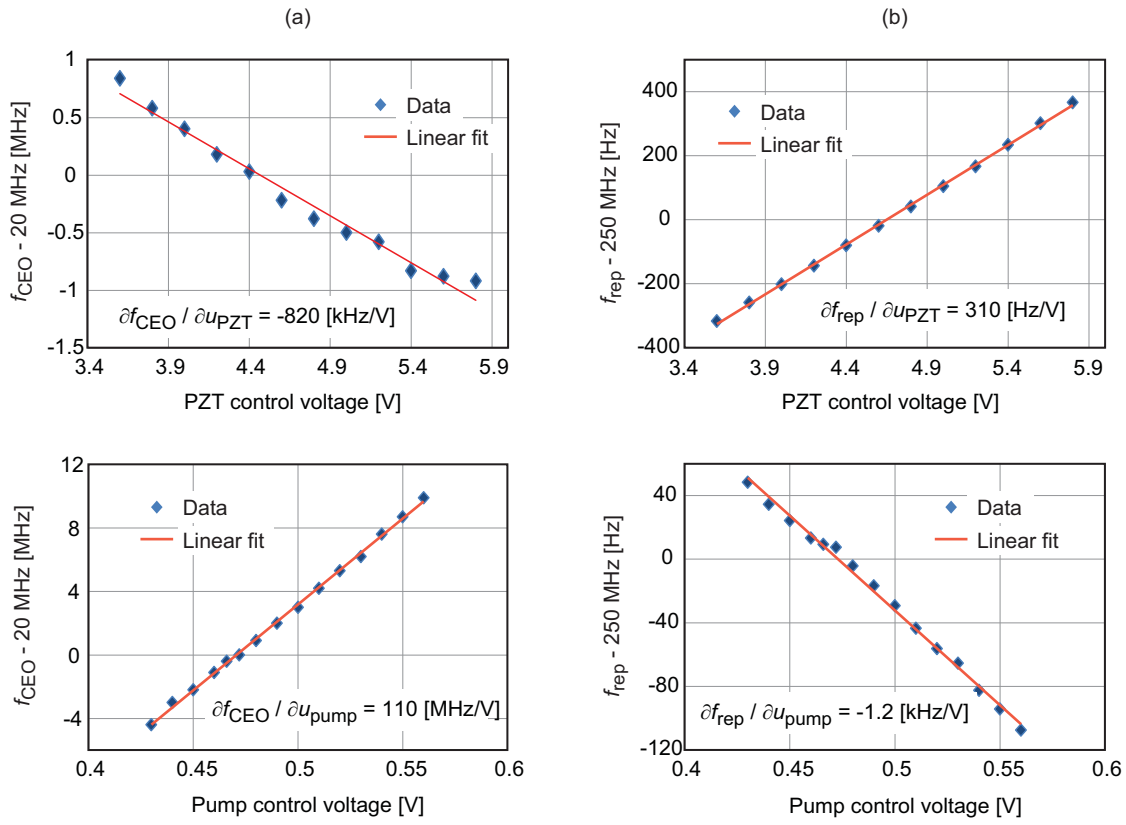

Figure 4.5: Tuning of the 20-MHz CEO frequency (a) and of the 250-MHz repetition rate (b) as a function of the input voltage of the PZT controlling the cavity length (upper row) and of the pump driving voltage (lower row). The repetition rate and the CEO frequency were measured using an electrical spectrum analyzer. The local tuning coefficients (around 250 MHz for f_{rep} and 20 MHz for f_{CEO}) are determined from a linear fit (straight lines).

For a change of the cavity length, one obtained $\partial f_{\mathrm{CEO}}/\partial u_{\mathrm{PZT}} \approx -820$ kHz/V and $\partial f_{\mathrm{rep}}/\partial u_{\mathrm{PZT}} \approx 310$ Hz/V. For a change of the pump power, $\partial f_{\mathrm{CEO}}/\partial u_{\mathrm{pump}} \approx 110$ MHz/V and $\partial f_{\mathrm{rep}}/\partial u_{\mathrm{pump}} \approx -1.2$ kHz/V. The effect of a variation of the cavity length on the frequency of an optical comb line is strongly dominated by the contribution of the repetition rate, because of the large mode index ($N \approx 7.7 \cdot 10^5$ at $\lambda = 1.56$ µm) that multiplies the repetition rate. However, both the CEO and the repetition rate have a similar contribution to the tuning of a comb line with the pump laser power.

In addition to the static tuning rates, the dynamic response of f_{rep} and f_{CEO} to a modulation of the pump power and of the cavity length was also measured. Such measurements show how the CEO and the repetition rate may be affected by external perturbations occurring at different frequencies, such as the noise on the pump laser current or mechanical noise induced by vibrations, air drafts or temperature effects. The dynamic response (transfer function) of the repetition rate and CEO frequencies was measured by modulating the cavity length (via the PZT input voltage u_{PZT} with an amplitude of 100 mV rms) or the pump laser current (with a 10-mV rms amplitude applied to the current driver control voltage u_{pump}), respectively, with a sine waveform of varying frequency $\omega/2\pi$ (in the range from 0.1 Hz to 100 kHz) and by detecting the changes in f_{rep} and f_{CEO} occurring at the modulation frequency with a lock-in amplifier after demodulation. In order to observe the small FM induced on the RF carrier (f_{rep} or f_{CEO}), different frequency discriminators have been used to demodulate the frequency-modulated signals as mentioned in Section 4.3.2. The discriminators operate around $f_{\mathrm{Discr}} = 20$ MHz, but signals at a different frequency f_{signal} may be analyzed after frequency down-conversion (by mixing with a reference signal at $f_{\mathrm{Discr}} \pm f_{\mathrm{signal}}$ and proper filtering). For example, due to the tiny variation of the repetition rate with the modulation signal (cavity length or pump current) compared to the corresponding effect on the CEO frequency, the detection has been performed at a high harmonic of the repetition rate in order to enlarge the frequency modulation depth to be detected by the frequency discriminator. For this purpose, the 12$^{\mathrm{th}}$ harmonic of f_{rep} ($12 \times f_{\mathrm{rep}} = 3$ GHz) has been detected using a fast photodiode (New-Focus 1434, 25 GHz bandwidth) and mixed with a reference signal at 2.98 GHz to produce the 20-MHz signal that was analyzed with either Miteq or HF2PLL frequency discriminator. The analyzed signal thus contained 12 times

the frequency modulation depth of f_{rep} and was later on scaled down by this factor in order to obtain the repetition rate transfer function. The output signal of the discriminator is proportional to the frequency modulation of the input signal and was subsequently analyzed with a lock-in amplifier to extract the component (in amplitude and phase) at the modulation frequency. Knowing the sensitivity of the frequency discriminator (in V/Hz) allowed the measured lock-in voltage to be converted into frequency modulation. The frequency discriminator has a sensitivity of 1.25 V/MHz for Miteq and is digitally adjustable for HF2PLL. A value in the range 10^{-3} – 10^{-2} V/Hz was usually used with this discriminator. The bandwidth is about 2 MHz for Miteq and 50 kHz for HF2PLL as shown in Section 2.5.1.

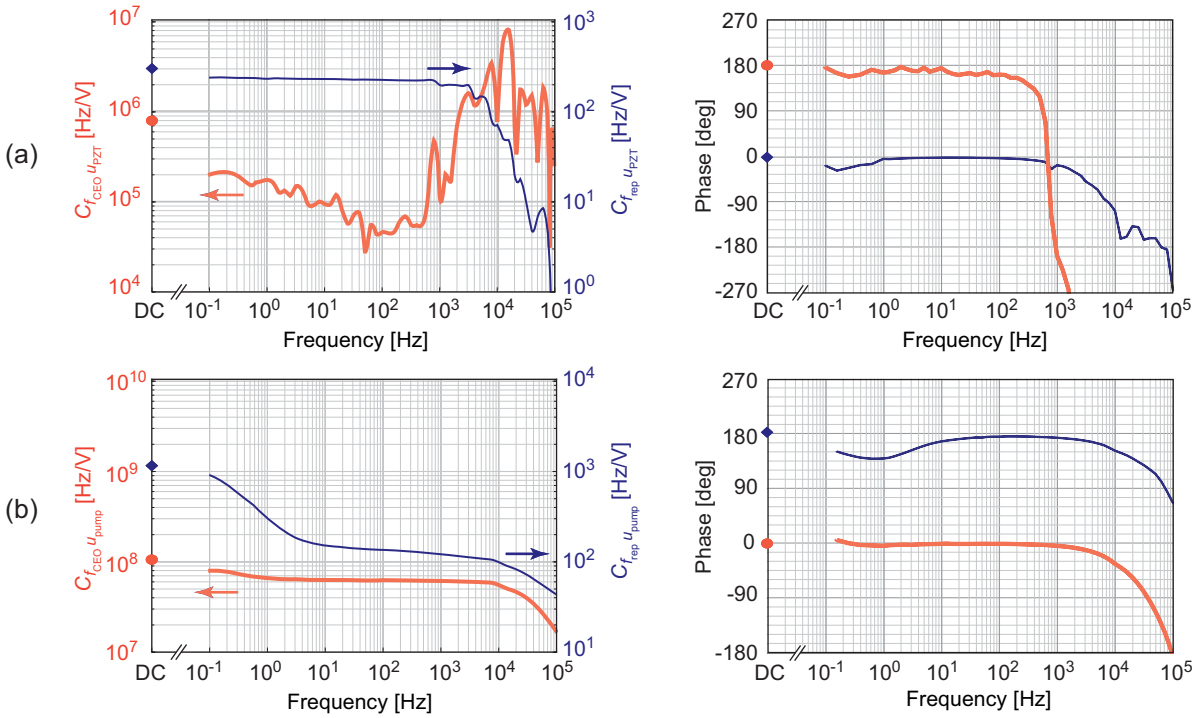

Figure 4.6: Transfer functions in amplitude (left plots) and phase (right plots) of f_{CEO} (light (red) thick curve, left vertical axis) and f_{rep} (dark (blue) thin curve, right vertical axis) in the Er:fiber comb for cavity length modulation, applied through a modulation of the PZT drive voltage (a) and for pump laser modulation (b). The points on the left vertical axes represent the DC values separately obtained from a static measurement.

The dynamic responses of f_{CEO} and f_{rep} to cavity length modulation are very different as shown in Figure 4.6a. The PZT has many mechanical resonances that

strongly affect the CEO response, especially above a few hundred hertz. This effect is believed to result from a tiny misalignment of the PZT from the optical axis, which induces changes in the polarization and amplitude of the pulses in the resonator via the complex laser dynamics. These resonances are only weakly visible on the repetition rate transfer function, which shows a cut-off frequency of a few kilohertz, whereas the CEO is affected by the PZT modulation up to a much higher frequency. The CEO and repetition rate tuning coefficients measured at low modulation frequency ($\omega/2\pi < 10$ Hz) are in a relatively good agreement with the static values previously determined. Some difference is however observed, which can arise from the following two reasons: (i) between DC and 0.1 Hz, some slow physical phenomena (mainly of thermal origin) might occur and affect the dynamic response at very low frequency; (ii) the measurement of the static tuning coefficients might be affected by the drift of f_{CEO} and f_{rep} that arises in the free-running comb and which is difficult to distinguish from the deliberate frequency change induced by a change of the cavity length or pump current.

In a similar way, the CEO and repetition rate transfer functions were measured for pump power modulation. In addition to the analyzed change in the repetition rate frequency (FM signal), pump laser modulation also induces a modulation of the modelocked laser optical power and thus an AM of both the repetition rate and CEO-beat signals. Due to the potential AM-sensitivity of some frequency discriminators discussed in Section 0, great care was taken all along the experiments to measure the true FM response of f_{CEO} and f_{rep} without being affected by residual AM effects. This was especially critical in the case of f_{rep}, as the FM depth is orders of magnitude smaller than for f_{CEO} and is thus more prone to AM-induced artefacts. For this reason, the dynamic response of f_{rep} has been measured by the digital PLL-discriminator HF2PLL, which proved to be affected only marginally by AM (see Section 0).

Figure 4.6b shows that a similar bandwidth is achieved in the transfer function of f_{rep} and f_{CEO} for pump current modulation, in the order of 10 kHz, limited by the lifetime of the excited state in the Er gain medium coupled with the laser dynamics [60]. The observed bandwidth is comparable to the value previously reported by B. Washburn *et al.* for the pump diode current-to-comb output power transfer function in another Er:fiber comb [60], but is smaller than the ~60-kHz roll-off fre-

quency recently reported by W. Zhang *et al.* for the pump diode current-to-comb amplitude transfer function measured in an Er:fiber comb equipped with an intracavity EOM [65]. One should point out that the laser dynamics and thus the CEO transfer function and bandwidth may slightly depend on the laser modelocked state, in a similar way as the phase noise PSD was shown to depend on the modelocking conditions in an analogous frequency comb [66]. To avoid any issue related to this possible effect, all the measurements reported here have been obtained with the laser operating in the same modelocked state. At low frequency (below 5 Hz), the behavior significantly differs between f_{rep} and f_{CEO}: a much steeper slope in the amplitude of the f_{rep} transfer function and a significant phase shift are observed. One believes that this effect arises from a thermally-induced change of the fiber-laser resonator length resulting from the slowly modulated optical power absorbed in the Er:fiber.

As an additional verification of the measured dynamic response of f_{rep}, which is potentially the most susceptible to AM-induced artefacts, the transfer function of an optical comb line was also measured with respect to pump laser modulation (1 mV rms applied to the laser driver, corresponding to 0.01% modulation of the laser pump current of 800 mA). This was realized by beating the free-running comb with the 1.56-µm cavity-stabilized ultra-narrow-linewidth laser and by analyzing the laser-comb beat note (f_{beat}) with the Miteq frequency discriminator. In order to distinguish between the contribution of the repetition rate and of the CEO in the heterodyne beat, the CEO contribution was first subtracted from the analyzed signal. This was performed by frequency-mixing the ~40-MHz heterodyne beat with the ~20-MHz CEO-beat and subsequently band-pass filtering the CEO-free component at 20 MHz ($f_{\mathrm{beat}} - f_{\mathrm{CEO}}$), which was demodulated with Miteq discriminator. With this proper choice of sign, the analyzed CEO-free beat contains N times the frequency modulation of the repetition rate. No AM issue is encountered in this measurement because of the huge enhancement of the FM amplitude compared to the direct measurement of f_{rep}. The perfect correspondence that was observed between the frequency response of the CEO-free laser-comb beat and $N \cdot f_{\mathrm{rep}}$ demonstrates the correctness of the measured repetition rate transfer function.

4.4.2 Frequency dependence of the comb quasi-fixed point

In the elastic tape model of the comb introduced by H. Telle and co-workers [59] the assumed full correlation between the noise of f_{CEO} and f_{rep} in a free-running frequency comb leads to a breathing motion of the comb around a fixed point N_{fix}, at which the two noise contributions compensate each other. In this model, the fixed point is given by the ratio of the static tuning coefficients of f_{CEO} and f_{rep} with respect to an external perturbations x (e.g. u_{pump} or u_{PZT}):

$$N_{\mathrm{fix}}^{x} = -\left(\frac{\partial f_{\mathrm{CEO}}}{\partial x}\right)\Big/\left(\frac{\partial f_{\mathrm{rep}}}{\partial x}\right). \tag{4.6}$$

In most experiments, the comb fixed point for a given external perturbation has been determined quasi-statically, i.e. by applying a square-waveform modulation at low frequency (typically 0.5-1 Hz) and by measuring the corresponding change in f_{CEO} and f_{rep} with a frequency counter (typ. with 100 ms gate time) [60,61]. In a different approach, D. Walker *et al.* [67] modulated the pump power in a Ti:Sa Kerr-lens modelocked laser at a higher (fixed) frequency of 167 Hz and analyzed the effect on the beat note between a tunable Ti:Sa cw laser and the nearest comb line. By phase-locking the beat note to a 20-MHz reference frequency via feedback to the cavity length of the modelocked laser, they used the control voltage of the phase lock loop, synchronously detected, as a sensitive measurement of the frequency shift of the optical comb line induced by the pump power modulation. By tuning the cw laser across the comb spectrum, they measured the change in optical frequency induced by the pump modulation for different comb modes, so as to extract the comb fixed point. But this measurement was performed at a single modulation frequency and the response of both f_{CEO} and f_{rep} to the applied modulation was considered as instantaneous, so that no possible phase shift between f_{CEO} and f_{rep} was accounted for.

Here, the dynamic measurements of the CEO and repetition rate complete transfer functions (in amplitude and phase) over a broad range of modulation frequencies lead to introduce two modifications to the original comb elastic tape model:

i) The measured transfer functions show that a phase shift might occur between the response of f_{CEO} and f_{rep} to a given modulation. The resulting

noise of a comb line of index N can thus be considered as a vector sum of two complex contributions $C_{f_{\mathrm{CEO}}\,x}(\omega)\cdot\tilde{x}(\omega)$ and $N\cdot C_{f_{\mathrm{rep}}\,x}(\omega)\cdot\tilde{x}(\omega)$, where the complex dynamic tuning rates are considered here, $C_{f\,x}=\left|C_{f\,x}\right|e^{i\varphi}$, φ being the phase of the transfer function and f stands for either f_{CEO} or f_{rep}. This vector sum can be zeroed at a particular value of N ($N=N_{\mathrm{fix}}^{x}$) only in the case of a perfect correlation ($\varphi_{\mathrm{CEO}}-\varphi_{\mathrm{rep}}=0$) or anti-correlation ($\varphi_{\mathrm{CEO}}-\varphi_{\mathrm{rep}}=\pi$) between the response of f_{CEO} and f_{rep} to a given modulation. This corresponds to the traditional fixed point considered in previous studies. In all other cases where $\varphi_{\mathrm{CEO}}-\varphi_{\mathrm{rep}}\neq k\pi$ ($k=0,\,1,\,\ldots$), a full compensation of the contributions of $C_{f_{\mathrm{CEO}}\,x}(\omega)\cdot\tilde{x}(\omega)$ and $N\cdot C_{f_{\mathrm{rep}}\,x}(\omega)\cdot\tilde{x}(\omega)$ cannot occur, so that a true fixed point does not exist. However, there is still one comb line for which the resulting noise is minimized (but is not zero) and the corresponding mode index is called the quasi-fixed point, which is given by

$$N_{\text{q-fix}}^{x}(\omega)=-\mathrm{Re}\left[\frac{C_{f_{\mathrm{CEO}}\,x}(\omega)}{C_{f_{\mathrm{rep}}\,x}(\omega)}\right]. \tag{4.7}$$

The resulting frequency deviation $\Delta\tilde{\nu}_N(\omega)$ of an arbitrary comb line ν_N is given by

$$\begin{aligned}\left|\Delta\tilde{\nu}_N(\omega)\right| &= \left|C_{f_{\mathrm{rep}}\,x}(\omega)\cdot\tilde{x}(\omega)\right| \\ &\cdot\sqrt{\left\{\mathrm{Im}\left[\frac{C_{f_{\mathrm{CEO}}\,x}(\omega)}{C_{f_{\mathrm{rep}}\,x}(\omega)}\right]\right\}^2+\left(N-N_{\text{q-fix}}^{x}(\omega)\right)^2},\end{aligned} \tag{4.8}$$

showing that a true fixed point exists only if the imaginary part of $C_{f_{\mathrm{CEO}}\,x}/C_{f_{\mathrm{rep}}\,x}$ is zero, i.e. $\varphi_{\mathrm{CEO}}-\varphi_{\mathrm{rep}}=k\pi$.

ii) The dynamic measurements performed over a broad frequency range enabled a quasi-fixed point to be determined at each Fourier frequency $\omega/2\pi$ of the considered perturbation, and thus to obtain a frequency distribution of the comb quasi-fixed point. Such an approach has not been applied earlier to the best of our knowledge. K. Kim *et al.* [61] reported a related approach in a Cr:forsterite 1.3-µm comb, but applied to the measurement of the frequency response of a comb line for pump power modulation. They analyzed the frequency response of the heterodyne beat note

between a comb line and a narrow-linewidth laser using a delay-line frequency discriminator. Performing such a measurement with a couple of lasers at different wavelengths (1319 nm close to the comb fixed point, 1064 nm and 1550 nm on both sides of the fixed point), they could show a significantly smaller response near the comb fixed point at 1319 nm and a ~180° phase difference between the frequency response of the 1064-nm and 1550-nm beat notes, showing the anti-correlation between them. As the analyzed beat note signals contain the combined contributions of both f_{CEO} and f_{rep}, which could not be individually inferred in these measurements, this approach did neither accurately determine the position of the comb fixed point (due to the very small number of different considered wavelengths), nor show any Fourier frequency dependence of the fixed point.

From the separate measurement of the dynamic response of f_{CEO} and f_{rep}, in amplitude and phase as reported in Section 4.4.1, the response of any comb line can be processed, which is the strength of the approach presented here. Moreover, this enables a frequency dependent comb quasi-fixed point $N^{x}_{\text{q-fix}}(\omega)$ to be introduced as shown in Eq. (4.7).

The frequency-dependent quasi-fixed points obtained for cavity length and pump power modulation are shown in Figure 4.7. In the case of cavity length fluctuations, the phase of $C_{f_{\mathrm{CEO}}\,u_{PZT}}$ and $C_{f_{\mathrm{rep}}\,u_{PZT}}$ is close to 0 and π, respectively, for modulation frequencies ranging from DC to ~200 Hz. A true fixed point thus arises in this case, varying from $N^{\mathrm{PZT}}_{\mathrm{fix}} \approx 200$ at $\omega/2\pi = 200$ Hz to $N^{\mathrm{PZT}}_{\mathrm{fix}} \approx 1'000$ at $\omega/2\pi = 0.1$ Hz and tending to the DC value of ~2'600 obtained from the static tuning coefficients of f_{CEO} and f_{rep}. This later value corresponds to an optical frequency $\nu^{\mathrm{PZT}}_{\mathrm{fix}} = N^{\mathrm{PZT}}_{\mathrm{fix}} \cdot f_{\mathrm{rep}} \approx 0.7$ THz, which is close to the value of 1 THz previously reported for the fixed point in another Er:fiber laser [68]. At Fourier frequencies higher than 200 Hz, the phase difference between the transfer functions of f_{CEO} and f_{rep} departs from π so that only a quasi-fixed point can be defined. This quasi-fixed point cannot be accurately determined because of numerous PZT resonances, which strongly influence the CEO transfer function (see Figure 4.6a). The sign reversals in the transfer function of f_{CEO} associated to these resonances lead to a quasi-fixed point for cavity length fluctuation that alternates between positive and negative

values at higher Fourier frequencies.

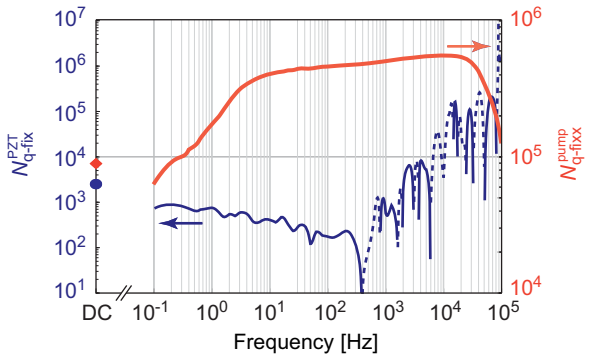

Figure 4.7: Spectral distribution of the comb quasi-fixed point obtained for cavity length modulation (left vertical scale, dark (blue) thin curve) and for laser pump power modulation (right vertical scale, light (red) thick curve). The points on the left vertical axis represent the static fixed points obtained from the ratio of the DC tuning coefficients of f_{CEO} and f_{rep}. The quasi-fixed point for cavity length modulation presents many sign reversals that result from mechanical resonances in the PZT. The solid curve corresponds to positive values of $N^{PZT}_{q\text{-}fix}$ and the dashed curve to negative values of $N^{PZT}_{q\text{-}fix}$.

For pump current modulation, a significant phase shift is observed at low modulation frequency (below ~10 Hz) in the transfer functions of f_{rep}. This leads to the absence of a true fixed point and only a quasi-fixed point can be defined according to Eq. (4.7). Furthermore, an important increase of the comb quasi-fixed point is observed at low frequency, from the static value $N^{pump}_{fix} \approx 9 \cdot 10^4$ and $N^{pump}_{q\text{-}fix} \approx 6.4 \cdot 10^4$ at $\omega / 2\pi = 0.1$ Hz to $N^{pump}_{q\text{-}fix} \approx 4 \cdot 10^5$ at $\omega / 2\pi \sim 5$ Hz. At higher modulation frequencies, the phase difference between the transfer functions of f_{CEO} and f_{rep} remains close to π so that a true fixed point can be considered here, which has a much weaker frequency dependence up to ~20 kHz. The quasi-fixed point corresponds to a quasi-fixed frequency $\nu^{pump}_{q\text{-}fix}$ ranging from ~16.2 THz ($\lambda \approx 19$ µm at $\omega/2\pi = 0.1$ Hz) to ~140 THz ($\lambda \approx 2.2$ µm at $\omega/2\pi = 20$ kHz), which is located much below the laser carrier (192 THz), especially for low frequency modulation. This is in contrast to previous observations made in other Er:fiber lasers [60,68,69], but also in other types of modelocked lasers such as Cr:forsterite lasers [61], using a different measurement method based on a low-frequency square waveform modulation and a fast counter. The origin of this discrepancy is not explained, but the possibility that the fixed point moves signifi-

cantly from the carrier was stated [68].

The observed frequency dependence of the (quasi) fixed point indicates that there is not a true fixed point in the comb neither for pump power modulation nor for cavity length modulation. This represents a new assessment about the noise distribution in a frequency comb, which has not been previously considered to our knowledge and which is an outcome of our dynamic response measurements.

4.5 Coupling between the two comb servo loops

In this section, the model that was developed to describe the coupled servo-loops is presented (Sections 4.5.1 and 4.5.2) and then it is shown how the impact of this coupling affects the stabilization of the comb repetition rate (Section 4.5.3).

4.5.1 Model of the coupled servo loops

A fully-stabilized optical frequency comb can be schematically described by two inter-connected feedback loops, labeled as (1) and (2) respectively, as illustrated in Figure 4.8. The comb is modeled here by a linear system, which is fully justified as f_{CEO} and f_{rep} were observed to change linearly with the pump power and cavity length, around the considered comb set point, over a broad range compared to the small changes considered in this study. The model presented here is described in the frequency (Fourier) domain as generally done for the description of closed loop transfer functions and uses the notation commonly adopted to describe laser stabilization loops [30,31]. This approach has two advantages compared to a time domain description. First, it is more pedagogic and intuitive as it leads to a multiplication of the different transfer functions of the loop components instead of a convolution of the corresponding impulse responses arising in the time domain representation. Second, the noise and transfer functions of the comb are experimentally obtained in the frequency domain.

In the model, loop (1) concerns the stabilization of the CEO frequency and loop (2) of the repetition rate. Following the standard description of servo systems [30,31], each loop is composed of the three following elements:

i) A phase detector, characterized by its transfer function $D_j(\omega)$ in V/Hz. The output of the phase detector constitutes the error signal $\tilde{e}_j(\omega)$, which is proportional to the difference $\delta\tilde{f}_j(\omega)$ between the stabilized input signal frequency $\tilde{f}_j^{\mathrm{stab}}(\omega)$ and the reference frequency $\tilde{f}_j^{0}$:

$\tilde{e}_j(\omega) = D_j(\omega) \cdot \delta\tilde{f}_j(\omega) = D_j(\omega) \cdot \left(\tilde{f}_j^{\,\mathrm{stab}}(\omega) - \tilde{f}_j^{\,0} \right)$.

ii) A servo-controller with a transfer function $G_j(\omega)$, which produces a correction signal $\tilde{u}_j^{\,\mathrm{cor}}(\omega) = G_j(\omega) \cdot D_{\,j}(\omega) \cdot \delta\tilde{f}_j(\omega)$.

iii) An actuator, with a transfer function $C_{jj}(\omega) = C_{f_j\,u_j}(\omega)$ (in Hz/V), which converts the correction voltage $\tilde{u}_j^{\,\mathrm{cor}}(\omega)$ into a correction $\tilde{f}_j^{\,\mathrm{cor}}(\omega) = C_{jj}(\omega) \cdot G_j(\omega) \cdot D_j(\omega) \cdot \delta\tilde{f}_j(\omega)$ of the free-running frequency $\tilde{f}_j^{\,\mathrm{free}}$.

More specifically, the DXD200 digital phase detector, with a measured transfer function $D_1(\omega) = -e^{-i\pi/2} 1.8 \cdot 10^{-3}/(\omega/2\pi)$ [V/Hz], is used in the CEO stabilization loop. In this case, the actuator is the pump laser current, which is controlled via the voltage $\tilde{u}_1(\omega) = \tilde{u}_{\mathrm{pump}}(\omega)$ applied to the modulation port of the pump laser driver. The pump current corrects the (free-running) CEO frequency $\tilde{f}_1^{\,\mathrm{free}}$ by $\tilde{f}_1^{\,\mathrm{cor}}(\omega) = C_{11} \cdot G_1 \cdot D_1 \cdot \delta\tilde{f}_1$, where $C_{11}(\omega) = C_{f_{\mathrm{CEO}}\,u_{\mathrm{pump}}}(\omega)$. The dependence on the Fourier frequency $\omega/2\pi$ has been omitted here and in the following expressions for the sake of clarity. At the same time, this correction signal changes the repetition rate frequency $\tilde{f}_2^{\,\mathrm{free}}$ by $\tilde{f}_2^{\,\mathrm{coupl}}(\omega) = C_{21} \cdot \tilde{u}_1^{\,\mathrm{cor}}$ (coupling term), where $C_{21}(\omega)$ is the dynamic response of the repetition rate to pump current modulation.

In the repetition rate stabilization loop, a double balanced mixer is used as a phase detector to compare the frequency $\left(4 \cdot f_{\mathrm{rep}} - f_{\mathrm{DRO}}\right)$ to a 20-MHz reference signal, where f_{DRO} is the frequency of the 980-MHz DRO referenced to the H-maser. The measured transfer function of the phase detector in the repetition rate loop is $D_2(\omega) = -e^{-i\pi/2} 0.86/(\omega/2\pi)$ [V/Hz]. The correction voltage $\tilde{u}_2 = \tilde{u}_{\mathrm{PZT}}$, applied at the input of the high voltage amplifier that drives the PZT of the laser resonator, induces a frequency correction $\tilde{f}_2^{\,\mathrm{cor}} = C_{22} \cdot G_2 \cdot D_2 \cdot \delta\tilde{f}_2$ of the free-running repetition rate $\tilde{f}_2^{\,\mathrm{free}}$, where C_{22} is the dynamic response of the repetition rate to cavity length modulation. At the same time, this correction signal changes the CEO frequency $\tilde{f}_1^{\,\mathrm{free}}$ by a coupling term $\tilde{f}_1^{\,\mathrm{coupl}} = C_{12} \cdot \tilde{u}_2^{\,\mathrm{cor}}$, where C_{12} is the dynamic response of the CEO to cavity length modulation.

The coupling between the servo loops is a direct consequence of the non-vanishing tuning coefficients C_{12} and C_{21} that lead to a change of $\tilde{f}_{\mathrm{rep}}$ ($\tilde{f}_{\mathrm{CEO}}$) with a change of $\tilde{u}_{\mathrm{pump}}$ ($\tilde{u}_{\mathrm{PZT}}$). As a result, two terms contribute to the feedback signal applied to the frequency $\tilde{f}_j^{\,\mathrm{free}}$. In addition to the correction signal $\tilde{f}_j^{\,\mathrm{cor}}$ produced by the main stabilization loop, a coupling term $\tilde{f}_j^{\,\mathrm{coupl}}$ originating from the other loop occurs. Following the standard description of servo systems [30,31], the CEO and

repetition rate frequencies $\tilde{f}_j^{\mathrm{stab}}$ in the fully-stabilized comb (closed loops) are related to the free-running frequencies $\tilde{f}_j^{\mathrm{free}}$ (open loops) by:

$$\tilde{f}_j^{\mathrm{stab}} = \tilde{f}_j^{\mathrm{free}} + \tilde{f}_j^{\mathrm{cor}} + \tilde{f}_j^{\mathrm{coupl}}. \tag{4.9}$$

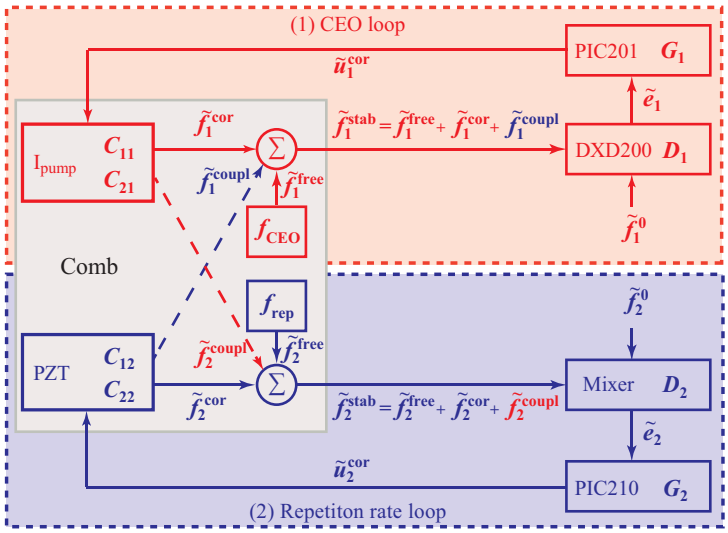

Figure 4.8: Schematic representation of the two coupled stabilization loops in the Er:fiber comb. Loop (1) stabilizes the CEO frequency and loop (2) the repetition rate.

The aforementioned description of the fully stabilized comb constitutes a multiple-input multiple-output (MIMO) system [70]. The feedback signals, made of the direct corrections plus the coupling terms, are obtained from the deviations $\Delta\tilde{f}_j = \tilde{f}_j^{\mathrm{free}} - \tilde{f}_j^0$ of the CEO and repetition rate frequencies from their reference values in the free-running frequency comb as

$$\begin{pmatrix} \tilde{f}_1^{\mathrm{cor}} + \tilde{f}_1^{\mathrm{coupl}} \\ \tilde{f}_2^{\mathrm{cor}} + \tilde{f}_2^{\mathrm{coupl}} \end{pmatrix} = \begin{pmatrix} C_{11} & C_{12} \\ C_{21} & C_{22} \end{pmatrix} \cdot \begin{pmatrix} G_1 & 0 \\ 0 & G_2 \end{pmatrix} \cdot \begin{pmatrix} D_1 & 0 \\ 0 & D_2 \end{pmatrix} \cdot \begin{pmatrix} \Delta\tilde{f}_1 \\ \Delta\tilde{f}_2 \end{pmatrix}. \tag{4.10}$$

Combining Eqs. (4.9) and (4.10) and defining $K_j = C_{jj}G_jD_j \big/ (1 - C_{jj}G_jD_j)$, the following expression is obtained for the residual frequency deviations of the fully-stabilized optical frequency comb:

$$\delta\tilde{f}_j = \frac{\left(1 + K_j\right)\left(\Delta\tilde{f}_j + K_k\Delta\tilde{f}_k\,\dfrac{C_{jk}}{C_{kk}}\right)}{1 - K_jK_k\,\dfrac{C_{jk}C_{kj}}{C_{jj}C_{kk}}}, \tag{4.11}$$

where $j,\ k = 1,\ 2$ and $j \neq k$.

With this model, the residual frequency deviations of the CEO and repetition rate in the fully-stabilized frequency comb, $\delta\tilde{f}_j(\omega)$, can be calculated from the frequency deviations of the free-running comb, $\Delta\tilde{f}_j(\omega)$, provided that the gain $K_j(\omega)$ of each loop is known, as well as the comb dynamic response matrix $C_{jk}(\omega)$. Using the definition of the PSD $S_{xy} = \lim_{T\to\infty}\left\langle \tilde{x}^*(\omega)\tilde{y}(\omega)/T \right\rangle$, Eq. (4.11) can be rewritten in terms of frequency noise PSD self-spectra (S_{xx}) and cross-spectra (S_{xy}) [71]:

$$\begin{pmatrix} S_{\delta f_1 \delta f_1} & S_{\delta f_1 \delta f_2} \\ S_{\delta f_2 \delta f_1} & S_{\delta f_2 \delta f_2} \end{pmatrix} = \begin{pmatrix} H_{11} & H_{12} \\ H_{21} & H_{22} \end{pmatrix}^{+} \cdot \begin{pmatrix} S_{\Delta f_1 \Delta f_1} & S_{\Delta f_1 \Delta f_2} \\ S_{\Delta f_2 \Delta f_1} & S_{\Delta f_2 \Delta f_2} \end{pmatrix} \cdot \begin{pmatrix} H_{11} & H_{12} \\ H_{21} & H_{22} \end{pmatrix}, \tag{4.12}$$

where

$$H_{jj}(\omega) = \left(1 + K_j\right) \cdot \left(1 - K_j K_k C_{jk} C_{kj} / (C_{jj} C_{kk})\right)^{-1} \tag{4.13}$$

$$\text{and } H_{jk}(\omega) = \left(1 + K_j\right) K_k C_{jk} C_{kk}^{-1} \left(1 - K_j K_k C_{jk} C_{kj} / (C_{jj} C_{kk})\right)^{-1} \tag{4.14}$$

are the elements of the closed loop transfer function matrix ($j,\ k = 1,\ 2$ and $j \neq k$) and the exponent $^{+}$ in the matrix H indicates the Hermitian conjugate. If all the terms on the right-hand side of Eq. (4.11) or (4.12) are known experimentally, the resulting noise of the fully-stabilized comb (left-hand side of Eq. (4.11) or (4.12)) can be calculated and the model can be applied to predict the noise properties of any comb line.

All the matrix elements $C_{jk}(\omega)$ have been measured as described in Section 4.4.1. The additional measurement of the open-loop transfer functions of the phase detectors $D_j(\omega)$ and of the servo controllers $G_j(\omega)$ enabled the entire closed loops transfer functions to be determined. Finally, the frequency noise PSDs of the repetition rate ($S_{\Delta f_2 \Delta f_2}$) and of the CEO-beat ($S_{\Delta f_1 \Delta f_1}$) in the free-running comb have been measured as described in the following sections. However, the cross-spectra $S_{\Delta f_j \Delta f_k}$ ($k \neq j$), which describe the correlation of the noise between the CEO and the repetition rate in the free-running comb, are not known from the performed experimental measurements.

In the most general case, fluctuations of f_{rep} and f_{CEO} can arise from different noise sources and thus the correlation between these frequency fluctuations can be

only partial. However, it will be assumed here that the fluctuations of f_{CEO} and f_{rep} in the free-running comb are 100% anti-correlated. One will see that this assumption is justified in the present case by the measured frequency noise PSD of an optical comb line used to infer some information about the unknown cross-spectra (see Section 4.6.2). This results from the fact that pump power fluctuations constitute the principal source of noise in the considered free-running comb as discussed later.

The model presented in this section is slightly simplified for the ease of understanding and to make it more didactic. The contribution of the noise of the RF references f_j^0 used in the two loops has not been taken into account here and ideal noiseless references have been considered. This is fully justified for the CEO stabilization loop, as the noise of the stabilized CEO-beat is usually orders of magnitude higher than the noise of the reference f_1^0. But the frequency stability of the repetition rate is known to be limited by the noise of the reference when the comb is locked to an RF oscillator [72,73]. Therefore, the noise of the reference f_2^0 used in the repetition rate servo-loop has to be taken into account for the completeness of the model, in order to properly determine the noise properties of the repetition rate and, thus, of an optical comb line. An extended model including the noise of the RF reference is detailed in the next section. All the results discussed later on in this chapter have been obtained from this complete model, i.e. using Eqs. (4.16)-(4.24).

4.5.2 Complete model of the coupled servo-loops accounting for the noise of the frequency references

In the model presented in Section 4.5.1, the error signal $\tilde{e}_j = D_j \cdot \delta\tilde{f}_j$ was considered to be proportional to the difference $\delta\tilde{f}_j = \tilde{f}_j^{\mathrm{stab}} - \tilde{f}_j^0$ between the stabilized input signal frequency $\tilde{f}_j^{\mathrm{stab}}$ and an ideal reference frequency $\tilde{f}_j^0$. There, the noise of this reference frequency was assumed to be negligible compared to the residual frequency noise of the stabilized frequencies $\tilde{f}_j^{\mathrm{stab}}$. In the real case of a reference signal having finite frequency fluctuations $\Delta\tilde{f}_j^{\mathrm{ref}}$ within the PLL bandwidth, these fluctuations are transferred to the stabilized signal frequency. This contribution is accounted for here by introducing a term describing for the noise of the reference frequency $\Delta\tilde{f}_j^{\mathrm{ref}} = \tilde{f}_j^{\mathrm{ref}} - \tilde{f}_j^0$. In this case, the error signal $\tilde{e}_j = D_j \cdot \delta\tilde{f}_j$ is replaced by $\tilde{e}_j = D_j\left(\tilde{f}_j^{\mathrm{stab}} - \tilde{f}_j^{\mathrm{ref}}\right) = D_j\left(\delta\tilde{f}_j - \Delta\tilde{f}_j^{\mathrm{ref}}\right)$. Here, as previously, $\delta\tilde{f}_j = \tilde{f}_j^{\mathrm{stab}} - \tilde{f}_j^0$ represents the deviations from an ideal reference frequency $\tilde{f}_j^0$ in the stabilized

comb and $\Delta\tilde{f}_j = \tilde{f}_j^{\,\mathrm{free}} - \tilde{f}_j^{\,0}$ are the deviations of the CEO and repetition rate frequencies from their reference values $\tilde{f}_j^{\,0}$ in the free-running frequency comb. Thus, the frequency correction signal $\tilde{f}_j^{\,\mathrm{cor}} = C_{jj}G_jD_j\left(\tilde{f}_j^{\,\mathrm{stab}} - \tilde{f}_j^{\,\mathrm{ref}}\right)$ and the coupling term $\tilde{f}_j^{\,\mathrm{coupl}} = C_{jk}\tilde{u}_k^{\mathrm{cor}}$ in Eq. (4.10) transform into

$$\begin{pmatrix} \tilde{f}_1^{\,\mathrm{cor}} + \tilde{f}_1^{\,\mathrm{coupl}} \\ \tilde{f}_2^{\,\mathrm{cor}} + \tilde{f}_2^{\,\mathrm{coupl}} \end{pmatrix} = \begin{pmatrix} C_{11} & C_{12} \\ C_{21} & C_{22} \end{pmatrix} \cdot \begin{pmatrix} G_1 & 0 \\ 0 & G_2 \end{pmatrix} \cdot \begin{pmatrix} D_1 & 0 \\ 0 & D_2 \end{pmatrix} \cdot \begin{pmatrix} \Delta\tilde{f}_1 - \Delta\tilde{f}_1^{\,\mathrm{ref}} \\ \Delta\tilde{f}_2 - \Delta\tilde{f}_2^{\,\mathrm{ref}} \end{pmatrix}. \tag{4.15}$$

In the resulting expression of the frequency deviations $\delta\tilde{f}_j(\omega)$ of the fully-stabilized comb, the contributions originating from the noise of the references can be separated from the contributions that are intrinsic to the comb. This latter term, that is labeled here $\delta\tilde{f}_j^{\,\mathrm{comb}}(\omega)$, corresponds to the ideal case encountered with perfect noiseless references as considered in Section 4.5.1. The additional term arising from the noise of the references is labeled $\delta\tilde{f}_j^{\,\mathrm{ref}}(\omega)$. The total residual frequency deviations are given by $\delta\tilde{f}_j(\omega) = \delta\tilde{f}_j^{\,\mathrm{comb}}(\omega) + \delta\tilde{f}_j^{\,\mathrm{ref}}(\omega)$ with the following expression for each noise source:

$$\delta\tilde{f}_j^{\,\mathrm{comb}} = \frac{\left(1 + K_j\right)\left(\Delta\tilde{f}_j + K_k\Delta\tilde{f}_k\,\dfrac{C_{jk}}{C_{kk}}\right)}{1 - K_jK_k\,\dfrac{C_{jk}C_{kj}}{C_{jj}C_{kk}}}, \tag{4.16}$$

$$\delta\tilde{f}_j^{\,\mathrm{ref}} = -\Delta\tilde{f}_j^{\,\mathrm{ref}}\,\frac{K_j\left(1 + K_k\,\dfrac{C_{jk}C_{kj}}{C_{jj}C_{kk}}\right)}{1 - K_jK_k\,\dfrac{C_{jk}C_{kj}}{C_{jj}C_{kk}}} - \Delta\tilde{f}_k^{\,\mathrm{ref}}\,\frac{K_k\left(1 + K_j\right)\dfrac{C_{jk}}{C_{kk}}}{1 - K_jK_k\,\dfrac{C_{jk}C_{kj}}{C_{jj}C_{kk}}}. \tag{4.17}$$

As follows from the definition of the frequency noise PSD, by multiplying $\delta\tilde{f}_j(\omega) = \delta\tilde{f}_j^{\,\mathrm{comb}}(\omega) + \delta\tilde{f}_j^{\,\mathrm{ref}}(\omega)$ by its complex conjugate and simply replacing all the frequency deviations in Eqs. (4.15) – (4.17) by the corresponding frequency noise PSDs and cross-spectral densities as $\delta\tilde{f}_j^{\,*}\delta\tilde{f}_k \to S_{\delta f_j\,\delta f_k}$, $\Delta\tilde{f}_j^{\,*}\Delta\tilde{f}_k \to S_{\Delta f_j\,\Delta f_k}$, and $\Delta\tilde{f}_j^{\,\mathrm{ref}\,*}\Delta\tilde{f}_k \to S_{\Delta f_j^{\mathrm{ref}}\,\Delta f_k}$, the experimentally measurable frequency noise PSDs in the fully stabilized optical frequency comb $S_{\delta f_j\,\delta f_j}$ can be obtained.

This model describes any pair of coupled loops. However, its implementation requires additional information about the phase of the frequency deviations of the free-running comb $\Delta\tilde{f}_j(\omega)$ (or the cross-spectra $S_{\Delta f_j\,\Delta f_k}$ in terms of PSDs). One thus

assumes on one hand that the CEO noise is of the same origin as the noise on the repetition rate and these contributions are considered as 100% anti-correlated as will be justified in Section 4.6.2. On the other hand, the noise contribution from the reference, $\delta\tilde{f}_j^{\mathrm{ref}}(\omega)$, is totally uncorrelated with the intrinsic comb contribution, $\delta\tilde{f}_j^{\mathrm{comb}}(\omega)$. The frequency noise of the stabilized comb is thus determined from Eqs. (4.16) and (4.17) using the frequency noise PSDs and summing $\delta\tilde{f}_j^{\mathrm{ref}}(\omega)$ and $\delta\tilde{f}_j^{\mathrm{comb}}(\omega)$ in quadrature to determine the frequency deviations of the stabilized comb

$$\left|\delta\tilde{f}_j\right| = \sqrt{\left|\delta\tilde{f}_j^{\mathrm{comb}}\right|^2 + \left|\delta\tilde{f}_j^{\mathrm{ref}}\right|^2}\,. \tag{4.18}$$

In terms of PSDs, Eqs. (4.15) – (4.18) can be written down as

$$S_{\delta f_j\,\delta f_j} = S_{\delta f_j^{\mathrm{comb}}\,\delta f_j^{\mathrm{comb}}} + S_{\delta f_j^{\mathrm{ref}}\,\delta f_j^{\mathrm{ref}}}\,, \tag{4.19}$$

where

$$\begin{aligned}&\begin{pmatrix} S_{\delta f_1^{\mathrm{comb}}\,\delta f_1^{\mathrm{comb}}} & S_{\delta f_1^{\mathrm{comb}}\,\delta f_2^{\mathrm{comb}}} \\ S_{\delta f_2^{\mathrm{comb}}\,\delta f_1^{\mathrm{comb}}} & S_{\delta f_2^{\mathrm{comb}}\,\delta f_2^{\mathrm{comb}}} \end{pmatrix} \\ &= \begin{pmatrix} H_{11} & H_{12} \\ H_{21} & H_{22} \end{pmatrix}^{+} \cdot \begin{pmatrix} S_{\Delta f_1 \Delta f_1} & S_{\Delta f_1 \Delta f_2} \\ S_{\Delta f_2 \Delta f_1} & S_{\Delta f_2 \Delta f_2} \end{pmatrix} \cdot \begin{pmatrix} H_{11} & H_{12} \\ H_{21} & H_{22} \end{pmatrix},\end{aligned} \tag{4.20}$$

$$\begin{aligned}&\begin{pmatrix} S_{\delta f_1^{\mathrm{ref}},\,\delta f_1^{\mathrm{ref}}} & S_{\delta f_1^{\mathrm{ref}},\,\delta f_2^{\mathrm{ref}}} \\ S_{\delta f_2^{\mathrm{ref}},\,\delta f_1^{\mathrm{ref}}} & S_{\delta f_2^{\mathrm{ref}},\,\delta f_2^{\mathrm{ref}}} \end{pmatrix} \\ &= \begin{pmatrix} H_{11}^{\mathrm{ref}} & H_{12}^{\mathrm{ref}} \\ H_{21}^{\mathrm{ref}} & H_{22}^{\mathrm{ref}} \end{pmatrix}^{+} \cdot \begin{pmatrix} S_{\Delta f_1^{\mathrm{ref}} \Delta f_1^{\mathrm{ref}}} & S_{\Delta f_1^{\mathrm{ref}} \Delta f_2^{\mathrm{ref}}} \\ S_{\Delta f_2^{\mathrm{ref}} \Delta f_1^{\mathrm{ref}}} & S_{\Delta f_2^{\mathrm{ref}} \Delta f_2^{\mathrm{ref}}} \end{pmatrix} \cdot \begin{pmatrix} H_{11}^{\mathrm{ref}} & H_{12}^{\mathrm{ref}} \\ H_{21}^{\mathrm{ref}} & H_{22}^{\mathrm{ref}} \end{pmatrix},\end{aligned} \tag{4.21}$$

and

$$H_{jj}(\omega) = \frac{\left(1 + K_j\right)}{1 - K_j K_k \dfrac{C_{jk} C_{kj}}{C_{jj} C_{kk}}}, \tag{4.22}$$

$$H_{jk}(\omega) = H_{jk}^{\mathrm{ref}}(\omega) = \frac{\left(1 + K_j\right) K_k \dfrac{C_{jk}}{C_{kk}}}{1 - K_j K_k \dfrac{C_{jk} C_{kj}}{C_{jj} C_{kk}}}, \tag{4.23}$$

$$H_{jj}^{\mathrm{ref}}(\omega) = \frac{K_j \left(1 + K_k \dfrac{C_{jk} C_{kj}}{C_{jj} C_{kk}}\right)}{1 - K_j K_k \dfrac{C_{jk} C_{kj}}{C_{jj} C_{kk}}}. \tag{4.24}$$

4.5.3 Impact of the CEO stabilization on the repetition rate

Our model of the fully-stabilized optical frequency comb with two feedback loops shows the cross-impact of the actuators that results from the non-vanishing coupling coefficients $C_{jk}(\omega)$ in Eqs. (4.11) and (4.12). In order to observe the influence of this coupling experimentally, the frequency noise PSD of the repetition rate and of the CEO-beat was measured in the Er:fiber comb in two different conditions. In the first case, only one comb parameter was stabilized (either f_{rep} or f_{CEO}) by closing the corresponding loop. The second loop was disabled, so that no signal was applied to the second actuator and thus no coupling occurred. In the second case, both feedback loops were simultaneously enabled, so that their reciprocal coupling influence was observed. In both cases, the frequency noise PSD of the repetition rate and of the CEO-beat was measured as described below.

The frequency noise of the repetition rate was measured by detecting the 6^{th} harmonic of f_{rep} at 1.5 GHz using an independent, out-of-loop, fast photodiode (New-Focus 1434, 25 GHz bandwidth). This signal was filtered, amplified and frequency-divided by 15 to be measured against a low-phase-noise 100-MHz synthesizer (SpectraDynamics Cs-1) using a phase noise measurement system (NMS from SpectraDynamics). As an alternative to overcome the noise floor of the phase noise measurement system occurring at high Fourier frequency, a second measurement was implemented using the HF2PLL frequency discriminator to demodulate the repetition rate. To increase the measurement sensitivity to the small frequency fluctuations of the repetition rate, a higher harmonic of f_{rep} has been used here, i.e. the

12th harmonic at 3 GHz. The HF2PLL frequency discriminator was operated with a 20-MHz carrier frequency. For this purpose, the 3-GHz repetition rate harmonic was frequency down-converted to 20 MHz by mixing with a reference signal at 2.98 GHz delivered by a frequency synthesizer referenced to an H-maser. The low-pass filtered 20-MHz signal was then demodulated in the digital HF2PLL discriminator and the demodulated signal was measured with an FFT spectrum analyzer. The data obtained with the two measurement systems were combined in order to minimize the limitation due to the instrumental noise floor. The resulting frequency noise spectra are displayed in Figure 4.9, together with the frequency noise of the free-running repetition rate to assess the effect of each actuator. The instrumental noise floor limits the measurement of the repetition rate in the range 10-100 kHz when the CEO is free-running, but in a larger range of 2-100 kHz when the CEO is stabilized.

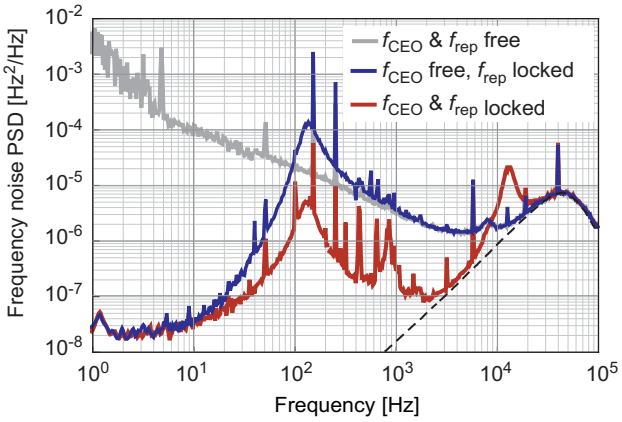

Figure 4.9: Measured frequency noise PSD of the repetition rate (at 250 MHz) in the free-running and stabilized Er:fiber comb (with and without CEO stabilization). At high frequency, the measurement is limited by the instrumental noise floor of the HF2PLL discriminator (dashed line).

Whereas the noise of the repetition rate is strongly reduced by the PZT feedback signal, the bandwidth of this servo-loop is limited by the PZT transfer function to a few hundred hertz. This bandwidth might be enlarged to the kilohertz range, but with the detrimental consequence of a degradation of the optical linewidth of the comb lines due to the larger contribution of the repetition rate servo bump to the comb frequency noise PSD. The repetition rate servo bandwidth was thus limited to a lower value to prevent this degradation. With only the repeti-

tion rate loop enabled, the frequency noise around 100 Hz is slightly higher than in the free-running comb as a result of the ~120-Hz servo bump. A significant improvement in the frequency noise of the repetition rate is observed when the CEO stabilization is enabled. The improvement is larger than one order of magnitude in terms of PSD in the frequency range 60 Hz – 4 kHz (however, the measurement with the stabilized CEO is limited by the instrumental noise floor at $\omega/2\pi > 3$ kHz). This results from the cross-sensitivity of f_{rep} to the pump power and to the larger bandwidth of the CEO servo-loop. These two features lead to an enhancement of the overall repetition rate feedback bandwidth. As a consequence, the noise of an optical comb line, which is dominated by the noise contribution of the repetition rate, is improved by the CEO stabilization loop (apart from the CEO servo-bump at around 10 kHz which appears in frequency noise of f_{rep}). In this context, the full stabilization of the comb is beneficial for beat-note experiments with external lasers, as it leads to improved noise properties in comparison with the alternative method where the CEO is not or only very smoothly controlled and then subtracted from the beat-note [66]. This effect will be experimentally demonstrated in Chapter 6.

The frequency noise PSD of the CEO-beat was also measured, both with the repetition rate servo-loop enabled and disabled, to observe the influence of the repetition rate stabilization onto the CEO. The frequency noise of the stabilized CEO-beat was measured from the signal of the in-loop DXD200 phase detector, recorded with an FFT spectrum analyzer, whereas the frequency noise of the free-running CEO-beat was measured using the Miteq frequency discriminator. We observed no significant impact of the repetition rate stabilization onto the CEO frequency noise.

These experimental results have been used to check the theoretical model. In Figure 4.10, the frequency noise of the repetition rate experimentally measured in the fully-stabilized comb is compared with the one calculated from the frequency noise of the free-running comb with the model using Eqs. (4.16) – (4.24). The experimental results are in a very good agreement with the model. The small difference observed in the range 2 to 10 kHz results from the instrumental noise floor in the measurement of the repetition rate frequency noise. The measurement of the repetition rate frequency noise is limited by the instrumental noise floor above ~2 kHz in the fully-stabilized comb (see Figure 4.9), but in a narrower frequency

range (10 to 100 kHz) for the free-running repetition rate, which is relevant for the spectrum calculated from the model, due to its higher noise.

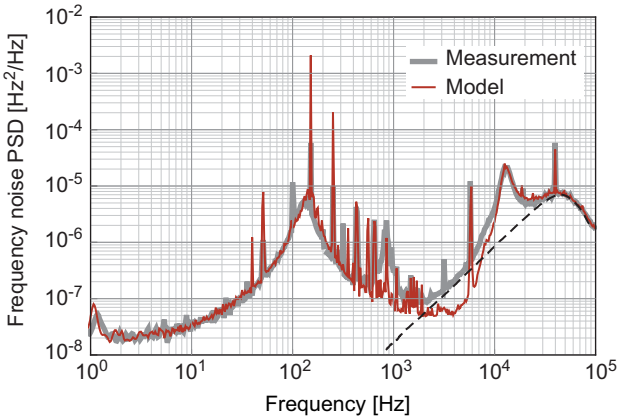

Figure 4.10: Measured frequency noise PSD of the repetition rate (at 250 MHz) in the free-running and stabilized Er:fiber comb (with and without CEO stabilization). At high frequency, the measurement is limited by the instrumental noise floor of the HF2PLL discriminator (dashed line).

These experimental results demonstrate the suitability of the presented theoretical approach in the calculation of the coupling between the repetition rate and CEO stabilization loops. In the next section, a further verification of the model will be presented, applied to the noise of an optical comb line at 1.56 µm. Then, the model will be used to quantitatively assess the impact of the servo-loops coupling at different wavelengths throughout the comb spectrum.

4.6 Noise of an optical comb line

In this section, the developed model is applied to quantify the impact of the servo-loops coupling onto the noise properties of the comb, when the comb is stabilized to the H-maser as described in Section 4.3.2. The contribution of the CEO to the frequency noise of a comb line is first shown (Section 4.6.1), then the impact of the servo-loops coupling is assessed by calculating the frequency noise of a comb line in presence and absence of coupling (Section 4.6.2). Finally, the linewidth of a comb line at different wavelengths is obtained using the theoretical predictions (Section 4.6.3).

4.6.1 CEO contribution to the optical frequency noise

To assess the impact of the servo-loops coupling on the noise properties of an optical comb line, the heterodyne beat between the comb and the 1.56-µm cavity-stabilized ultra-narrow linewidth laser was characterized. The beat signal was measured with a fiber-coupled photodiode by combining ~1 mW from the ultra-stable laser with ~60 µW from the comb, spectrally filtered to a 0.3-nm (40 GHz) width using a diffraction grating. About 160 comb lines contribute to the detected comb optical power, corresponding to an average power of less than 400 nW per comb line. Despite this low power, a beat signal with a signal-to-noise ratio of more than 30 dB (at 100 kHz resolution bandwidth) was detected in the range 20-40 MHz depending on the laser fine tuning. The beat note was amplified to ~0 dBm, band-pass filtered at 20 MHz and then demodulated with the Miteq frequency discriminator. The noise of the demodulated beat signal was recorded with an FFT spectrum analyzer and converted into frequency noise using the discriminator sensitivity. The frequency noise PSD of the heterodyne beat signal represents the frequency noise of the optical comb line as the contribution of the ultra-narrow linewidth laser is negligible.

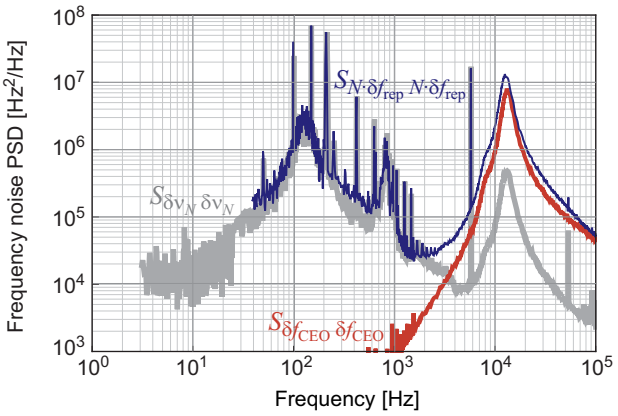

Figure 4.11: Measured individual contributions of the CEO and repetition rate frequency noise PSD ($S_{\delta f_{CEO}\ \delta f_{CEO}}$ and $S_{N\cdot\delta f_{rep}\ N\cdot\delta f_{rep}}$) to an optical comb line at 1.56 µm and comparison with the measured frequency noise of the optical comb line ($S_{\delta\nu_N\ \delta\nu_N}$) experimentally assessed from the heterodyne beat with a cavity-stabilized laser.

Figure 4.11 displays the measured frequency noise PSD of the 1.56-µm comb line and of the CEO-beat for comparison (measured from the in-loop DXD200 phase detector as described in Section 4.5.3). One observes that the CEO frequency

noise is significantly higher than the noise of the comb line in the range 3 to 100 kHz corresponding to the CEO servo bump. This is possible only if the frequency noise of f_{CEO} is anti-correlated and of similar amplitude as the contribution of $N \cdot f_{\mathrm{rep}}$, as the total fluctuations of the comb line ν_N corresponds to $\delta\nu_N = \delta f_{\mathrm{CEO}} + N \cdot \delta f_{\mathrm{rep}}$, which arises from the well-known comb equation $\nu_N = f_{\mathrm{CEO}} + N \cdot f_{\mathrm{rep}}$. In order to verify this statement, the contribution of the CEO-beat to the optical comb line was subtracted from the laser-comb heterodyne beat as explained in Section 4.4.1. The CEO-free beat signal, demodulated with Miteq frequency discriminator and measured with an FFT spectrum analyzer, simply represents the noise of the repetition rate multiplied to the optical domain by the mode number N (i.e. $S_{N\cdot\delta f_{\mathrm{rep}}\, N\cdot\delta f_{\mathrm{rep}}}$). The similar noise feature observed at 10 kHz for both f_{CEO} and $N \cdot f_{\mathrm{rep}}$, resulting from the servo-loops coupling, confirms that the CEO frequency noise is anti-correlated with the noise of the repetition rate. This leads to a strong reduction of the CEO contribution in the noise of the optical comb line. This anti-correlation is also in agreement with the inverse sign obtained in the static tuning coefficients of f_{CEO} and f_{rep} for pump current variation reported in Section 4.4.1. Comparing the experimentally measured frequency noise PSD of the CEO-free beat ($S_{N\cdot\delta f_{\mathrm{rep}}\, N\cdot\delta f_{\mathrm{rep}}}$) with the frequency noise PSD of the repetition rate ($S_{\delta f_{\mathrm{rep}}\, \delta f_{\mathrm{rep}}}$) calculated from the model and multiplied by N^2 shows again a very good agreement, as shown in Figure 4.12.

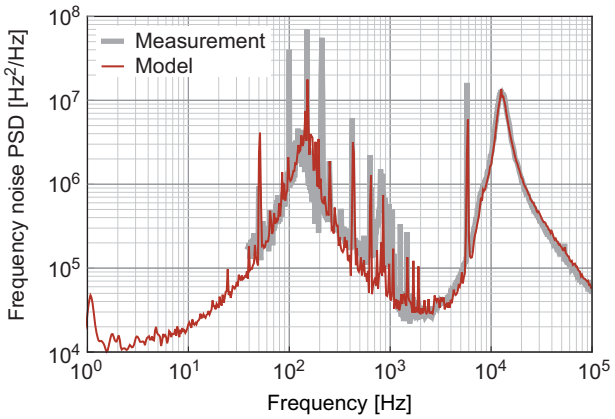

Figure 4.12: Comparison of the frequency noise of the CEO-free heterodyne beat ($\nu_N - f_{\mathrm{CEO}} = N \cdot f_{\mathrm{rep}}$) experimentally measured (thick grey curve) and calculated from the model (thin red curve). In order to overcome the limitation in the frequency noise of the free-running repetition rate used in the model that results from the instrumental noise floor (see Figure 4.9), the frequency noise PSD of f_{rep} was obtained from the CEO-free optical beat at 1.56 µm ($N \cdot f_{\mathrm{rep}}$ with $N \sim 770'000$) divided by N^2.

4.6.2 Impact of the servo-loops coupling

It was experimentally shown in the previous section that the coupling between the CEO and the repetition rate servo-loops leads to a strong reduction of the noise of an optical comb line in the 1.5-µm wavelength range. The beneficial influence of the servo-loop coupling onto the comb noise can be quantified with the model by comparing the frequency noise computed in presence and in absence of coupling. However, this procedure is less straightforward than the calculation presented in Section 4.6.1 for the CEO-free comb line, where only the noise of the repetition rate ($N \cdot f_{\mathrm{rep}}$) was contributing. Here, both the frequency noise of f_{rep} and f_{CEO} in the free-running comb (i.e. $\Delta\tilde{f}_{\mathrm{rep}}(\omega)$ and $\Delta\tilde{f}_{\mathrm{CEO}}(\omega)$) must be accounted for to determine their resulting noise in the fully-stabilized comb, $\delta\tilde{f}_{\mathrm{rep}}(\omega)$ and $\delta\tilde{f}_{\mathrm{CEO}}(\omega)$, using Eqs. (4.16) – (4.24). Then, these quantities must be combined with their respective phase to determine the resulting noise of a comb line $\delta\tilde{\nu}_N(\omega) = \delta\tilde{f}_{\mathrm{CEO}}(\omega) + N \cdot \delta\tilde{f}_{\mathrm{rep}}(\omega)$. In these processes, the correlation between the noise of f_{rep} and f_{CEO} has to be taken into account for a correct application of the model. This can be done either using the cross-spectra $S_{\Delta f_j\,\Delta f_k}$ in Eq. (4.12), or by knowing the phase of the frequency deviations $\Delta\tilde{f}_j$ of the free-running comb in Eq. (4.11) and later on in the stabilized comb ($\delta\tilde{f}_j$). However, none of these pa-

rameters is known in the experiments as only the PSD spectra (self-spectra) have been measured for the CEO and repetition rate frequencies. As mentioned in Section 4.5.1, a 100% anti-correlation between $\Delta\tilde{f}_{\mathrm{rep}}(\omega)$ and $\Delta\tilde{f}_{\mathrm{CEO}}(\omega)$ has been considered when applying the model to the noise of an optical comb line and this assumption will be justified here.

To infer the correlation between the noise of the CEO and repetition rate in the free-running comb, the basic comb equation enables the frequency deviations of an optical comb mode to be related to the frequency deviation of the CEO and repetition rate: $\Delta\tilde{\nu}_N = \Delta\tilde{f}_{\mathrm{CEO}} + N \cdot \Delta\tilde{f}_{\mathrm{rep}}$. This can be written down in terms of the frequency noise PSDs as $S_{\Delta\nu_N\,\Delta\nu_N} = S_{\Delta f_{\mathrm{CEO}}\,\Delta f_{\mathrm{CEO}}} + S_{N\cdot\Delta f_{\mathrm{rep}}\,N\cdot\Delta f_{\mathrm{rep}}} + S_{\Delta f_{\mathrm{CEO}}\,N\cdot\Delta f_{\mathrm{rep}}} + S_{N\cdot\Delta f_{\mathrm{rep}}\,\Delta f_{\mathrm{CEO}}}$, where the cross-spectra $S_{\Delta f_{\mathrm{CEO}}\,N\cdot\Delta f_{\mathrm{rep}}}$ and $S_{N\cdot\Delta f_{\mathrm{rep}}\,\Delta f_{\mathrm{CEO}}}$ can be replaced by self-spectra using the complex coherence defined in the general case as $\gamma_{xy}(\omega) = S_{xy}(\omega)/\sqrt{S_{xx}(\omega)\cdot S_{yy}(\omega)}$. The resulting frequency noise PSD of the free-running optical comb line is given by the following expression:

$$\begin{aligned} S_{\Delta\nu_N\,\Delta\nu_N} &= S_{\Delta f_{\mathrm{CEO}}\,\Delta f_{\mathrm{CEO}}} + S_{N\cdot\Delta f_{\mathrm{rep}}\,N\cdot\Delta f_{\mathrm{rep}}} \\ &+\left(\gamma_{\Delta f_{\mathrm{CEO}}\,N\cdot\Delta f_{\mathrm{rep}}} + \gamma_{N\cdot\Delta f_{\mathrm{rep}}\,\Delta f_{\mathrm{CEO}}}\right)\sqrt{S_{\Delta f_{\mathrm{CEO}}\,\Delta f_{\mathrm{CEO}}}\cdot S_{N\cdot\Delta f_{\mathrm{rep}}\,N\cdot\Delta f_{\mathrm{rep}}}}. \end{aligned} \tag{4.25}$$

The sum of the complex coherences can be determined from Eq. (4.25) as

$$\begin{aligned} \Gamma_{\Delta}(\omega) &= \gamma_{\Delta f_{\mathrm{CEO}}\,N\cdot\Delta f_{\mathrm{rep}}} + \gamma_{N\cdot\Delta f_{\mathrm{rep}}\,\Delta f_{\mathrm{CEO}}} \\ &= \frac{S_{\Delta\nu_N\,\Delta\nu_N} - S_{\Delta f_{\mathrm{CEO}}\,\Delta f_{\mathrm{CEO}}} - S_{N\cdot\Delta f_{\mathrm{rep}}\,N\cdot\Delta f_{\mathrm{rep}}}}{\sqrt{S_{\Delta f_{\mathrm{CEO}}\,\Delta f_{\mathrm{CEO}}}\cdot S_{N\cdot\Delta f_{\mathrm{rep}}\,N\cdot\Delta f_{\mathrm{rep}}}}}. \end{aligned} \tag{4.26}$$

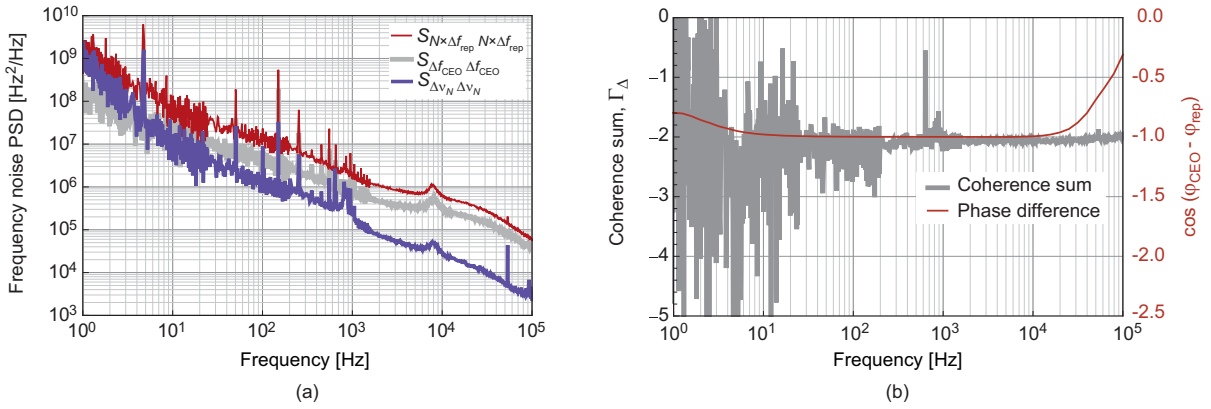

Figure 4.13: (a) Measured individual contributions of the CEO and repetition rate frequency noise PSD ($S_{\Delta f_{\mathrm{CEO}}\,\Delta f_{\mathrm{CEO}}}$ and $S_{N\cdot\Delta f_{\mathrm{rep}}\,N\cdot\Delta f_{\mathrm{rep}}}$) to an optical comb line at 1.56 µm and comparison with the measured frequency noise of the optical comb line ($S_{\Delta\nu_N\,\Delta\nu_N}$) experimentally assessed from the heterodyne beat between a cavity-stabilized laser and the free-running comb. (b) Frequency dependence of the sum of the complex coherences $\Gamma_\Delta(\omega) = \left(\gamma_{\Delta f_{\mathrm{CEO}}\,N\cdot\Delta f_{\mathrm{rep}}} + \gamma_{N\cdot\Delta f_{\mathrm{rep}}\,\Delta f_{\mathrm{CEO}}}\right)$ between the frequency variations of the CEO and repetition rate in the free-running comb (left vertical axis). The correlation between the phase of the variations of f_{CEO} and f_{rep} induced by pump current modulation is also shown, represented by $\cos\left\{\varphi_{\mathrm{CEO}}(\omega) - \varphi_{\mathrm{rep}}(\omega)\right\}$ (right vertical axis), where φ_{CEO} and φ_{rep} are the phases of the transfer functions of Figure 4.6.

The frequency noise PSDs of the 1.56-µm comb line, of the CEO-beat and of the CEO-free beat (representing the repetition rate contribution to the frequency noise of the optical comb mode) in the free-running comb, measured as described in Section 4.5.3, are shown in Figure 4.13a. From these spectra, the sum of the complex coherences has been calculated according to Eq. (4.26) and is displayed in Figure 4.13b as a function of the Fourier frequency. We observe that the sum of the coherences remains nearly constant at a value of $\Gamma_\Delta(\omega) \approx -2$ in a wide frequency range of 10 Hz – 100 kHz. As $|\gamma_{xy}(\omega)| \leq 1$, this is only possible if the CEO and repetition rate fluctuations in the free-running optical frequency comb are 100% anti-correlated, which confirms the hypothesis made in Section 4.5.1. One should point out that this observation is not in contradiction with the frequency dependent comb fixed point that was introduced in Section 4.4.2. Here, the observed value of the coherence sum $\Gamma_\Delta(\omega)$ just tells us how the phases of the fluctuations of f_{CEO} and f_{rep} in the free-running comb are related to each other, but does not indicate anything about their relative amplitude. On the other hand, the frequency dependence of the comb fixed point that was shown in Figure 4.7 is only related to the varying rela-

tive amplitude of the transfer functions of f_{CEO} and f_{rep} for a given modulation, not to their phase. Therefore, a frequency-dependent fixed point may occur when the noise in f_{CEO} and f_{rep} is fully correlated. The existence of a quasi-fixed point instead of a fixed point is however due to the phase difference between the modulation of f_{CEO} and f_{rep}, $\varphi_{\mathrm{CEO}} - \varphi_{\mathrm{rep}} \neq k\pi$. In Figure 4.13b, the cosine of the phase difference $(\varphi_{\mathrm{CEO}} - \varphi_{\mathrm{rep}})$ obtained for pump power modulation was also plotted, for comparison with the coherence sum $\Gamma_{\Delta}(\omega)$ assessed from the PSDs. A good agreement between these two curves is observed up to ~10 kHz, even if $\Gamma_{\Delta}(\omega)$ becomes noisy below ~30 Hz. This is an indication that pump power fluctuation is the dominant source of noise in the comb, as already pointed out in other Er:fiber combs [65,74]. At higher Fourier frequencies, a discrepancy is observed between $\Gamma_{\Delta}(\omega)$ and $\cos\left\{\varphi_{\mathrm{CEO}}(\omega) - \varphi_{\mathrm{rep}}(\omega)\right\}$, which seems to indicate that pump fluctuation is no longer the dominant source of noise in the comb, but the anti-correlation between f_{CEO} and f_{rep} remains ($\Gamma_{\Delta}(\omega) \approx -2$).

In the general model described in Section 4.5.2, one still has to take into account the noise of the RF reference in the repetition rate stabilization loop. When doing so, we lose the information about the phase of the frequency deviations $\delta\tilde{f}_{\mathrm{rep}}(\omega)$ of the stabilized repetition rate (see Eq. (4.18)), which generally becomes uncorrelated with the CEO deviations $\delta\tilde{f}_{\mathrm{CEO}}(\omega)$ within the bandwidth of the repetition rate stabilization loop. For the determination of the residual frequency deviations of an optical comb line in the fully-stabilized comb ($\delta\tilde{\nu}_N(\omega)$), 100% anti-correlation between $\delta\tilde{f}_{\mathrm{rep}}(\omega)$ and $\delta\tilde{f}_{\mathrm{CEO}}(\omega)$ was nevertheless considered. This is justified by the following two facts:

i) At low Fourier frequency (below a couple of kilohertz), the contribution of the CEO residual noise to a comb line is much smaller than the contribution of the repetition rate $N \cdot \delta\tilde{f}_{\mathrm{rep}}(\omega)$ (see Figure 4.11), which is limited by the noise $\delta\tilde{f}_2^{\mathrm{ref}}(\omega)$ of the RF reference. Therefore, it does not matter if $\delta\tilde{f}_{\mathrm{CEO}}(\omega)$ and $N \cdot \delta\tilde{f}_{\mathrm{rep}}(\omega)$ are added here in quadrature or by considering a phase relation between these two quantities.

ii) At higher Fourier frequency, the noise of the RF reference no longer contributes to $\delta\tilde{f}_{\mathrm{rep}}(\omega)$ due to the limited bandwidth of the repetition rate stabilization loop with the PZT. As a consequence, the repetition rate noise is dominated by the CEO servo bump due to the servo-loops cou-

pling and it is thus highly correlated with $\delta\tilde{f}_{\mathrm{CEO}}(\omega)$. This was experimentally confirmed by determining the sum of the complex coherences $\Gamma_{\delta}(\omega) = \gamma_{\delta f_{\mathrm{CEO}}\, N\cdot\delta f_{\mathrm{rep}}} + \gamma_{N\cdot\delta f_{\mathrm{rep}}\, \delta f_{\mathrm{CEO}}}$ in the stabilized comb in a similar way as done in Eq. (4.26) and in Figure 4.13b for the free-running comb.

The frequency noise of the fully-stabilized comb was calculated in two different cases, with and without servo-loops coupling. Results are shown in Figure 4.14 for a comb line at 1.56 µm. The first case, with the servo-loops coupling taken into account, corresponds to the real behavior of the comb. The calculated spectrum is in good agreement with the frequency noise PSD experimentally measured from the heterodyne beat between the optical frequency comb and the ultra-stable laser. This confirms the assumptions about the correlation of the noise of f_{CEO} and f_{rep} in both the unstabilized and stabilized comb. In the second case, nullified coupling coefficients $(C_{jk}(\omega) = 0)$ were considered to simulate the hypothetical case where no coupling would be present between the two servo-loops. In that case, the calculated frequency noise PSD of the stabilized comb line is two orders of magnitude higher in a wide Fourier frequency range (100 Hz – 10 kHz) than in the presence of coupling. This result demonstrates the positive impact induced by the cross-influence between the CEO and the repetition rate servo-loops onto the frequency noise of an optical comb line.

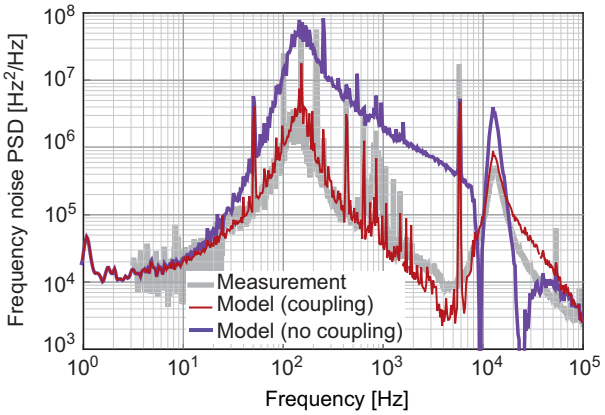

Figure 4.14: Frequency noise PSD of a comb line at 1.56 µm calculated from the model in presence and absence of coupling between the two servo-loops. The frequency noise spectrum experimentally measured for a 1.56-µm comb line from the heterodyne beat between the comb and an ultra-stable laser is also shown for comparison (thick grey curve). In order to overcome the limitation in the frequency noise of the free-running repetition rate used in the model that results from the instrumental noise floor (see Figure 4.9), the frequency noise PSD of f_{rep} was obtained from the CEO-free optical beat at 1.56 µm ($N \cdot f_{\mathrm{rep}}$ with $N \sim 770'000$) divided by N^2.

4.6.3 Noise suppression by the servo loop coupling at different wavelengths

The servo bump resulting from the CEO stabilization loop that appears in both the repetition rate and the CEO frequency noise spectra (see Figure 4.11) contributes with a 180° phase shift to the respective frequency deviations $\delta\tilde{f}_{\mathrm{rep}}(\omega)$ and $\delta\tilde{f}_{\mathrm{CEO}}(\omega)$ in the fully-stabilized comb. From the comb equation $\nu_N = f_{\mathrm{CEO}} + N \cdot f_{\mathrm{rep}}$, it is obvious that the frequency deviation $N \cdot \delta\tilde{f}_{\mathrm{rep}}(\omega)$ originating from the repetition rate increases with a raising comb mode number N, whereas the CEO contribution is constant for all comb lines. Hence, the frequency noise of a comb line increases with N for all Fourier frequencies below ~4 kHz where the CEO contribution is negligible. However, in a higher Fourier frequency range of 4-100 kHz, the anti-correlated repetition rate and CEO contributions tend to compensate each other and the frequency noise PSD of a comb line is given by $S_{\delta\nu_N\,\delta\nu_N} = S_{\delta f_{\mathrm{CEO}}\,\delta f_{\mathrm{CEO}}} + N^2 S_{\delta f_{\mathrm{rep}}\,\delta f_{\mathrm{rep}}} - 2N\sqrt{S_{\delta f_{\mathrm{CEO}}\,\delta f_{\mathrm{CEO}}} \cdot S_{\delta f_{\mathrm{rep}}\,\delta f_{\mathrm{rep}}}}$, where a full anti-correlation has been assumed here between f_{CEO} and f_{rep}, leading to the replacement of the sum of the complex coherences $\Gamma_\delta(\omega)$ by -2. This assumption was verified in the fully-stabilized comb by calculating the sum of the complex coherences $\Gamma_\delta(\omega)$ in the same way as done in Figure 4.13 for the free-running comb. An effective reduc-

tion of the frequency noise of a comb line is observed around 10 kHz Fourier frequency, resulting in a narrowing of the comb optical linewidth at a particular wavelength where the two contributions cancel each other. The model can be applied to calculate the frequency noise of a comb line at different wavelengths (i.e. for different mode number N) throughout the comb spectrum and thus to determine the wavelength at which the noise is minimized. Figure 4.15 shows the frequency noise PSD calculated by this approach for various comb modes at different wavelengths. The strong reduction of the CEO servo bump at ~10 kHz that occurs for long wavelength modes as a result of the servo-loops coupling is clearly visible. On the opposite, the low-frequency part of the spectra is affected only marginally by the mode index N. At $\lambda \approx 2.1$ µm, the CEO servo bump cancels out from the comb line spectrum.

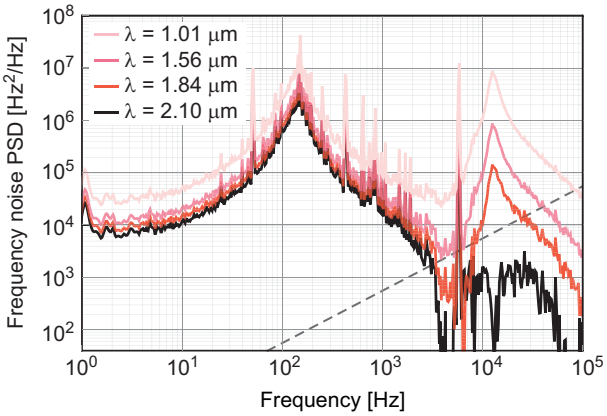

Figure 4.15: Frequency noise PSD of a comb line calculated at various wavelengths throughout the comb spectrum. The dashed line represents the β-separation line that is relevant for the determination of the comb linewidth (see Section 2.3).

Based on the calculated frequency noise spectra at various wavelengths (Figure 4.15), the corresponding comb linewidth (FWHM) was determined using the simple approximation presented in Section 2.3 (Eqs. (2.13) and (2.14)) for each spectrum, i.e. at each different wavelength. Following this approach, the linewidth is simply calculated from the surface A of the slow modulation area for which the frequency noise PSD exceeds the β-separation line, defined as $S_\beta(\omega) = (8 \ln 2/\pi^2) \cdot (\omega/2\pi)$ and displayed as a dashed line in Figure 4.15. One notices that at a wavelength around 2.1 µm, the frequency noise contributes to the linewidth for Fourier frequencies up to ~5 kHz only, due to the disappearance of the ~10 kHz CEO servo bump. At

shorter wavelengths, this servo bump exceeds the β-separation line and contributes to the linewidth, which increases. Figure 4.16 shows the evolution of the calculated linewidth across the comb spectrum, with a minimum value of ~50 kHz achieved at $\lambda = 2.1$ µm. At $\lambda = 1.5$ µm, the linewidth is more than three times broader. As an outcome of this work, the noise properties of the comb can be predicted across its entire spectrum.

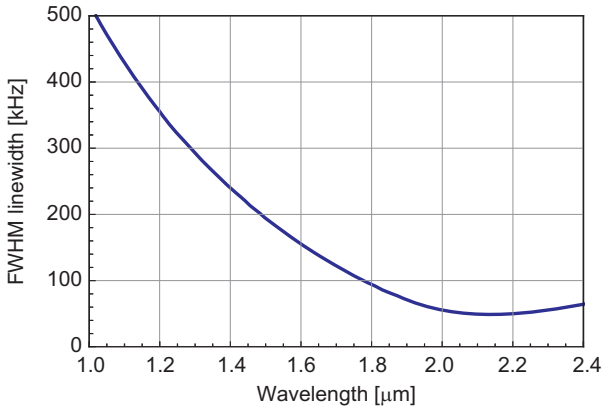

Figure 4.16: Calculated evolution of the comb mode linewidth (FWHM) as a function of wavelength.

4.7 Conclusion

In order to study the coupled influence of the repetition rate and CEO servo-loops in an Er:fiber comb, the comb dynamic response to a given perturbation, either pump power or cavity length variations, was first measured. The experimental data led one to introduce two modifications to the elastic tape model originally described by H. Telle and co-workers [59]. Firstly, it was shown that a fixed point does not always exist for a given source of perturbation and this notion has to be replaced by a quasi-fixed point at which the noise of the comb optical line is minimized but is not zero, due to the incomplete correlation between the fluctuations of f_{CEO} and f_{rep} arising from a phase shift $\varphi_{\mathrm{CEO}} - \varphi_{\mathrm{rep}} \neq k\pi$ in the dynamic responses of f_{CEO} and f_{rep}. Secondly, it was shown that the quasi-fixed point is not unique for a given source of perturbation, but varies with the Fourier frequency of the perturbation instead. All these experimental evidences led one to extend the former concept of the comb fixed point to a frequency-dependent quasi-fixed point. For cavity length fluctuations, the quasi-fixed point varies by more than one order of magni-

tude from DC ($N_{\text{fix}}^{\text{PZT}} \approx 2'600$) to 200 Hz Fourier frequency ($N_{\text{q-fix}}^{\text{PZT}} \approx 200$). The frequency dependence of the quasi-fixed point for pump current modulation is also significant, showing an important increase from $N_{\text{q-fix}}^{\text{pump}} \approx 6.4 \cdot 10^4$ at $\omega/2\pi \approx 0.1$ Hz to $N_{\text{q-fix}}^{\text{pump}} \approx 4 \cdot 10^5$ at $\omega/2\pi \approx 5$ Hz, followed by a weaker frequency dependence from ~5 Hz up to ~20 kHz.

Whereas the quasi-fixed point results from the noise correlation between the CEO and repetition rate in the free-running comb, the influence of this correlation was also studied in the fully-stabilized comb. This correlation leads to a coupling between the two servo-loops used to phase-lock the repetition rate and the CEO frequency to a common RF reference using feedback to the cavity length (via a PZT) and to the pump power, respectively. It was experimentally observed that the repetition rate loop (via the PZT) does not induce any noticeable effect to the CEO stabilization. On the opposite, a significant coupling of the CEO loop (via the pump diode current) to the repetition rate stabilization is observed, leading to a 10-fold reduction of the frequency noise PSD of the repetition rate over a wide range of Fourier frequencies (100 Hz – 10 kHz) compared to the case where no coupling would occur. A theoretical model was developed to quantify the impact of the servo-loops coupling on the comb frequency noise. The model has been validated by experimental data obtained through an extensive characterization of the frequency noise properties of the comb, measured for the CEO-beat f_{CEO}, the repetition rate f_{rep}, the repetition rate contribution to an optical comb line $N \cdot f_{\text{rep}} = \nu_N - f_{\text{CEO}}$ and for a comb line ν_N at 1557 nm. This model enabled the frequency noise PSD of an optical comb line at 1557 nm to be predicted in presence and in absence of coupling between the servo-loops. The results of this modeling show a reduction of the frequency noise of the comb line by almost two orders of magnitude in terms of PSD in a wide frequency range due to the beneficial influence of the CEO stabilization, via feedback to the pump diode current, onto the noise of the repetition rate. This is a consequence of the fact that the comb noise results primarily from pump power noise, which leads to a strong correlation between the noise of the repetition rate and of the CEO-beat. Therefore, reducing the noise of one of the comb parameters with a feedback loop should also affect the second parameter due to the cross-influence. In the present experiment no effect of the repetition rate stabilization is observed onto the CEO because of the limited feedback bandwidth (around 150 Hz)

and of the much smaller frequency noise present in the repetition rate as compared to the CEO-beat (which makes the corrections induced to the CEO insignificant). On the opposite, the CEO loop has a significant effect onto the repetition rate because of the large correction signal applied to the pump current (which results from the high noise present in the free-running CEO-beat and from the much larger bandwidth of the CEO feedback loop, on the order of 12 kHz).

In addition, the model also predicted a significant reduction of the comb mode linewidth at 2.1 µm wavelength as a result of the coupling between the CEO and the repetition rate servo loops with a minimum FWHM value of ~50 kHz at $\lambda = 2.1$ µm compared to ~170 kHz at $\lambda = 1.56$ µm.

Finally, the model reported here can be extended with minor adaptations to the case of ultra-stable microwave generation, when the comb is locked to an optical reference and used as an optical-to-microwave frequency divider [75]. In such a case, the repetition rate stabilization loop can be slightly modified to account for the stabilization of one comb line to an optical reference (ultra-stable laser) instead of directly stabilizing the repetition rate to an RF reference. The impact of the CEO stabilization on the phase noise PSD of the microwave signal generated using the Er:fiber comb will be discussed in Section 6.6.4.

Chapter 5

Full stabilization and characterization of a novel 1.5-μm DPSSL comb

5.1 Introduction

Er:fiber combs discussed in Chapter 4 is a well-established technology, used for instance for the dissemination of ultra-stable frequency references through stabilized fiber link [55] or for ultra-stable microwave generation [76]. The main advantages of fiber combs are their diode-pumping, their moderate cost and their reliability. The main drawbacks of fiber combs in comparison to Ti:Sa combs is their significantly higher frequency noise and broader optical comb lines resulting from their high gain, low Q-factor cavity and strong fiber nonlinearities. Significant improvements have been realized in the past years, in particular through the achievement of sub-Hz CEO linewidth [74,77-80]. However noise suppression in fiber lasers remains more challenging and generally requires a wide feedback bandwidth in the 100-kHz range [78]. Notable exceptions are the Er:fiber comb developed at NIST operating with a reduced bandwidth of ~25 kHz [76] and the multi-branch Er:fiber comb of Y. Nakajima *et al.* that achieved a CEO-beat linewidth of 10-30 kHz in free-running conditions [79].

A promising alternative to fiber-lasers are semiconductor saturable absorber mirror (SESAM)-modelocked DPSSLs [81,82]. DPSSLs have low intrinsic noise ow-

ing to their high-Q cavities with low residual losses and can access substantially higher average power levels than unamplified femtosecond fiber oscillators [83]. Repetition rates larger than 100 GHz have already been achieved in fundamental modelocking in the picosecond pulse width regime [84,85] and more recently larger than 1 GHz in the femtosecond regime [86,87].

A novel technology of DPSSL emitting in the same 1.5-µm spectral range as Er:fiber combs is reported in this chapter. This comb technology, based on the same gain medium as Er:fiber laser, i.e. erbium ions, but embedded in a thin glass matrix located in a high-Q free-space optical cavity, presents nice noise properties in comparison to Er:fiber combs. A SESAM [82], which is composed of a distributed Bragg reflector and an absorber layer on top, is used in this DPSSL comb to initiate the modelocking process. The noise properties of this Er:Yb:glass oscillator, that is referred to as ERGO, are presented in this chapter in comparison with the commercial Er:fiber comb previously described in Chapter 4.

This chapter is organized as follows. The ERGO laser oscillator is presented in Section 5.2. The control of the comb, along with the static and dynamic response with the corresponding quasi-fixed point concept introduced in Section 4.4.2 are reported in Section 0. The noise properties of the CEO and of an optical mode of the ERGO comb are investigated in comparison to the Er:fiber comb in Section 0.

5.2 Er:Yb:glass oscillator based ultrafast laser

The ERGO comb (Figure 5.1) was developed in the Ultrafast Laser Physics laboratory in ETH Zurich in the frame of a national collaboration and was then permanently moved to Neuchâtel. It is based on a passively modelocked femtosecond Er:Yb:glass laser oscillator emitting a ~15-nm wide spectrum (FWHM) centered at 1558 nm. It achieves sub-200 fs transform-limited pulses with more than 100 mW average output power at a repetition rate of $f_{\mathrm{rep}} = 75$ MHz [88]. The active medium is made of a 2-mm thick Brewster-angled phosphate glass plate (Kigre ER/QX) with Erbium (Er^{3+}) and Ytterbium (Yb^{3+}) doping densities of $1.5 \cdot 10^{20}$ cm^{-3} and $1.9 \cdot 10^{21}$ cm^{-3}, respectively, pumped by a 600-mW fiber-coupled telecom-grade laser diode emitting at 976 nm. The gain is provided by the Er^{3+} ions, which constitute a three-level system with an upper state lifetime of 7.9 ms [89]. Yb^{3+} co-doping is used for efficient absorption of the pump power

through the strong Yb^{3+} absorption band at 976 nm, associated with the efficient resonant energy transfer from the Ytterbium ions to the Erbium ions [90]. Due to the much higher Yb^{3+} concentration, pumping essentially occurs through Yb and direct Er pumping is marginal. The 2-m long resonator contains 10 dispersive GTI (Gires-Tournois interferometer) dielectric mirrors with a total negative dispersion of -2000 fs^2 per cavity round-trip and an output coupler with 1.7% transmission. A significant advantage is the direct pumping by a 600-mW fiber-coupled telecom-grade laser diode at 976 nm for reliable and efficient laser operation, and the SESAM for stable and self-starting soliton modelocking [91]. The SESAM is mounted on a PZT and on a stepper-motor for fine and coarse adjustment of the cavity length, respectively. The total round-trip losses of the cavity are well below 3%, which leads to a substantially higher Q-factor and a significantly lower quantum noise limit as compared to typical fiber lasers [92]. The duration of the pulses, determined by the amount of negative dispersion and self-phase modulation, can be adjusted with the pump power and this property is used to control the CEO frequency as discussed in Section 0. The spectrum is subsequently broadened to one octave for CEO generation in a 1.5-m long, dispersion-flattened, polarization-maintaining, highly nonlinear fiber (PM-HNLF) without any prior amplification or pulse compression. The CEO-beat is detected in a standard f-to-2f interferometer (see Section 4.2.2).

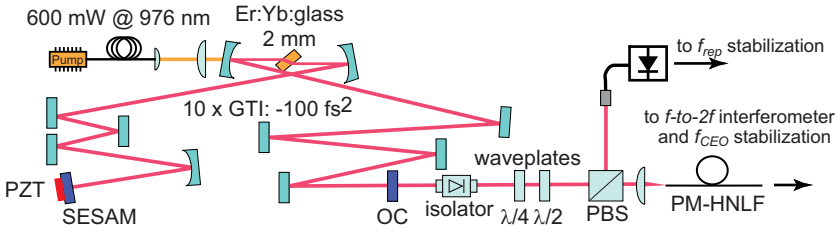

Figure 5.1: Schematic of the diode-pumped Er:Yb:glass laser oscillator (ERGO). SESAM: semiconductor saturable absorber mirror; GTI: highly reflective Gires-Tournois interferometer type mirror, dispersion -100 fs^2; OC: output coupler; PBS: polarization beamsplitter cube; PM-HNLF: polarization-maintaining highly non-linear fiber. The laser output passes through an isolator for protection against optical feedbacks and waveplates for polarization control.

5.3 Comb control

Full control and stabilization of the frequency comb requires two independent actuators to adjust the repetition rate f_{rep} and the CEO frequency f_{CEO} as it has been discussed in Section 4.2.1. Once these parameters are stabilized to a proper frequency reference, the frequency of any comb line is determined, given by the well-known comb equation

$$\nu_N = N \cdot f_{\text{rep}} - f_{\text{CEO}} \tag{5.1}$$

where the large integer number N is the comb mode index. A negative sign is considered in Eq. (5.1) for convenience, in order that f_{CEO} corresponds to the smallest positive frequency signal observed in the RF spectrum at the output of the f-to-$2f$ interferometer (i.e. $0 < f_{\text{CEO}} < f_{\text{rep}}/2$). The offset frequency f_{CEO} represents the shift of the comb from the origin as the mode index N is extrapolated towards zero, according to the standard comb representation in the frequency domain (see Eq. (4.4) in Section 4.2.1). It corresponds to a down-shifted value of the GPO frequency f_{GPO} [49] that results from the pulse-to-pulse change in the carrier-envelope offset phase $\Delta\phi_{\text{CEO}}$ [60]:

$$f_{\text{GPO}} = f_{\text{rep}}\, \Delta\phi_{\text{CEO}}/2\pi \tag{5.2}$$

Physically, the GPO frequency f_{GPO} results from a difference between the group and phase velocity in the laser resonator and is related to the phase evolution of the electrical field of the light pulse with respect to the pulse envelope [56]. f_{GPO} usually is in an inaccessible frequency range of ~1-3 THz in an Er:fiber laser [56,60,68], so that the down-shifted value $f_{\text{CEO}} = f_{\text{GPO}} \pm k f_{\text{rep}}$ is generally considered and is referred to as the CEO frequency [49]. The sign of the CEO-beat in the ERGO comb has been unambiguously determined by observing the displacement of the beat frequency between one comb line and the 1.56-µm cavity-stabilized ultra-narrow linewidth laser described in Section 3.6 when f_{rep} and f_{CEO} were successively scanned. The result of this measurement led us to adopt the sign convention of Eq. (5.1).

5.3.1 Static control

The comb repetition rate directly scales with the inverse of the resonator length, so that it can be straightforwardly adjusted by tuning the cavity length. The control of the cavity length is implemented in the ERGO laser with a stepper-

motor for coarse tuning and a PZT for fine adjustment, both devices acting on the position of the SESAM in the resonator. The PZT is connected to the output of a high-voltage amplifier (0-150 V), which is driven by an input control voltage u_{PZT} (0-10 V). Figure 5.2a illustrates the effect of the PZT control voltage on the 75-MHz laser repetition rate, measured using an electrical spectrum analyzer when changing the cavity length step-by-step (static tuning coefficient). A large, linear and precise control of the repetition rate can be achieved with the PZT, with a tuning coefficient $\partial f_{\mathrm{rep}}/\partial u_{\mathrm{PZT}}$ around 30 Hz/V. Besides its direct effect on the repetition rate, a change of the cavity length has also a coupled effect on the 20-MHz CEO frequency, as illustrated in Figure 5.2b, with a tuning coefficient that is four orders of magnitude larger ($\partial f_{\mathrm{CEO}}/\partial u_{\mathrm{PZT}} \approx 3 \cdot 10^5$ Hz/V).

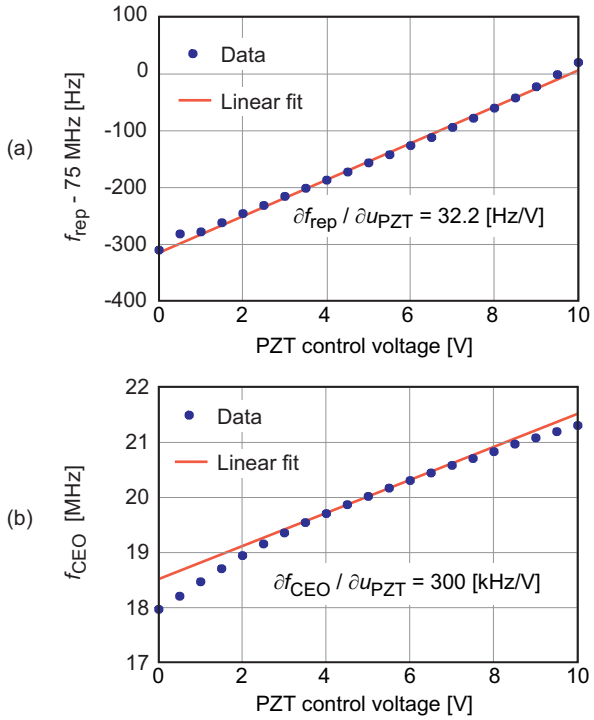

Figure 5.2: Tuning of the 75-MHz repetition rate (a) and of the 20-MHz CEO frequency (b) as a function of the input voltage of the PZT controlling the cavity length. The repetition rate and the CEO frequency were measured using an electrical spectrum analyzer. The local tuning coefficients (around 75 MHz for f_{rep} and 20 MHz for f_{CEO}) are determined from a linear fit (straight lines).

Different reasons may explain the origin of the dependence of the CEO frequency f_{CEO} on the cavity length. A first contribution arises from the fact that f_{GPO}

is the product of $\Delta\phi_{\mathrm{CEO}}$ and f_{rep}, according to Eq. (5.2). Therefore, the GPO frequency critically depends on f_{rep} and so does the CEO frequency [67], which thus directly scales with the inverse of the cavity length. Furthermore, the carrier-envelope phase $\Delta\phi_{\mathrm{CEO}}$ can change due to a shift in the pulse envelope arrival time or due to a shift in the carrier phase [60], so that the CEO frequency depends on the difference between phase and group velocities in the resonator [68]. Changing the cavity length with the PZT should only change a tiny portion of the cavity length in air if one neglects other side effects such as a change in the intra-cavity beam diameter. Because of the very small dispersion and nonlinearities of air, it is believed that the air length change should have a minor impact on the CEO phase and thus on the CEO frequency [57]. However, this reasoning is valid for the group-phase offset frequency f_{GPO} only. This means that the static fixed point of the comb introduced in Section 4.4.2 for a variation of the cavity length should correspond to f_{GPO}. Considering the down-converted value f_{CEO}, the effect of the large frequency shift between f_{CEO} and f_{GPO} ($\pm k \cdot f_{\mathrm{rep}}$ in Eq. (5.2)) can induce a significant dependence of f_{CEO} with respect to the cavity length. The comb fixed point for cavity length change can also be determined from the ratio of the tuning coefficients of f_{CEO} and f_{rep} for PZT modulation: $N_{\mathrm{fix}}^{\mathrm{PZT}} = (\partial f_{\mathrm{CEO}}/\partial u_{\mathrm{PZT}})/(\partial f_{\mathrm{rep}}/\partial u_{\mathrm{PZT}})$, which is in the order of 10'000 in the ERGO comb. This leads to a fixed point of ~0.75 THz, which is very close to the value of 0.7 THz previously obtained for the Er:fiber laser in Section 4.4.2.

Finally, one should point out that the effect of a variation of the cavity length on the frequency of an optical comb line is strongly dominated by the contribution of the repetition rate compared to the CEO contribution, due to the large mode index ($N \approx 2.5 \cdot 10^6$ at $\lambda = 1.55$ µm) that multiplies f_{rep}.

As f_{CEO} depends on the difference between phase velocity and group velocity in the resonator, it is affected by optical nonlinearities. Almost every component in the optical resonator affects the group-phase velocity offset, either directly or indirectly, and thus modifies f_{CEO} [93]. For instance, moving any mechanical component in the cavity (flat or spherical mirror, SESAM, gain position or tilt angle, pump beam collimator, etc.) slightly affects the pulses and their overlap with the pump beam, leading to a change in the group velocity. These intra-cavity components can thus be used for coarse adjustment of the CEO-beat in order to tune it into a frequency range where it can be more precisely adjusted by the pump power. Indeed,

the pump power has a direct influence on the pulse parameters, such as pulse duration and energy, which directly translates into a change of f_{CEO}. Therefore, the current of the pump laser can be used for fine tuning and stabilization of f_{CEO}, which is the standard stabilization method for diode-pumped femtosecond lasers [56]. The dependence of f_{CEO} on the pump power may be nonlinear and even non-monotonous as observed in Ti:Sa combs [94]. For this reason, an initial coarse adjustment is usually done with an intra-cavity element. In a next step, the local dependence of f_{CEO} with the pump power is used for precise control and stabilization. In Figure 5.3a, the dependence of f_{CEO} on the pump current in the ERGO laser is shown. A tuning coefficient in the range of $\partial f_{\mathrm{CEO}}/\partial i_{\mathrm{pump}} \approx -100$ kHz/mA is achieved around 20 MHz (frequency at which f_{CEO} is stabilized in the ERGO comb, see Section 5.4.1), but this value can be changed by a significant amount and its sign can even be reversed, depending on the resonator configuration (precise adjustment of the intra-cavity elements).

In addition to its effect on f_{CEO}, the pump power also affects the repetition rate (Figure 5.3b) due to the resulting change in the resonator optical path length (combination of thermal and Kerr lensing as well as a slight red-shift of the center wavelength at higher pump power due to the inversion dependent gain profile). The tuning coefficient is about one million times smaller ($\partial f_{\mathrm{rep}}/\partial i_{\mathrm{pump}} \approx -100$ mHz/mA). However, this small tuning factor is not negligible considering the effect of the pump current on an optical comb line. Due to the large scaling of the repetition rate by the mode index $N \approx 2.5 \cdot 10^6$, both the change of the CEO and the repetition rate for a variation of the pump current introduce similar contributions to the tuning of an optical comb line.

The cavity PZT and the pump laser current are used as two actuators for the full stabilization of the ERGO comb. More precisely, the cavity PZT is used for the stabilization of the repetition rate and the pump laser current for the stabilization of the CEO frequency, as discussed in the next sections.

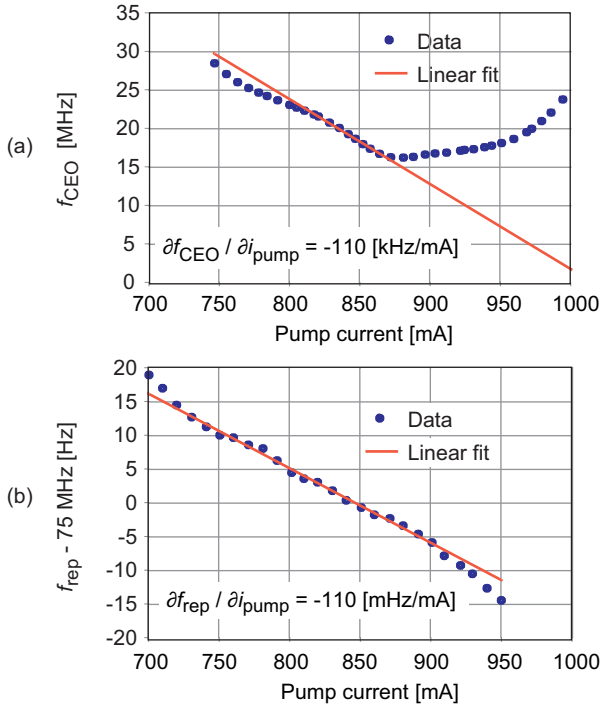

Figure 5.3: Tuning of the 20-MHz CEO frequency (a) and of the 75-MHz repetition rate (b) as a function of the pump laser current. The repetition rate and the CEO frequency were measured using an electrical spectrum analyzer. The local tuning coefficients (around 20 MHz for f_{CEO} and 75 MHz for f_{rep}) are determined from a linear fit (straight lines).

5.3.2 Dynamic control

The experimental results shown in Section 5.3.1 (Figure 5.2 and Figure 5.3) were obtained in static conditions, i.e. the cavity length and the pump current were changed step by step. More interesting is to look at the dynamic response of the CEO and repetition rate for pump power and cavity length modulation as was done in Section 4.4.1 in the case of the Er:fiber comb. These measurements were performed in a similar way as for the Er:fiber comb by modulating the cavity length (via the PZT input voltage) or the pump laser current, respectively, with a sine waveform and by detecting the changes in f_{rep} and f_{CEO} using the PLL frequency discriminator described in Section 2.4.1. In this PLL, the VCO operates in the range f_{VCO} = 203-210 MHz, but signals at a different frequency f_{signal} may be analyzed after frequency conversion (by mixing with a reference signal at $f_{VCO} \pm f_{signal}$ and proper filtering). For instance, transfer functions of the CEO were measured by mixing the 20-MHz CEO-beat with a reference signal at 225 MHz, and the 205-MHz difference

frequency signal was analyzed with the PLL frequency discriminator. The output signal of the discriminator (i.e. the control voltage of the VCO) is proportional to the frequency fluctuations of the input signal and was subsequently analyzed with a lock-in amplifier to extract the component at the modulation frequency. Knowing the sensitivity of the frequency discriminator (in V/Hz) allowed us to convert the measured lock-in voltage into frequency fluctuations. The frequency discriminator has a sensitivity of 0.7 V/MHz and a bandwidth of about 200 kHz (see Section 0).

The CEO dynamic response obtained for cavity length (PZT) modulation and pump laser modulation is shown in Figure 5.4 and Figure 5.6, respectively. Similar measurements are also shown in the same figures for the repetition rate. Due to the tiny variation of the repetition rate with the modulation signal (cavity length or pump current) compared to the corresponding effect on the CEO, the detection has been performed at a high harmonic of the repetition rate in order to enlarge the frequency modulation depth to be detected by the frequency discriminator. For this purpose, the 20^{th} harmonic of f_{rep} ($20\times f_{\text{rep}} = 1.5$ GHz) has been detected using a fast photodiode (New-Focus 1434, 25 GHz bandwidth) and mixed with a reference signal at 1.705 GHz to produce the 205-MHz signal that was analyzed with the PLL frequency discriminator. The analyzed signal thus contains 20 times the frequency variations of f_{rep}, and the repetition rate transfer function was obtained by dividing the measured curve by this scaling factor.

5.3.2-1 Cavity length modulation

The dynamic responses of f_{CEO} and f_{rep} to cavity length modulation are very similar as displayed in Figure 5.4. Both curves show a low-pass filter behavior with 2 to 3 kHz bandwidth (at −3 dB), mainly due to the PZT bandwidth. However, at higher Fourier frequencies a significant phase difference is observed. The CEO and repetition rate tuning coefficients measured at low modulation frequency ($\omega/2\pi < 10$ Hz) correspond very well to the static values extracted from Figure 5.2 and Figure 5.3 and obtained in the same resonator configuration.

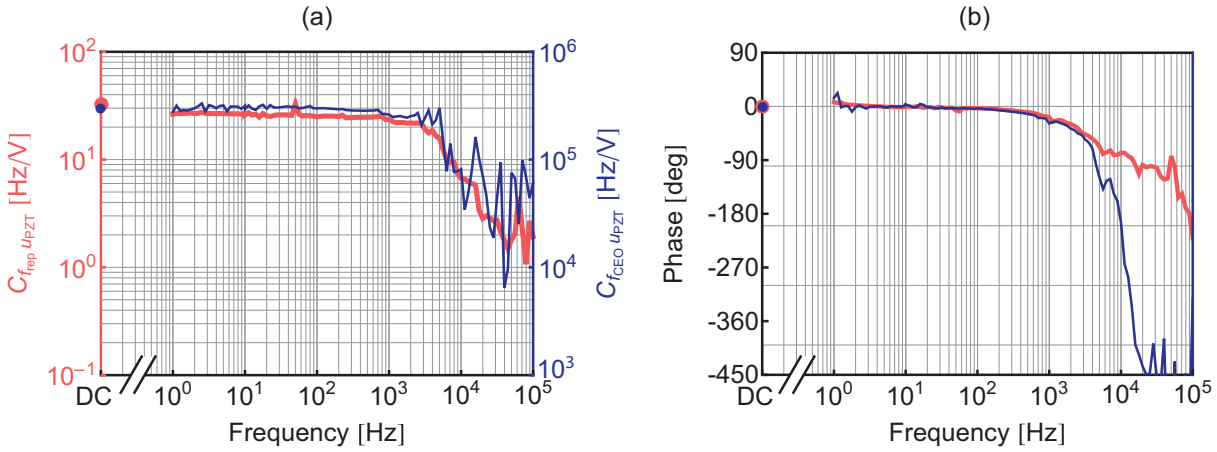

Figure 5.4: Transfer functions in (a) amplitude and (b) phase of f_{CEO} (light (red) thick curve, right vertical axis) and f_{rep} (dark (blue) thin curve, left vertical axis) in the ERGO comb for cavity length modulation, applied through a modulation of the PZT drive voltage. The points on the left vertical axes represent the DC values separately obtained from a static measurement.

In an optical frequency comb, fluctuations of the repetition rate and CEO induced by a specific type of intra-cavity perturbation are usually correlated [57,58], as the noise source affects both f_{CEO} and f_{rep}. The comb mode for which the resulting noise at each modulation frequency is minimized according to the quasi-fixed point concept introduced in Section 4.4.2 is determined from the dynamic measurements. Depending on the magnitude and phase of the transfer functions, the quasi-fixed point (and the corresponding quasi-fixed frequency $\nu_{\text{q-fix}} = N_{\text{q-fix}} \cdot f_{\mathrm{rep}} - f_{\mathrm{CEO}}$) may be within the comb optical spectrum or out of it.

Figure 5.5 shows the comb quasi-fixed point as a function of the cavity length modulation frequency. In that case, a constant fixed point $N^{\mathrm{PZT}}_{\text{q-fix}} \approx 11'000$ is obtained for any Fourier frequency up to 3 kHz. At higher Fourier frequency, the determined fixed point becomes noisier due to additional noise occurring in the measured CEO transfer function. This quasi-fixed point corresponds to a frequency $\nu^{\mathrm{PZT}}_{\text{q-fix}} \approx 0.75$ THz, which is similar to the static fixed frequency of 0.7 THz obtained for the Er:fiber comb in Section 4.4.2. For the comparison, the measured frequency distribution of the quasi-fixed point in our Er:fiber comb presented in Section 4.4.2 is also shown in the same graph.

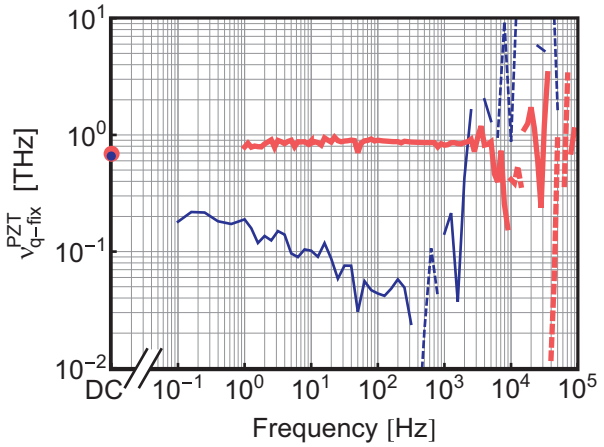

Figure 5.5: Frequency-dependent quasi-fixed frequency for cavity length modulation in (a) the ERGO (light (red) thick curve) and (b) the Er:fiber (dark (blue) thin curve) combs. The circles correspond to the fixed point values determined from the CEO and repetition rate static responses to the change of the cavity length in the ERGO comb (red tiny circle) and in the Er:fiber comb (blue large circle, data from Section 4.4.2). The solid curve corresponds to positive values of $\nu^{PZT}_{q\text{-fix}}$ and the dashed curve to negative values of $\nu^{PZT}_{q\text{-fix}}$.

5.3.2-2 Pump power modulation

Similar CEO and repetition rate transfer functions have been measured for pump power modulation. The injection current of the pump laser was modulated via a voltage applied to the laser driver (with 100 mA/V conversion factor and 100 kHz bandwidth) and the frequency modulation induced on f_{CEO} and f_{rep} was measured as before using the PLL frequency discriminator. Due to the tiny effect of the pump modulation to the repetition rate, the measurement was performed at the 20th harmonic of the repetition rate as before ($20\times f_{rep} = 1.5$ GHz). In addition to the analyzed change in the repetition rate frequency (FM signal), pump laser modulation also induces a modulation of the modelocked laser optical power and thus an AM of both repetition rate and CEO beat signals. Due to the potential sensitivity of the PLL frequency discriminator to AM (see Section 0), great care was taken all along the experiment to measure the true FM response of f_{CEO} and f_{rep} without being affected by residual AM effects. This was especially critical in the case of f_{rep} as the FM signal amplitude to be measured is orders of magnitude smaller than for f_{CEO} and is thus more prone to AM-induced artifacts. The dynamic responses of f_{CEO} and f_{rep} to pump laser modulation are shown in Figure 5.6.

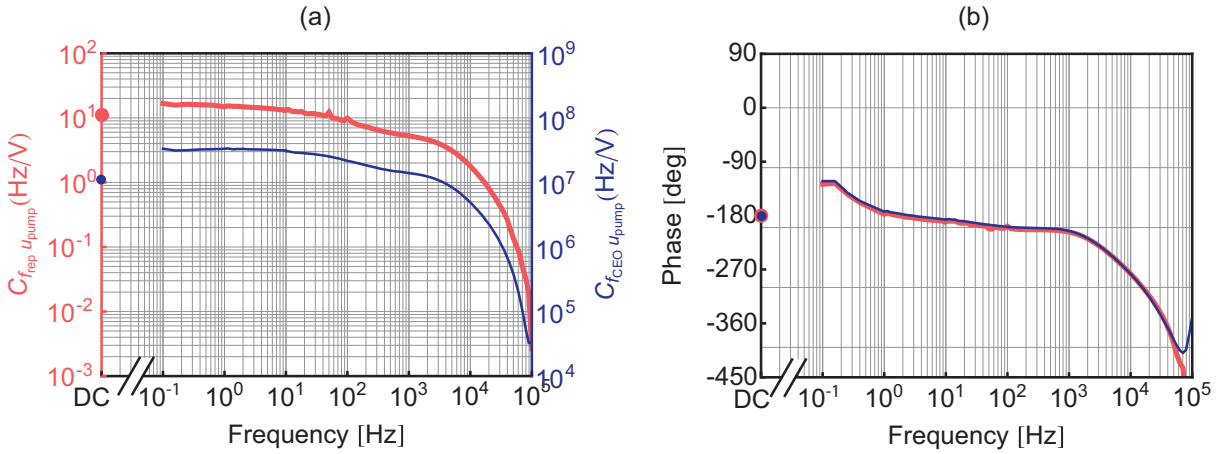

Figure 5.6: Transfer functions in (a) amplitude and (b) phase of f_{CEO} (light (red) thick curve, right vertical axis) and f_{rep} (dark (blue) thin curve, left vertical axis) in the ERGO comb for cavity length modulation, applied through a modulation of the pump laser drive voltage. The points on the left vertical axes represent the DC values separately obtained from a static measurement.

A similar bandwidth is achieved for f_{CEO} and f_{rep}, in the order of a few kilohertz, limited by the response bandwidth of the Er^{3+} gain medium coupled with the laser dynamics [60]. At low frequency, the behaviour slightly differs from a first-order low-pass filter by the presence of a small slope in the frequency response between 10 Hz and 1 kHz. One should notice that the amplitude of the response of f_{CEO} and f_{rep} to pump laser modulation depends on the precise configuration of the optical resonator. As a result, some changes (by up to a factor 3 in the low-frequency tuning coefficient $\partial f_{\mathrm{CEO}}/\partial i_{\mathrm{pump}}$ or $\partial f_{\mathrm{rep}}/\partial i_{\mathrm{pump}}$) have been observed between different measurements performed after slight re-adjustments of the resonator. This might explain the small difference observed between the static and dynamic response values. Also the shape of the transfer function (in the low frequency range, $\omega/2\pi < 300$ Hz) can be slightly different and was sometimes observed to be flatter. However, the bandwidth of the CEO and repetition rate frequency response is not affected by small resonator changes. In order to avoid any undesired influence of the resonator configuration in this experiment, great care was taken to successively perform the measurements of f_{CEO} and f_{rep} in the same resonator configuration and the reproducibility of the measurements was carefully checked.

As an additional verification of the measured dynamic response of f_{rep}, which is potentially the most susceptible to AM-induced artifacts, the transfer function of an

optical comb line was also measured with respect to pump laser modulation. This was realized by heterodyning the free-running comb with a 1.56-µm cavity-stabilized ultra-narrow-linewidth laser and by analyzing the laser-comb beat note (f_{beat}) with the PLL frequency discriminator. In order to distinguish between the contribution of the repetition rate and of the CEO in the heterodyne beat, the CEO was first subtracted from the analyzed signal. This was performed by frequency-mixing the 10-MHz heterodyne beat with the 20-MHz CEO and subsequently band-pass filtering the CEO-free component at 30 MHz ($f_{\text{CEO}} - f_{\text{beat}}$), which was input in the PLL discriminator. With this proper choice of sign, the analyzed CEO-free beat should contain N times the frequency modulation of the repetition rate. Due to this huge enhancement of the FM amplitude compared to the measurement of f_{rep}, no AM issue is encountered in this measurement.

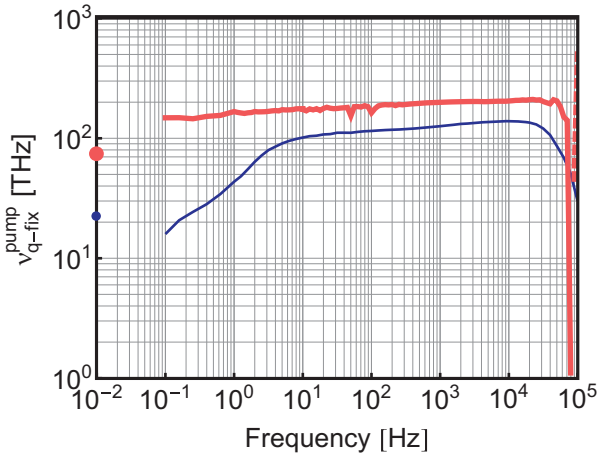

Figure 5.7: Frequency-dependent quasi-fixed frequency for pump laser modulation in (a) the ERGO (light (red) thick curve) and (b) Er:fiber (dark (blue) thin curve) combs. The circles correspond to the fixed point values determined from the CEO and repetition rate static responses to the change of the cavity length in the ERGO comb (red tiny circle and in the Er:fiber comb (blue large circle, data from Section 4.4.2). The solid curve corresponds to positive values of $\nu^{\text{pump}}_{\text{q-fix}}$ and the dashed curve to negative values of $\nu^{\text{pump}}_{\text{q-fix}}$.

The small qualitative difference between the frequency response of f_{rep} and f_{CEO} translates into a quasi-fixed point that slightly depends on the Fourier frequency of the pump power fluctuations, as displayed in Figure 5.7. In the reported configuration, the quasi-fixed point increases from $N^{\text{pump}}_{\text{q-fix}} \approx 2 \cdot 10^6$ at $\omega/2\pi \approx 1$ kHz to $N^{\text{pump}}_{\text{q-fix}} \approx 3 \cdot 10^6$ at $\omega/2\pi \approx 30$ kHz, which corresponds to a quasi-fixed frequency

ranging from 150 THz ($\lambda = 2$ µm) to 225 THz ($\lambda = 1.3$ µm). The quasi-fixed frequency is located close to the femtosecond laser carrier (192 THz) at Fourier frequencies of a few hundreds of hertz, but is shifted towards lower (higher) optical frequencies for pump laser fluctuations at lower (higher) Fourier frequencies. In comparison to the quasi-fixed frequency measured in the Er:fiber comb reported in the same graph (for details see Section 4.4.2), the quasi-fixed frequency is situated much closer to the carrier and varies in a smaller range (Figure 5.7).

5.4 Comb noise properties

5.4.1 Carrier-envelope offset

Figure 5.8 schematizes the CEO stabilization loop. A commercial locking electronics (Menlosystems XPS800-E) is used to phase-stabilize the CEO-beat to a 20-MHz external reference (frequency-doubled 10-MHz signal from an H-maser). Phase fluctuations between the CEO-beat and the reference signal are detected with a digital phase detector (DXD200 from Menlosystems, see Section 2.4.4) with a large, linear detection range of $\pm 32 \times 2\pi$ phase difference. The wide dynamic range of this phase detector can track large phase fluctuations of much more than 2π, which makes the system stable in cycle-slip-free operation against large and sudden external perturbations. The error signal is forwarded to a PI servo-controller (Menlo PIC201) that drives the pump laser current source.

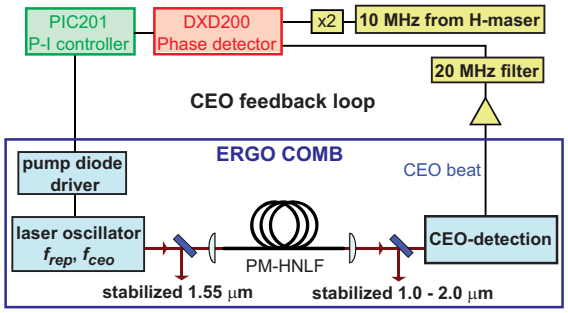

Figure 5.8: Scheme of the CEO stabilization loop, including a frequency-doubled 10-MHz reference from an H-maser, a digital phase detector, a PI servo-controller and feedback to the pump laser current.

The overall loop transfer function (amplitude and phase), obtained from the experimentally measured transfer functions for each loop component (phase detector, PI servo, and pump laser driver), is shown in Figure 5.9. From this transfer

function, one observes that the feedback bandwidth is only 5.5 kHz, mainly limited by the dynamics of the Er gain medium in the femtosecond laser [60]. At the 5.5-kHz unity gain, the phase margin is ~15°.

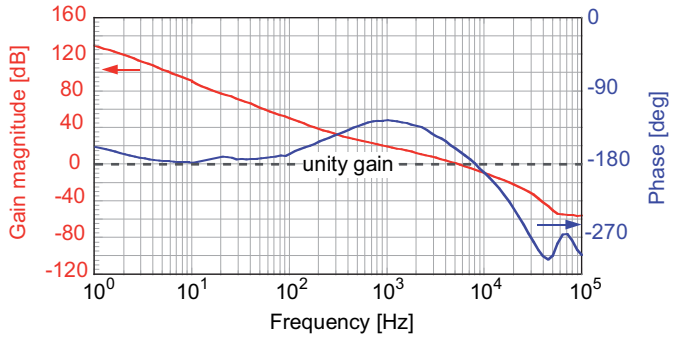

Figure 5.9: Overall transfer function (gain on the left scale and phase on the right scale) of the CEO stabilization loop.

5.4.1-1 Frequency noise PSD

Despite the limited bandwidth of the CEO stabilization loop, a tight phase lock of the CEO-beat can be achieved. This is made possible with the low-noise properties of the free-running CEO-beat, whose frequency noise PSD was measured using the analog PLL frequency discriminator (see Section 2.4.1). At any Fourier frequency $\omega/2\pi$, the CEO frequency noise PSD $S_{\mathrm{CEO}}(\omega)$ only contributes to the CEO-beat linewidth if its value lies above the β-separation line (see Section 2.3), i.e. if $S_{\mathrm{CEO}}(\omega) > (8\ln 2/\pi^2)\cdot(\omega/2\pi)$. From the measured spectrum shown in Figure 5.10, this corresponds only to Fourier frequencies smaller than 3 kHz, which demonstrates that the CEO linewidth can be significantly narrowed using a feedback bandwidth of a few kilohertz only.

The frequency noise spectrum of the phase-stabilized CEO-beat was measured from the in-loop error signal of the digital phase detector, taking into account the measured phase discrimination sensitivity (see Section 2.5.1). In addition to the reduction of the CEO frequency noise, it was also observed that stabilization through the pump current slightly reduces the relative intensity noise of the femtosecond laser (apart from the frequency range centered at the servo bump). One believes that the frequency noise of the CEO-beat in the ERGO comb essentially results from pump power fluctuations, as previously shown in the case of Er:fiber lasers (see Section 4.6), Therefore, feedback to the pump current must reduce pump power fluc-

tuations to get a stable CEO phase-locked operation and the relative intensity noise of the femtosecond laser is reduced accordingly.

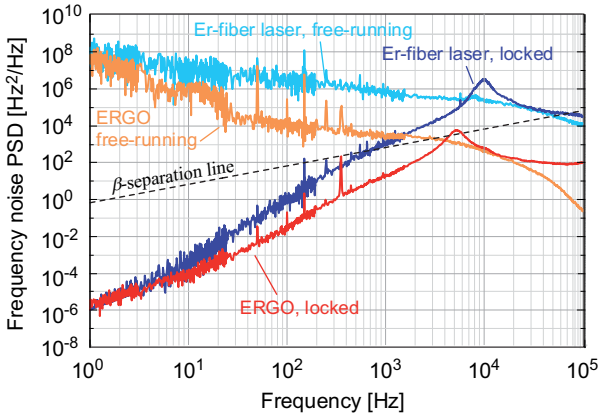

Figure 5.10: Comparison of the CEO frequency noise PSD in the ERGO comb and in the commercial Er:fiber comb in free-running and phase-locked modes.

The noise properties of the ERGO and of the Er:fiber comb described in Chapter 4 are compared, both in free-running and phase-locked conditions, in Figure 5.10. The 5.5-kHz feedback bandwidth used in the ERGO comb is slightly lower than in the commercial self-referenced Er-fiber comb (~10 to 20 kHz), but is sufficient to fully reduce the frequency noise PSD of the CEO-beat below the β-separation line. The lower CEO frequency noise in the ERGO comb and in particular its crossing with the β-separation line that occurs at a much lower frequency of ~3 kHz compared to ~100 kHz in the fiber comb makes it much easier to achieve a tight phase lock characterized by the suppression of the CEO linewidth. In the fiber comb a feedback bandwidth of at least 100 kHz would be required. This is not possible with the present electronics and a phase lead filter would be needed to compensate for the phase delay induced by the limited response bandwidth of the Er^{3+} gain medium coupled with the laser dynamics [60].

5.4.1-2 Integrated phase noise

The achieved frequency noise leads to a drastic reduction of the CEO linewidth and a tight phase-lock is thus realized, as proved by the coherent peak observed in the CEO spectrum with 30 dB signal-to-noise ratio (at 30 Hz resolution bandwidth) with respect to the servo bumps (see inset in figure Figure 5.11). The residual noise

in the pedestal underneath the stabilized CEO coherent peak corresponds to an integrated phase noise $\Delta\phi_{\mathrm{rms}} = \left[\int d(\omega/2\pi)\ S_{\mathrm{CEO}}(\omega)/(\omega/2\pi)^2\right]^{1/2}$ of 0.72 rad rms (integrated from 0.1 Hz to 100 kHz in Figure 5.11, but the phase noise at higher frequency has an insignificant contribution), which is the lowest CEO phase noise obtained to date for an optical frequency comb in the 1.5-µm range achieved with such a low feedback bandwidth of only ~5.5 kHz.

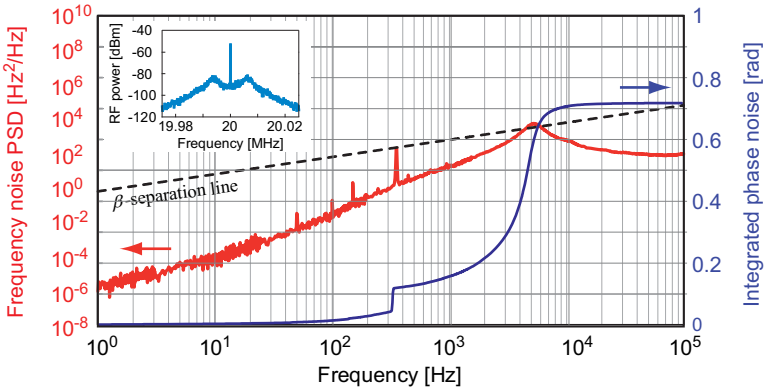

Figure 5.11: ERGO comb frequency noise properties. Left scale: frequency noise PSD of the phase-locked CEO-beat, measured from the in-loop phase detector. Right scale: integrated phase noise (integration from 0.1 Hz up to the cut-off frequency). Inset: coherent peak with 30 dB signal-to-noise ratio (at 30 Hz resolution bandwidth) observed in the CEO-beat RF spectrum.

In comparison with fiber lasers, the best reported values for the integrated phase noise in Er:fiber combs in the same spectral range are generally around 1 rad [55,78], achieved with a much larger feedback bandwidth of hundred kilohertz. Improved performances have been demonstrated very recently for an Er:fiber comb developed at NIST [76], while Y. Nakajima *et al.* showed a relative comb line stability of $3.7 \cdot 10^{-16}$ (at 1 s averaging time) in the comparison of two multi-branch Er:fiber combs stabilized to a common optical frequency standard [79]. But the best performance for an Er-fiber comb results from the figure-eight laser reported by E. Baumann *et al.* [80], where a CEO phase-lock bandwidth of 59 kHz combined with a stabilization of the comb to an optical reference (cavity-stabilized laser) with a large bandwidth of 1.6 MHz achieved with an intra-cavity EOM leads to an integrated in-loop phase noise of the heterodyne beat between the comb and the reference laser of 32 mrad from 1 Hz to 1 MHz, limited by the residual noise of the CEO.

In comparison with Ti:Sa lasers, the best performances in terms of CEO phase noise have been achieved with Ti:Sa combs at the <100 mrad level [95,96] which however comes at the expense of complexity and cost as mentioned in Section 4.1.

The major contribution to the integrated phase noise in the ERGO comb originates from the 5.5-kHz servo bump as shown in Figure 5.11, but a small technical contribution of ~10% results from a peak at 360 Hz which is also visible in the frequency noise spectrum. This noise peak is due to a mechanical resonance in a translational stage holding the pump laser focusing lens in the laser resonator, which is excited by ambient acoustic noise. The residual phase noise in the ERGO comb could certainly be further reduced by improving the mechanical stability of the resonator and by adding a proper phase lead filter in the feedback loop in order to extend the loop bandwidth to higher frequencies [74].

5.4.1-3 Allan deviation

The CEO long-term stability was assessed by recording the stabilized CEO frequency with a 1-s gate time counter (Menlo FXM200). Figure 5.12a shows a time series of more than 10 hours of continuous stable operation of the ERGO comb. The Allan deviation (Figure 5.12b) shows a fractional frequency instability of $10^{-8} \cdot \tau^{-1}$ for the 20-MHz CEO frequency, which thus contributes only 10^{-15} to the optical carrier frequency instability ($\nu_N \approx 192$ THz) at 1 s integration time. For comparison, Figure 5.12b also displays the same measurement performed with the self-referenced Er:fiber comb described in Chapter 4. The 20-fold improvement in the CEO fractional frequency stability observed in the ERGO comb compared to a standard commercial Er:fiber comb demonstrates the excellent CEO noise properties of the solid-state frequency comb. This partially results from the three times higher repetition rate of the fiber comb [72], but more significantly from the larger Q-factor of the ERGO laser resonator. The lower CEO frequency stability in the Er:fiber comb arises from the larger frequency noise at high Fourier frequency as shown by the Allan deviation calculated from the frequency noise spectra and presented in dashed lines in Figure 5.12.

The low-noise properties of the CEO make the ERGO comb very attractive as an optical-to-microwave frequency divider for all-optical ultra-low noise microwave generation [4,75,76,97,98], despite its low repetition rate, as the CEO contribution

to the phase noise and relative stability of the generated microwave are negligible. This will be shown in Chapter 6.

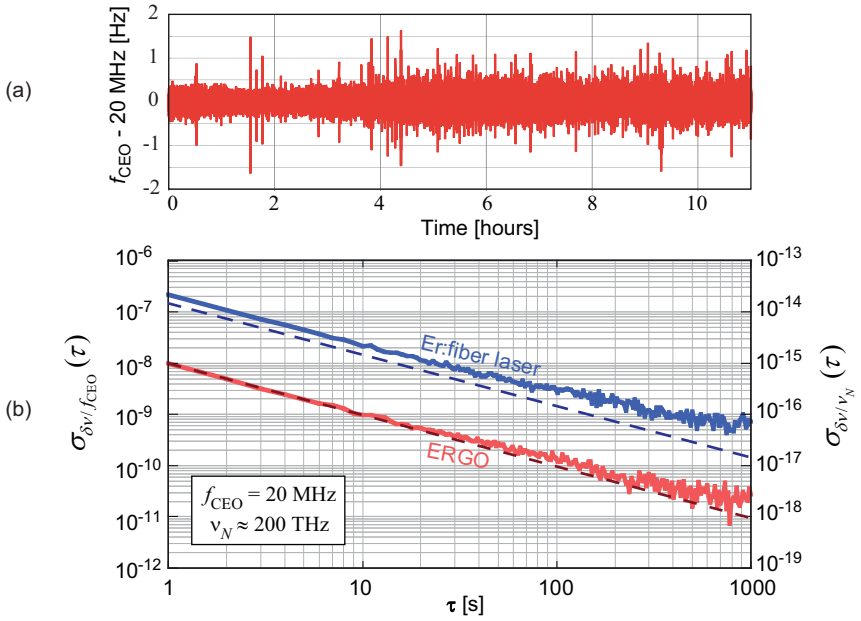

Figure 5.12: ERGO frequency comb: recorded time series of more than 10 hours of continuous stabilized operation of f_{CEO} acquired on a 1-s gate time counter. (b) Allan deviation of the CEO frequency in the ERGO comb and in the commercial self-referenced Er:fiber comb for comparison. The fractional stability is shown with respect to the CEO frequency $f_{CEO} = 20$ MHz on the left scale and with respect to the optical frequency $\nu_N = 200$ THz on the right scale. The fractional frequency stability calculated from the CEO frequency noise PSD (Figure 5.10) is also shown for comparison. The frequency noise PSDs were extrapolated to lower Fourier frequencies in this calculation.

5.4.2 Noise of an optical comb line

For the comparison of the noise properties of an optical line of the ERGO and Er:fiber combs, the phase-stabilization of the repetition rate to an RF reference has been performed using the same commercial stabilization electronics (MenloSystems) as depicted in Figure 5.13. Less than 300 µW of the ERGO laser output power was used for detection in a fiber-coupled fast photodiode (NewFocus 1434 with 25 GHz bandwidth). The 13th harmonic of f_{rep} at 975 MHz was used to enhance the detection sensitivity to phase fluctuations. This spectral component was bandpass-filtered, amplified and mixed with a 980-MHz reference signal. The reference signal is provided by a DRO referenced to the same H-maser as used for the CEO stabili-

zation. The resulting difference frequency component was compared to the 5-MHz reference signal from the H-maser in an analog phase comparator (double-balanced mixer). The error signal at the output of the phase comparator was low-pass filtered and forwarded to a PI servo-controller (Menlo PIC210) to generate the correction signal, which was amplified in a high voltage amplifier with 23 dB gain to drive the PZT that controls the laser cavity length.

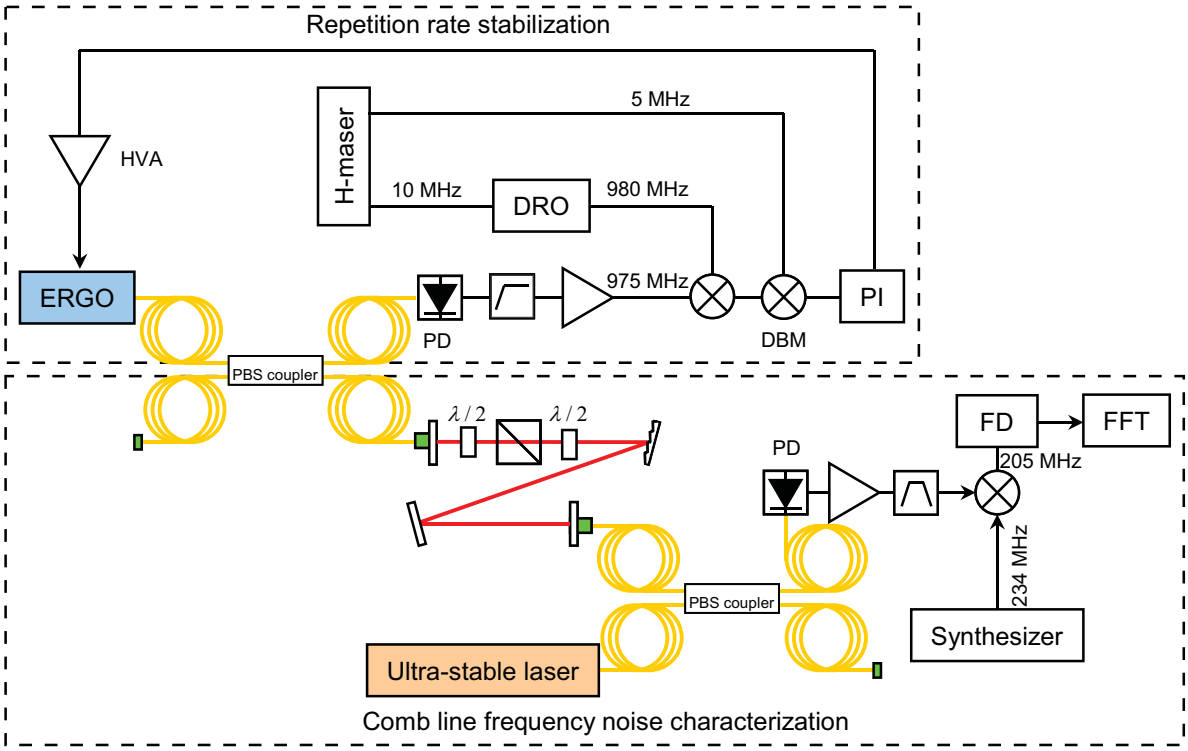

Figure 5.13: Scheme of the repetition rate phase-lock loop (upper frame), including a 980-MHz DRO referenced to an H-maser, an analog phase comparator (DBM: double balanced mixer), a PI servo-controller, a high voltage amplifier (HVA) and feedback to the PZT to stabilize the laser cavity length. The lower frame shows the measurement scheme used to characterize the frequency noise of the comb optical line against an ultra-stable laser (see Chapter 3) using the PLL frequency discriminator (FD).

The noise properties of an optical comb line at 1.56 µm have been characterized from the heterodyne beat signal with a cavity-stabilized ultra-narrow linewidth laser (see details in Section 3.6). The beat signal was measured with a fiber-coupled photodiode by combining ~800 µW from the 1557.5-nm ultra-stable laser with ~200 nW from the ERGO laser output beam, spectrally filtered to a 0.3-nm

(40 GHz) width using a diffraction grating. About 500 comb lines contributed to the detected comb optical power, corresponding to an average power of less than 0.5 nW per comb line. Despite this low power, a beat signal with a signal-to-noise ratio higher than 30 dB (at 100 kHz resolution bandwidth) was detected at ~29 MHz. After filtering and amplification, the beat signal was mixed with a 236-MHz reference signal to be demodulated by the analog PLL frequency discriminator operating at 207 MHz (see Section 2.4.1). The noise of the demodulated beat signal was measured on an FFT spectrum analyzer. The measured frequency noise PSD of the beat signal corresponds to the noise of the optical comb line $S_\nu(\omega)$ because the contribution of the ultra-stable laser is negligible.

Figure 5.14a compares the frequency noise of an optical comb line at 1558 nm in the ERGO and Er:fiber combs, obtained from the heterodyne beat with the ECDL stabilized to the ULE cavity (see Section 3.6). For comparison, the contribution of the reference oscillator, separately measured and scaled to the optical frequency, is also displayed. The DRO-980 is referenced (phase-locked) to the 10-MHz H-maser with a broad bandwidth. As a consequence, some noise components that are present in the H-maser phase noise spectrum are transferred to the DRO-980 and subsequently to the comb through the repetition rate stabilization loop. This is, e.g., the case for the 5.7-kHz peak (as well as the 11.4-kHz harmonic) that originates from the particular realization of the PLL that locks the quartz local oscillator to the hydrogen atomic transition in the maser.

The frequency noise of the optical mode is very similar in both combs up to 5 kHz Fourier frequency. However, the frequency noise PSD in the Er:fiber comb is almost two orders of magnitude higher than in the ERGO comb between 5 kHz and 100 kHz. The noise in this frequency range is mainly attributed to the contribution of the CEO servo-bump occurring at 10 to 20 kHz in the Er:fiber comb (see Section 4.6.1). This noise depends on the wavelength of the considered optical line as a result of the coupling between the servo-loops in the Er:fiber comb discussed in Section 4.6.3. At the measured wavelength of 1558 nm, partial noise compensation occurs as previously shown in Section 4.6.1. In contrast, no CEO servo bump contribution is observed in the noise spectrum of the optical line in the ERGO comb when stabilized to the same RF reference and with a similar feedback loop bandwidth as the Er:fiber comb. This difference results from the much lower frequency

noise PSD in the free-running CEO of the ERGO comb compared to the Er:fiber comb, which is a consequence of the higher resonator Q-factor. The resulting tight lock achieved with a moderate feedback bandwidth for the CEO in the ERGO comb reported in Section 5.4.1 leads to a negligible contribution of the CEO to an optical line.

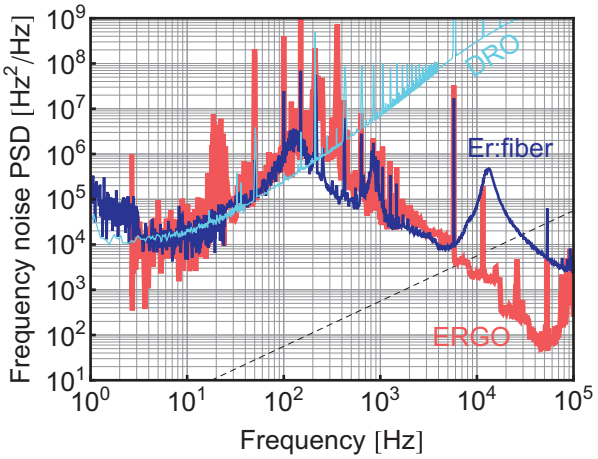

Figure 5.14: Frequency noise PSD of an optical line at ~1558 nm in the ERGO (light (red) thick line) and Er:fiber (dark (blue) thin line) combs, both fully stabilized to the same RF reference. The noise of the DRO scaled to 1558 nm (light (blue) thin line) and the β-separation line (dashed black line) are also shown.

5.5 Conclusion

The noise properties of the first fully stabilized optical frequency comb from a DPSSL in the 1.5-µm spectral region have been carefully characterized. The laser is a SESAM-modelocked Er:Yb:glass laser oscillator referred to as ERGO.

The high Q-factor of the ERGO laser resonator results in a low-noise CEO-beat and leads to the narrowest free-running CEO linewidth observed in this spectral region, with less than 4 kHz FWHM. The excellent noise properties allow for a tight phase-lock of the CEO frequency to a 20-MHz external reference using pump-power control with a feedback bandwidth of less than 5.5 kHz. The CEO integrated phase noise of 0.72 rad rms is one of the smallest values obtained to date in the 1.5-µm region, especially for such a low servo-loop bandwidth. This result could be further improved with the use of a phase lead filter, in order to compensate for the slow dynamics of the ERGO laser and to consequently extend the feedback bandwidth

while maintaining a stable loop operation. However, even with such an improvement, the ERGO comb will probably not compete with the record low CEO phase noise from Ti:Sa laser combs (<100 mrad rms), which benefit from the very short upper state lifetime of the Ti:Sa gain medium to achieve a high stabilization bandwidth.

As a result of the low-noise properties of the CEO-beat, the noise of an optical comb line is only limited by the repetition rate when the comb is stabilized to an RF reference and the CEO contribution is negligible at all Fourier frequencies. This is a major improvement in comparison with the commercial Er:fiber comb for which the CEO servo-bump contribution to the optical line observed at 10 to 20 kHz leads to a 100-fold higher frequency noise PSD than in the ERGO comb at 1558 nm. It should be mentioned that the CEO noise contribution to an optical comb line in the Er:fiber comb is significantly reduced due to the positive effect of the cross-coupling between the stabilization loops (see Section 4.6.3).

In terms of long-term fractional frequency stability, an Allan deviation of $10^{-8} \cdot \tau^{-1}$ has been achieved for the 20-MHz CEO-beat. This is 20-time better than measured in the self-referenced Er:fiber comb for comparison. The CEO contribution to the fractional frequency stability of an optical comb line thus amounts to only 10^{-15} at 1 s averaging time, which is totally negligible in comparison to the contribution of the repetition rate. The low-noise and high-stability properties of the CEO-beat make the ERGO comb attractive for ultra-low noise microwave generation, as will be shown in Chapter 6, despite its low repetition rate that decreases the available power at a given harmonic of the repetition rate and might thus reduce the ultimate phase noise performances of the generated microwave far from the carrier due to photodetection shot-noise [98]. The transfer of the relative frequency stability of a cavity-stabilized laser to the microwave domain using the ERGO comb can be envisaged using the simplest possible scheme, i.e. by simply phase-locking one line of the self-referenced comb to the laser, without the need for CEO subtraction [75] or to use the comb as a transfer oscillator [59], as the CEO is not expected to have an observable contribution to the phase noise or stability of the generated microwave. This assessment will be experimentally demonstrated in Chapter 6.

The frequency noise of a comb line at 1558 nm, characterized from the hetero-

dyne beat signal between the comb line and an ultra-narrow linewidth laser, showed to be limited by the DRO used as an RF reference in the stabilization of the comb repetition rate. Using feedback to the cavity length applied through a PZT, the frequency noise characteristics of the DRO are properly transferred to the comb line. No contribution of the CEO servo-bump has been observed in the phase noise of the optical line in contrast to the case of the Er:fiber comb.

Chapter 6

Ultra-stable microwave generation with optical frequency combs

6.1 Introduction

Ultra-stable lasers are very attractive for the generation of ultra-low noise microwave using a frequency comb as an optical-to-microwave frequency divider to transfer the fractional frequency stability of the laser to a microwave signal [4]. Fiber-based optical frequency combs have proved high reliability and robustness for low phase noise microwave generation [66,75]. State-of-the-art comparison of the optical-to-microwave frequency division with two similar Er:fiber combs stabilized to a common ultra-stable laser has shown the lowest phase noise of -120 dBc/Hz at 1 Hz offset from a 11.55-GHz carrier frequency [66]. State-of-the-art microwave generated from a Ti:Sa frequency comb has achieved a level of fractional instability of 8×10^{-16} at 1 s, corresponding to a phase noise of -104 dBc/Hz at 1 Hz offset from a 10-GHz carrier, with a stability mainly limited by the performance of the ultra-stable laser [4].

In this chapter, the first microwave generation from a PW-ECL stabilized to a ULE glass Fabry-Perot cavity is reported, using a commercial Er:fiber frequency comb as an optical-to-microwave frequency divider. Ultra-stable microwave generation using the SESAM-modelocked diode-pumped ERGO comb described in Chapter 5 is also demonstrated for the first time here.

In the conclusion of Chapter 5, it was mentioned that the low-noise properties of the CEO-beat in the ERGO comb make it attractive for ultra-low noise microwave generation due to the minor CEO contribution to the fractional frequency

stability of an optical comb component. Here, we demonstrate and compare the ultra-stable microwave signals generated from the ERGO and the Er:fiber combs. The evaluation of the microwave has been realized in collaboration with Femto-ST in Besançon with the use of a transportable cryogenic sapphire oscillator (CSO). The transportable ultra-low instability signal source ULISS [3], based on a high quality factor whispering gallery mode (WGM) in a cryo-cooled sapphire resonator, was developed by Femto-ST for the European Space Agency (ESA) and was moved to LTF in Neuchâtel for a measurement campaign. ULISS offers a relative frequency stability (Allan deviation) better than 3×10^{-15} at short term ($\tau < 300$ s) and still better than 5×10^{-15} over one day, which makes it very valuable for the evaluation of the microwave signals generated from optical frequency standards.

6.2 Optical-to-microwave frequency division using an optical frequency comb

Microwave signals with extremely low fractional frequency instabilities were demonstrated with CSOs [99,100]. Microwave generation with photonic systems has shown a similar stability of $\leq 10^{-15}$ at time intervals from 1 to 10 s [4] and even lower phase noise in a wide frequency range of 10 Hz – 100 kHz [4,101]. Among the different photonic approaches for microwave generation, a very promising approach is based on optical-to-microwave frequency division using an optical frequency comb. It was demonstrated that the process of all-optical frequency division can result in an extremely low phase noise [66,4]. With ultra-stable optical references demonstrating fractional frequency instabilities as low as 2×10^{-16} at 1 to 10 s [21], microwaves generated in this way can yield extreme short-term frequency stabilities and phase noise. Even lower phase noise might be achieved in the future with new improved optical references based on spectral hole-burning techniques [102] or cryogenic silicon cavities [103]. The noise floor of the all-optical frequency division process can also be improved by the use of combs with a higher repetition rate, for which an increased power per comb mode can be achieved, which reduces the noise floor resulting from the photodetection shot-noise [104].

We built an ultra-stable optical reference based on a PW-ECL stabilized to a high-finesse Fabry-Perot cavity as discussed in Chapter 3. Our goal is to transfer its fractional frequency stability to the microwave domain. Basically, the process of op-

tical-to-microwave frequency division involves a self-referenced comb, one line of which is locked to an ultra-stable optical reference. The two degrees of freedom of the comb being fixed, the comb is entirely stabilized and the repetition rate (or any of its harmonics) acquires the relative frequency stability of the laser and thus constitutes an ultra-stable microwave signal [105]. The principle of the microwave generation via an all-optical frequency division process is displayed in Figure 6.1.

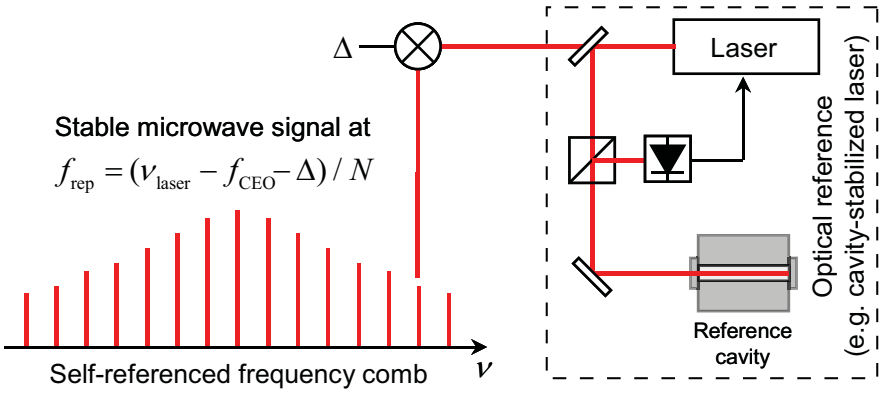

Figure 6.1: Illustration of the principle of an all-optical frequency division with an optical frequency comb. The beat signal between an ultra-stable optical reference oscillator and an adjacent comb mode is phase-locked to an RF synthesizer by feedback to a comb actuator that controls the cavity round-trip time (PZT, pump diode or intracavity EOM).

In the simplest stabilization scheme, the heterodyne beat of frequency Δ between the ultra-stable laser and the nearest tooth of a self-referenced comb is phase-locked to a reference frequency oscillator [105]. In this scheme, the CEO frequency f_{CEO} is stabilized to an RF reference by the standard f-to-$2f$ method (see Section 4.2.2). Then the fractional frequency stability of the reference optical oscillator with an optical frequency ν_{laser} is transferred to the repetition rate frequency f_{rep} which can be detected with a fast photodiode in the microwave domain:

$$f_{rep} = \frac{\nu_{laser} - f_{CEO} + \Delta}{N}, \tag{6.1}$$

where N is a large integer, corresponding to the comb mode number.

Alternatively, the CEO-beat frequency stabilization can be avoided by phase-locking the heterodyne beat between the ultra-stable laser and the comb line after subtraction of the CEO-beat frequency. In this stabilization scheme the heterodyne-

beat Δ between the ultra-stable laser ν_{laser} and a comb tooth with an index N and a corresponding optical frequency $\nu_N = f_{\text{CEO}} + N \cdot f_{\text{rep}}$ is mixed with the CEO frequency in a double-balanced mixer to obtain a signal δ, which does no longer contain the CEO:

$$\delta = \Delta - f_{\text{CEO}} = (f_{\text{CEO}} + N \cdot f_{\text{rep}}) - \nu_{\text{laser}} - f_{\text{CEO}}\,, \tag{6.2}$$

and which is then stabilized to a reference oscillator.

Eq. (6.1) for the repetition rate thus transforms into

$$f_{\text{rep}} = \frac{\nu_{\text{laser}} + \delta}{N}\,. \tag{6.3}$$

Ti:Sa ultrafast lasers are advantageous for optical-to-microwave frequency division owing to of their high Q-factor and low intra-cavity noise. The drawback of these systems is that the modelocking process is not self-starting and high-cost pump lasers are required. Alternatively, the cheaper Er:fiber-based systems are widely used for microwave generation. These systems are more favourable in terms of reliability and cost, however, they suffer from a lower control bandwidth and higher noise as compared to Ti:Sa combs. Usually the PZT actuator that controls the ultrafast laser cavity length is used to stabilize the repetition rate and the pump current stabilizes the CEO. Alternatively, the pump diode current can be used to stabilize the comb to the optical reference with a larger loop bandwidth, in combination with the CEO-subtraction method mentioned here above. Finally, a further increase of the loop bandwidth was recently demonstrated using an intra-cavity EOM [76].

6.3 Cryogenic sapphire oscillator

The evaluation of the microwave signals generated from the PW-ECL and either the Er:fiber or the ERGO frequency comb has been realized by comparison with the transportable ultra-low instability signal source ULISS [3] developed by Femto-ST in Besançon and moved to LTF in Neuchâtel for a measurement campaign. This ultra-stable microwave oscillator is based on the same design as the first cryo-cooled sapphire oscillator, named ELISA, built by Femto-ST for ESA [99,106]. CSOs have extremely low phase noise close to the carrier [107-109] and fractional frequency instabilities in the low 10^{-15} at timescales ranging up to a few hundred

seconds.

The core element of ULISS is a cylindrical sapphire resonator excited on a high order quasi-transverse magnetic WGM ($WGH_{15,0,0}$), cooled down to cryogenic temperature and maintained at about 6 K where its thermal sensitivity nulls at first order. In these conditions, a loaded Q-factor of about 7×10^8 is achieved at the resonant frequency of 9,988 GHz. Practically, the resonator is placed inside a copper cavity and is cooled inside a specially designed pulse-tube cryocooler comprising a thermal filter and a mechanical filter. The resonator is maintained at the turnover temperature, where its frequency temperature dependence is zeroed in a similar way as in the ULE optical cavity discussed in Section 3.8, with a resolution of ±1 mK. Two servo-loops are used to optimize the CSO performance that is affected by the environmental sensitivity of the oscillator. A first loop stabilizes the RF power injected into the resonator to decrease the thermal fluctuations produced by the power variations. A second loop ensures the CSO being locked to the resonator frequency by stabilizing the phase of the RF signal along the loop using the Pound stabilization principle (similar to the PDH stabilization described in Section 3.2.2, but applied to a microwave oscillator) [110]. Phase modulation at a frequency in the order of a few tens of kHz is used to create sidebands with a first voltage controlled phase shifter (VCPS 1 in Figure 6.2). A feedback signal is applied to the DC bias of a second VCPS (VCPS 2).

ULISS offers a relative frequency stability (Allan deviation) better than 3×10^{-15} at short term ($\tau < 300$ s) and still about 10^{-14} over one day, which makes it very valuable for the evaluation of microwave signals generated from optical frequency standards.

Moreover, besides the fundamental oscillator frequency of 9.988 GHz, a frequency synthesis generates additional output signals at 5 MHz, 100 MHz and 10 GHz. The principle and performances of the synthesis are described in [111]. Basically, the high frequency output signals (10 GHz and 100 MHz) have the same fractional frequency stability as the fundamental oscillator frequency, whereas the 5 MHz outputs are slightly degraded due to the frequency division process and the performance of typical RF components. A phase comparator enables the synthesized outputs to be locked to a 100-MHz reference signal (e.g. from an H-maser) to ensure the long-term stability of all output frequencies.

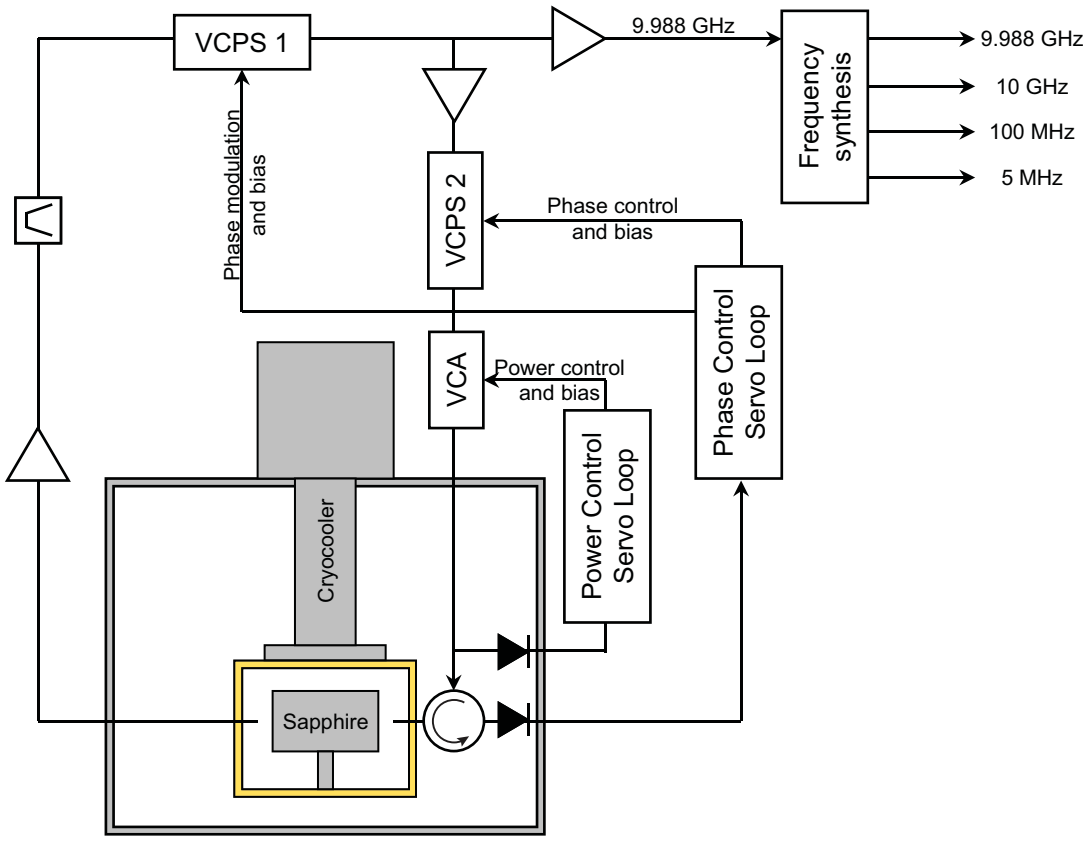

Figure 6.2: Schematic representation of ULISS. The cryogenic sapphire oscillator is based on a WGM sapphire resonator placed into a vacuum chamber at a cryogenic temperature of 6 K obtained with a cryocooler. A Pound stabilization is used to stabilize the phase of the microwave signal, whereas the RF power is maintained fixed by a second control in order to obtain a stable fundamental output frequency. The frequency synthesis is used to generate several useful output frequencies with a similar fractional frequency stability (5 MHz, 100 MHz, 10 GHz). VCPS: voltage controlled phase shifter, VCA: voltage controlled amplifier.

The ULISS instrument is made of for major parts: (i) a closed-cycle pulse-tube cryocooler with (ii) an air-cooled compressor; (iii) a sustaining loop fixed to the cryocooler frame and (iv) an electronic rack.

This instrument generates some acoustic noise, especially the cryocooler that is pulsed at a low frequency of about 1 Hz and the air-cooled compressor which is pretty noisy. As the oscillator was placed in the same laboratory room as the ultra-stable laser and combs, some precautions were taken in order to minimize the mechanical and acoustical perturbations to the photonics microwave generation. A degradation of the laser phase noise may occur due to the sensitivity of the reference cavity to vibrations and acoustic noise. To minimize a possible coupling of

acoustic noise to the cavity, the sapphire oscillator was placed in the far end of the laboratory, separated by several meters from the combs and the ultra-stable laser. The air-cooled compressor, which was potentially the most critical component due to its high emitted noise and dissipated heat, was positioned outside the laboratory room to avoid large temperature fluctuations and acoustic disturbance of the cavity. Some photographs of the system placed in a van for the move to Neuchâtel and in-operation during the measurements in LTF are shown in Figure 6.3.

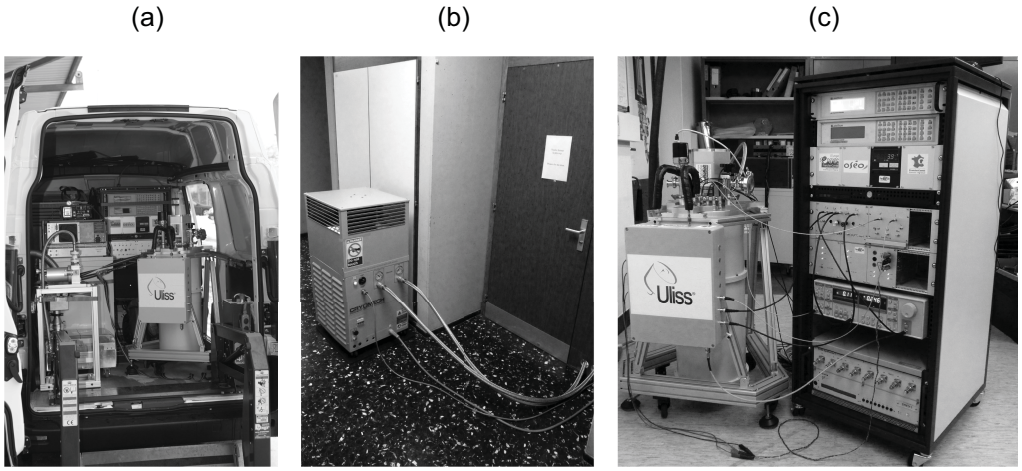

Figure 6.3: Photograph of the ULISS setup moved to Neuchâtel. (a) ULISS in a van. (b) The air-cooled compressor is placed outside the lab in order to reduce the potential impact of its acoustic noise on the performances of the ultra-stable laser. (c) ULISS oscillator with the cryocooler and the sustaining loop (left) and the electronics rack (right).

6.4 Ultra-stable microwave generation

The core element of the low-noise microwave generation is the ultra-stable laser described in Chapter 3. An all-optical frequency division with a frequency comb requires some challenging performances in terms of noise and stability for all the RF and optical components used in the experiment. As mentioned in the previous section, ULISS was placed in the far end of the laboratory accommodating the ultra-stable laser in order to minimize its thermal and vibrational disturbances onto the ULE reference cavity. The measurement of fractional frequency instabilities in the low 10^{-15} range required the microwave detection and evaluation parts to be placed as close as possible to ULISS to minimize the noise and losses introduced in the cables. The necessity to transport the light from the combs to the detection parts

with a minimal fractional stability or phase noise degradation was the second issue. In order to minimize the noise that could be introduced by the fibers to the disseminated comb spectrum, the shortest possible fiber lengths of 10 m and 7 m were used for the Er:fiber and ERGO combs, respectively, as the noise introduced by an optical fiber scales with the fiber length. Furthermore, these fibers were mounted with care and were tentatively protected from thermal fluctuations and mechanical perturbations. The optical fiber patchcords with 3-mm jacket were placed inside a thermal insulation tube made of polyurethane foam with a low thermal conductivity and some capability to attenuate vibrations. These tubes were loosely fixed in a rigid channel bar and at each end an FC through adaptor was mounted and fixed on either an optical table or an optical breadboard handling the microwave components. A photograph of the insulated fibers attached to the breadboard is depicted in Figure 6.4. It should be mentioned that the ultra-stable reference laser was placed on the same optical table as the Er:fiber comb, however the ERGO comb was placed on a separate optical table. Thus an extra 8-m long fiber was used to deliver the light of the ultra-stable laser to the ERGO comb. This fiber was also passively isolated from vibrations and thermal fluctuations in a similar manner.

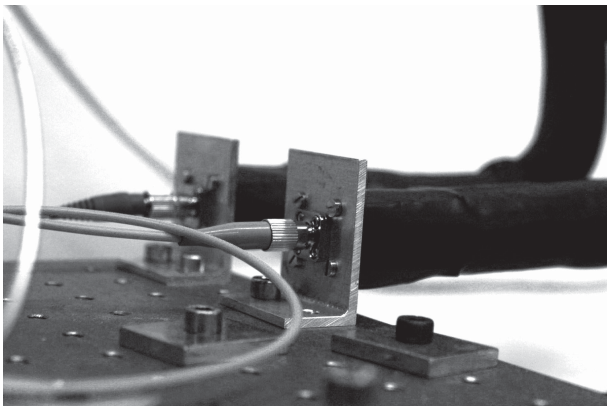

Figure 6.4: Photograph of the fiber patchcord protected from vibrations and thermal fluctuations. The fiber patchcord with 3 mm jacket on the left side and the protected fiber on the right side are connected to each other via an FC through adaptor.

An additional precaution is related to the electronic RF components used for the measurements in the 10-GHz range. The sensitivity to vibrations of the RF circuit may become critical for fractional frequency instabilities at a level of 10^{-15}. It is extremely important to avoid mechanical perturbations induced on the low-noise

RF components and cables during the measurements. Thus all the amplifiers, mixers and filters used in the measurement scheme were tightly screwed onto the optical breadboard. In-between every RF components used in the GHz frequency range, an RF isolator was connected in order to avoid electrical reflections, which can potentially degrade the measurement. A photograph of the breadboard with the RF components used for the evaluation of the ultra-stable microwaves against ULISS is shown in Figure 6.5. The detection schemes used with the Er:fiber and ERGO combs will be detailed in Section 6.5.

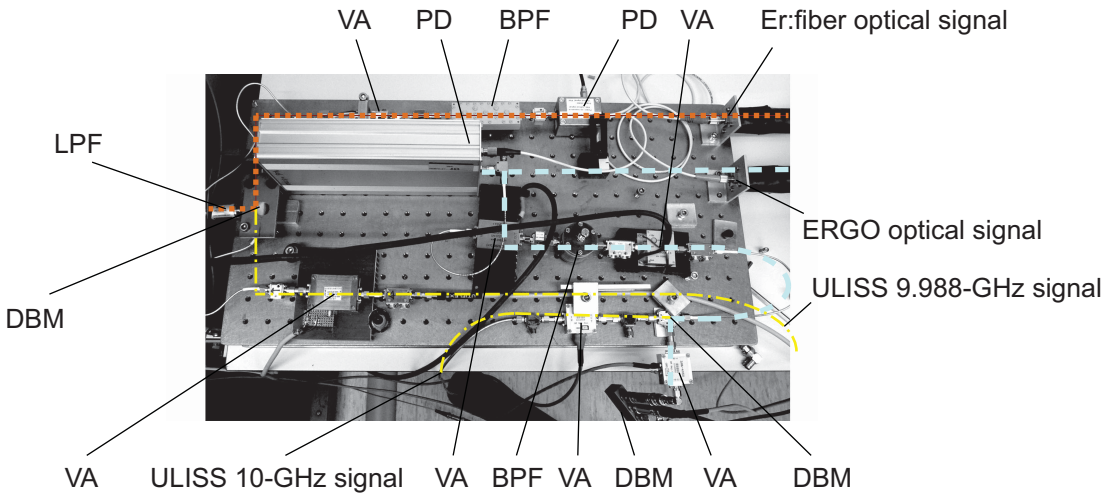

Figure 6.5: Photograph of the breadboard accommodating the electronic components used for the evaluation of the ultra-stable microwave signals generated from each frequency comb against ULISS. PD: fast photodetector; VA: voltage amplifier; BPF: bandpass filter; DBM: double-balanced mixer; LPF: low-pass filter. The (red) dotted line shows the electronics components for the comparison of the Er:fiber comb with ULISS. The light (blue) thick dashed line shows the components used in the detection and evaluation of the repetition rate of the ERGO comb. The (yellow) thin dash-dotted line shows the path of the ULISS reference signals used for comparison with the microwave generated from either the Er:fiber or the ERGO comb.

6.4.1 Optical-to-microwave frequency division using an Er:fiber comb

The commercial passively modelocked Er^{3+} fiber ring frequency comb described in Chapter 4 has been used to transfer the relative frequency stability of the PW-ECL, locked to the ULE cavity, into a microwave signal. The repetition rate of the comb can be changed in the range of -2.034 MHz to $+0.495$ MHz around

f_{rep} = 250 MHz. A heterodyne optical beat was obtained by mixing ~125 µW from the PW-ECL with ~25 µW of the Er:fiber comb, spectrally-filtered in a 0.8-nm spectral window with a diffraction grating, in a fiber-coupled photodiode (Thorlabs DET01CFC). The beat signal was compared to a 30-MHz reference signal from a DDS in a digital phase detector (Menlo DXD200). The resulting error signal was amplified in a PID controller (Menlo PIC210) and was fed back to a high-voltage amplifier with 23 dB gain driving a PZT that makes fine control of the Er:laser cavity length. A scheme of the stabilization of the Er:fiber frequency comb to the optical reference is shown in Figure 6.6.

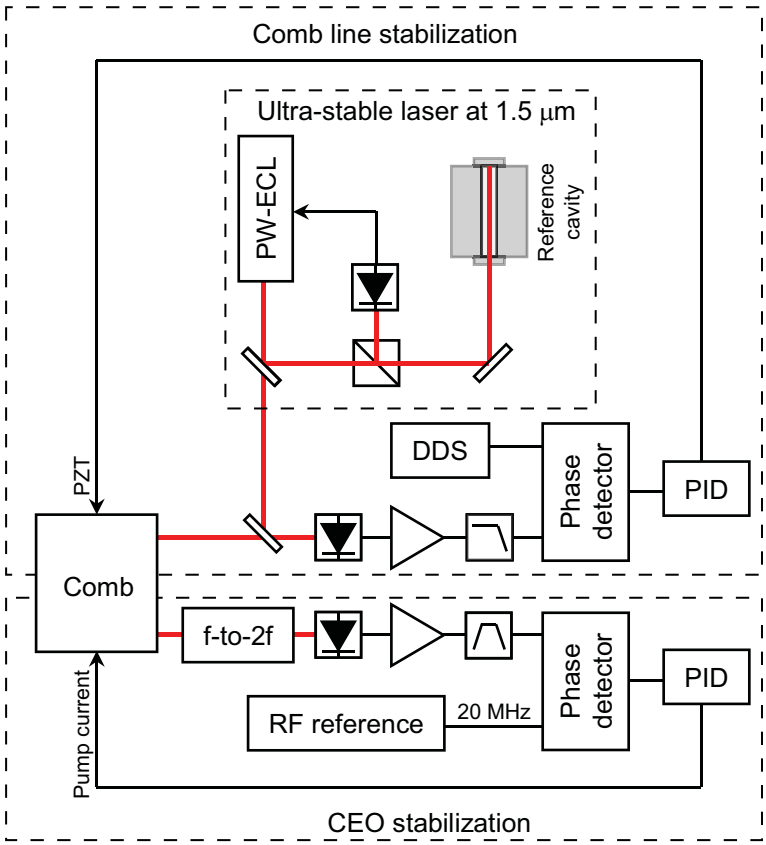

Figure 6.6: Schematic representation of the stabilization of a frequency comb to an optical reference. One comb line is stabilized to the ultra-stable laser by control of the cavity length with a PZT. The CEO is independently stabilized via feedback to the pump current. Both frequency references are stabilized to the same H-maser.

As discussed in the beginning of Section 6.4, we used a 10-m long fiber patchcord protected from vibrations and thermal fluctuations to deliver the optical signal of the Er:fiber comb to a pigtailed InGaAs fast photodiode (DSC40S from

Discovery Semiconductor Inc.) with 16 GHz bandwidth, placed as close as possible to ULISS. Multiple harmonics of the repetition rate of the stabilized Er:fiber comb are detected in the photodiode. From the overall 11 mW incident optical power of the comb, the 40th harmonic of the repetition rate at ~10 GHz was band-pass filtered and amplified to be evaluated by comparison with ULISS.

6.4.2 Optical-to-microwave frequency division with a DPSSL comb

The ERGO DPSSL comb described in Section 5.2 has been used for microwave generation and comparison with the performances achieved with the Er:fiber comb.

The stabilization scheme of the ERGO comb to the ultra-stable optical reference is very similar to the one implemented with the Er:fiber comb (see Figure 6.6). An optical line of the self-referenced ERGO comb was phase-locked to the ultra-stable reference laser. The CEO of the comb was stabilized as described in Section 5.4.1. The output of the comb was split between two optical fibers. In the first arm, the ~15-nm wide spectrum with ~400 µW average power was combined with ~100 µW from the ultra-stable reference PW-ECL in a 50/50 fibered power combiner. The resulting beatnote signal detected in a 2-GHz photodiode (Thorlabs DET01CFC) was compared to a 10-MHz external reference frequency from a DDS in a digital phase detector (Menlo DXD200). This signal was phase-stabilized via feedback applied to the PZT controlling the cavity length. The PZT transfer function limits the achievable servo loop bandwidth in the kilohertz range. Nevertheless, a robust and reliable servo lock was achieved.

In the second arm, 10 mW optical power was delivered to the photodiode used for microwave detection via a 7-m long singlemode fiber patchcord, passively protected from vibrations and thermal fluctuations as described in the beginning of Section 6.4. The microwave detection scheme consisted in a pigtailed InGaAs fast photodiode (Discovery Semiconductors Inc. DSC30) with 14 GHz bandwidth. Among the multiple harmonics of the repetition rate of the stabilized ERGO comb detected in the photodiode, the 132nd harmonic at ~9.9 GHz was band-pass filtered and amplified to be evaluated by comparison with ULISS.

6.5 Ultra-stable microwave characterization

6.5.1 Frequency stability

6.5.1-1 Experimental setup

The repetition rate of the Er:fiber comb was tuned in order that its 40th harmonic was close to 9.988 GHz, corresponding to the fundamental frequency of ULISS. The two signals at ~9.988 GHz were mixed in a double-balanced mixer to produce a frequency down-converted beat signal at ~188 kHz. This 188-kHz signal was counted in a Λ-type frequency counter (Agilent HP53132A) referenced to a hydrogen maser, with 1 s gate time. The schematic representation of the setup is shown in Figure 6.7. The measurement noise floor in this scheme was limited by the fractional frequency fluctuations of ULISS, which has been evaluated in Besançon by direct comparison with ELISA before and after the trip to Neuchâtel [112]. The measured frequency stability is shown in Figure 6.9 by the dashed line. No data post-processing has been done and the result directly represents the combination of the stability of the two oscillators. No scaling by a factor $\sqrt{2}$ has been performed, which is generally adopted when comparing two equivalent oscillators. The measurement noise floor given in Figure 6.9 is thus conservative.

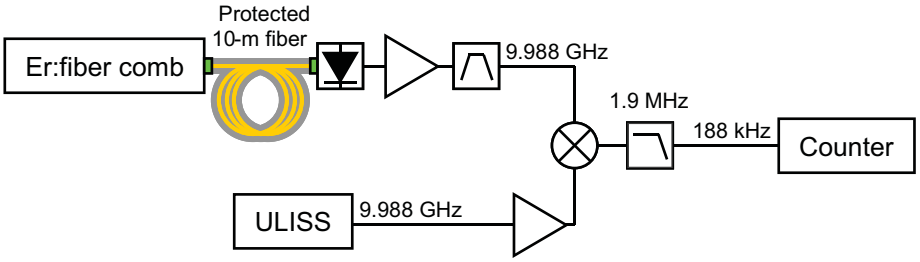

Figure 6.7: Schematic representation of the experimental setup used to characterize the microwave signal generated from the Er:fiber comb in comparison with ULISS.

The detection and evaluation of the microwave generated from the ERGO comb is schematically represented in Figure 6.8. The ERGO comb repetition rate was tuned in order that the beat note between the 10-GHz synthesized output from ULISS and the 132nd harmonic of the ERGO comb repetition rate at 9.9 GHz was slightly shifted from 100 MHz (by ~200 kHz). The two signals were mixed in a double-balanced mixer. The down-converted frequency at ~100 MHz was compared

to the 100-MHz output from ULISS using a second mixer to produce a frequency down-converted beat signal at ~200 kHz. The frequency of this signal was recorded with a high precision Λ-type frequency counter (Agilent HP56132A) to determine its relative frequency stability.

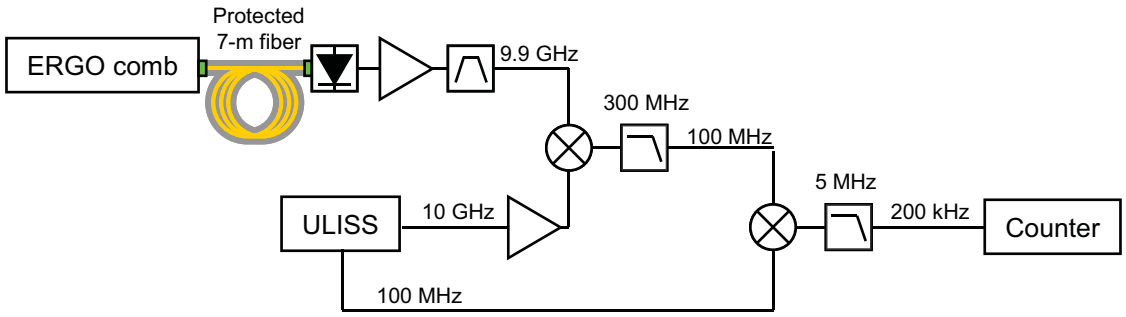

Figure 6.8: Schematic representation of the evaluation of the microwave signal generated from the ERGO comb with ULISS.

6.5.1-2 Results

The Allan deviation of the microwave signal generated from the Er:fiber comb stabilized to the ultra-stable PW-ECL and analyzed using the scheme previously described is reported in Figure 6.9. A relative frequency stability of 6×10^{-15} is achieved at 1 s, followed by a slight increase up to 9×10^{-15} at $\tau \approx 8$ s. When the linear drift of 74 mHz/s, attributed to the isothermal "creep" of the ULE material [24], is removed from the time series of the measured frequency, the presence of a bump centered at $\tau \approx 8$ s in the Allan deviation becomes clearly visible. The origin of this bump has not yet been identified. It is believed to arise from the stabilization of the laser to the cavity rather than from the microwave generation process (a comparison between the two combs locked to a common laser may clarify this). This effect presently limits the fractional frequency stability achieved by our system at a higher level than the flicker frequency noise floor corresponding to the thermal noise of the ULE mirror substrates and coatings of our 10-cm long cavity, estimated to correspond to $\sigma_y \approx 7 \times 10^{-16}$ based on the analysis reported by Webster and co-workers for a similar cavity [24] and with a detailed calculation presented in Section 3.4.2. The state-of-the-art fractional frequency stability of the microwave generated via an all-optical frequency division is obtained from a direct comparison of two independent photonic systems based on Ti:Sa combs stabilized to two independent

optical references, as low as 8×10^{-16} at 1 s.

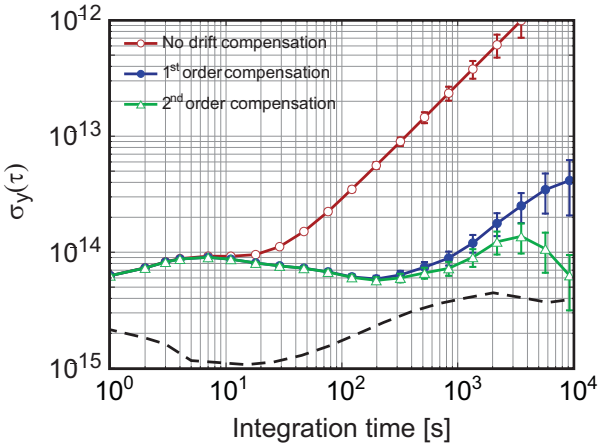

Figure 6.9: Relative frequency stability of the microwave generated with the Er:fiber comb and PW-ECL compared to ULISS. The dashed line represents the direct comparison between two CSOs. The linear and the second order drift were compensated by subtracting the corresponding polynomial fit from the time series data before calculating the Allan deviation.

The Allan deviation of the microwave signal generated from the ERGO comb stabilized to the ultra-stable PW-ECL is depicted in Figure 6.10 in comparison with the Allan deviation of the microwave signal generated from the Er:fiber comb. We observe that a similar relative frequency stability of 5×10^{-15} at 1 s is achieved with both ERGO and Er:fiber combs. In general, the fractional frequency stability of the comb might be limited by the stability of the CEO frequency in the presented microwave generation scheme. In the case of the Er:fiber comb, it was shown that the CEO stability is limited to 2×10^{-14} at 1 s (see Section 5.4.1). Nevertheless, a lower value of the generated microwave signal was achieved. This improvement can arise from the two following facts: (i) the use of a frequency counter with a lower bandwidth for the measurement of the microwave signal as discussed in [113], (ii) the positive impact of the servo-loops in the Er:fiber comb (see Sections 4.6 and 6.6.4).

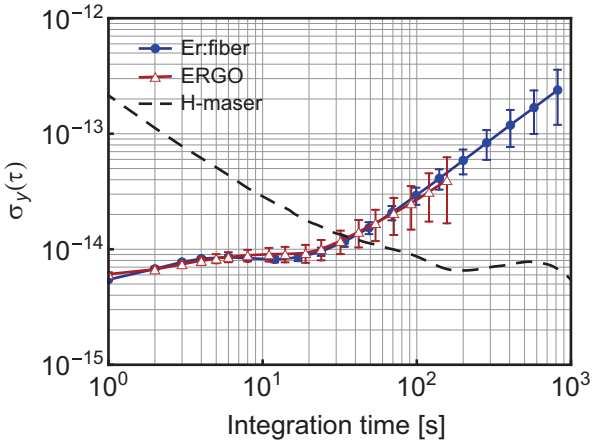

Figure 6.10: Relative frequency stability of the microwave generated from the Er:fiber comb (red triangles) and from the ERGO comb (blue circles) locked to the ultra-stable laser and measured against ULISS. The stability of an active H-maser (dashed line) is also shown for comparison.

6.5.2 Phase noise

6.5.2-1 Setup

The phase noise of the microwave signals obtained from the Er:fiber and ERGO combs, down-converted to ~188 kHz and ~200 kHz, respectively, as described in Section 6.5.1, was measured using the digital PLL discriminator HF2PLL (see Section 2.4.3). Due to the low carrier frequency, the bandwidth of the digital PLL was limited to only a few kHz. Thus the phase noise at Fourier frequencies higher than the PLL bandwidth was not straightforward to access due to a decreased signal-to-noise ratio. The transfer function of the PLL was consecutively measured and used to correct the measured phase noise spectra to account for the limited bandwidth. In order to verify the correctness of the measurements performed with the HF2PLL frequency discriminator, the phase noise was additionally measured for the Er:fiber comb in a different scheme, using a phase noise measurement system (NMS from SpectraDynamics Inc.). In that case, the comb repetition rate was tuned in order that its 40^{th} harmonic was close to 9.978 GHz. This harmonic was band-pass filtered and mixed with the fundamental frequency of ULISS at ~9.988 GHz in a double-balanced mixer to produce a frequency down-converted beat signal at ~10 MHz. This 10-MHz signal was compared with a 10-MHz high-quality quartz reference synthesizer (CS-1 from SpectraDynamic Inc.) in the noise measurement system. An

error signal was produced and fed back to the quartz voltage controlling the reference frequency in order to weakly phase-lock it (0.3 Hz bandwidth) to the input signal to maintain the two signals in quadrature. In this condition, the phase fluctuations between the two oscillators are linearly converted into voltage fluctuations by the measured slope in the linear range of the phase detector, acting as a phase discriminator. The phase noise spectrum was recorded with the internal FFT spectrum analyzer of the noise measurement system. The detection and evaluation scheme of the microwave signal using the noise measurement system NMS is schematized in Figure 6.11.

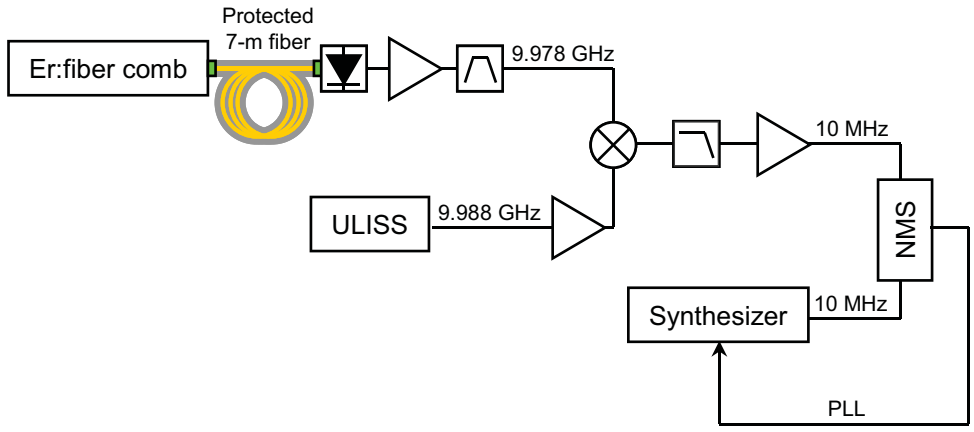

Figure 6.11: Schematic representation of the experimental setup used to measure the phase noise of the microwave signal generated from the Er:fiber comb in comparison with ULISS using the NMS noise measurement system.

The measurement noise floor in this scheme is limited by the phase noise of the 10-MHz output of the reference synthesizer, which has been evaluated by direct comparison between two similar frequency synthesizers, indicated by the dashed line in Figure 6.12. No data post-processing has been done and the result directly represents the combination of the phase noise of the two oscillators. The measurement noise floor given in Figure 6.12 is thus conservative.

The good agreement between the phase noise obtained with the HF2PLL discriminator and the NMS in the case of the Er:fiber comb, which will be presented in the next section (see Figure 6.12), validates the use of the HF2PLL discriminator to measure the phase noise of the microwave signal generated in this scheme.

6.5.2-2 Results

The phase noise of the microwave signal generated from the Er:fiber comb stabilized to the ultra-stable PW-ECL and analyzed using either the HF2PLL frequency discriminator or the NMS with the schemes previously described is reported in Figure 6.12.

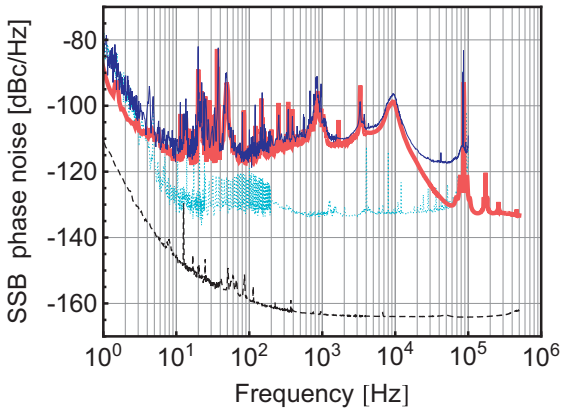

Figure 6.12: Single-sideband (SSB) phase noise PSD of the 9.978-GHz microwave generated with the Er:fiber comb and PW-ECL compared with ULISS using NMS (light (red) thick curve) and HF2PLL frequency discriminator (dark (blue) thin curve). The black dashed line represents the direct comparison between two identical RF synthesizers used to evaluate the microwave signal at 10 MHz with NMS (noise floor of the measurement setup with NMS). The light (blue) dotted line represents the noise floor of the HF2PLL frequency discriminator.

A phase noise of -118 dBc/Hz is achieved between 10 Hz and 100 Hz offset from the 9.978-GHz carrier frequency, followed by a slight increase up to -100 dBc/Hz at $f = 10$ kHz. The phase noise then decreases and the achieves a level of -137 dBc/Hz at 100 kHz $< f <$ 600 kHz. For Fourier frequencies lower than 5 Hz the phase noise measured with HF2PLL frequency discriminator is limited by the instrumental noise floor. However, for higher Fourier frequencies, a good agreement between the phase noise obtained using the HF2PLL frequency discriminator and the NMS is observed. A slight difference at 20 to 100 kHz could be explained by the reduced signal-to-noise ratio outside the PLL bandwidth. The good agreement between the two measurements confirms that the HF2PLL frequency discriminator can be effectively used to evaluate the phase noise of a signal with a low carrier frequency (~200 kHz). Consequently, this measurement principle was adopted to assess the phase noise of the ERGO-comb-generated ultra-stable micro-

wave as well. The use of the NMS with the ERGO comb was made difficult by the precise microwave frequency adjustment required with this system. The measurement scheme requires a tiny adjustment of the repetition rate to achieve a down-converted frequency of 10 MHz ± 40 mHz. This requires to change the alignment of the ERGO comb cavity. Due to the complex comb dynamic, it was difficult to achieve a tight lock of the ERGO comb to the ultra-stable laser at a precise desired frequency.

The phase noise of the microwave signals generated from the Er:fiber and ERGO combs stabilized to the ultra-stable PW-ECL is depicted in Figure 6.13. A significant improvement in terms of phase noise is observed with the ERGO comb compared to the Er:fiber comb in similar conditions. The observed phase noise below 5 Hz offset frequency is limited by the instrumental noise floor, which can slightly differ between the two measurements. Therefore, the difference between the low-frequency part of the spectra in Figure 6.13 is not representative. The observed phase noise at an offset frequency ranging from 5 Hz to 100 Hz from the 10-GHz carrier is attributed to the noise of ULISS used in the characterization of the microwaves generated from each comb. This noise is believed to arise from the high servo gain of the Pound stabilization of the phase lag along the ULISS circuit. Unfortunately, the phase noise of ULISS as used in our experiments is not precisely known. The only data available from Femto-ST concerns an early comparison made between two CSOs, i.e. ELISA and a liquid Helium CSO built with the resonator used later on in ULISS. This measurement is shown in Figure 6.13 by the dotted line, where 3-dB have been subtracted as generally adopted when comparing two equivalent oscillators. However, since this measurement, the short term frequency stability of ULISS has been improved, but no more recent measurement of the phase noise spectrum is available. Therefore, we have to stick to this early measurement as a first estimation of ULISS phase noise, but the actual phase noise is very likely lower than indicated in Figure 6.13.

This explains why the phase noise measured for the microwave generated with the ERGO comb appears lower than the estimated noise floor of the CSO at offset frequencies between 100 Hz and 100 kHz from the 10-GHz carrier. At this point, we cannot distinguish whether the measured phase noise was limited by the ERGO comb microwave or by ULISS. Anyway, the measured ultra-stable microwave gen-

erated from the ERGO comb has up to 20 dB improved phase noise compared to the microwave obtained from the Er:fiber comb at 1 kHz – 100 kHz offset from the 10-GHz carrier frequency.

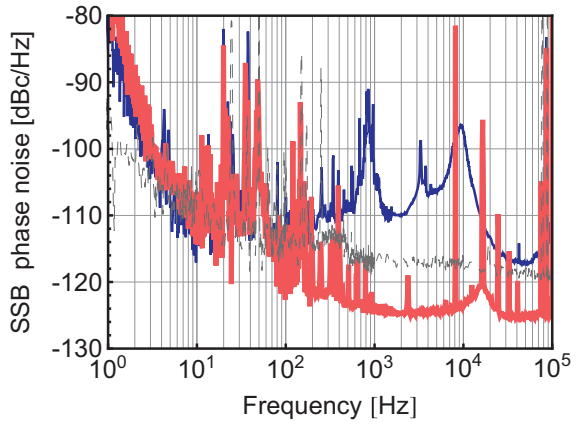

Figure 6.13: Single-sideband (SSB) phase noise PSD of the microwave signals generated from the PW-ECL using the Er:fiber comb (light (red) thick curve) and from the ERGO comb (dark (blue) thin curve) compared to ULISS at 10 GHz carrier frequency. Measurements were performed using the HF2PLL frequency discriminator. The dotted line represents an early direct comparison between ELISA and a liquid Helium CSO built with the resonator used later on in ULISS, at 10 GHz carrier frequency. 3 dB have been subtracted as it is usually done when two identical oscillators are compared. This measurement is presented as the estimation of the phase noise of ULISS. The actual noise floor appears to be lower than this curve.

6.5.2-3 Discussion

State-of-the-art microwave generation was demonstrated by T. Fortier *et al* in 2011 [4]. In that work, ultra-stable microwave signals were generated via all-optical frequency division of a 518-THz fiber laser and a 282-THz solid-state cw laser, each PDH-stabilized to an ULE cavity, using two Ti:Sa ring lasers. These two ultra-stable microwave signals were compared against each other, leading to a relative fractional stability of 8×10^{-16} at 1 s and to an SSB phase noise of -104 dBc/Hz at 1 Hz offset from the 10-GHz carrier. This setup benefits from the very low noise properties of the Ti:Sa combs, and the extreme performances of the ultra-stable lasers. The phase noise showed a decrease from ≈ -130 dBc/Hz at 40 Hz offset from the carrier to ≈ -150 dBc/Hz at 4 kHz offset from the carrier.

The phase noise of the microwave signal generated with the ERGO comb is 10 to 25 dB higher than these state-of-the-art results obtained with Ti:Sa combs. How-

ever, it is comparable or even slightly better (by 3 to 5 dB) than the phase noise of the microwave signals obtained at SYRTE from Er:fiber combs in the same spectral range, at 10 Hz – 10 kHz offset from a 9.2-GHz carrier [75]. Later results reported by the same group have shown a lower contribution of the optical-to-microwave frequency division with Er:fiber combs, at the level of ≈ -127 dBc/Hz at 10 Hz – 100 kHz offset frequency from a 11.55-GHz carrier, but these results refer to the frequency division process by the frequency combs only and not to the characteristics of the generated microwave. These results have shown the lowest phase noise reported to date for a frequency division process at the level of -120 dBc/Hz at 1 Hz offset from the carrier obtained from the comparison of similar Er:fiber combs locked to a common laser [66]. However, at frequency offsets ranging from 100 Hz to 1 MHz the lowest phase noise (<-140 dBc/Hz) is achieved with Ti:Sa combs [4]. The lowest phase noise reported to date for the microwave signal generated using an Er:fiber comb was ~10 dB higher than the phase noise of the microwaves generated using the Ti:Sa combs by the same group at 1 Hz – 1 MHz offset from a 10 GHz carrier [76]. To achieve such a low phase noise, special tools were implemented to increase the control-loop bandwidth, such as the use of an intra-cavity EOM.

Nevertheless, the ultra-stable microwave signal generated from the ERGO comb demonstrates only 8-15 dB higher phase noise than the state-of-the-art microwave signal generated with Er:fiber combs at 10 Hz – 100 kHz offset from the carrier and these performances were limited at 5 to 100 Hz offset from the carrier by the phase noise of the ULISS oscillator used in the evaluation. At higher frequencies, one cannot assess if the observed noise arises from the comb or from the reference oscillator due to the lack of knowledge of the actual noise floor of ULISS. Anyway, these results show that microwave generation from the ERGO comb can produce very low phase noise performances even without the implementation of special tricks as used in the state-of-the-art optical-to-microwave frequency division obtained with Er:fiber combs, such as an intra-cavity EOM for high bandwidth stabilization [76] or a pump current-based power lock [66]. The noise floor of the all-optical frequency division process can also be improved by the use of combs with a higher repetition rate, which allows increasing the power-per-mode impinging on a high-power photodiode, thus reducing the noise floor due to the photodetection shot-noise [98].

Group	NIST [4]	NIST [76]	SYRTE [75]	SYRTE [66]	LTF
Frequency comb	1-GHz Ti:Sa	200-MHz Er:fiber	250-MHz Er:fiber	250-MHz Er:fiber	75-MHz ERGO
Microwave frequency	10 GHz	10 GHz	9.2 GHz	11.55 GHz	10 GHz
Cavity-stabilized laser	Fiber laser		Fiber laser		PW-ECL
Wavelength	1068 nm [4]		1542 nm		1560 nm
Cavity spacer/mirrors	ULE cavity		10 cmULE spacer + ULE mirrors [115]		10-cm ULE spacer + ULE mirrors
Compared to	Ti:Sa		LHe CSO @11.93 GHz (Stability) Ti:Sa @9.2 GHz (phase noise)	250-MHz Er:fiber	ULISS [3]
Referenced to	Solid-state laser		Yb:fiber laser [35]	Common laser	
	578 nm		1062.5 nm		
	29-cm ULE spacer + fused silica mirrors [21]		10-cm ULE spacer + fused silica substrates		
CEO control	Pump current		CEO free (subtracted)		Pump current
f_{rep} control	Cavity length PZT	HF: Intracavity EOM LF: Cavity length PZT	Pump current (120 kHz)	HF (>20 kHz): FF VCPS LF (<20 kHz): PZT+pump-current based power lock	Cavity length PZT
Stability @1 s	8×10^{-16}		3×10^{-15}		5×10^{-15}
Offset from a carrier	SSB phase noise scaled to 10 GHz				
@1Hz	~-104 dBc/Hz	~-100 dBc/Hz	~-89 dBc/Hz	~-121 dBc/Hz	~-80 dBc/Hz
@10Hz	~-120 dBc/Hz	~-120 dBc/Hz	~-107 dBc/Hz	~-127 dBc/Hz	~-112 dBc/Hz
@100Hz	~-140 dBc/Hz	~-132 dBc/Hz	~-117 dBc/Hz	~-130 dBc/Hz	~-120 dBc/Hz
>1 kHz	~-150 dBc/Hz	~-140 dBc/Hz	~-120 dBc/Hz	~-130 dBc/Hz	~-124 dBc/Hz

Table 6.1: Comparison of notable results obtained for ultra-stable microwave generation by all-optical frequency division. LF: low frequency, HF: high frequency, FF: feed-forward, VCPS: voltage control phase shifter, SSB: single-sideband.

The results obtained with the ERGO comb are compared in Table 6.1 to the most notable results of ultra-stable microwave generation obtained with other comb systems.

The achieved results show that ultrafast DPSSL optical frequency combs stabilized onto an ultra-stable reference lasers are attractive candidates for low-noise ultra-stable microwave generation, providing a comparable phase noise level as CSOs and an improved phase noise as compared to a commercial Er:fiber comb stabilized in similar conditions.

6.6 Investigation of possible limitations

The presence of a bump centered at $\tau \approx 8$ s in the Allan deviation of the microwave generated from both Er:fiber and ERGO combs (Figure 6.9 and Figure 6.10) presently limits the fractional frequency stability achieved by our system at short timescales at a higher level than expected for similar cavities [24]. The origin of this limitation has not yet been identified, but different possible sources have been investigated and are presented in the following sections:

- excess phase noise arising from power-to-phase noise conversion in the photodetection of the comb pulse train, which can affect the fidelity of the optical-to-microwave frequency division;
- fluctuations of the laser power coupled to the cavity, which can lead to a shift of the cavity resonance due to thermal effects in the mirror coatings, substrates and in the cavity spacer itself;
- excess phase noise induced in optical fibers used to transport the light between the laser, the combs and the microwave characterization setup. This effect depends on the type of fiber and on the environmental perturbations.

6.6.1 AM-to-PM conversion in microwave generation

A first potential cause of excess phase noise in the generated microwave is due to amplitude-to-phase noise conversion in the photodiode that detects the comb pulse train and generates the microwave signal [114], due to fluctuations of the detected comb power. To investigate this effect, the power of the Er:fiber comb impinging on the photodiode that generates the microwave signal, was stabilized using an AOM (FCM-401E6AP from IntraAction Corp.). A bias-tee was used at the out-

put of the photodiode to separate the low-frequency component from the harmonics of the comb repetition rate. The low-frequency component was used to monitor the fluctuations of the average optical power incident on the photodiode. An error signal, generated in a voltage comparator, was amplified in a PID controller and sent to the AM input of the AOM driver to close the loop. The power stabilization loop is schematized in Figure 6.14.

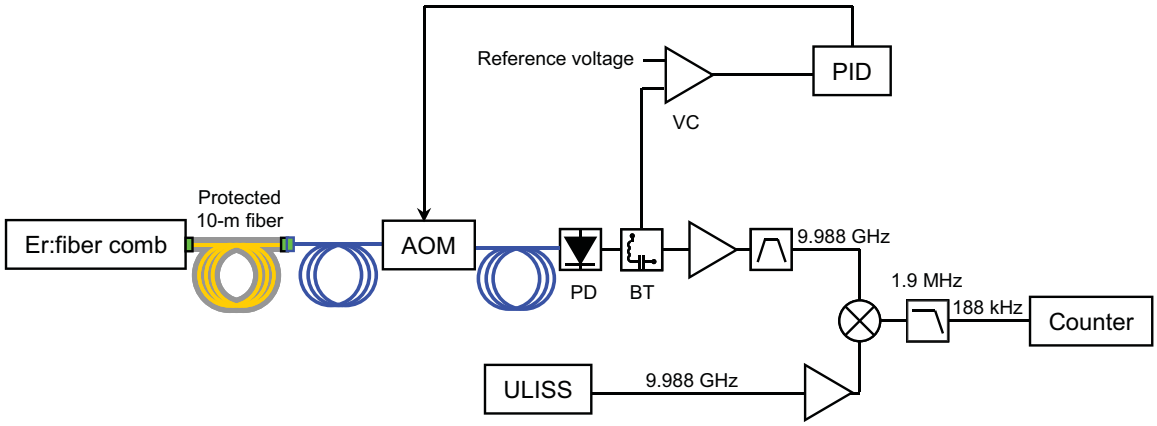

Figure 6.14: Schematic representation of the stabilization of the frequency comb optical power impinging onto the photodiode used for microwave generation. AOM: acousto-optic modulator, PID: proportional-integral-derivative controller, PD: photodetector, BT: bias-tee, VC: voltage comparator.

The power stabilization showed no significant improvement of the measured Allan deviation or phase noise, as shown in Figure 6.15. A small difference in the fractional frequency stability is observed, but it is mainly due to different environmental conditions in which the measurements were performed, rather than to the power stabilization. The difference results from the fact that these measurements have not been performed consecutively and slight differences in the absolute measured stability have been frequently observed between different measurements, regarding the effect of the power stabilization. We have observed these slight changes in the measured stability both with the comb power stabilized or not stabilized. Furthermore, the bump in the Allan deviation at $\tau \approx 8$ s is still present with the power stabilization.

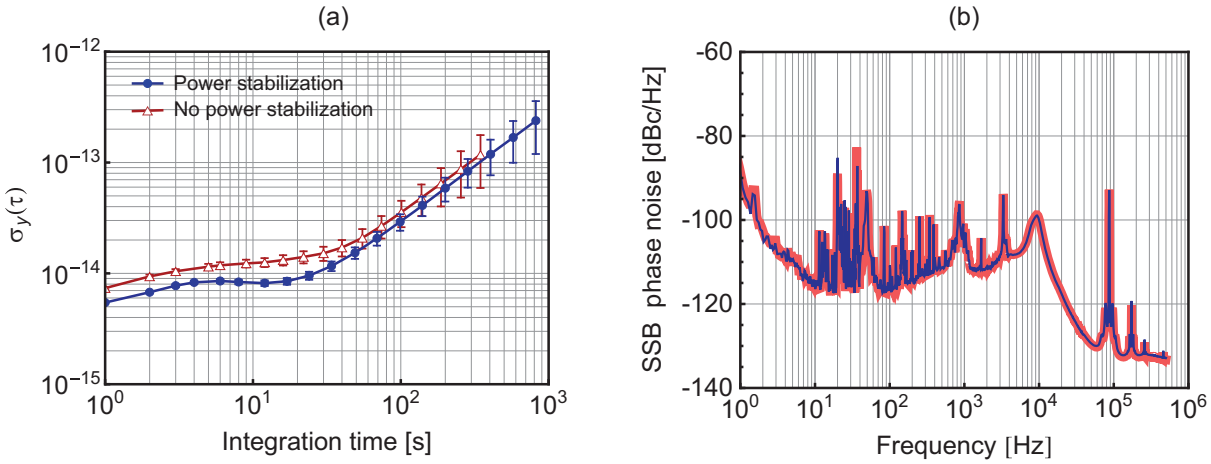

Figure 6.15: Relative frequency stability (a) and phase noise PSD (b) of the microwave signal at 10 GHz generated from the Er:fiber comb with the power stabilization disabled (light (red) thick curve) and enabled (dark (blue) thin curve).

6.6.2 Power-to-frequency conversion in the reference cavity

Another potential cause of excess phase noise in the generated microwave is amplitude-to-phase noise conversion of the laser power impinging on the ULE reference cavity [38]. A variation of the optical power impinging onto the cavity causes a frequency shift of the cavity resonance, and, as a consequence, a corresponding frequency deviation of the cavity-stabilized laser. This effect can be described by the ratio between the resonance frequency shift and the change of the optical power impinging onto the cavity, referred to as the power-to-frequency conversion coefficient.

The laser power at the input of the ULE cavity was kept low (~50 µW) to minimize the frequency noise induced by the power-to-frequency conversion process in the cavity. The conversion coefficient was experimentally determined by simultaneously monitoring the optical power impinging onto the cavity with a reference photodiode and the frequency of the microwave generated with the Er:fiber comb, down-converted to 188 kHz. The change in the ULE cavity resonance frequency $\Delta\nu$ is related to the change of the microwave frequency $\Delta f_{\mu\text{wave}}$ by $\Delta\nu = 192\ \text{THz} \cdot \Delta f_{\mu\text{wave}}/9.988\ \text{GHz}$. The optical power incident on the cavity was manually changed by discrete large steps by changing the RF power driving the AOM used in the PW-ECL frequency-stabilization scheme depicted in Figure 3.15

in Section 3.6.1. Large enough power steps were required in order to easily distinguish between the frequency deviations due to the power change and other frequency variations due, e.g., to the isothermal "creep" of the cavity. The result of the simultaneous monitoring of the optical power impinging onto the cavity and of the shift of the cavity resonance frequency, after removal of the linear frequency drift is shown in Figure 6.16.

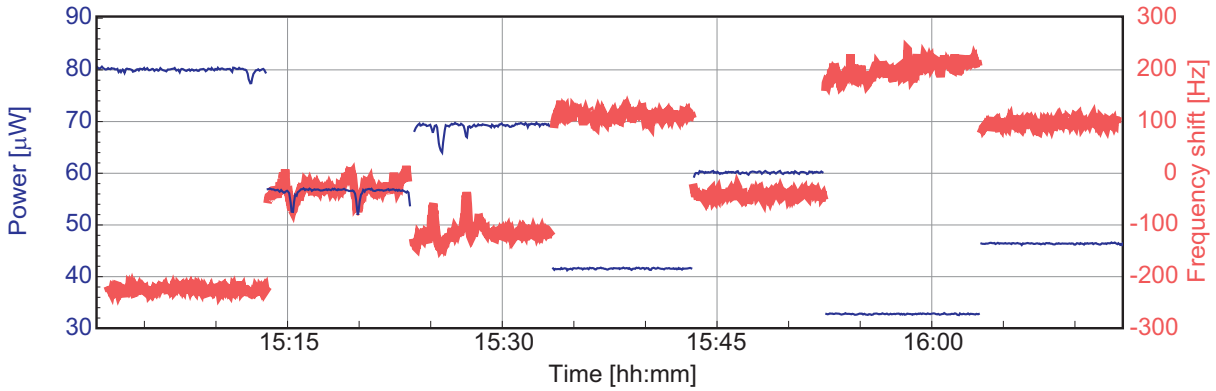

Figure 6.16: Simultaneous monitoring of the cavity resonance frequency detuning, obtained from the microwave signal generated using the Er:fiber comb compared with ULISS (light (red) thick curve, right scale), and of the optical power impinging onto the ULE cavity (dark (blue) thin curve, left scale) evolving in time. The linear drift attributed to the isothermal "creep" of the cavity was subtracted.

A power-to-frequency conversion coefficient of the ULE cavity of (-9.1 ± 0.3) Hz/µW is obtained from the linear fit of the ULE cavity frequency shift reported as a function of the optical power impinging on the cavity, displayed in Figure 6.17.

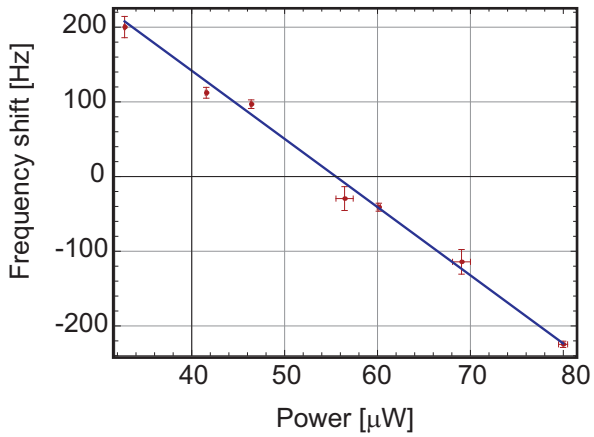

Figure 6.17: Power-to frequency conversion of the ULE cavity. The points correspond to the mean of the measured frequency shift and power in each step of Figure 6.16, and the error bars correspond to the standard deviations. The power-to-frequency conversion coefficient is obtained from a linear fit (straight line).

The fluctuations of the optical power impinging onto the cavity were recorded with an external photodiode while the laser was frequency-stabilized to the cavity. Using the measured power-to-frequency conversion coefficient, the contribution of the absolute power fluctuations of the stabilized PW-ECL to the phase noise of the ultra-stable microwave was calculated and is shown as a dashed line in Figure 6.18. The contribution of the measured incident power fluctuations to the phase noise of the ultra-stable microwave was observed to be negligible.

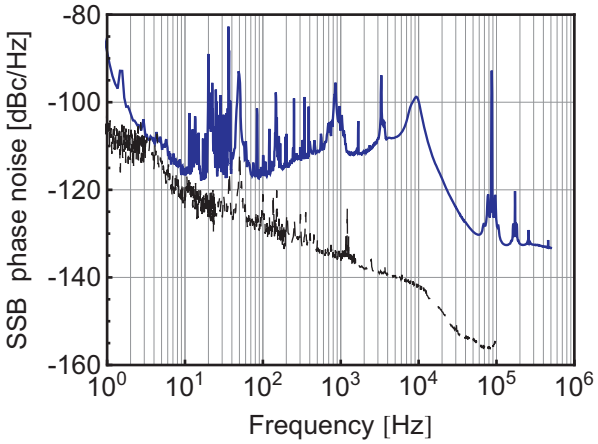

Figure 6.18: SSB phase noise PSD of the microwave signal at 10 GHz generated from the Er:fiber comb and PW-ECL stabilized to the ULE cavity compared to ULISS (dark (blue) thin curve). The power stabilization of the comb radiation detected on the photodiode which generates the microwave (see Section 6.6.1) was maintained enabled during these measurements. Phase noise of the PW-ECL stabilized to the ULE cavity due to power-to-frequency conversion when no power stabilization was implemented, scaled to 10 GHz (black dashed line).

6.6.3 Fiber noise contribution to microwave fractional frequency stability

The ultra-stable optical reference signal is obtained by the stabilization of the PW-ECL to the ULE cavity in a fibered configuration with an overall fiber length of 8 m into the loop. It is well known that optical fibers introduce additional phase noise when disseminating ultra-narrow linewidth lasers due to their thermal and mechanical sensitivity. Therefore, active optical link stabilization is required when transferring an ultra-stable optical reference signal between distant points via a fiber [115]. If excess noise is introduced by the fiber in the laser stabilization loop, the laser can be considered as ultra-stable only in the free-space optic part of the setup close to the cavity. Everywhere else in the loop, the excess phase noise that might be introduced by the fibers could degrade the stability of the laser.

Optical fibers are also used to deliver the laser light for the stabilization of the optical frequency combs. This can be a potential cause of additional phase noise in the generated microwave.

In order to assess the possible impact of the fibers onto the measured frequency stability of the microwave generated via all-optical frequency division with the combs, different extra fiber lengths have been inserted between the laser and the

combs. Figure 6.19 shows that no significant alteration of the Allan deviation is observed with extra fiber lengths of up to 20 m added between the ultra-stable laser and the Er:fiber comb.

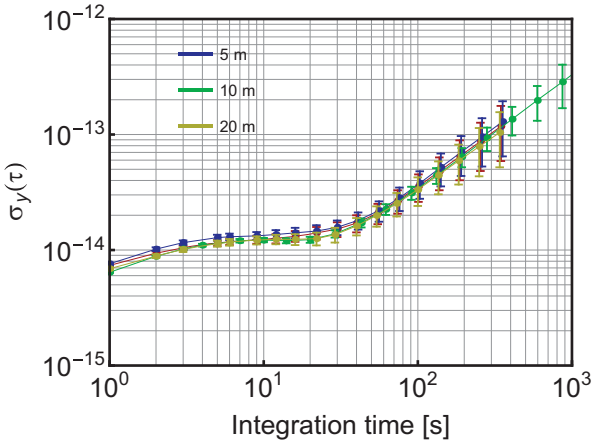

Figure 6.19: Relative frequency stability of the microwave signal generated from the Er:fiber comb compared with ULISS, measured for different extra fiber lengths to distribute the ultra-stable laser to the combs.

The ERGO comb was placed even further away from the ultra-stable laser and an extra 8-m long protected fiber (see Section 6.4) was used to distribute the ultra-stable laser light to the comb. In order to quantify the contribution of this fiber to the instability of the generated microwave, the experimental setup depicted in Figure 6.20 has been implemented. An interferometric measurement between the local laser and the laser that propagated back and forth in the fiber under test, following the same approach as used in active fiber stabilization schemes [115] was performed. We used the PW-ECL stabilized to the ULE cavity as described in Section 3.6.1 with an AOM (FCM-401E6AP from IntraAction Corp.) driven with 32.5 MHz, working as a frequency shifter. The detected beat signal at 65 MHz after a round-trip in the fiber was mixed with the doubled modulation frequency shifted by 20 MHz with a frequency mixer in order to remove the AOM frequency drift. This 20-MHz signal was counted with a frequency counter (Menlo FXM200).

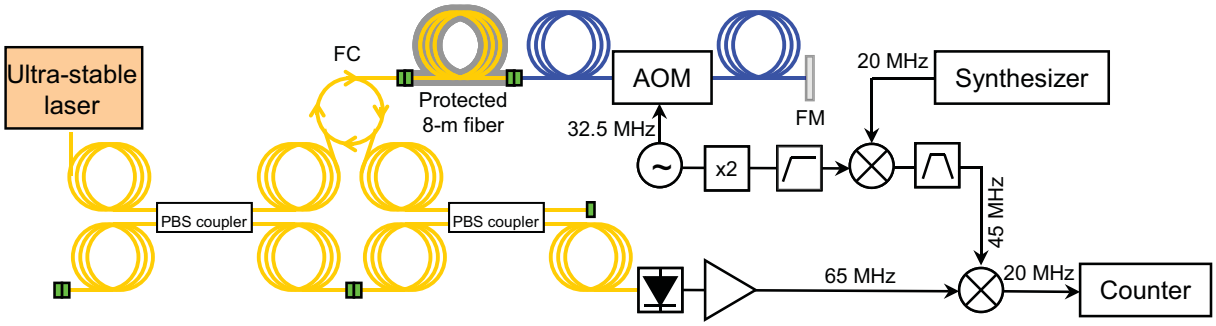

Figure 6.20: Schematic representation of the setup implemented to quantify the excess fractional frequency instabilities induced in the 8-m long protected fiber used to send the light of the ultra-stable laser to the ERGO comb. FM: Faraday mirror, FC: fiber circulator, AOM: acousto-optic modulator.

The measured fractional frequency instability induced in the 8-m long protected fiber used to send the ultra-stable laser light to the ERGO comb is shown in Figure 6.21. We observe that the frequency fluctuations introduced by the fiber ($\sim 1 \times 10^{-15}$ at 1 s) are negligible compared to the $\sim 5 \times 10^{-15}$ instability measured for the generated microwave (at 1 s).

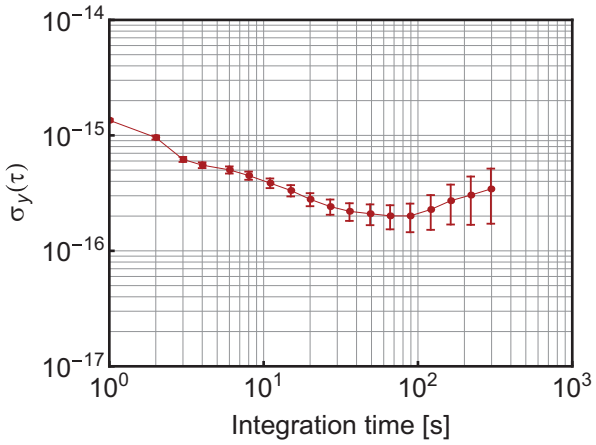

Figure 6.21: Relative frequency instability introduced by the 8-m long protected fiber link used in the stabilization of the ERGO comb.

6.6.4 Feedback to various actuators

The microwave generation presented so far was achieved with each comb (ERGO or Er:fiber) using the simplest stabilization scheme, in which one line of the self-referenced comb was stabilized to the ultra-stable laser by feedback to the PZT controlling the length of the femtosecond laser cavity. This scheme has several dis-

advantages. Firstly, a stabilization of the CEO is required and the contribution of the CEO residual frequency fluctuations to an optical comb line should remain smaller than the residual fluctuations of the optical reference not to degrade the performance of the generated microwave. Secondly, it limits the type of actuators that could be used to improve the noise properties of the microwave generated from the comb. For instance, it was demonstrated that the use of the pump current instead of an external AOM for the stabilization of the comb power at the photodetection is advantageous in terms of noise of the detected microwave [66]. But, in such a case, the pump power cannot be used for CEO stabilization and the CEO-beat has to be subtracted from the heterodyne beat between the ultra-stable laser and the comb in order to remove the noise of the unstabilized CEO [75]. More importantly, the stabilization of the comb to the optical reference using a PZT actuator has a limited bandwidth. Feedback to the pump current can be used to achieve a higher bandwidth or, alternatively, an intra-cavity EOM has been recently shown to further increase the stabilization bandwidth [76].

On the other hand, a simple stabilization scheme using the cavity PZT might benefit from the complex comb dynamics and from the coupling between the feedback loops, which can lead to a positive impact of the CEO-stabilization on the noise properties of the generated microwaves in a similar way as for the comb stabilized to an RF reference discussed in Chapter 4.

Here, we demonstrate how the phase noise can differ in various stabilization schemes implemented with the Er:fiber comb. Firstly, we implemented a scheme with the CEO-beat contribution subtracted from the heterodyne beat between the comb optical mode and the ultra-stable laser. This CEO-free beat signal was afterwards stabilized to an RF reference. This was performed by mixing the heterodyne beat signal between the comb and the ultra-stable laser with the CEO-beat. The output of the mixer thus contained two components: one with the double CEO-beat contribution to the output frequency, and the other one was CEO-free. After proper filtering, the CEO-free beat frequency signal was phase-locked to a reference frequency oscillator. A diagram describing the CEO-beat frequency subtraction in the stabilization of the comb optical component is schematically shown in Figure 6.22.

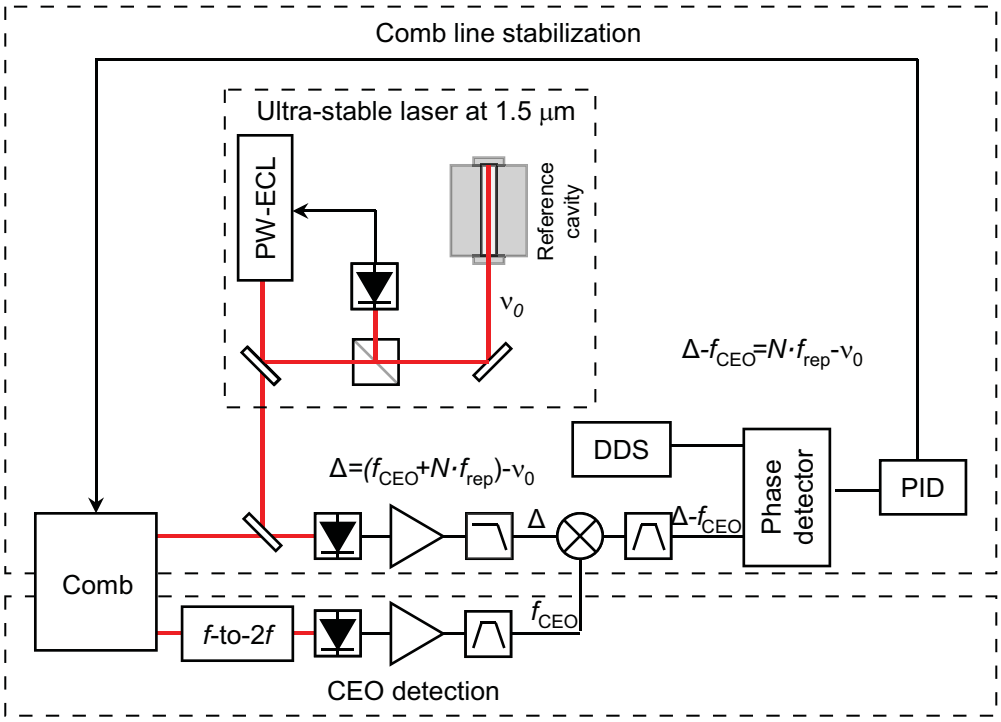

Figure 6.22: Schematic representation of the microwave generation using an optical frequency comb with the CEO-beat frequency subtracted. Feedback can be applied to either the PZT or the pump current.

In principle, this scheme enables comb stabilization to an optical reference without any need for CEO stabilization. Thus the feedback can be applied to the comb pump power instead of the PZT controlling the cavity length. Potentially this can lead to a lower phase noise of the generated microwave due to the higher achievable feedback bandwidth. The phase noise of the microwave generated using the CEO-free beat scheme with the feedback applied either to the PZT actuator or to the pump current was recorder using the NMS as described in Section 6.5.2. The achieved phase noise is shown in Figure 6.23, where it is compared to the phase noise measured in the previous scheme. One observes that when the comb stabilization is achieved via the PZT, the stabilization of the CEO plays an important role (Figure 6.23a). When the CEO is stabilized, the phase noise of the microwave with the CEO-beat subtracted is identical to the phase noise measured without CEO subtraction, with only a slight difference observed at 2 to 5 kHz offset from the 10-GHz carrier frequency. However, when the CEO-beat frequency is let free-running, the phase noise at frequencies up to 6 kHz offset from the 10-GHz carrier is at least 20 dB higher. We believe this difference to arise from the positive impact of the

CEO stabilization on the noise of the comb repetition rate due to the cross-coupling between the servo loops in the Er:fiber frequency comb, in a similar way as discussed in Chapter 4 for the comb stabilized to an RF reference. Thus, without the positive impact of the CEO stabilization on the noise of the repetition rate, mainly attributed to pump current fluctuations, the bandwidth of the PZT appears to be insufficient to guarantee a tight lock of the frequency comb to the optical reference. Indeed, when the feedback is applied to the pump current instead of the PZT in a similar scheme, the measured phase noise of the generated microwave is only slightly degraded as compared to the simplest stabilization scheme previously used with both CEO and comb optical component stabilized without any CEO-beat subtraction.

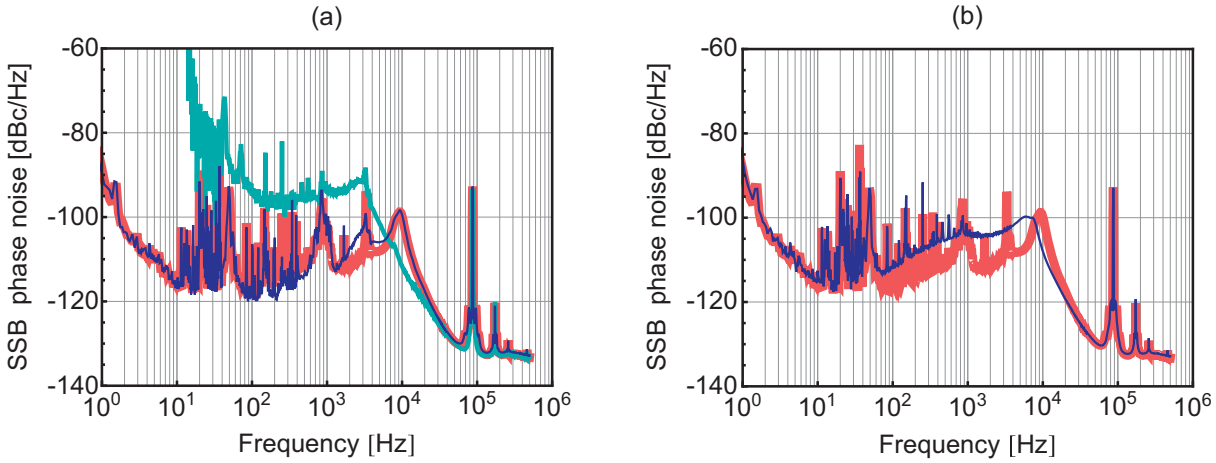

Figure 6.23: Single sideband phase noise PSD of the microwave signal at 10 GHz generated from the Er:fiber comb compared to ULISS in the basic stabilization scheme, where the heterodyne beat between the ultra-stable laser and the nearest tooth of the self-referenced comb is phase-locked to a reference frequency oscillator (light (red) thick curve) compared to different stabilization schemes. (a) The CEO-free beat signal is phase-locked via corrections to the cavity PZT with the CEO free-running (light (green) curve) or stabilized (dark (blue) thin curve). (b) The CEO-free beat signal is phase-locked via corrections to the Er:fiber frequency comb pump power (blue thin curve).

6.7 Conclusion

The first generation and characterization of an ultra-stable microwave signal obtained from a PW-ECL referenced to a high-finesse ULE cavity, described in

Chapter 3 has been reported here. Two types of frequency combs have been used for the all-optical frequency division process to transfer the relative frequency stability of the laser into the microwave domain: a commercial Er:fiber frequency comb discussed in Chapter 4 and the SESAM-modelocked DPSSL ERGO comb described in Chapter 5, both centered at 1.56 µm.

The performances of the generated microwave have been characterized by comparison with the transportable cryocooled sapphire oscillator ULISS [3], developed at Femto-ST in Besançon and moved to Neuchâtel for a measurement campaign. This measurement campaign was a start for the first field tests of the operation of such a transportable CSO.

Similar relative frequency stability of 5×10^{-15} at 1 s was achieved with both combs and is presently limited by excess noise of the ultra-stable laser, whose origin has to be further investigated. When removing the linear drift, attributed to the isothermal "creep" of the ULE reference cavity, the residual fractional frequency instabilities remain below 10^{-14} over 1000 s.

The residual frequency stability in our system is presently limited by a bump centered at ~8 s in the Allan deviation. The origin of this instability has not yet been identified. However, several possible limitations were analyzed.

i) In order to verify that no excess phase noise arises from power-to-phase noise conversion in the photodetection of the comb repetition rate and its harmonics, a power stabilization scheme was implemented. No significant difference was noticed neither in the phase noise, nor in the fractional frequency stability of the microwave signal generated using an Er:fiber comb.

ii) The power-to-frequency sensitivity of the ULE cavity resonance frequency to the variation of the incident optical power was measured to be -9.1 ± 0.3 Hz/µW. With this measured coefficient the contribution of the fluctuations of the laser power impinging onto the ULE cavity to the phase noise of the microwave signal generated using the Er:fiber comb was found to be negligible.

iii) The measured fractional frequency instability introduced by the optical fibers used to deliver the light from the ultra-stable laser to the combs was found to be negligible.

The phase noise of the microwave generated from the ERGO comb was observed to be up to 20 dB lower than obtained from the Er:fiber comb in a large Fourier frequency range of 100 Hz – 100 kHz offset from a 10 GHz carrier in similar conditions. The microwave phase noise obtained using the ERGO comb is still 10-25 dB higher than state-of-the-art results reported using Ti:Sa combs [4]. However, it is comparable or even 3 to 5 dB lower than the lowest phase noise reported for a microwave signal generated from a commercial Er:fiber comb by J. Millo *et al.* [75] without the implementation of special tools, such as pump-current based power lock [66] or an intra-cavity EOM [76].

The optical-to-microwave frequency division reported by J. Millo *et al.* [75] was done using a commercial Er:fiber comb similar to our Er:fiber comb, but in a different stabilization scheme. As the phase noise obtained with our Er:fiber comb was up to 20 dB higher than the phase noise reported in [76], it was decided to study the effect of the actuator used in the comb stabilization. We observed that when the CEO is subtracted from the heterodyne beat between the comb tooth and the ultra-stable laser as in [75], then the measured phase noise differs from the results obtained using a self-referenced comb without the CEO subtraction.

i) If the CEO is not stabilized and the feedback is applied to the PZT controlling the cavity length of the comb, then the measured phase noise degrades for the offset frequencies ranging from 10 Hz to 6 kHz from the carrier up to 50 dB at 10 Hz.
ii) If the CEO frequency is stabilized with the corrections applied to the pump current and the comb repetition rate is controlled via the feedback to the PZT, then the phase noise is comparable to the results obtained using a self-referenced comb without the CEO subtraction with a small difference around 2 kHz – 5 kHz offset from the carrier. We believe this difference to arise from the positive effect of the coupling between the servo-loops in an Er:fiber frequency comb discussed in Chapter 4.
iii) If the CEO frequency is not stabilized, but the feedback is applied to the laser current, then the phase noise bandwidth is increased and the phase noise is comparable to the results obtained using a self-referenced comb without the CEO subtraction with a slightly worse performance at 70 Hz – 7 kHz offset from the carrier.

Here we demonstrated the beneficial performances of the microwave signal generated using the ERGO comb in comparison to the Er:fiber comb and demonstrated the phase noise level comparable to the state-of-the-art CSO at 5 Hz – 100 Hz offset from the carrier. At higher frequencies the noise of ULISS has not yet been evaluated, but in comparison to a similar CSO, namely ELISA, the noise floor of the oscillator was overcome.

Chapter 7

Conclusion and outlook

In this thesis, an all-optical ultra-stable microwave generation using both an Er:fiber and a diode-pumped solid state laser (DPSSL) optical frequency combs has been studied, developed and characterized. Three key components are required for the generation and evaluation of such an all-optical ultra-stable microwave oscillator, consisting in (i) an optical frequency standard (an ultra-stable laser) having a high fractional frequency stability in the optical domain; (ii) an optical frequency comb acting as an optical-to-microwave frequency divider to transfer the relative stability of the optical standard into a microwave signal; and finally (iii) another highly stable microwave reference for comparison.

The core element of an all-optical microwave oscillator is the ultra-stable laser, an ultra-narrow linewidth laser obtained by frequency stabilization to a highly isolated reference cavity. The use of a relatively new laser technology, a planar-waveguide external cavity laser (PW-ECL), has been demonstrated for the realization of the ultra-stable laser in this work and was compared with an external-cavity diode laser (ECDL). The commercial PW-ECL was frequency-stabilized to an ultra-high finesse ULE cavity using the Pound-Drever-Hall method. An acousto-optic modulator was used to apply fast feedback signal to the laser as a result of the limited control bandwidth of the laser injection current.

A 2-layer thermal enclosure has been designed, built and characterized to ensure a high thermal insulation of the ULE cavity mounted under high-vacuum. The special emphasis put on the high homogeneity of the cavity temperature and on its high insulation from external temperature fluctuations resulted in a thermal time constant of more than 6 days.

The low-noise characteristics of the PW-ECL enabled also an accurate characterization of the narrow resonance of the Fabry-Perot cavity to be performed. By phase-locking this laser to a cavity-stabilized ECDL using feedback to the injection current only, a very low-noise probe laser was realized to characterize the narrow cavity resonance of 8.2 kHz, not only in terms of its lineshape, but also by measuring its complete dynamic response to a frequency modulation, both in reflection and in transmission. Due to the unavailability of a second independent ultra-stable laser or optical cavity, it has not been possible to evaluate the characteristics of the ultra-stable laser directly in the optical domain. However, the laser has been evaluated indirectly through the ultra-stable microwave signal measured after optical frequency division with a frequency comb as discussed later.

The second important component for the all-optical microwave generation is the optical frequency comb acting as an optical-to-microwave frequency divider. In this thesis, a novel DPSSL comb in the 1.5-µm spectral region, referred to as ERGO, has been extensively characterized before being used for microwave generation. This comb is the first self-referenced DPSSL comb demonstrated in this spectral region, where Er:fiber combs constitute a widely deployed technology. The issue of self-referencing is important for ultra-stable microwave generation, as all the degrees of freedom of the comb need to be stabilized in order to transfer the relative frequency stability of the reference laser to the microwave domain with a high fidelity.

The high Q-factor of the ERGO laser resonator results in a low-noise CEO-beat and leads to the narrowest free-running CEO linewidth observed in this spectral region, with less than 4 kHz FWHM. The excellent noise properties of the ERGO comb allow for a tight phase-lock of the CEO frequency to a 20-MHz external reference using pump-power control with a feedback bandwidth of less than 5.5 kHz. The resulting CEO integrated phase noise of 0.72 rad rms is one of the smallest values obtained to date in the 1.5-µm region, especially for such a low servo-loop bandwidth. This low phase noise make this comb extremely attractive for low-noise microwave generation and the ERGO represents a promising alternative to Er:fiber combs in this spectral range.

A second comb used in this work is a widely-deployed commercial Er:fiber comb from Menlosystems. This comb was further characterized in terms of noise and dynamic response to a modulation of the pump power and cavity length, leading to a

better understanding of the coupling between the feedback loops used to stabilize the two degrees of freedom of the comb, i.e. the repetition rate (via a PZT controlling the cavity length) and the CEO (via pump diode current). This coupling leads to a reduction of the frequency noise of the stabilized comb compared to the hypothetical case where no coupling would occur, as a result of the positive impact of the CEO servo-loop to the noise of the repetition rate. Another outcome from this study is the modification introduced to the elastic tape model describing the noise contributions in the combs [59]. It was thus demonstrated that in the free-running comb, the noise contributions to the CEO and to the repetition rate have different impact at different modulation frequencies, resulting in a modification of the generally-considered comb fixed point by a frequency-dependent quasi-fixed point. This represents a new assessment about the noise distribution in a frequency comb, which has not been previously considered to the best of our knowledge and which is an outcome of the measurements of the dynamic response of the comb.

A comparison of the noise performances of the Er:fiber and ERGO combs stabilized to the same RF reference showed that the noise of an optical comb line was only limited by the repetition rate in the ERGO comb, whereas the contribution of the CEO was found to be negligible. In comparison, the CEO has a large contribution to the noise of an optical comb line in the Er:fiber comb, despite the positive effect of the cross-coupling between the stabilization loops that leads to a significantly reduction of the phase noise of an optical comb line. The CEO was assessed to contribute only 10^{-15} at 1 s averaging time to the fractional frequency stability of an optical comb line in the ERGO comb, which makes this comb attractive for ultra-low noise microwave generation.

Finally, ultra-stable microwave has been generated using each comb, phase-locked to the optical reference using feedback to the PZT of the ultrafast laser resonator. The performances of the microwave signals generated with each comb have been characterized by comparison with the transportable cryocooled sapphire oscillator ULISS [3], developed at Femto-ST in Besançon and moved to Neuchâtel for a measurement campaign. This measurement campaign was the first field tests of this transportable CSO. A similar relative frequency stability of 5×10^{-15} at 1 s was achieved with both combs and is believed to be limited by excess noise of the ultra-stable laser, whose origin has not yet been identified and needs further investiga-

tions. When removing the linear drift of ~70 mHz/s, attributed to the isothermal "creep" of the ULE reference cavity, the residual fractional frequency instabilities remain below 10^{-14} over 1000 s.

In terms of phase noise, the microwave generated from the ERGO comb showed up to 20 dB better performances than obtained from the Er:fiber comb in a large Fourier frequency range of 100 Hz – 100 kHz offset from the 10-GHz carrier in similar locking conditions. The phase noise obtained using the ERGO comb is still 10 to 25 dB higher than state-of-the-art results reported using Ti:Sa combs [4]. However, it is comparable or even 3 to 5 dB better than the lowest phase noise reported for a microwave signal generated from a commercial Er:fiber comb by J. Millo *et al.* [75] without the implementation of special tools, such as pump current-based power stabilization [66] or the use of an intra-cavity EOM for high-bandwidth stabilization of the comb to the ultra-stable laser [76]. The state-of-the-art microwave generation with fiber combs was obtained in NIST by F. Quinlan *et al.* [76] with a reported phase noise of −100 dBc/Hz at 1 Hz offset from a 10 GHz carrier, achieved using an intra-cavity EOM. That is still almost 10 dB lower than the phase noise obtained with the ERGO comb but obtained with a much higher feedback bandwidth.

These results demonstrate the beneficial use of the ERGO comb for ultra-stable microwave generation in comparison to a commercial Er:fiber comb. A phase noise level comparable to the state-of-the-art CSO at 5 Hz – 100 Hz offset from the carrier (at 10 GHz) was also demonstrated, whereas one could not distinguish whether the measured phase noise was limited by the ERGO comb microwave or by ULISS at higher offset frequencies, due to the lack of a precise knowledge of the present phase noise of the CSO oscillator.

The overall results obtained in this thesis show that DPSSL frequency combs constitute a valuable alternative to the well-established fiber comb technology. Apart from the lower free-running frequency noise that results from the high Q-factor of their optical resonator, they can access substantially higher average power levels than unamplified femtosecond fiber oscillators and much higher repetition rates in the multi-GHz range [86], which is an important property in applications such as ultra-stable microwave generation or for the calibration of astronomical spectrometers [116].

Bibliography

1. K. Szymaniec, S.E. Park, G. Marra, and W. Chalupczak, *"First accuracy evaluation of the NPL-CsF2 primary frequency standard,"* Metrologia 47(4), 363–376 (2010).
2. B.C. Young, F.C. Cruz, W.M. Itano, and J.C. Bergquist, *"Visible lasers with subhertz linewidths,"* Phys. Rev. Lett., 82(19), 3799–3802 (1999).
3. S. Grop, B. Dubois, P.-Y. Bourgeois, Y. Kersalé, G. Haye, and V. Giordano, *"ULISS: a mobile cryogenic ultra-stable oscillator,"* Proc. of the 2011 EFTF/IFCS Joint Meeting, San Francisco (CA), US, May 2–5, 2011.
4. T.M. Fortier, M.S. Kirchner, F. Quinlan, J. Taylor, J.C. Bergquist, T. Rosenband, N. Lemke, A. Ludlow, Y. Jiang, C.W. Oates, and S. A. Diddams, *"Generation of ultrastable microwaves via optical frequency division,"* Nature Photon. 5(7), 425–429 (2011).
5. J.J. McFerran, E.N. Ivanov, A. Bartels, G. Wilpers, C.W. Oates, S.A. Diddams, and L. Hollberg, *"Low-noise synthesis of the microwave signals from an optical source,"* Electron. Lett. 41(11), 650–651 (2005).
6. G. Di Domenico, S. Schilt, and P. Thomann, *"Simple approach to the relation between laser frequency noise and laser line shape,"* Appl. Opt. 49, 4801–4807 (2010).
7. P.B. Gallion, and G. Debarge, *"Quantum phase noise and field correlation in single frequency semiconductor-laser systems,"* IEEE J. Quantum Electron. QE-20(4), 343–349 (1984).
8. C.H. Henry, *"Theory of the linewidth of semiconductor-lasers,"* IEEE J. Quantum Electron. QE-18(2), 259–264 (1982),
9. A.L. Schawlow, and C.H. Townes, *"Infrared and optical masers,"* Phys. Rev. 112(6), 1940–1949 (1958).
10. D.S. Elliott, R. Roy, and S.J. Smith, *"Extra-cavity laser band-shape and bandwidth modification,"* Phys. Rev. A 26(1), 12–18 (1982).
11. S. Spießberger, M. Schiemangk, A. Wicht, H. Wenzel, G. Erbert, and G. Tränkle, *"DBR laser diodes emitting near 1064 nm with a narrow intrinsic linewidth of 2 kHz,"* Appl. Phys. B 104 (4), 813–818 (2011).
12. S. Bartalini, S. Borri, P. Cancio, A. Castrillo, I. Galli, G. Giusfredi, D. Mazzotti, L. Gianfrani, and P. De Natale, *"Observing the intrinsic linewidth of a quantum-cascade laser: beyond the Schawlow-Townes limit,"* Phys. Rev. Lett. 104(8), 083904 (2010).
13. S.T. Cundiff, and J. Ye, *"Colloquium: Femtosecond optical frequency combs,"* Rev. Mod. Phys. 75(1), 325–342 (2003).
14. L. Tombez, J. Di Francesco, S. Schilt, G. Di Domenico, J. Faist, P. Thomann, and D. Hofstetter, *"Frequency noise of free-running 4.6 μm distributed feedback quantum cascade lasers near room temperature,"* Opt. Lett. 36(16), 3109–3111 (2011).

15. G. Galzerano, A. Gambetta, E. Fasci, A. Castrillo, M. Marangoni, P. Laporta, and L. Gianfrani, *"Absolute frequency measurement of a water-stabilized diode laser at 1.384 μm by means of a fiber frequency comb,"* Appl. Phys B 102(4), 725–729(2011).
16. P. Tourrenc, *"Caractérisation et modélisation du bruit d'amplitude optique, du bruit de fréquence et de la largeur de raie de VCSELs monomode,"* Ph.D. dissertation (Université de Montpellier II, 2005).
17. D.M. Baney, and W.V. Sorin, *"High resolution optical frequency analysis,"* in *Fiber optic test and measurements*, Ed. D. Derickson, (Prentice Hall, N. J. 1998), Chap. 5.
18. L.D. Turner, K.P. Weber, C.J. Hawthorn, and R.E. Scholten, *"Frequency noise characterisation of narrow linewidth diode lasers,"* Opt. Comm. 201(4-6), 391–397 (2002).
19. M. Prevedelli, T. Freegarde, T.W. Hänsch, *"Phase-locking of grating-tuned diode-lasers,"* Appl. Phys. B 60(2-3), S241–S248 (1995).
20. E. Rubiola, *"The Leeson effect – Phase Noise in Quasilinear Oscillators,"* in *Phase noise and frequency stability in oscillators*, Cambridge University Press, 2008, Chap. 3.
21. Y.Y. Jiang, A.D. Ludlow, N.D. Lemke, R.W. Fox, J.A. Sherman, L.-S. Ma, and C.W. Oates, *"Making optical clocks more stable with 10^{-16} level laser stabilization,"* Nature Photon. 5(3), 158–161 (2011).
22. M. Armano *et al.*, *"LISA Pathfinder: the experiment and the route to LISA,"* Class. Quantum Grav. 26(9), 094001 (2009).
23. K. Predehl, G. Grosche, S.M.F. Raupach, S. Droste, O. Terra, J. Alnis, Th. Legero, T.W. Hänsch, Th. Udem, R. Holzwarth, and H. Schnatz, *"A 920-kilometer optical fiber link for frequency metrology at the 19th decimal place,"* Science 336(6080) 441–444 (2012).
24. S.A. Webster, M. Oxborrow, S. Pugla, J. Millo, and P. Gill, *"Thermal-noise-limited optical cavity,"* Phys. Rev. A 77(3), 033847 (2008).
25. A.D. Ludlow, X. Huang, M. Notcutt, T. Zanon-Willette,, S.M. Foreman, M.M. Boyd, S. Blatt, and J. Ye, *"Compact, thermal-noise-limited optical cavity for diode laser stabilization at 1×10^{-15},"* Opt. Lett. 32(6), 641–643 (2007).
26. R.W.P. Drever, J.L. Hall, F.V. Kowalski, J. Hough, G.M. Ford, A.J. Munley, and H. Ward, *"Laser phase and frequency stabilization using an optical resonator,"* Appl. Phys. B. 31(2), 97–105 (1983).
27. M. Alalusi, P. Brasil, S. Lee, P. Mols, L. Stolpner, A. Mehnert, and S. Li, *"Low noise planar external cavity laser for interferometric fiber optic sensors,"* Proc. SPIE 7316, 73160X (2009).
28. K. Numata, J. Camp, M. A. Krainak, and L. Stolpner, *"Performance of planar-waveguide external cavity laser for precision measurements,"* Opt. Express 18(22), 22781–22788 (2010).
29. C. Clivati, A. Mura, D. Calonico, F. Levi, G.A. Costanzo, C.E. Calosso, and A. Godone, *"Planar-waveguide external cavity laser stabilization for an optical link with 10^{-19} frequency stability,"* IEEE Trans. Ultrason. Ferroelectr. Freq. Control 58(12), 2582–2587 (2011).
30. F. Riehle, *Frequency Standards, Basics and Applications* (Wiley, 2004), Chap. 2.
31. O. Svelto *et al.*, *"Lasers and Coherent Light Sources,"* in *Springer handbook of lasers and optics*, Ed. F. Träger, Springer (2007), Chap.11.
32. M.G. Littman, and H.J. Metcalf, "*Spectrally narrow pulsed dye laser without beam expander*," Appl. Optics, 17(14), 2224–2227 (1978).

33. User's guide.Model TLB 6300-LN The Velocity tunable diode laser. http://assets.newport.com/webDocuments-EN/images/15224.pdf.
34. L. Stolpner, S. Lee, S. Li, A. Mehnert, P. Mols, and S. Siala, *"Low noise planar external cavity laser for interferometric fiber optic sensors,"* 19th International Conference on Optical Fiber Sensors, Proc. SPIE 7004, 700457 (2008).
35. J. Millo, D.V. Magalhães, C. Mandache, Y. Le Coq, E.M.L. English, P.G. Westergaard, J. Lodewyck, S. Bize, P. Lemonde, and G. Santarelli, *"Ultrastable lasers based on vibration insensitive cavities,"* Phys. Rev. A 79(5), 053829 (2009).
36. K. Numata, A. Kemery, and J. Camp, *"Thermal-noise limit in the frequency stabilization of lasers with rigid cavities,"* Phys. Rev. Lett. 93(25), 250602 (2004).
37. S.A. Akhmanov, and S. Yu. Nikitin, *"The diffraction of paraxial beams,"* in *Physical optics*, Oxford University Press 1997, Chap. 14.
38. J. Alnis, A. Matveev, N. Kolachevsky, Th. Udem, and T.W. Hänsch *"Subhertz linewidth diode lasers by stabilization to vibrationally and thermally compensated ultralow-expansion glass Fabry-Pérot cavities,"* Phys. Rev. A 77, 053809 (2008).
39. K.P. Birch and M.J. Downs, *"An updated Edlèn equation for the refractive index of air,"* Metrologia, 30(3), 155–162 (1993).
40. T.W. Hänsch, *"Nobel lecture: Passion for precision,"* Rev. of Modern Physics 78(4), 1297–1309 (2006).
41. J. Ye, H. Schnatz, and L.W. Hollberg, *"Optical frequency combs: From frequency metrology to optical phase control,"* IEEE J. Sel. Top. Quantum Electron. 9(4), 1041–1058 (2003).
42. S.A. Diddams, Th. Udem, J.C. Bergquist, E.A. Curtis, R.E. Drullinger, L. Hollberg, W.M. Itano, W.D. Lee, C.W. Oates, K.R. Vogel, and D.J. Wineland, *"An Optical Clock Based on a Single Trapped $^{199}Hg^{+}$ Ion,"* Science 293, 825–828 (2001).
43. P.G. Westergaard, J. Lodewyck, L. Lorini, A. Lecallier, E.A. Burt, M. Zawada, J. Millo, and P. Lemonde, *"Lattice-induced frequency shifts in Sr optical lattice clocks at the 10^{-17} level,"* Phys. Rev. Lett. 106(21), 210801 (2011).
44. T. Rosenband *et al.*, *"Frequency ratio of Al+ and Hg+ single-ion optical clocks; Metrology at the 17th decimal place,"* Science 319(5871), 1808–1812 (2008).
45. U. Sterr, C. Degenhardt, H. Stoehr, C. Lisdat, H. Schnatz, J. Helmcke, F. Riehle, G. Wilpers, C. Oates, and L. Hollberg, *"The optical calcium frequency standards of PTB and NIST,"* C. R. Physique 5(8), 845–855 (2004).
46. G. Steinmeyer, D.H. Sutter, L. Gallmann, N. Matuschek, and U. Keller, *"Frontiers in ultrashort pulse generation: pushing the limits in linear and nonlinear optics,"* Science 286(5444), 1507–1512 (1999).
47. U. Keller, *"Ultrafast solid-state laser oscillators: a success story for the last 20 years with no end in sight,"* Appl. Phys. B 100(1), 15–28 (2010).
48. U. Keller, *"Recent developments in compact ultrafast lasers,"* Nature 424(6950), 831–838 (2003).
49. H.R. Telle, G. Steinmeyer, A.E. Dunlop, J. Stenger, D.H. Sutter, and U. Keller, *"Carrier-envelope offset phase control: A novel concept for absolute optical frequency measurement and ultrashort pulse generation,"* Appl. Phys. B 69(4), 327–332 (1999).

50. R. Holzwarth, T. Udem, T.W. Hänsch, J.C. Knight, W.J. Wadsworth, and P.S.J. Russell, *"Optical frequency synthesizer for precision spectroscopy,"* Phys. Rev. Lett. 85(11), 2264–2267 (2000).
51. D.J. Jones, S.A. Diddams, J.K. Ranka, A. Stentz, R.S. Windeler, J.L. Hall, and S.T. Cundiff, *"Carrier-envelope phase control of femtosecond mode-locked lasers and direct optical frequency synthesis,"* Science 266, 635–639 (2000).
52. R. Ell, U. Morgner, F.X. Kärtner, J.G. Fujimoto, E.P. Ippen, V. Scheuer, G. Angelow, T. Tschudi, M.J. Lederer, A. Boiko, and B. Luther-Davies, *"Generation of 5 fs pulses and octave-spanning spectra directly from a Ti:sapphire laser,"* Opt. Lett. 26, 373–375 (2001).
53. A. Bartels, D.C. Heinecke, and S.A. Diddams, *"10 GHz self-referenced optical frequency comb,"* Science 326, 681 (2009).
54. B.R. Washburn, S.A. Diddams, N.R. Newbury, J.W. Nicholson, M.F. Yan, and C.G. Jørgensen, *"Phase-locked, erbium-fiber-laser-based frequency comb in the near infrared,"* Opt. Lett. 29, 250–252 (2004).
55. G. Marra, R. Slavik, H.S. Margolis, S.N. Lea, P. Petropoulos, D.J. Richardson, and P. Gill, *"High-resolution microwave frequency transfer over an 86-km-long optical fiber network using a mode-locked laser,"* Opt. Lett. 36(4), 511–513 (2011).
56. J. Rauschenberger, T.M. Fortier, D.J. Jones, J. Ye, and S.T. Cundiff, *"Control of the frequency comb from a mode-locked Erbium-doped fiber laser,"* Opt. Express 10(24), 1404–1410 (2002).
57. R. Paschotta, A. Schlatter, S.C. Zeller, H.R. Telle, and U. Keller, "*Optical phase noise and carrier-envelope offset of mode-locked lasers*," Appl. Phys. B 82, 265–273 (2006).
58. E. Benkler, H.R. Telle, A. Zach, and F. Tauser, *"Circumvention of noise contributions in fiber laser baser frequency combs,"* Opt. Express 13(15), 5662–5668 (2005).
59. H.R. Telle, B. Lipphardt, and J. Stenger, *"Kerr-lens, mode-locked lasers as transfer oscillators for optical frequency measurements,"* Appl. Phys. B 74, 1–6 (2002).
60. B.R. Washburn, W.C. Swann, and N.R. Newbury, *"Response dynamics of the frequency comb output from a femtosecond laser,"* Opt. Express 13 (26), 10622–10633 (2005).
61. K. Kim, J.W. Nicholson, M. Yan, J.C. Knight, N.R. Newbury, and S.A. Diddams, *"Characterization of frequency noise on a broadband infrared frequency comb using optical heterodyne techniques,"* Opt. Express 15(26), 17715–17723 (2007).
62. L. Hollberg, S. Diddams, A. Bartels, T. Fortier, and K. Kim, *"The measurement of optical frequencies,"* Metrologia 42, S105–S124 (2005).
63. F.W. Helbing, G. Steinmeyer, J. Stenger, H.R. Telle, and U. Keller, *"Carrier–envelope-offset dynamics and stabilization of femtosecond pulses,"* Appl. Phys. B. 74, S35–S42 (2002).
64. N. Newbury, and B. Washburn, *"Theory of the frequency comb output from a femtosecond fiber laser,"* IEEE J. Quantum Electron. 41(11), 1388 (2005).
65. W. Zhang, M. Lours, M. Fischer, R. Holzwarth, G. Santarelli, and Y. Le Coq, "*Characterizing a fiber-based frequency comb with electro-optic modulator*," IEEE Trans. Ultrason. Ferroelectr. Freq. Control, 59(3), 432–438 (2011).

66. W. Zhang, Z. Xu, M. Lours, R. Boudot, Y. Kersalé, A.N. Luiten, Y. Le Coq, and G. Santarelli, *"Advanced noise reduction techniques for ultra-low phase noise optical-to-microwave division with femtosecond fiber combs,"* IEEE Trans. Ultrason. Ferroelectr. Freq. Control, 58(5), 900–908 (2011).
67. D.R. Walker, T. Udem, C. Gohle, B. Stein, and T.W. Hänsch, *"Frequency dependence of the fixed point in a fluctuating frequency comb,"* Appl. Phys. B 89, 535–538 (2007).
68. N.R. Newbury, and W.C. Swann, *"Low-noise fiber-laser frequency combs,"* J. Opt. Soc. Am. B 24(8), 1756–1770 (2007).
69. N. Haverkamp, H. Hundertmark, C. Fallnich, and H.R. Telle, "*Frequency stabilization of mode-locked Erbium fiber lasers using pump power control*," Appl. Phys. B 78, 321–324 (2004).
70. J. Bechhoefer, "*Feedback for Physicists: A tutorial essay on control*," Rev. Mod. Phys. 77, 783–836 (2005).
71. E. Rubiola, and F. Vernotte, *"The cross-spectrum experimental method,"* http://arxiv.org/abs/1003.0113
72. D.C. Heinecke, A. Bartels, and S.A. Diddams, *"Offset frequency dynamics and phase noise properties of a self-referenced 10 GHz Ti:sapphire frequency comb,"* Opt. Express 19(19), 18440–18451 (2011).
73. S. Schilt, N. Bucalovic, V. Dolgovskiy, C. Schori, M. C. Stumpf, G. Di Domenico, S. Pekarek, A.E.H. Oehler, T. Südmeyer, U. Keller, and P. Thomann, *"Fully stabilized optical frequency comb with sub-radian CEO phase noise from a SESAM-modelocked 1.5-μm solid-state laser,"* Opt. Express 19(24), 24171–24181 (2011).
74. J.J. McFerran, W.C. Swann, B.R. Washburn, and N.R. Newbury, *"Suppression of pump-induced frequency noise in fiber-laser frequency combs leading to sub-radian f_{ceo} phase excursions,"* Appl. Phys. B 86(2), 216–227 (2007).
75. J. Millo, M. Abgrall, M. Lours, E.M.L. English, H. Jiang, J. Guéna, A. Clairon, S. Bize, Y. Le Coq, G. Santarelli, and M.E. Tobar, *"Ultra-low noise microwave generation with fiber-based optical frequency comb and application to atomic fountain clock,"* Appl. Phys. Lett. 94, 141105 (2009).
76. F. Quinlan, T.M. Fortier, M.S. Kirchner, J.A. Taylor, M.J. Thorpe, N. Lemke, A.D. Ludlow, Y. Jiang, and S.A. Diddams, *"Ultralow phase noise microwave generation with an Er:fiber-based optical frequency divider,"* Opt. Lett. 36(16), 3260–3262 (2011).
77. J.J. McFerran, W.C. Swann, B.R. Washburn, and N.R.Newbury, *"Elimination of pump-induced frequency jitter on fiber-laser frequency combs,"* Opt. Lett. 31(13), 1997–1999 (2006).
78. I. Hartl, G. Imeshev, M.E. Fermann, C. Langrock, and M.M. Fejer, *"Integrated self-referenced frequency-comb laser based on a combination of fiber and waveguide technology,"* Opt. Express 13(17), 6490–6496 (2005).
79. Y. Nakajima, H. Inaba, K. Hosaka, K. Minoshima, A. Onae, M. Yasuda, T. Kohno, S. Kawato, T. Kobayashi, T. Katsuyama, and F.-L. Hong, *"A multi-branch, fiber-based frequency comb with millihertz-level relative linewidths using an intra-cavity electro-optic modulator,"* Opt. Express 18(2), 1667–1676 (2010).

80. E. Baumann, F.R. Giorgetta, J.W. Nicholson, W.C. Swann, I. Coddington, and N.R. Newbury, *"High-performance, vibration-immune, fiber-laser frequency comb,"* Opt. Lett. 34(5), 638–640 (2009).
81. U. Keller, D.A.B. Miller, G.D. Boyd, T.H. Chiu, J.F. Ferguson, and M.T. Asom, *"Solid-state low-loss intracavity saturable absorber for Nd:YLF lasers: an antiresonant semiconductor Fabry-Perot saturable absorber,"* Opt. Lett. 17, 505–507, (1992).
82. U. Keller, K.J. Weingarten, F.X. Kärtner, D. Kopf, B. Braun, I.D. Jung, R. Fluck, C. Hönninger, N. Matuschek, and J. Aus der Au, *"Semiconductor saturable absorber mirrors (SESAMs) for femtosecond to nanosecond pulse generation in solid-state lasers,"* IEEE J. Sel. Top. Quantum Electron. 2(3), 435–453 (1996).
83. T. Südmeyer, S.V. Marchese, S. Hashimoto, C.R.E. Baer, G. Gingras, B. Witzel, and U. Keller, *"Femtosecond laser oscillators for high-field science,"* Nature Photonics 2, 599–604 (2008).
84. A.E.H. Oehler, M.C. Stumpf, S. Pekarek, T. Südmeyer, K.J. Weingarten, and U. Keller, *"Picosecond diode-pumped 1.5 μm Er:Yb:glass lasers operating at 10-100 GHz repetition rate,"* Appl. Phys. B 99, 53–62 (2010).
85. L. Krainer, R. Paschotta, S. Lecomte, M. Moser, K. J. Weingarten, and U. Keller, *"Compact Nd:YVO_4 lasers with pulse repetition rates up to 160 GHz,"* IEEE J. Quantum Electron. 38, 1331–1338 (2002).
86. S. Pekarek, C. Fiebig, M.C. Stumpf, A.E.H. Oehler, K. Paschke, G. Erbert, T. Südmeyer, and U. Keller, *"Diode-pumped gigahertz femtosecond Yb:KGW laser with a peak power of 3.9 kW,"* Opt. Express 18, 16320–6326 (2010).
87. S. Yamazoe, M. Katou, T. Adachi, and T. Kasamatsu, *"Palm-top-size, 1.5 kW peak-power, and femtosecond (160 fs) diode-pumped mode-locked Yb^{+3}:$KY(WO_4)_2$ solid-state laser with a semiconductor saturable absorber mirror,"* Opt. Lett. 35, 748–750 (2010).
88. M.C. Stumpf, S. Pekarek, A.E.H. Oehler, T. Südmeyer, J.M. Dudley, and U. Keller, *"Self-referencable frequency comb from a 170-fs, 1.5-μm solid-state laser oscillator,"* Appl. Phys. B 99(3), 401–407 (2010).
89. G. Karlsson, F. Laurell, J. Tellefsen, B. Denker, B. Galagan, V. Osiko, and S. Sverchkov, *"Development and characterization of Yb-Er laser glass for high average power laser diode pumping,"* Appl. Phys. B 75, 41–46 (2002).
90. R. Wu, J.D. Myers, M.J. Myers, and C. Rapp, *"Fluorescence lifetime and 980nm pump energy transfer dynamics in erbium and ytterbium co-doped phosphate laser glasses,"* Proc. SPIE 4968, 11–17 (2003).
91. F.X. Kärtner, I.D. Jung, and U. Keller, *"Soliton mode-locking with saturable absorbers,"* IEEE J. Sel. Top. Quantum Electron. 2(3), 540–556 (1996).
92. A. Schlatter, B. Rudin, S.C. Zeller, R. Paschotta, G.J. Spühler, L. Krainer, N. Haverkamp, H.R. Telle, and U. Keller, *"Nearly quantum-noise-limited timing jitter from miniature Er:Yb:glass lasers,"* Opt. Lett. 30(12), 1536–1538 (2005).
93. F.W. Helbing, G. Steinmeyer, and U. Keller, *"Carrier-envelope offset phase-locking with attosecond timing jitter,"* IEEE J. Sel. Top. in Quantum Electron. 9(4), 1030–1040 (2003).

94. K.W. Holman, R.J. Jones, A. Marian, S.T. Cundiff, and J. Ye, *"Detailed studies and control of intensity-related dynamics of femtosecond frequency combs from mode-locked Ti:sapphire lasers,"* IEEE J. of Sel. Top. in Quantum Electron. 9(4), 1018–1024 (2003).
95. T. Fuji, J. Rauschenberger, C. Gohle, A. Apolonski, T. Udem, V.S. Yakovlev, G. Tempea, T.W. Hänsch, and F. Krausz, *"Attosecond control of optical waveforms,"* New J. Phys. 7, 116 (2005).
96. H.M. Crespo, J.R. Birge, M.Y. Sander, E.L. Falcao-Filho, A. Benedick, and F.X. Kärtner, *"Phase stabilization of sub-two-cycle pulses from prismless octave-spanning Ti:sapphire lasers,"* J. Opt. Soc. Am. B 25(7), B147–B154 (2008).
97. A. Bartels, S.A. Diddams, C.W. Oates, G. Wilpers, J.C. Bergquist, W.H. Oskay, and L. Hollberg, *"Femtosecond-laser-based synthesis of ultrastable microwave signals from optical frequency references,"* Opt. Lett. 30(6), 667–669 (2005).
98. A. Haboucha, W. Zhang, T. Li, M. Lours, A.N. Luiten, Y. Le Coq, and G. Santarelli, *"An optical fibre pulse rate multiplier for ultra-low phase-noise signal generation,"* Opt. Lett. 36(18), 3654–3656 (2011).
99. S. Grop, P.-Y. Bourgeois, N. Bazin, Y. Kersalé, E. Rubiola, C. Langham, M. Oxborrow, D. Clapton, S. Walker, J. De Vicente, and V. Giordano, *"ELISA: A cryocooled 10 GHz oscillator with 10^{-15} frequency stability,"* Rev. Sci. Instrum. 81, 025102 (2010).
100. N.R. Nand, J.G. Hartnett, E.N. Ivanov, and G. Santarelli, *"Ultra-stable and very low noise signal source using a cryocooled sapphire oscillator for VLBI,"* IEEE Trans. Microw. Theory Tech. 59(11), 2978–2986 (2011).
101. D. Eliyahu, D. Seidel, and L. Maleki, *"Phase noise of a high performance OEO and an ultra low noise floor cross-correlation microwave photonic homodyne system,"* Proc. IEEE Frequency Control Symposium, 811–814 (2008).
102. M.J. Thorpe, L. Rippe, T.M. Fortier, M.S. Kirchner, and T. Rosenband, *"Frequency stabilization to 6×10^{-16} via spectral-hole burning,"* Nature Photonics 5, 688–693 (2011).
103. T. Kessler, C. Hagemann, C. Grebing, T. Legero, U. Sterr, F. Riehle, M.J. Martin, L. Chen, and J. Ye, *"A sub-40 mHz linewidth laser based on a silicon single-crystal optical cavity,"* arXiv:1112.3854v2
104. S.A. Diddams, M. Kirchner, T. Fortier, D. Braje, A.M. Weiner, and L. Hollberg, *"Improved signal-to-noise ratio of 10 GHz microwave signals generated with a mode-filtered femtosecond laser frequency comb,"* Opt. Express 17, 3331–3340 (2009).
105. E.N. Ivanov, S.A. Diddams, and L. Hollberg, *"Analysis of noise mechanisms limiting the frequency stability of microwave signals generated with a femtosecond laser,"* IEEE J. Sel. Topics Quantum Electron. 9(4), 1059–1065 (2003).
106. S. Grop, *"Elisa, une référence de fréquence ultrastable pour l'Agence Spatiale Européenne,"* Thesis FEMTO-ST - Franche-Comté Électronique Mécanique, Thermique et Optique - Sciences et Technologies 2010.
107. G. Marra, D. Henderson, and M. Oxborrow, *"Frequency stability and phase noise of a pair of X-band cryogenic sapphire oscillators,"* Meas. Sci. Technol. 18(5), 1224 (2007).

108. S. Grop, P.-Y. Bourgeois, R. Boudot, Y. Kersalé, E. Rubiola, and V. Giordano, *"10 GHz cryocooled sapphire oscillator with extremely low phase noise,"* Electron. Lett. 46(6), 420–422 (2010).
109. J.G. Hartnett, N.R. Nand, and C. Lu, *"Ultra-low-phase-noise cryocooled microwave dielectric-sapphire-resonator oscillators,"* Appl. Phys. Lett. 100, 183501 (2012).
110. R.V. Pound, *"Electronic Frequency Stabilization of Microwave Oscillators,"* Rev. Sci. Instrum. 17, 490 (1946).
111. S. Grop, P.-Y. Bourgeois, E. Rubiola, W. Schäfer, J. De Vicente, Y. Kersalé, and V. Giordano, *"Frequency synthesis chain for ESA deep space network,"* Electron. Lett. 47(6), 386–388 (2011).
112. S. Grop, B. Dubois, J.L. Masson, G. Haye, P.Y. Bourgeois, Y. Kersalé, E. Rubiola, and V. Giordano, *"ULISS project: First comparison of two cryocooled sapphire oscillators at the 10^{-15} level,"* Proc. of the 2012 IEEE International Frequency Control Symposium, Baltimore, May 21-24, 2012.
113. S. Schilt, V. Dolgovskiy, N. Bucalovic, C. Schori, M.C. Stumpf, G. Di Domenico, S. Pekarek, A.E.H. Oehler, T. Südmeyer, U. Keller, and P. Thomann, *"Noise properties of an optical frequency comb from a SESAM-mode-locked 1.5-µm solid-state laser stabilized to the 10^{-13} level,"* Appl. Phys. B 109(3), 391–402 (2012).
114. W. Zhang, Z. Xu, M. Lours, R. Boudot, Y. Kersalé, G. Santarelli, and Y. Le Coq, *"Sub-100 attoseconds stability optics-to-microwave,"* Appl. Phys. Lett. 96, 211105 (2010).
115. H. Jiang, F. Kéfélian, S. Crane, O. Lopez, M. Lours, J. Millo, D. Holleville, P. Lemonde, Ch. Chardonnet, A. Amy-Klein, and G. Santarelli, *"Long-distance frequency transfer over an urban fiber link using optical phase stabilization,"* J. Opt. Soc. Am. B 25(12), 2029–2035 (2008).
116. D.A. Braje, M.S. Kirchner, S. Osterman, T. Fortier, and S.A. Diddams, *"Astronomical spectrograph calibration with broad-spectrum frequency combs,"* Eur. Phys. J. D 48, 57–66 (2008).